Stability Assessments of Unbonded Fiber Reinforced Elastomeric Isolators

A Ph.D Thesis by

Simone Galano, M.Sc

Stability Assessments of Unbondend Fiber-Reinforced Elastomeric Isolators

Valutazioni sulla Stabilità degli Isolatori Fibro-Rinforzati non Vincolati

Simone Galano

University of Naples Federico II
University of California State Long Beach

Doctor of Philosophy in Engineering
(Ph.D Eng.)

Ph.D course in
`Structural, Geotechnical and Seismic Risk Engineering`

Coordinator Dr. Iunio Iervolino

ended in 31 December 2021 at
University of Naples Federico II
Polytechnic and Basic Science School
Department of Structures for Engineering and Architecture

Advisor Dr. Giorgio Serino
Co-Advisors Dr. Andrea Calabrese
Dr. Daniele Losanno

He stayed late on deck, after dinner, but that did not help him, for when he went below, he could not sleep. This surcease from life had failed him. It was too much. He turned on the electric light and tried to read. One of the volumes was a Swinburne. He lay in bed, glancing through its pages, until suddenly he became aware that he was reading with interest. He finished the stanza, attempted to read on, then came back to it. He rested the book face downward on his breast and fell to thinking. That was it. The very thing. Strange that it had never come to him before. That was the meaning of it all; he had been drifting that way all the time, and now Swinburne showed him that it was the happy way out. He wanted rest, and here was rest awaiting him. He glanced at the open port–hole. Yes, it was large enough. For the first time in weeks he felt happy. At last he had discovered the cure of his ill. He picked up the book and read the stanza slowly aloud:-

’From too much love of living,
From hope and fear set free,
We thank with brief thanksgiving
Whatever gods may be
That no life lives forever;
That dead men rise up never;
That even the weariest river
Winds somewhere safe to sea.’

He looked again at the open port. Swinburne had furnished the key. Life was ill, or, rather, it had become ill—an unbearable thing. "That dead men rise up never!" That line stirred him with a profound feeling of gratitude. It was the one beneficent thing in the universe. When life became an aching weariness, death was ready to soothe away to everlasting sleep. But what was he waiting for? It was time to go.

Jack London

ACKNOWLEDGMENTS

It is my duty here to express my heartfelt thanks to the people who've tried to help me during this journey.

My gratitude goes to my academic tutors, Dr. Giorgio Serino, Dr. Andrea Calabrese and Dr. Daniele Losanno. They gave me the opportunity for this Ph.D program, introduced me to scientific research and taught me a lot.

This thesis is mostly for my parents and my fiancée. Their support and their patience has been the basis of my work. They've always pushed me to do my best, and I hope this small milestone could be a repay for them.

Sincerely,
Simone

ABSTRACT

Fiber Reinforced Elastomeric Isolators (FREIs) have been proposed as a low-cost alternative to Steel Reinforced Elastomeric Isolators (SREIs), replacing the reinforcing steel plates with fiber fabrics. Despite having a similar elastic stiffness, fibers are cheaper and lighter than steel, and a simpler and faster manufacturing process, such as cold-vulcanization, can be used for FREIs instead of expensive hot-vulcanization process used for SREIs.

Over the last two decades, a significant research effort has been dedicated to point out the improvement on the response of elastomeric seismic devices when using fiber reinforcement. Several studies have highlighted the advantages of this technology over conventional seismic rubber bearings. Experimental tests and finite element analysis have shown how fiber reinforced bearings can exhibit a quite high vertical/horizontal stiffness ratio, an equivalent damping ratio higher than the SREIs and a lower horizontal stiffness.

When FREIs are unbonded to the top and bottom substructure, the bearings exhibit softening under imposed lateral deformations with or without instability. The stable/unstable response of the bearing depends on its mechanical and geometric parameters, and mostly on the secondary shape factor. Rather high secondary shape factor values ensure a stable response of the bearing, while below a limit threshold the response would be unstable, also depending on the shear modulus of the rubber and the vertical applied pressure.

Also, it is well known how the frequency of an elastomeric isolation

system depends on the vertical applied pressure. Thus, seismic isolation of lightweight structures with elastomeric devices is quite challenging. This limits the enforcing of FREIs to non-engineered buildings of developing countries.

Research studies available in the literature have focused on the vertical and horizontal response of the FREIs, but few of these have been dedicated to the influence of the different mechanical and geometric parameters on the stability of the FREIs under combined axial and shear loads. Even fewer studies have focused on the bearings stability under combined vertical and bidirectional horizontal loads. Finally, no studies were developed on how to change the lateral response of the FREIs from unstable to stable through proper modifications of the geometry.

This thesis studies the stability of fiber reinforced elastomeric isolators under simultaneous axial and both mono and bi-directional shear loads. Three types of FREIs are considered, namely i) infinite long strip-shaped, ii) rectangular-shaped and iii) square-shaped FREIs, through analytical, numerical and experimental approaches.

As a matter of fact, analytical equations involving the main parameters affecting the vertical response and the lateral stability are introduced. Easy-to-use design stability charts are provided and a simple strategy to improve the stability range of the different-shaped FREIs under combined vertical and horizontal loads are also shown.

Conclusions of this study could help disseminate knowledge on the use of FREIs for seismic base isolation of structures in both developed and developing countries.

SUMMARY

This thesis is divided into three parts:

Part I *Introduction*: introduces the main results on seismic protection systems achieved in previous research studies.

Part II *Finite Element Analyses of FREIs*: shows the results of an extensive numerical study by finite element modeling of fiber reinforced elastomeric isolators in three different configurations, i.e. infinite long strip-, rectangular-, and square-shaped FREIs.

Part III *Modified FREIs*: reports the outcome of experimental tests on lateral stability of a number of FREIs in different configurations, including modified geometry.

Through these three parts, seven chapters are developed.

Chapter 1 *State of art on low-cost seismic protection measures*. An overview of the main low-cost seismic protection measures for developing countries is presented. Base isolation systems are widely discussed, with emphasis on the use of both natural and recycled rubber in developing bearings of different shape. Sliding isolation systems and hybrid systems (such as geothecnical isolation) are also accounted.

Chapter 2 *Analytical Solutions for Rectangular, Square and Strip-shaped Fiber Reinforced Elastomeric Isolators*: the main analytical solutions for the vertical and horizontal response parameters

of three different-shaped FREIs (i.e. strip-, rectangular- and square-shaped FREIs) are shown. Also, equations from literature on buckling behavior and stable/unstable response of fiber reinforced bearings under axial and shear loads are accounted.

Chapter 3 *Stability of strip-shaped Fiber Reinforced Elastomeric Isolators.* The results of a large number of finite element analyses on infinite-long strip-shaped FREIs are presented. The vertical and horizontal responses of the bearings with different mechanical and geometric parameters are studied. An analytical-numerical comparison is also provided on the total vertical displacement at the top of a FREI under combined vertical and horizontal loads.

Chapter 4 *Variation of the vertical response of square-shaped Fiber Reinforced Elastomeric Isolators.* An analytical solution for the vertical response parameters of U-FREIs under combined axial and shear loads are provided starting from available literature results. The vertical stiffness and the effective compressive modulus of square-shaped U-FREIs are calculated accounting the horizontal deformation of the bearings. The analytical variations are then compared with outcomes from finite element analyses on square-shaped U-FREIs with different mechanical and geometric variable parameters.

Chapter 5 *Stability of square-shaped Fiber Reinforced Elastomeric Isolators.* The stability of square-shaped FREIs under axial and shear load is addressed. With combinations of different mechanical and geometric parameters, the key role of the secondary shape factor on the stable/unstable response of the bearing is investigated. The buckling load of square-shaped U-FREIs are computed both via analytical and numerical method, with a useful comparison. Finally, stability charts correlating the stable/unstable response of the bearing to the secondary shape factor are proposed.

Chapter 6 *Stability of rectangular-shaped Fiber Reinforced Elastomeric Isolators under bidiractional shear loads.* Recangular FREIs are studied under combined axial and bidirectional shear loads. Novel lateral response parameters of bearings under bidirectional shear load are introduced. The ruling influence on the stability of FREIs of the secondary shape factor in different horizontal directions is addressed in detail. Easy-to-use design formula for the maximum stable horizontal displacement of FREIs under axial and bidirectional shear loads is provided.

Chapter 7 *Tuning the horizontal response of Unbonded Fiber Reinforced Elastomeric Isolators.* An innovative technique allowing the modify of the lateral response of the U-FREIs and the improvement of the stability range are presented. Bearings with modified geometry with horizontal holes are subjected to experimental tests and the results compared with finite element analyses.

Chapter 8 *Conclusions & Outlook.* Conclusions to the proposed results and outlook for further developments are given.


Chapter 1
Chapter 2
Part I: Introduction
Chapter 6
Chapter 5
Chapter 4
Part II: Finite Element Analysis
Chapter 3
Stability Assesments of U-FREIs
Conclusions
Part III: Modified U-FREIs
Chapter 8
Chapter 7

LIST OF ACRONYMS

EB: Engineered Buildings

NEB: Non-Engineered Buildings

LRB: Laminated Rubber Bearing

FRB: Fiber Reinforced Bearing

SREI: Steel Reinforced Elastomeric Isolator

FREI: Fiber Reinforced Elastomeric Isolator

B-FREI: Bonded Fiber Reinforced Elastomeric Isolator

U-FREI: Unbonded Fiber Reinforced Elastomeric Isolator

SU-FREI: Stable Unbonded Fiber Reinforced Elastomeric Isolator

UU-FREI: Unstable Unbonded Fiber Reinforced Elastomeric Isolator

RR-FREI: Recycled Rubber Fiber Reinforced Elastomeric Isolator

FEA: Finite Element Analysis

FEM: Finite Element Model

LIST OF SYMBOLS

A_c	Contact area betweeen bearing and supports
t_r	Total rubber height
E_c	Effective compressive modulus of the rubber-reinforcement compound
S_1	Primary shape factor
G_e	Shear modulus of the elastomer
K_v	Vertical stiffness of the FREI
ν_e	Poisson's ratio of the elastomer
E_f	Young's modulus of the fiber reinforcement
t_f	Equivalent thickness of the fiber reinforcement
t_e	Thickness of the single elastomeric layer

ν_f	Poisson’s ratio of the fiber reinforcement
$2a$	Base side of a rectangular-shaped FREI in the x direction
$2b$	Base side of a rectangular-shaped FREI in the y direction
K	Bulk modulus of the elastomer
K_H	Horizontal stiffness of the FREI
F_v	Vertical force applied to a FREI
δ_v	Vertical displacement
σ_v	Vertical pressure applied to a FREI
H	Total height of a FREI
δ_H	Horizontal displacement
F_H	Horizontal response force of a FREI
S_2	Secondary shape factor

CONTENTS

LIST OF FIGURES

LIST OF TABLES

Part I

Introduction

CHAPTER 1

STATE OF ART ON LOW-COST SEISMIC PROTECTION MEASURES

Summary

This chapter collects the main information available in the literature on low-cost seismic protection measures. The techniques proposed for the protection of the so-called "non-engineered buildings", typical of rural areas of developing countries, are illustrated. The information in this chapter is part of the in progress paper [1].

1.1 Introduction

During the last decades, in the largest earthquakes most casualties occurred in rural areas of developing countries, i.e. countries with a less developed industrial base and a low Human Development Index [2]. According to World Bank most of this type of countries are in Asia and Latin America [3].

In the last 25 years, among Indonesia, Haiti, Nepal, Pakistan, India, Iran and Afghanistan, more than half a million people have lost their lives due to the tragic seismic event occurred (**Table 1.1**).

Table 1.1: List of deadliest earthquakes in the last 25 years [5].

N°	Fatalities	Magnitude	Location	Event	Date
1	227,898	9.1	Indonesia	2004 Indian Ocean Earthquake and tsunami	12/26/2004
2	160,000	7	Haiti	2010 Haiti earthquake	01/12/2010
3	87,587	7.9	China	2008 Sichuan earthquake	05/12/2008
4	87,351	7.9	Pakistan	2005 Kashmir earthquake	10/08/2005
5	26,271	6.6	Iran	2003 Bam earthquake	12/26/2003
6	20,896	9	Japan	2011 Tōhoku earthquake and tsunami	03/11/2011
7	20,085	7.7	India	2001 Gujarat earthquake	26/01/2001
8	8,964	7.8	Nepal	2015 Nepal earthquake	04/25/2015
9	5,782	6.4	Indonesia	2006 Yogyakarta earthquake	05/26/2006
10	4,340	7.5	Indonesia	2018 Sulawesi earthquake and tsunami	09/28/2018
11	2,968	6.9	China	2010 Yoshu earthquake	04/13/2010
12	2,266	6.8	Algeria	2003 Boumerdès earthquake	05/21/2003
13	2,189	7.2	Haiti	2021 Haiti earthquake	08/14/2021
14	1,313	8.6	Indonesia	2005 Nias-Simeulue earthquake	03/28/2005
15	1,115	7.6	Indonesia	2009 Sumatra earthquake	09/30/2009
16	1,000	7.4	Afghanistan	2002 Hindu Kush earthquakes	03/25/2002

In these countries, several factors contribute to increasing seismic vulnerability: growing populations, uncontrolled development in marginal areas, faulty constructions, local governments lacking of technical qualified staff and funds, slow code updating, illegalities in construction etc. [4].

Buildings can be divided into two main categories, namely *engineered buildings* (EB) and *non-engineered buildings* (N-EB), their percentages being quite different in developed, developing, and underdeveloped countries. Engineered constructions are the result of a process that involves different types of professional figures. They are designed to be durable and safe and built following the most recent engineering techniques implemented in modern seismic design codes. Non-engineered buildings are those which are *spontaneously and informally constructed in various countries in the traditional manner without any or little intervention by qualified architects and engineers in their design* [6].

Non-engineered buildings con be divided into two categories [7]:

i N-EB built according to the culture and using the typical materials of the area in which they arise, also called *indigenous* or *vernacular buildings* (**Figure 1.1 (a)**). Such buildings typically use field stone, baked brick, concrete block, adobe or rammed earth and wood (or a combination of these traditional

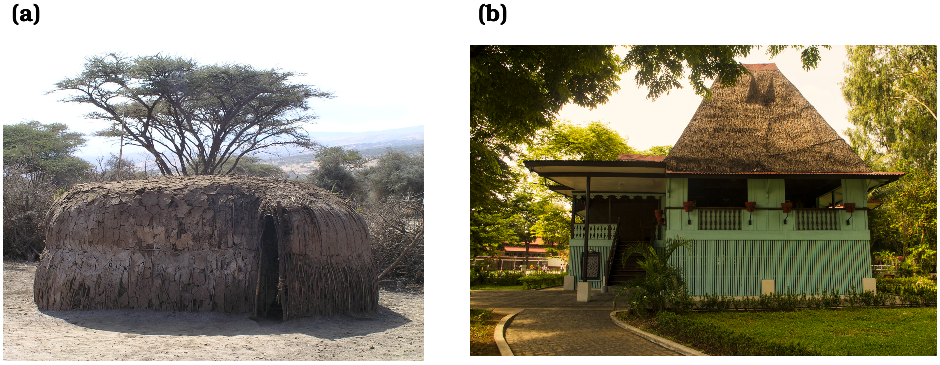

Figure 1.1: Examples of Non Engineered-Buildings: (a) *Maasai house* in Tanzania (indigenous houses), (b) *nipa hut*, traditional house of the Philippines (from [8]).

materials locally available) in the construction of the walls; cement, lime or clay mud are used for the mortars [6].

ii Single-family residences and small commercial structures built by local landowners or craftsmen without engineering or architectural assistance (**Figure 1.1 (b)**). This category includes buildings with load-bearing masonry walls, stud wall and brick nogged constructions in timber and composite constructions that use combinations of load-bearing walls and masonry pillars, reinforced concrete, wood and similar [7].

The seismic protection of non-engineered buildings is a major concern since in seismic areas of developing world more than 90% of the population still lives and works in such buildings and most of the loss of human lives during earthquakes occurred due to their failure [9]. These types of buildings are prevalent in rural areas of countries with a high seismic risk; indeed, countries with many people below the poverty threshold living in N-EB appear on the list of the deadliest earthquakes (**Table 1.1**).

Alongside the seismic protection of non-engineered buildings, an additional challenge may be to protect the valuable architecture of developing countries. Countries of the Middle East, Far East or Latin America are home to millenary historical artifacts, often exposed to the natural disasters' risks as seen for instance in Nepal or Peru [9].

Scientific research has moved and is moving towards the mitigation of seismic risk in less developed or developing countries. In this chapter a review of the main low-cost seismic protection techniques with rubber is presented. A large part relating to the strand of elastomeric seismic isolation is reported, accounting the developments made by researchers to reduce manufacturing and installation costs. Hence, hybrid systems that modify the properties of classical structures, such as foundations, are also recalled.

1.2 Advances in seismic protection in developing countries

Typically, in developing countries it is easy to recognize highly populated areas with rich residential neighborhoods, and rural areas with a high rate of people below the poverty threshold. As said, in these rural areas the constructions are built on local experience and poorness hampers access to high quality and certified materials. Therefore, solutions for seismic risk's mitigation must be easily accessible and low-cost. This target could be achieved using low-cost seismic-protection devices.

Different approaches have been proposed in the literature, either as an evolution of the already known and used seismic-protection devices, or as a development of alternative techniques.

1.2.1 Seismic Base Isolation

Base isolation basically consists of interposing a layer with low horizontal stiffness between the foundation and the structure. This allows to decouple the structure from the ground motion induced by the earthquake [10]. The best known and most popular isolation systems consist of rubber bearing and/or sliding devices. In most cases, the individual devices are very large, heavy and expensive.

Their manufacturing process is lengthy and expensive, and on-site installation is also costly [11].

Apparently, the structures can be decoupled from ground motions using a number of deformable devices. Starting from this idea, several proposals have been put forward for low-cost seismic isolation systems.

1.2.1.1 Fiber-Reinforced Elastomeric Isolators (FREIs)

Common rubber bearings consist of alternating layers of elastomer and thin steel sheets, and two thick steel plates are placed at the top and the bottom (**Figure 1.2 (a)**). They are commonly called Laminated Rubber Bearings (LRBs) or Steel Reinforced Elastomeric Isolators (SREIs). The reinforcements provide adequate vertical stiffness to the devices, avoiding large lateral bulging of the rubber; the external plates allow the connection of the devices to the structure and the distribution of the vertical load (i.e. the weight of the structure) [12]. Since most of the weight and cost of SREIs came from the manufacturing process involving the end plates and the steel reinforcement (i.e. hot vulcanization), Kelly [11] proposed replacing the steel sheets with layers of fiber fabrics (such as fiberglass) and to remove the external plates by placing the devices in direct contact with the structure (**Figure 1.2 (b)**). Suchlike for steel reinforced ones, these devices are named Fiber Reinforced Bearings (FRBs) or Fiber Reinforced Elastomeric Isolators (FREIs) [11].

FREIs can be used either in bonded or unbonded configuration. When bonded (Bonded Fiber Reinforced Elastomeric Isolators, B-FREIs), the isolators are connected to same external steel plates of the SREIs and their lateral deformation is linear (**Figure 1.3 (a)**) [13–15]; when unbonded (Unbonded Fiber Reinforced Elastomeric Isolators, U-FREIs), the marginal area can detach from the supports and rotate during the horizontal displacement [16, 17]; this type of deformation is named *rollover* (**Figure 1.3 (b)**).

In bonded FREIs, tensile stresses arise at the edges during the horizontal deformation, which can cause damage [18]. Using the FREI in unbonded configuration, the detached areas are stress

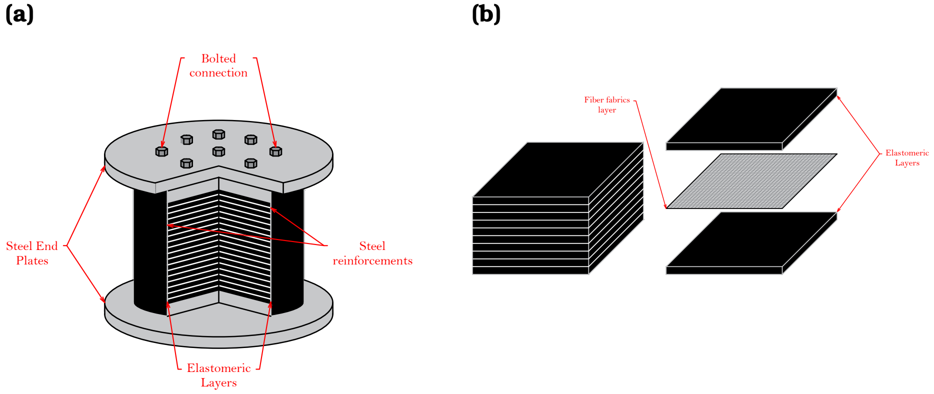

Figure 1.2: Elastomeric bearing: (a) SREI, (b) FREI.

free [19] and the vertical load is fully carried by the *overlap area* (**Figure 1.4 (a)**). Furthermore, as the contact area between bearing and support decreases during the horizontal displacement, the lateral stiffness is consequently reduced, and the isolation system is more efficient [20].

As the lateral deformation continues, the initially vertical faces of the bearing touch the supports gradually becoming horizontal, leading to the so-called *full rollover* (**Figure 1.4 (b)**). This condition allows greater stability of the system at large horizontal displacements, since the lateral stiffness starts growing when the vertical faces begin to touch the supports. Therefore, FREIs are generally studied in unbonded configuration [19].

The use of fabric reinforcements allows to reduce the weight of the devices, as the fibers are much lighter than steel despite having a similar Young's modulus [21]; removing the external plates further reduces the weight, so the fiber reinforced bearing is much lighter and easier to install than the steel reinforced one [11]. Costs can be further reduced by around 50% compared to SREIs by using cheap fibers, such as polyester [22–24].

The fiber reinforcement allows for a simpler and cheaper manufacturing process (i.e. cold vulcanization) than the hot vulcanization required between steel and rubber. Also, FREIs can be produced

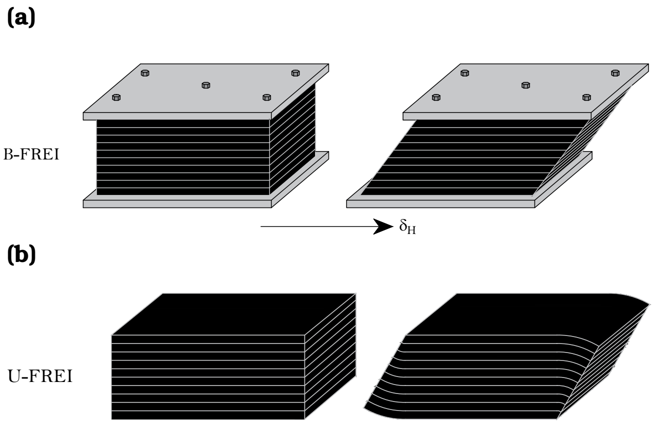

Figure 1.3: FREI under combined axial and shear loads: (a) bonded, (b) unbonded.

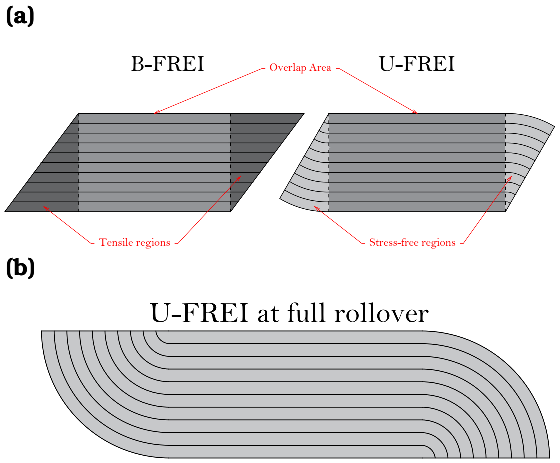

Figure 1.4: Deformed FREI: (a) B-FREI vs U-FREI, (b) U-FREI at full rollover.

in larger pads from which the devices of the desired size can be cut [16, 17]. Finally, it has been theorized that strip-shaped FREIs (i.e. long rectangular FREIs) can be placed in direct contact with reinforced concrete shear walls or masonry walls without the use of specific and expensive transfer beams (i.e. reinforced concrete beams) [25].

Several studies demonstrated the feasibility of FREIs as seismic isolators. First, analytical solutions for vertical [11, 26–31] and horizontal stiffness were proposed [32–36], starting from already known equations for SREIs and considering the elastomer as incompressible in a first attempt. These relationships were also compared with results from experimental tests [26, 34, 35, 37] and finite element analysis [19, 38–40]. Then, analytical solutions for vertical stiffness including compressibility of the rubber (i.e. bulk modulus) have been proposed [41–44].

It has been seen how FREIs show a vertical stiffness almost equal to SREIs, a lower horizontal stiffness [45] and a greater or at least similar equivalent viscous damping [13, 14, 46–50] with the same geometry and elastomer mechanical properties.

The excellent responses obtained from experimental tests and finite element analysis, combined with the rather low manufacturing costs, make these devices suitable for the isolation of structures in developing countries, as indeed studied in different papers [51–54].

1.2.1.2 Recycled Rubber Fiber Reinforced Elastomeric Isolators (RR-FREIs)

Having already reduced the costs of steel reinforced bearings through fiber reinforcements, a further reduction in the unit cost of a rubber bearing can be achieved by using elastomeric layers made of recycled rubber [55]. This type of isolators, namely RR-FREI (Recycled Rubber Fiber Reinforced Elastomeric Isolator) is therefore made by alternating recycled rubber pads and fiber reinforcement sheets (**Figure 1.5**). As for FREIs, a simple and cheaper manufacturing process can be used for packaging of RR-FREIs (i.e. cold vulcanization) [56].

Figure 1.5: RR-FREI sample.

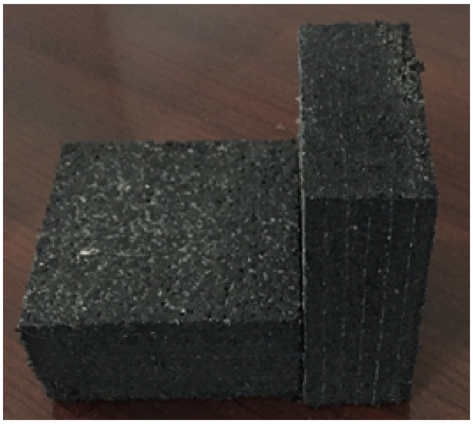

Figure 1.6: Rubber scraps for recycled rubber pads. From the left: SBR, EPDM, TDM

The elastomer layer can than consist of SBR (Styrene Butadiene Rubber), EPDM (Ethylene Propylene Dien Monomer) or TDMs (Tire Derived Materials) type rubber scraps [57–59] (**Figure 1.6**). The obtained particles are generally in the shape of granules (rounded) or fibers (elongated) [60]. These particles are then mixed with polymeric glue (e.g., polyurethane) and hot pressed, getting pads of a generic size from which the individual layers of the desired size can be cut [60].

Elastomeric pads made of recycled rubber with different density have been tested experimentally obtaining the main mechanical parameters, such as the Young's modulus of the compound, its vertical stiffness, the shear response and the volumetric behavior. Good responses in vertical direction were obtained, not far from those of natural rubber; the shear modulus and the volumetric modulus, however, are lower due to the very nature of the compound [57, 60, 61].

Several types of RR-FREIs with different fiber reinforcement were then studied both with experimental tests and finite element analysis [62]. In general, experimental tests showed a good response of the RR-FREIs under combined axial and shear load. RR-FREIs exhibit greater vertical compressibility than natural rubber FREIs [63], due to volumetric compression settling of the granules-adhesive compound. However, shaking table tests have shown good recentering capacity of the devices and no damage up to a threshold of approximately 100% of shear strain [64]. Above this limit the lateral response of the bearings becomes unstable and potential overturning could occur [65]. However, finite element analysis have shown that these bearings have suitable characteristics for practical cases in developing countries [66–68].

1.2.1.3 Scrap-Tire Rubber Bearings

As a further alternative to SREIs, the so-called Scrap Tire Pad (STP) made of used car tires have been proposed [69]. Indeed, car tires are commonly made of vulcanized rubber with bidirectional steel mesh, but nylon tires (cross ply tires), i.e. layers made from nylon cord, were also studied [70]. Alternating layers of scrap tires allows to reproduce an elastomeric isolator, with the embedded steel mesh acting as the steel reinforcement in the common SREIs and preventing the lateral bulging of the rubber compound and ensuring good vertical stiffness (**Figure 1.7**).

Each STP is obtained by cutting the sidewalls of a car tire into a ring, further divided into equal lengths tire layers and then placing each layer on the top of each other with no adhesive (i.e. just touch countact).

Experimental compression tests have shown how the initial elastic

Figure 1.7: Scrap Tire Rubber Bearing

compression modulus of a multilayers (4 – 6 layers) STP and the modulus at the same compression strain of a SREI are of the same order of magnitude [69]. However, the vertical ultimate stress of an STP (8-9 MPa) is 4-5 times lower the vertical strength of a SREI. The STPs also showed equivalent damping ratios between 18% and 22%, similar to those of an high damping rubber bearing [69, 71]. Pseudo-dynamic tests on a three-story building isolated with STRPs have also shown how a reduction up to 70% of the interstory drift, absolute acceleration and base shear force transmitted to the superstructures could be obtained [72]. Experimental shear tests in unbonded configuration under a vertical pressure of 5 MPa showed a load capacity up to 100% of shear strain [73, 74]. Past this threshold, the force-displacement curve shows a softening as the marginal tire layers tend to detach from the other. However, finite element analysis have shown that by avoiding the rubber layers delamination a stable lateral response could be achieved up to 150% of shear strain [75].

1.2.1.4 Recycled Tire Isolators

The idea of re-using tires to isolate buildings (**Figure 1.8**) was proposed through the criteria of creating a low/no-cost isolation system to be applied in developing countries [76]. In the first proposal, automotive tires filled with 3/4 inch rock aggregate were used and was shown how 85% of earthquake induced accelerations could

Figure 1.8: Recycled Tires used as isolation system.

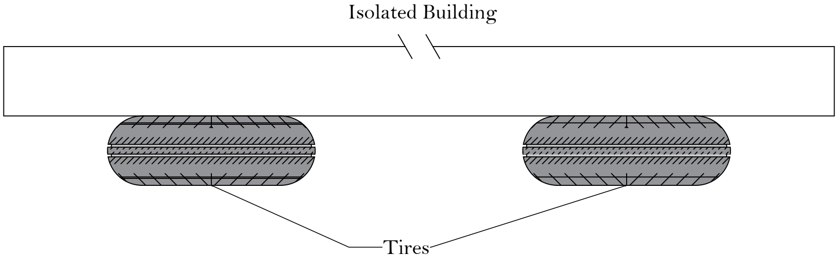

be reduced. Then, sand was used as filled materials too [77], as well as elastomeric recycled materials [78]. When sand was used, although the isolation system significantly reduces accelerations protecting the building, the ratio between vertical and lateral stiffness of these devices is not as high as common rubber bearings. This could cause rocking motions, as the structure rigidly rotates on the top of the bearings [77]. However, as a rigid motion, it does not damage the building. When filled with elastomeric recycled materials, the system is more stable in the vertical direction as the vertical stiffness is suitably high compared to the horizontal one [78]. In addition, from shaking table tests it has been seen how a structure could be adequately isolated with such a system, with a reduction in the acceleration as well as inter-story drift [78].

Therefore, another innovative isolation system based on recycled tires has been proposed. The so-called Recycled Tire Bearing (RTB) system uses recycled automobile rubber tires cut along an horizontal plane across the diameter and inserted underneath the unit to be isolated (**Figure 1.9**) [79, 80]. The system was proposed for the isolation of essential care units of hospitals in developing countries. System stability is provided avoiding rocking motions, by using a four-tires coupling configuration. In addition, the vertical and horizontal period are uncoupled through an Horizontal Sliding Recycle Tire Bearing (HSRTB) system, that allows the rubber tires to slide sideways with almost zero horizontal stiffness under service load while retaining adequate vertical stiffness. The system was tested under quasi-static vertical and horizontal protocol, showing

Figure 1.9: Recycled Tire Bearing under service loads

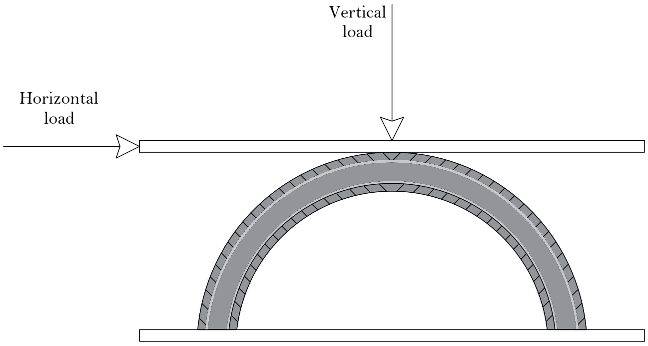

a good energy dissipation with a quite high equivalent damping ratio (around 8% for vertical response, around 15% for horizontal response).

1.2.1.5 Sliding Isolators

In sliding isolation system, the structure slide with respect to the foundation due to devices with a low friction coefficient [81]. Typically, the sliding devices are composed of a mirror-finish stainless steel sliding surface and a layer of PTFE (Polytetrafluoroethylene) traditionally used for the low friction coefficient (e.g., 0.05 – 0.15).

The two most common types of sliding devices are: *pure friction* (PF) *sliding isolators* and *friction pendulum systems* (FPS). In the first case, the structure is isolated through sledges with a low friction coefficient; in the second, based on the pendulum principle, the structure oscillates along a concave surface [82].

Sliding systems were initially proposed as a low-cost alternative to SREIs for masonry structures, experimental testing and verifying how the accelerations could be reduced by up to 80% [83].

One way to reduce the costs of the PF isolation system is to use low-tech methods. Sand, lighting ridge pebble, polypropylene, PVC sheet, polythene membrane, marble–marble, marble–high-density polyethylene, marble–rubber sheet, and marble–geosynthetic were proposed as materials for the friction isolation system layer. From shaking table tests on the different layers material, the acceleration cut-off imposed by the friction level of the system was observed [84] and a reduction for the maximum roof acceleration [85]. Finite element analysis have shown how low-cost pure friction systems can significantly improve the performance of non-engineered masonry [86, 87] or RC buildings [88, 89] in developing countries.

A further way of savings could be coupling a seismic friction base isolation system with a structure made with a percentage of demolished waste material [90]. Replacing 20% of cement with demolished waste material does not lead to a significant reduction in strength. The same structure isolated with a pure friction system showed a decreasing acceleration of 50% and an energy dissipation of 70% compared to the non-isolated structure.

In the field of oscillating devices, a low-cost technique has been proposed for masonry N-EB, namely *rocking pillars* used as supports [91]. The system is made with steel pipes filled with concrete and bearing caps at the top and the bottom. Shaking table tests on 1/4 scaled masonry structures showed the good isolation capacity of the system with acceleration reduction at the top of the structure between 25% and 80% [91–93]. However, the rocking pillar isolation system showed no good re-centering capacity and therefore damping devices must be provided to limit the excessive motion of the pillars. The system is very easy to implement and no particular skills are needed; this makes it attractive to full-scale application in developing countries.

A comparative experimental study between flat and concave surface sliding isolators was also proposed [94]. Generally, the PF system has no restoring capacity, but using a medium-high coefficient of friction (e.g. 0.18), the maximum horizontal displacement can be limited (around 30 to 42 cm). The concave-surface system re-centers the building close to the initial position.

Hybrid systems between geotechnical and sliding isolation has been proposed as a low-cost alternative for masonry N-EB. The basic principle is to use foundations that allow the structure to slide under seismic actions. Among the proposals, Natural Sone

Pebbles (NSP) below the foundation [95], or two layers of PVC that encapsulate sand [96, 97] or spherical roller bearings [98].

The first technology is based on the oldest isolation technique found (the *orthostat foundation* [99]), using natural materials as a support for the underlayer of foundation (**Figure 1.10 (c)**). Under the long-lasting action of rivers and seas, the weak parts of the stones are straggled, and only smooth and rounded pebbles remain. Showing a compressive strength around 80 MPa, they proved to be particularly useful as building materials. Shaking table tests on a fixed-base and isolated with NSP foundation sample building, have shown a strong reduction in stress/strain (on average of around 36%) demand and horizontal displacements (on average of around 29%). However, there may be residual displacements (horizontal and vertical due to rotations) in the foundation on a real structure. The efficiency of the system does not seem to depend on the thickness of the NSP layer.

In the second technology, a sliding layer is encapsulated between two flat PVC surfaces, creating an innovative foundation that incorporates the principles of sliding isolation. Systems with interposed sand (**Figure 1.10 (a)**) or with metal or glass roller spheres (**Figure 1.10 (b)**) between the PVC surfaces were subjected to shaking table tests, applied to reinforced masonry sample structures. In both cases, the system starts working by mobilizing some acceleration (around 0.05g and 0.1g or with a friction coefficient of 0.2), avoiding unintentional displacements due to ambient noise. The structures were found undamaged even when subjected to strong ground motion (around 0.8g). The system, however, did not show great re-centering capacity, but this can be corrected with preventive additional measures.

1.2.2 Geotechnical Seismic Isolation

Geotechnical Seismic Isolation (GSI) is a relatively newly developed seismic protection technique. It consists of a layer placed under the foundations of the structure, designed to dissipate the energy introduced by the earthquake. As in the case of base isolation, layers

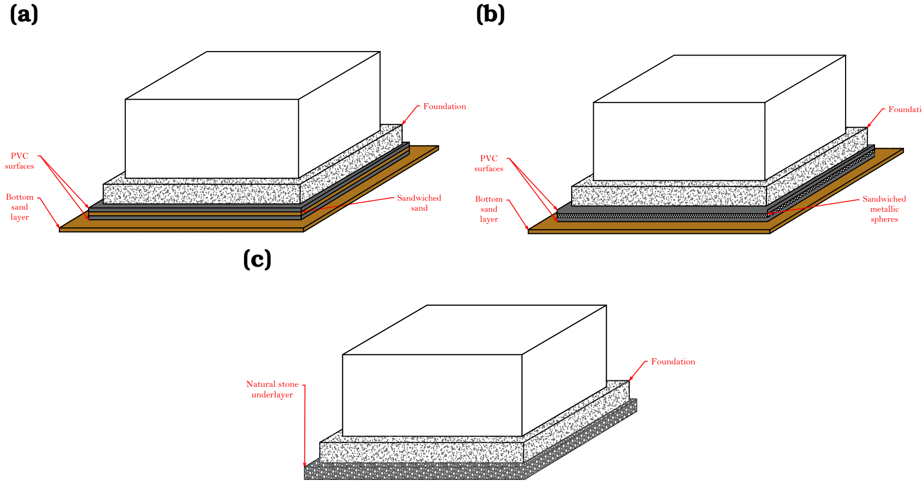

Figure 1.10: Sliding foundation layer: (a) PVC sandwich isolation with sand, (b) PVC sandwich isolation with metallic spheres, (c) natural stone pebbles.

of different materials and properties can be used. A low-cost technique that uses rubber as an additional material for geotechnical isolation will be shown below.

1.2.2.1 Rubber-Soil Mixture

The Rubber-Soil Mixture (RSM) is a geotechnical seismic isolation system consisting of placing underneath the foundation of a building (whether footing or pile), a layer in the order of 10 m of soil mixed with rubber (**Figure 1.11**) [100]. The soil layer below the foundation allows to reduce the amplitude of the seismic waves incoming, with only a small part amplified in frequency spectrum (1-2 Hz). The amplification and de-amplification of the waves depends on the geometric and dynamic properties of the materials of the layer. Hence the introduction of rubber as a "reinforcement", provides large energy absorption capability and increasing shear strength if more than 10% tire chips is used [101].

A number of parametric numerical simulations were conducted to

Figure 1.11: Rubber-Soil Mixture

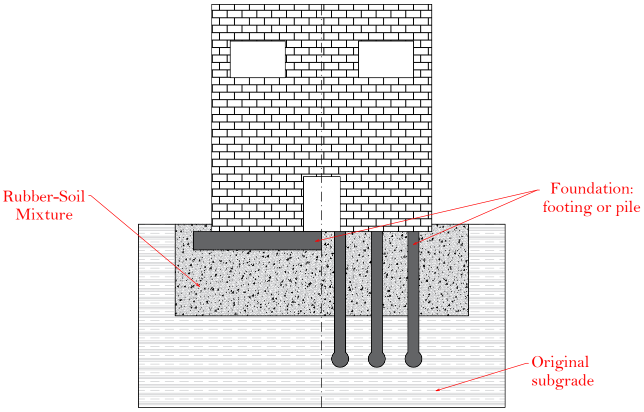

demonstrate the effectiveness and applicability of the system [100, 102–106], varying the thickness of RSM layer, dynamic properties (percentage of rubber inside soil, initially assumed around 75%) of the layer, building geometry (width, height, number of storey etc.), type and geometry of the foundation and acceleration input from the earthquake. The mixed layer manages to reduce the earthquake-induced horizontal accelerations up to 60% compared to the solely-soil layer, while a lower but still quite good reduction up to around 20% could be obtained for the vertical accelerations.

The qualities of the system were also investigated experimentally through dynamic tests on shaking table, by varying the ratio between rubber and soil to identify the best design mix [107]. A ratio between the size of the rubber and sand aggregates equal to 2 appears to ease the rigid sliding of the structure subjected to strong ground motion.

Although the system brings unequivocal advantages, it must be taken into account the potential risks of liquefaction and resonance. In the first case, the rubber inserts reduce the density of the pure soil and consequently the shear strength (but only if the quantity of rubber is quite low, i.e. $< 10\%$ of the total weight), increasing the liquefaction potential [108]. However, rubber has been seen to increase the friction angle and cohesion of the soil [101, 109]. This, combined with the reduction of the intensity of the ground shaking, can however lead to an advantageous response of the system.

In the same fashion for resonance, the vibration period of the underlying RSM must not match the main ones of the earthquake-induced ground shaking, thus avoiding amplified response.

CHAPTER 2

OVERVIEW OF THE EXISTING ANALYTICAL SOLUTIONS FOR FIBER REINFORCED ELASTOMERIC ISOLATORS

Summary

This chapter recalls the analytical equations proposed in the literature on the main mechanical properties of FREIs.
First, the analytical solutsions on the vertical response of rubber pads of different shapes with flexible reinforcements are shown. Hence, horizontal stiffness equations of elastomeric bearings under combined axial and horizontal loads will be shown. Finally, the stable/unstable response of FREIs in unbonded configuration is studied.

2.1 Vertical behavior

An important property of rubber bearings is the vertical stiffness. Typically, the behavior of rubber materials under pure compression is strongly non-linear from the very first stages of loading, depending on several factors. However, an initial prediction of the vertical stiffness of rubber-based devices such as elastomeric bearings can be done by the designer with a linear analysis, with an adequate level of accuracy.

Following this path, the vertical stiffness of a rubber bearing with equal thickness elastomeric layers, regardless the reinforcement type, is given by the formula [12]:

$$K_v = \frac{E_c A_c}{t_r} \tag{2.1}$$

Being A_c the *loaded area* (or the *contact area* between bearing and support), t_r the *total thickness of rubber* in the bearing (nt_e, with t_e thickness of a single elastomeric layer and n total number of elastomeric layers), and E_c is the *effective compressive modulus* of the rubber-reinforcement composite under the specified level of vertical load (i.e. the Young's modulus of a single layer of elastomer between two reinforcement sheets at the top and the bottom).

In **Equation 2.1** the two parameters A_c and t_r are generally known in a design phase, while E_c is unknown. The value of E_c depends on several parameters, the main ones being the *primary shape factor* S_1, defined as [81]:

$$S_1 = \frac{\text{Loaded Area}}{\text{Force-Free Area}} \tag{2.2}$$

Or, equivalently, the ratio between the plan area of the elastomer and its lateral area. Research over the years has provided several analytical solutions for predicting the compressive modulus, first considering rubber as incompressible and then removing this hypothesis and accounting its compressibility too. There are two main vein for the effective compressive modulus solutions:

1. *Pressure Solution* (PS) [11, 27, 110]
2. *Pressure Approach* (PA) [28–30]

The first approach is based on the following assumptions:

i. A single elastomeric layer is perfectly bonded to two reinforcement layers.

ii. Horizontal plane remain plane and parallel after compression.

iii. Points on a vertical line before deformation lie on a parabola after loading (parabolic bulging).

iv. The extension of the reinforcement is uniform through the layer.

v. The shear stresses in the horizontal plane are negligible.

vi. The stress state is assumed to be dominated by the internal pressure p, such that the normal stress components are all approximately equal to p.

In the Pressure Approach, the hypothesis vi. is removed. The main results obtained for two types of bearings, strip- and rectangular (square) - shaped, are shown below.

2.1.1 Effective compressive modulus of incompressible strip-shaped elastomeric pads

For an infinitely long strip-shaped elastomeric layer of width $2a$ and thickness t_e under a compression load F_v (**Figure 2.1 (a)**), the effective compressive modulus is:

$$\text{PS: } E_c = G_e S_1^2 \frac{12}{(\alpha a^2)} \left(1 - \frac{\tanh \alpha a}{\alpha a}\right) \tag{2.3a}$$

$$\text{PA: } E_c = 2\mu + \frac{2\mu\lambda}{\lambda + 2\mu} + \frac{\lambda^2}{\lambda + 2\mu} \left(\frac{\alpha_0^2}{\beta_1^2}\right) \left(1 - \frac{\tanh \beta_1 a}{\beta_1 a}\right) \tag{2.3b}$$

where in **Equation 2.3a**:

- $S_1 = a/t_e$ is the primary shape factor of an infinite strip-shaped elastomeric pad.
- $\alpha = \sqrt{12 G_e \left(1 - \nu_e^2\right) / E_f t_f t_e}$.

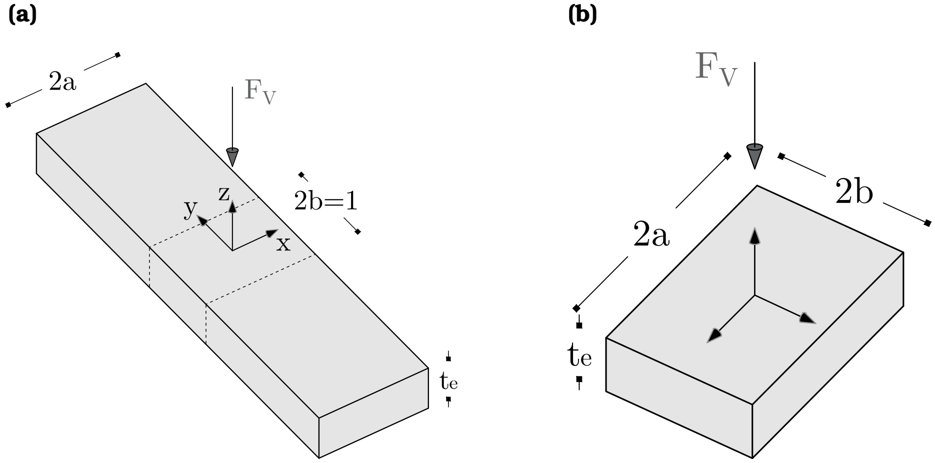

Figure 2.1: Elastomeric pads: (a) infinitely long strip, (b) rectangular.

- G_e, t_e and ν_e are the shear modulus, the thickness and the Poisson's ratio of the elastomer.
- E_f and t_f are the Young's modulus and thickness of the reinforcement.

while in **Equation 2.3b**:

- μ and λ are the Lame's constants.
- $\alpha_0 = 1/t_e\sqrt{12\mu/\lambda + 2\mu}$.
- $\beta_1 = \sqrt{\alpha_0^2 + 0.75\alpha_1^2}$.
- $\alpha_1 = \sqrt{12\mu\left(1 - \nu_f^2\right)/E_f t_f t_e}$.
- ν_f is the Poisson's ratio of the reinforcement.

2.1.2 Effective compressive modulus of incompressible rectangular(square)-shaped elastomeric pads

For a rectangular(square)-shaped elastomeric pad of base dimension $2a \ x \ 2b$ and thickness t_e under a compression load F_v (**Figure 2.1 (b)**), the effective compressive modulus is:

$$
\begin{aligned}
\text{PS}: \ E_c =& \frac{24G_eS_1^2}{\pi(\alpha a)^2}\left(1+\frac{a}{b}\right)^2 \sum_{n=1}^{\infty} \frac{1}{(n-1/2)^2} \\
& \left[\frac{\tanh(\gamma_n b)}{\gamma_n b} - \frac{\tanh(\beta_n b)}{\beta_n b} + \frac{\tanh(\bar{\gamma}_n a)}{\bar{\gamma}_n a} - \frac{\tanh(\bar{\beta}_n a)}{\bar{\beta}_n a}\right]
\end{aligned}
\tag{2.4a}
$$

$$
\begin{aligned}
\text{PA}: \ E_c =& 2\mu + \lambda\left[1 - \frac{\tanh^2(\alpha b)}{\left(1+\frac{\mu}{\lambda}\right)(\alpha b)^2}\right] - \\
& \frac{2\lambda(\alpha b)^2\left\{1 + \frac{\tanh(\alpha b)}{\alpha b}\left[1 - \frac{2\mu}{\lambda+\mu} + \frac{4(\alpha b)^2}{\pi^2}\right]\right\}}{\left[\frac{\pi^2}{4} + (\alpha b)^2 + \frac{\beta_1 b}{\tanh(\beta_1 b)}\left[\left(1+\frac{\mu}{\lambda}\right)\frac{\pi^2}{4} + \left(1+2\frac{\mu}{\lambda}\right)(\alpha b)^2\right]\right]}
\end{aligned}
\tag{2.4b}
$$

in **Equation 2.4a**:

- $S_1 = ab/(a+b)t_e$ is the primary shape factor of a rectangular-shaped elastomeric pad ($S_1 = a/2t_e = b/2t_e$ for a square-shaped pad).
- $\gamma_n = (n-1/2)\pi/a$.
- $\beta_n = \sqrt{\gamma_n^2 + \alpha^2}$.
- $\bar{\gamma}_n = (n-1/2)\pi/b$.
- $\bar{\beta}_n = \sqrt{\bar{\gamma}_n^2 + \alpha^2}$.

while in **Equation 2.4b** $\alpha = \sqrt{6\mu/t_e^2(\lambda+2\mu)}$.

2.1.3 Effective compressive modulus of compressible strip-shaped elastomeric pads

Results for the effective compressive modulus including the compressibility of the rubber were obtained only with the assumptions of the pressure solution. For the same infinite strip-shaped pad of **Section 2.1.1**, E_c becomes [19]:

$$E_c = K\frac{\beta^2}{\alpha^2+\beta^2}\left(1-\frac{\tanh\lambda}{\lambda}\right) \tag{2.5}$$

where:

- $K = 2G(1+\nu_e)/3(1-2\nu_e)$ is the *bulk modulus* of the rubber.
- $\alpha = \sqrt{(12G_e a^2)/E_f t_f t_e}$.
- $\beta = \sqrt{12G_e a^2/Kt_e^2}$
- $\lambda^2 = \alpha^2+\beta^2$

2.1.4 Effective compressive modulus of compressible rectangular(square)-shaped elastomeric pads

For the rectangular (square) pads of **Section 2.1.2** with compressible elastomer, two approaches are hearein reported; in the first one, the effective compressive modulus is given by the equation [111]:

$$E_c = 96G_eS_1^2\left(2+\frac{a}{b}\right)^2\sum_{n=1,3,5\ldots}^{\infty}\frac{1}{(n^2\pi^2)\left(\alpha_1^2+\beta_1^2\right)\left(2+\frac{a}{b}\right)^2+n^2\pi^2}\left(1-\frac{\tanh\lambda_1}{\lambda_1}\right) \tag{2.6}$$

with the following parameters:

- $\alpha_1^2 = 24G_eS_1^2t_e/E_ft_f$
- $\beta_1^2 = 12G_eS_1^2/t_e^2K$

- $\lambda_1 = \frac{\sqrt{(\alpha_1^2+\beta_1^2)(2+a/b)^2+n^2\pi^2}}{a/b}$

In the second approach [41], E_c is given by:

$$E_c = \frac{768 G_e S_1^2}{\pi^4}\left(\frac{b}{a}+1\right)^2 \sum_{n,m=1}^{\infty} \frac{\sin^2\left(\frac{n\pi}{2}\right)\sin^2\left(\frac{m\pi}{2}\right)}{n^2 m^2\left[\left(\frac{n\pi}{2}\right)^2+\left(\frac{m\pi b}{2a}\right)^2+2(\alpha b)^2+(\beta b)^2\right]} \tag{2.7}$$

where $\alpha = \sqrt{24G_e/E_f t_f t_e}$ and $\beta = \sqrt{12G_e/Kt_e^2}$.

2.2 Horizontal behavior

As mentioned in **Section 1.2.1.1**, FREIs under combined axial and shear loads expierence a rollover deformation as the marginal areas detach from the supports during lateral deformation. The contact area between bearing and supports therefore reduces. Plus, the shear modulus of the elastomer depends on the shear strain, reducing as it increases. Thus, the lateral response of the FREIs is somewhat challenging to render analytically.

However, analytical solutions have been proposed for the horizontal stiffness of FREIs based on simplified hypotheses and starting from the classic formula used for SREIs [112]:

$$K_H = \frac{G_e A_c}{t_r} \tag{2.8}$$

This simplified equation does not take into account the reduction of the contact area between the bearing and the supports and the reduction of the shear modulus with the shear strain. The different analytical solutions proposed introduce corrective coefficient to **Equation 2.8**, or modify the mechanical and geometrical properties of the bearing (i.e. G_e or A_c). The main results achieved are presented below.

2.2.1 Horizontal stiffness of a strip-shaped FREI with corrective coefficient

In one of the first approaches [33], a bearing with total height H and width $2a$ is treated as a beam and the infinitesimal deformation theory is adopted. Plane sections normal to the vertical (undeformed) axis were assumed to remain plane but not necessarily normal after deformation. The warping of the cross-section of the bearing due to the flexibility of the reinforcement is taken into account through a kinematics displacement function that measures the deviation from plane of the deformed cross-section. The material is assumed to be linear elastic.

For such a beam with its bottom end fixed and its top end solely fixed against rotation and warping, the horizontal stiffness is expressed by the following equations:

$$K_H = \left(\frac{G_e A_c}{H}\right) \frac{\bar{F}_v}{\frac{2\bar{F}_v\left(1+\bar{F}_v\right)+\beta_2}{\bar{F}_v(\beta_1+\beta_2)}\sqrt{2\rho\beta_1}\tan\sqrt{\frac{\beta_1}{8\rho}} + \frac{2\bar{F}_v\left(1+\bar{F}_v\right)+\beta_1}{\bar{F}_v(\beta_1+\beta_2)}\sqrt{2\rho\beta_2}\tan\sqrt{\frac{\beta_2}{8\rho}} - 1} \tag{2.9a}$$

$$K_H = \left(\frac{G_e A_c}{H}\right) \frac{\bar{F}_v}{\frac{2\bar{F}_v\left(1+\bar{F}_v\right)+\beta_2}{\bar{F}_v(\beta_1+\beta_2)}\sqrt{2\rho\beta_1}\tan\sqrt{\frac{\beta_1}{8\rho}} + \frac{2\bar{F}_v\left(1+\bar{F}_v\right)+\beta_1}{\bar{F}_v(\beta_1+\beta_2)}\sqrt{2\rho|\beta_2|}\tan\sqrt{\frac{|\beta_2|}{8\rho}} - 1} \tag{2.9b}$$

The first equation apply when $\left(1+\bar{F}_v\right)\kappa_c - \kappa_b \geq 0$, while the second when $\left(1+\bar{F}_v\right)\kappa_c - \kappa_b < 0$. In **Equation 2.9**, for an homogeneous beam (constant Young's and shear modulus) with a rectangular cros-section with plan area $A = 4ab$:

- H: is the total height of the undeformed bearing.
- $\bar{F}_v = F_v/G_e A_c$: is the dimensionless compression force, with F_v the vertical applied force.
- $\kappa_b = \frac{7}{3}\left(1+\bar{F}_v\right)^2$: is the first parameter corresponding to cross-section warping.

- $\kappa_c = 14\left(1+\bar{F}_v\right)$: is the second parameter corresponding to cross-section warping.
- $I = \frac{4}{3}ba^3$: is the second moment of area.
- $J = \frac{16}{175}ba$: is a cross-section property of the warping shape.
- $\Omega(X) = \left(\frac{X}{a}\right)^3 + \frac{3}{5}\left(\frac{X}{a}\right)$: is the warping function.
- $B = \frac{8}{5}b$: is a cross-section property of warping.
- $C = \frac{96b}{25a}$: is a cross-section property of warping.
- $\beta_1 = \frac{10}{3}\left(1+\bar{F}_v\right)\left[\left(\bar{F}_v - \frac{7}{2}\right) + \sqrt{\left(\bar{F}_v - \frac{7}{2}\right)^2 + \frac{21}{5}\bar{F}_v}\right]$.
- $\beta_2 = \frac{10}{3}\left(1+\bar{F}_v\right)\left[-\left(\bar{F}_v - \frac{7}{2}\right) + \sqrt{\left(\bar{F}_v - \frac{7}{2}\right)^2 + \frac{21}{5}\bar{F}_v}\right]$.
- $\rho = \frac{EI}{G_e A_c H^2}$: is the ratio of the flexure to shear rigidity.

2.2.2 Horizontal stiffness of rectangular(square)-shaped FREIs with corrected contact area

Analytical equations for the horizontal stiffness stiffness have been proposed considering a costant value for G_e and t_r, while a reduced contact area due to the rollover deformation in unbonded configuration:

$$K_H = \frac{G_e A_c^r}{t_r} \tag{2.10}$$

where $A_c^r \propto A_c$ is the reduced contact area, proportional to the plan area of the undeformed bearing with the following expression:

$$A_c^r = 2b\left[2a - f(\delta_H, H)\right] \tag{2.11}$$

being $f(\delta_H, H)$ a generic function generally depending on the horizontal displacement and bearing height. Three approaches have been proposed for deriving the function $f(\delta_H, H)$:

$$[113] : f_1(\delta_H, H) = \frac{25}{16} H\alpha(\delta_H, H) \tag{2.12a}$$

$$[114] : f_2(\delta_H) = \frac{3}{4}\delta_H \tag{2.12b}$$

$$[34] : f_3(\delta_H, H) = \delta_H - \delta_{H_0} \tag{2.12c}$$

In **Equation 2.12a** $\alpha(\delta_H, H)$ is a geometric function of the horizontal displacement through the expression:

$$\delta_H = \frac{25}{64} H\left[2\alpha\sqrt{1+4\alpha^2} + \ln\left(2\alpha + \sqrt{1+4\alpha^2}\right)\right] \tag{2.13}$$

and this equation could be solved for a generic δ_H value.

In **Equation 2.12c** $\delta_{H_0} = \sqrt{H^2 - h^2}$ is the horizontal displacement at the first detachment of the bearing from the supports and $h = F_v/K_v = F_v t_r/E_c A_c$ the reduced height of the isolator under the compressive load.

Following, the horizontal stiffness can be calculated as follows:

$$K_H = \frac{G_e 2b}{t_r}\left[2a - \begin{cases} \frac{25}{16} H\alpha(\delta_H, H) \\ \frac{3}{4}\delta_H \\ \delta_H - \sqrt{H^2 - h^2} \end{cases}\right] \tag{2.14}$$

In these equations, it is suggested to consider a shear modulus at 100% of shear strain.

2.2.3 Horizontal stiffness with corrected shear modulus

The complementary approach to the prevoius one is obtained using a constant contact area and a variable and decreasing shear modulus [115]:

$$K_H = \frac{G_e^r A_c}{t_r} \tag{2.15}$$

where $G_e^r \propto G_e$ is the reduced shear modulus, proportional to a constant value of the shear modulus at a fixed shear strain of 20%. The proposed expression for the reduced shear modulus is:

$$G_e^r = G_{e,20}\left(1 - \frac{\delta_H}{2a}\right)\left\{1 - \left[\frac{F_v}{f_{cr_0}\left(1 - \left(\frac{\delta_H}{2a}\right)^2\right)}\right]^2\right\} \tag{2.16}$$

In **Equation 2.16**:

- $f_{cr_0} = F_{v,cr}/A_c$: is the critical value of vertical stress.
- $F_{v,cr} = \frac{\sqrt{2}\pi G_{e,20} A_c S_1 r}{t_r}$: is the critical vertical load of the bearing.
- $r = \frac{2a}{2\sqrt{3}}$

2.2.4 Horizontal stiffness with corrected shear modulus and contact area

Using both approaces of **Sections 2.2.2** and **2.2.3**, a formula for the horizontal stiffness that takes into account the reduction of both the contact area and the shear modulus can be obtained:

$$K_H = \frac{G_e^r A_c^r}{t_r} \tag{2.17}$$

and with the positions from **Equations 2.11** and **2.16**, it follows the full expression for the horizontal stiffness with corrected shear modulus and contact area:

$$K_H = \frac{2b}{t_r} G_{e,20} \left(1 - \frac{\delta_H}{2a}\right) \left\{ 1 - \left[\frac{F_v}{f_{cr_0}\left(1 - \left(\frac{\delta_H}{2a}\right)^2\right)} \right]^2 \right\} \cdot \left[2a - \left\{ \begin{array}{r} \frac{25}{16} H\alpha(\delta_H, H) \\ \frac{3}{4}\delta_H \\ \delta_H - \sqrt{H^2 - h^2} \end{array} \right. \right] \tag{2.18}$$

2.3 Instability and buckling behavior

U-FREIs can show two types of unstable behavior [112]:

1. *Buckling under large vertical load.* Under large value of vertical pressure the bearing, subject to an horizontal displacement, shows a buckling type of instability similar to an ordinary column (**Figure 2.2 (a)**).

2. *Lateral instability.* Since the horizontal force-displacement curve of the FREIs tends to decrease with horizontal displacement, the tangent stiffness could become negative beyond a lateral deformation threshold and the bearing is said to be unstable (*Unstable Unbonded Fiber-Reinforced Elastomeric Isolators* (UU-FREIs [116]); bearings always showing a positive tangent stiffness in the lateral response force-displacement curve are called stable (*Stable Unbonded Fiber-Reinforced Elastomeric Isolators*, SU-FREIs [117]) (**Figure 2.2 (b)**).

In the first case, the *buckling load* F_{v,cr_0} corresponds to the vertical load value where any horizontal displacement, whatever small, results in a zero or negative horizontal stiffness. The bearing becomes unstable under pure compression load, showing no lateral capacity.

In the second case, the *critical load* $F_{v,cr}$ is the vertical force at the peak horizontal force of the bearing lateral response curve, i.e.

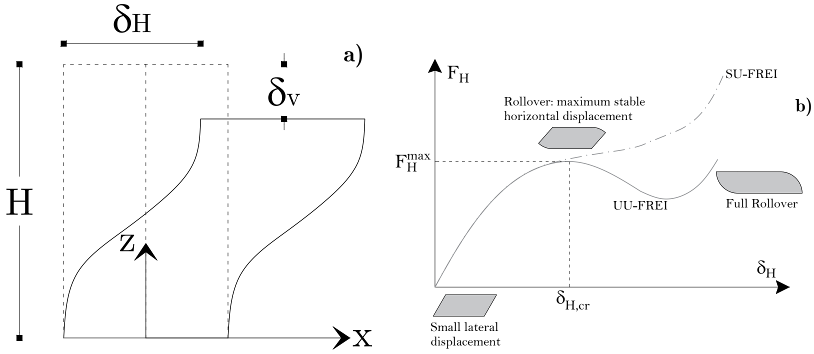

Figure 2.2: Limit horizontal response: (a) buckling of short beam, (b) lateral curve response with and without instability.

where the tangent stiffness is zero. Unlike the previous case, the bearing shows a stable response up to the peak; past this threshold the response is no longer reliable.

The main theories on these two topics are shown below.

2.3.1 Buckling load

Buckling load analysis of elastomeric bearings with flexible reinforcement were based on beam theory. Assuming the material to be linear elastic and with the hypothesis of planar sections preserving (but not necessary normal to the deformed vertical axis), the buckling load was obtained by equaling the horizontal stiffness of **Equation 2.9** to zero. Thus, for a rectangular homogeneous beam, the buckling load could be obtained by solving the following non-linear equation [33]:

$$\bar{F}^3_{v,cr_0} + \left(2+\frac{2}{7}\pi^2\rho\right)\bar{F}^2_{v,cr_0} + \left(1-\frac{5}{7}\pi^2\rho\right)\bar{F}_{v,cr_0} - \left(\pi^2\rho+\frac{3}{35}\pi^4\rho^2\right) = 0 \qquad (2.19)$$

where ρ has been defined in **Section 2.2.1**. Cubic **Equation 2.19** could be solved via numerical method once ρ is known.

For a strip-shaped FREI, a cubic equation as well could be solved for the buckling load [32]:

$$\begin{gathered}
\frac{(EI)_{eff}}{(EJ)_{eff}}\left[\frac{f_C}{A_c}-\left(\frac{f_B}{A_c}\right)^2\right]\bar{F}^3_{v,cr_0}+\Bigg\{\frac{(EI)_{eff}}{(EJ)_{eff}}\left(\frac{C}{A_c}+\frac{f_C}{A_c}-2\frac{f_B B}{A_c^2}\right)+\pi^2\rho \\
\Bigg[1+\frac{(EI)_{eff}}{(EJ)_{eff}}\left(\frac{f_B}{A_c}\right)^2\Bigg]\Bigg]\Bigg\}\bar{F}^2_{v,cr_0}+\Bigg\{\frac{(EI)_{eff}}{(EJ)_{eff}}\left[\frac{C}{A_c}\left(\frac{B}{A_c}\right)^2\right]+\pi^2\rho \\
\Bigg[1+\frac{(EI)_{eff}}{(EJ)_{eff}}\left(2\frac{f_b B}{A_c^2}-\frac{f_c}{A_c}\right)\Bigg]\Bigg]\Bigg\}\bar{F}_{v,cr_0}-\left\{\pi^2\rho\frac{(EI)_{eff}}{(EJ)_{eff}}\left[\frac{C}{A_c}-\left(\frac{B}{A_c}\right)^2\right]+\pi^4\rho^2\right\}=0
\end{gathered} \tag{2.20}$$

with:

- $(EI)_{eff} \approx a^3 G_e S_1^2 \frac{8}{15}\left[1-\frac{2}{21}(\alpha a)^2\right]$.
- $(EJ)_{eff} \approx a G_e S_1^2 \left\{\frac{32}{3675}\left[1-\frac{2}{77}(\alpha a)^2\right]+\frac{1}{2\lambda S_1^2 (b/t_f)^3}\right\}$.
- $B \approx \frac{8}{7}\left[1-\frac{(\alpha a)^2}{210}\right]$.
- $C \approx \frac{1}{a}\left\{\frac{552}{245}\left[1-\frac{4(\alpha a)^2}{1449}\right]+\frac{2S_1}{\lambda (b/t_f)^3}\right\}$.
- $f_B \approx \frac{12}{35}\left[1+\frac{16(\alpha a)^2}{315}\right]$.
- $f_C \approx \frac{216}{245a}\left[1+\frac{26(\alpha a)^2}{945}\right]$.
- $\rho \approx \frac{4S_1^2}{15}\left(\frac{a}{H}\right)^2\left[1-\frac{2(2\alpha a)^2}{21}\right]$.

2.3.2 Critical load

As said in **Section 2.3**, instability occurs when:

$$K_H^{tan}=\frac{\partial F_H}{\partial \delta_H}=0 \tag{2.21}$$

A first simplified approach for the horizontal displacement at the peak horizontal force, was proposed considering the rubber incompressible, the shear modulus constant with the lateral deformation and negleting the roll-off marginal areas contributions [118]. In such assumptions, the lateral resisting force of a rectangular bearing can be written as:

$$F_H = \frac{G_e}{t_r}[A_c - A(\delta_H)]\delta_H = \frac{G_e}{t_r}[2a \cdot (2b - \delta_H)]\delta_H \tag{2.22}$$

and then, following from **Equation 2.21**:

$$\frac{\partial F_H}{\partial \delta_H} = \frac{G_e}{t_r}4a(b - \delta_H) = 0 \tag{2.23}$$

which shows how the bearing has a stable response up to an horizontal displacement value equal to *half the base side in the direction of displacement*. This simple formula provide an easy-to-use results for a preliminary estimate of the displacement at peak of horizontal force.

In a further approach [119], the horizontal force is calculated divideng the isolator into three zones: the central overlap area and the two marginal rollover areas. The shear deformation is supposed to happens in each elastomeric layers, while the fibers are stretched.

The central area shows an horizontal reaction force F_{H_1} while the lateral areas two horizontal forces F_{H_2}. Then, the total horizontal force is the sum of these three rates:

$$F_H = F_{H_1} + 2F_{H_2} \tag{2.24}$$

The horizontal force F_{H_1} is computed with **Equation 2.22**. The rollover portions are then subdivided into two type of deformation patterns: a pure shear horizontal displacement δ_H^s and a bending - induced displacement δ_H^b, with the resultant displacemente being $\delta_H^r = \delta_H^s + \delta_H^b$. First displacement comes straight from the plane-section assumption:

$$\delta_H^s = \frac{F_{H_2} t_r}{a G_e \delta_H} \tag{2.25}$$

For the bending-derived displacement the rollover area is assumed to be a cantilever beam with a follower point load V and is written as a function of the rotation angle ϑ of the vertical face of the bearing[1]:

$$\delta_H^b = H \cdot \sin\vartheta \tag{2.26}$$

Then, the F_{H_2} force due to rollover areas is obtained from the sum of all the horizontal components of the shear force V in the elastomerc layers:

$$F_{H_2} = \left(2E_r I_r \sum_{i=1}^{n} \frac{1}{l_i^2} + 2E_f I_f \sum_{i=1}^{n-1} \frac{1}{l_i^2} \right) \vartheta \tan\vartheta \tag{2.27}$$

being E_r the Young's modulus of the rubber and $l_i = i \cdot t_e \cdot \delta_H / t_r$ is the length of the cantilever-equivalent i-th rubber layer. Substituting **Equation 2.27** in **Equation 2.25** and then summing with **Equation 2.26** a non linear equation for F_{H_2} is obtained:

$$F_{H_2} = \frac{A_c \cdot t_r^2}{\delta_H^2} \tan\left[\arcsin\left(\frac{\delta_H}{H} - \frac{F_{H_2} \cdot t_r}{a G_e \delta_H H} \right) \right] \arcsin\left(\frac{x}{H} - \frac{F_{H_2} \cdot t_r}{a G_e \delta_H H} \right) \tag{2.28}$$

and using this equation with **Equation 2.22** into **Equation 2.24**, a final non linear equation for the total shear force F_H is achieved:

$$\begin{aligned} F_H - \frac{2a\delta_H}{t_r}(2b - \delta_H)G_e - \frac{2A_c \cdot t_r^2}{\delta_H^2} \cdot \\ \tan\left[\arcsin\left(\frac{A_c G_e \gamma_H - F_H}{2a G_e \gamma_H H} \right) \right] \arcsin\left(\frac{A_c G_e \gamma_H - F_H}{2a G \gamma_H H} \right) = 0 \end{aligned} \tag{2.29}$$

The equation can be solved via numerical methods, obtaining the horizontal force as a function of δ_H.

[1] Assuming that all the elastomer layers rotate by the same angle

2.3.2.1 Influence on stability of FREIs

The stability of the FREIs has mostly been studied with experimental tests. These studies have shown that the stability of FREIs under combined axial and shear loads mainly depends on the *secondary shape factor* S_2 [18, 20, 120], defined as the ratio between the base size (in the direction of the imposed horizontal displacement) to the total height of rubber [121]. For instance, for a rectangular FREIs with base dimension $2a$ x $2b$, S_2 would be:

$$S_2^{2a} = \frac{2a}{t_r} \tag{2.30}$$

or

$$S_2^{2b} = \frac{2b}{t_r} \tag{2.31}$$

A critical value of this parameter appears to be 2.5 [116, 117]: bearings with a lower secondary shape factor can be considered unstable, otherwise they can be considered stable.

Part II

Finite Element Analysis of FREIs

CHAPTER 3

STABILITY OF STRIP-SHAPED FIBER REINFORCED ELASTOMERIC ISOLATORS

Summary

This chapter introduces the results obtained from parametric finite element analysis of FREIs. The vertical and horizontal response of infinite long strip-shape FREIs under combined axial and horizontal loads has been studied with combinations of mechanical and geometric parameters of the bearings. The total vertical displacement of U-FREIs has been studied comparing the numerical results with a modified version of available analytical equation.
This chapter is based on the journal paper [122].

3.1 Introduction

As mentioned in **Section 2.2**, analitycal modeling of the response of FREIs under combined vertical and horizontal loads is quite challenging due to strongly non linear vertical and horizontal responses. The experimental tests proposed in the literature are limited to a reduced number of different bearings and do not provide wide-general results.

Therefore, Finite Element Analysis (FEA) has proved to be a powerful tool to study the response of a large number of FREIs with different geometries. In this thesis, the finite element analysis were carried out with the MSC.Marc/Mentat [123], a general purpose FEA software optimized for non-linear analyses.

The ultimate behavior of FREIs is challenging for finite element codes because of large and strongly non-linear strain, nearly - incompressible rubber conditions, multiple contacts between rubber-rubber and rubber-supports, sliding and/or separation, etc. Also, mesh-locking can occur when dealing with elastomers as for incompressible materials the dilatation would shrinks to zero when Poisson's ratio approaches to 0.5, while for some elements (e.g. 4 nodes quad elements) remains finite. Locking can occurs both for element type and shape, but it seems only happens when "an element cannot interpolate a field property correctly with the nodal values and the element's shape functions" [124]. In MSC.Marc locking can be prevented by using *constant dilatation*[2] or *assumed strain*[3] when selecting geometric properties, or by using *reduced integration*[4] or *Hermann formulation*[5] when choosing the element types [125]. In the analysis herein shown, the Hermann method was used.

3.1.1 Set of Finite Element Models

An infinite long strip-shaped FREI under combined axial and shear loads deforms in a plane strain state and can be studied referring to a generic cross section with unitary out-of-plane width. Therefore, two-dimensional Finite Element Models (FEM) have been used in MSC.Marc, under the plane strain assumption.

A large number of FEM (4320) were obtained by varying geometric and mechanical parameters, such as (**Figure 3.1**):

- The base side $2a$.
- The thickness of the elastomeric layers t_e.

[2] Deleting spurious terms.

[3] Problem is splitted into deviatoric and dilatational parts, and the dilatational parts of the shape functions matrice is replaced with a modified version.

[4] Reduction of used Gauss points in numerical integration.

[5] The method takes the pressure on an element as an extra variable next to the displacement, creating a two-field problem.

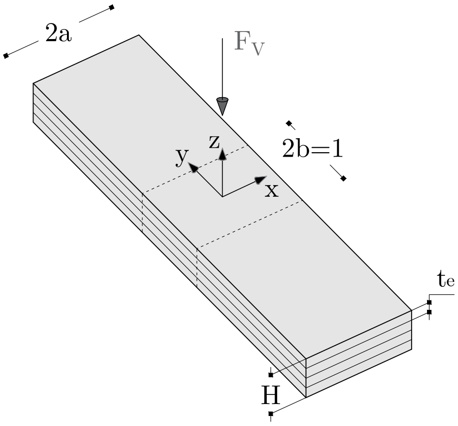

Figure 3.1: Schematic of an infinite long strip-shaped FREI.

- The shear modulus of the rubber G_e.
- The bulk modulus of the rubber K.
- The vertical pressure σ_v at zero horizontal displacement.

in the ranges shown in **Table 3.1**. Other parameters were instead kept constant, such as:

- The total height of the bearing $H = 180$ mm.
- The thickness of the reinforcement $t_f = 0.27$ mm.
- The Young's modulus of the reinforcement $E_f = 50000$ MPa.

With the values of $2a$ and t_e of **Table 3.1** and constant height and reinforcement thickness, 18 secondary shape factors S_2 are obtained in the range 1.41 - 2.92. During the FEAs, the axial load was applied first and held constant; then a displacement-controlled analysis was performed with increasing lateral displacements to push the bearings past their stable response.

Table 3.1: Variable parameters in the total set of FEM on strip-shaped FREIs.

$2a$ [mm]	t_e [mm]	G_e [MPa]	K [MPa]	σ_v [MPa]
250	5	0.5	1400	1.5 to 8.5
300	10	0.7	1600	
350	15	0.9	1800	with
400		1.1	2000	increments
450				of 0.5 MPa
500				

3.1.2 FEAs specifications

3.1.2.1 Materials modeling: elastomer and fiber fabrics modeling

The elastomer was modeled using an incompressible Neo-Hookean hyperelastic material model. The strain energy density function for a compressible generalized Rivlin model is described by the equation [126]:

$$W_{comp} = \sum_{p,q}^{n} C_{p,q}\left(\bar{I}_1 - 3\right)^p \left(\bar{I}_2 - 3\right)^q + \sum_{r=1}^{m} \frac{1}{D_r}(J-1)^{2r} \tag{3.1}$$

where:

$$\bar{I}_1 = J^{-2/3} I_1 \quad I_1 = \lambda_1^2 + \lambda_2^2 + \lambda_3^2 \tag{3.2a}$$

$$\bar{I}_2 = J^{-4/3} I_2 \quad I_2 = \lambda_1^2\lambda_2^2 + \lambda_2^2\lambda_3^2 + \lambda_3^2\lambda_1^2 \tag{3.2b}$$

with λ_i as the principal stretches. $\bar{I}_1$ and $\bar{I}_2$ are first and the second invariant of the unimodular component of the left Cauchy-Green deformation tensor $\boldsymbol{B} = \boldsymbol{F}\boldsymbol{F}^T$; I_1 and I_2 are the first and the second invariant of the right Cauchy-Green deformation tensor $\boldsymbol{C} = \boldsymbol{F}^T\boldsymbol{F}$; $J = \det(\boldsymbol{F}) = \lambda_1\lambda_2\lambda_3$ is the determinant of the deformation gradient $\boldsymbol{F}$.

C_{pq} and D_m are material constants related to the distortional response and the volumetric response, respectively.

For a compressible Neo-Hookean material, $n = 1$, $m = 1$, $C_{10} = C_1$, $C_{01} = 0$, $C_{11} = 0$ and **Equation 3.1** reduced to:

$$W^{NH}_{comp} = C_1\left(\bar{I}_1 - 3 - 2\ln J\right) + D_1(J-1)^2 \tag{3.3}$$

For an incompressible material $J = 1$ and the strain energy density function of a Rivlin material is:

$$W_{incomp} = \sum_{p,q=0}^{n} C_{p,q}(I_1 - 3)^p(I_2 - 3)^q \tag{3.4}$$

while for the Neo-Hookean materials, with the same position of **Equation 3.3**:

$$W^{NH}_{incomp} = C_1(I_1 - 3) \tag{3.5}$$

For consistency with linear elasticity, it must be:

$$C_1 = \frac{G_e}{2} \tag{3.6a}$$

$$D_1 = \frac{K}{2} \tag{3.6b}$$

The fiber reinforcement is modeled with a linear elastic isotropic material, fully defined by two parameter: the Young's modulus E_f and the thickness t_f (see **Section 3.1.1** for numerical values).

General results on the response of the bearings under combined axial and shear loads are required in a design phase of a seismic isolation system with U-FREIs. The parametric finite element analyses proposed in this thesis aim to obtain easy-to-use results involving the minim number of mechanical and geometric parameters. Thus, FEAs presented in this thesis used a constant value of the shear modulus. According to the material's model used (i.e. Neo-Hookean), each value of G_e corresponds to the initial shear modulus of the rubber (**Equation 3.6**). Specific shear tests on rubber materials [127] demonstrated how simplified hyperelastic material model, such as Neo-Hookean or 2-parameters Mooney – Rivlin, predicted the stress – strain response with good accuracy up to a shear strain of 25%. Thus, the shear modulus values used in this thesis could be related to elastomeric materials showing a stress – strain curve with similar values of secant shear modulus at the same shear strain threshold.

The values of the shear modulus presented in **Table 3.1** are chosen as common values of rubber compounds generally used in seismic isolators.

3.1.2.2 FEM elements

The elastomer is modeled with arbitrary quadrilateral plane strain with Hermann formulation element (element 80 in Marc [128]). It is a four-node, isoparametric element written for plane strain incompressible applications. This element uses bilinear interpolation functions and the strains tend to be constant throughout the element and a fine mesh is needed. The stiffness is formed using four-point Gaussian integration. This element is preferred over higher-order elements when used in a contact analysis.

Both the mapping and the function assumption take a bilinear form:

$$x = a_0 + a_1\xi + a_2\eta + a_3\xi\eta \tag{3.7a}$$

$$\psi = b_0 + b_1\xi + b_2\eta + b_3\xi\eta \tag{3.7b}$$

and either the coordinate or function can be expressed in terms of the nodal quantities by the interpolation functions:

$$x = \sum_{i=1}^{4} x_i\phi_i \tag{3.8}$$

where:

$$\phi_1 = \frac{1}{4}(1-\xi)(1-\eta) \tag{3.9a}$$

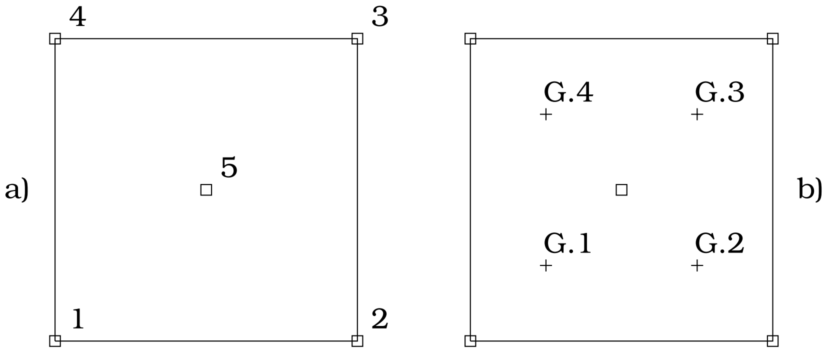

Figure 3.2: (a): Four-node isoparametric element with extra node, (b): Gaussian integration points.

$$\phi_2 = \frac{1}{4}(1+\xi)(1-\eta) \tag{3.9b}$$

$$\phi_3 = \frac{1}{4}(1+\xi)(1+\eta) \tag{3.9c}$$

$$\phi_4 = \frac{1}{4}(1-\xi)(1+\eta) \tag{3.9d}$$

The element has four nodes with 2 degrees of freedom for each one and a four-point Gaussian integration is used **Figure 3.2 (b)**; an extra fifth node with a single degree of freedom (negative hydrostatic pressure) is placed in the center **Figure 3.2 (a)**.

The reinforcement is modeled with four-node plane strain rebar element (element 143 in Marc [128]). It's an isoparametric, 4-node hollow quadrilateral element, in which a single strain members (such as reinforcing rods or cords) could be placed. The element is then used in conjunction with the 4-node plane strain continuum element of the rubber, to represent cord reinforced composite materials. Serveral "layers" up to a maximum of 5 can be used within this rebar element. Each layer is similar to a pair of opposite edges, so that the thickness of the element is parallel to one of the orthogonal edges (**Figure 3.3**). The element is integrated using a numerical scheme based on Gauss quadrature. Each layer contains two integration points.

In each FEM, the top and the bottom surfaces are modeled as

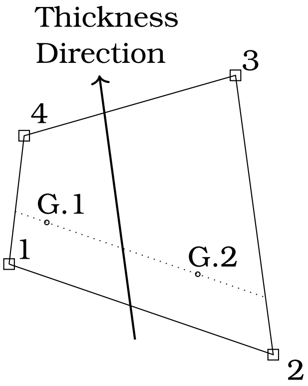

Figure 3.3: Four-node Rebar Element.

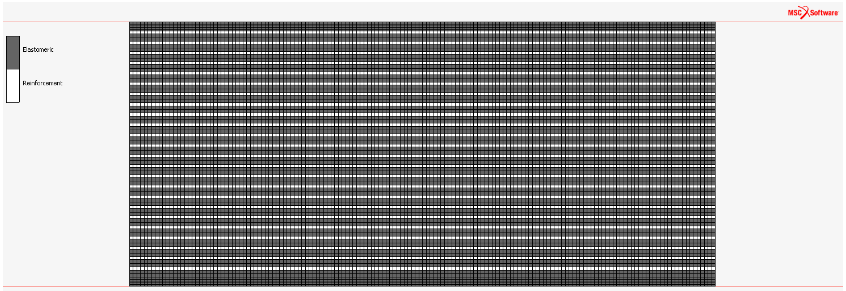

Figure 3.4: Geometry and discretization of a FREI for 2D FEAs in MSC.Marc.

rigid lines and a contact "touch" type has been set between bearing and supports with Coulomb friction coefficient of $\mu_c = 0.9$. Thus, the bearing could detach from the support to simulate the unbonded configuration.

The geometry and discretization of one of the 2D FEMs in MSC.Marc is shown in **Figure 3.4**.

3.1.2.3 FEAs validation

Experimental tests on samples of FREIs (**Figure 3.5 (a)**) were reproduced in MSC.Marc, comparing the numerical output with the experimental results to calibrate the FEMs.

The bearings for this study were manufactured by Kirkhill Manufacturing Company, Downey, CA following Caltrans specifications [129]. As per specifications, laminated pads were made by bonding together elastomeric layers and fabric reinforcements. Each of the tested bearings was cut from a pad of bigger dimensions. The samples were made by bonding 9 layers of neoprene to 8 layers of glass fiber reinforcements. The FREIs for testing had a cubic shape with dimensions of 50x50x50 mm (**Figure 3.5 (a)**).

The experimental tests on the bearings were performed in shear, using a classic dual lap configuration, and a universal testing machine MTS 810 (**Figure 3.5 (b)**). The axial load was applied using a hydraulic jack, and then the bolts of the testing rig were tightened to retain the desired distance between the steel plates (i.e., compression load). Displacement controlled procedures were performed up to a shear deformation amplitude of 50% (i.e., maximum horizontal displacement of 25 mm). For the experimental tests, the FRBs were not bonded to the plates of the testing rig and a variable axial pressure in the range of 1.5 MPa to 6.5 MPa was applied to the bearings to obtain the lateral force-displacement curves under different axial loads.

In the FEAs used for this validation, the vertical displacement obtained from each experimental test was first imposed to the upper support; then, helding constant both the supports, each bearing is sheared up to a horizontal displacement threshold of 25 mm.

Figure 3.6 shows the comparison between the horizontal force-displacement curves obtained by experimental tests (solid lines) and FEAs (marked lines). As clear from the plots, the FEAs are able to capture with a good level of approximation the lateral response of the bearings, including softening. This comparison confirms the validity of the procedures and assumptions used for the analyses of FREIs under axial and shear loads.

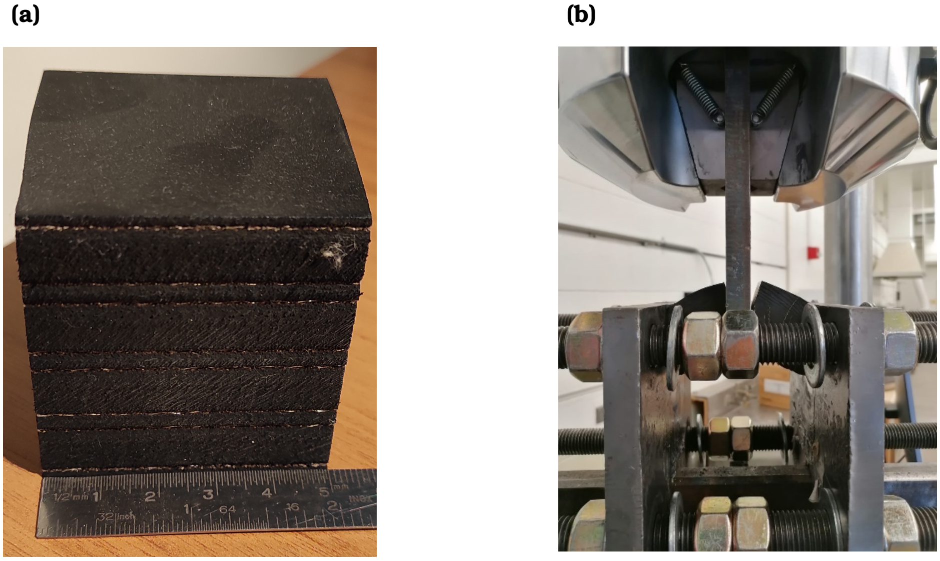

Figure 3.5: Samples of FREIs for FEAs validation: (a) tested sample, (b) experimental shear tests.

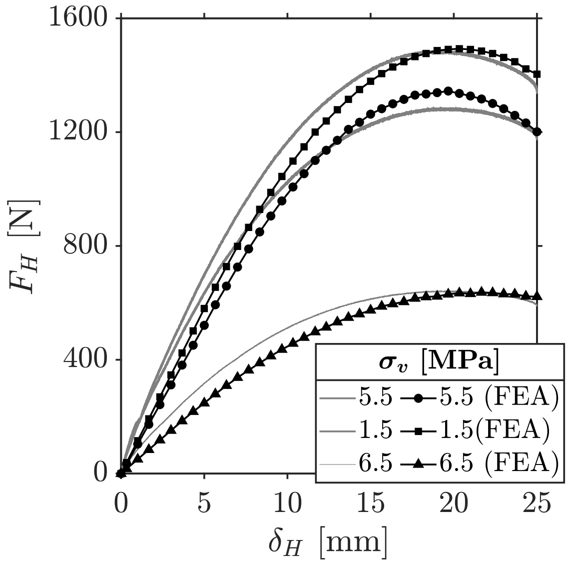

Figure 3.6: FEAs validation: experimental vs numerical tested bearings.

3.2 Results: influence of geometric and mechanical parameters on the peak response

The typical response of a FREI under combined axial and shear load is shown in **Figures 3.7 (a)** and **3.7 (b)**. As already discussed in **Section 1.2.1.1** when a bearing with a flexible reinforcement is deformed in shear, as the marginal elastomeric layers detach from the lower and the upper surfaces, no tensile stresses are generated at the edges of the device. At peak horizontal load, the axial stress in the layers of reinforcement substantially increases because of the reduction of the effective area. This effect is less pronounced for bearings with a large base (**Figure 3.7 (b)**), while for small bearings (**Figure 3.7 (a)**); an increase of tensile stress up to 200% can be expected in the fiber reinforcements.

In the range of secondary shape factor selected, the bearings are all unstable and a peak (local maximum) can be identified in the horizontal force-displacement curve.

Figure 3.8 shows two early average results on G and K from FEAs on the lateral response peaks. **Figure 3.8 (a)** shows the effect of the axial pressure on the peak shear deformation capacity of bearings of different base (i.e. S_2). An increase of axial pressure leads to a reduction of the maximum shear deformation capacity of the bearings. This effect is nonlinear with the applied load, more for large compression loads and for bearings with smaller S_2. Under shear loads, the overturning moment generated by the second order effects becomes significant for large axial loads. As result, the stability range of the bearing is reduced with increasing axial loads. The peak shear stress capacity vs secondary shape factor is plotted in **Figure 3.8 (b)** for the values of axial pressure in the range of **Table 3.1**. Again, the shear capacity decreases as the pressure increases while it clearly increases with greater S_2. The variation of the peak shear stress is nonlinear with the base of the bearing. The slope of the curves is greater for small S_2 values (i.e.

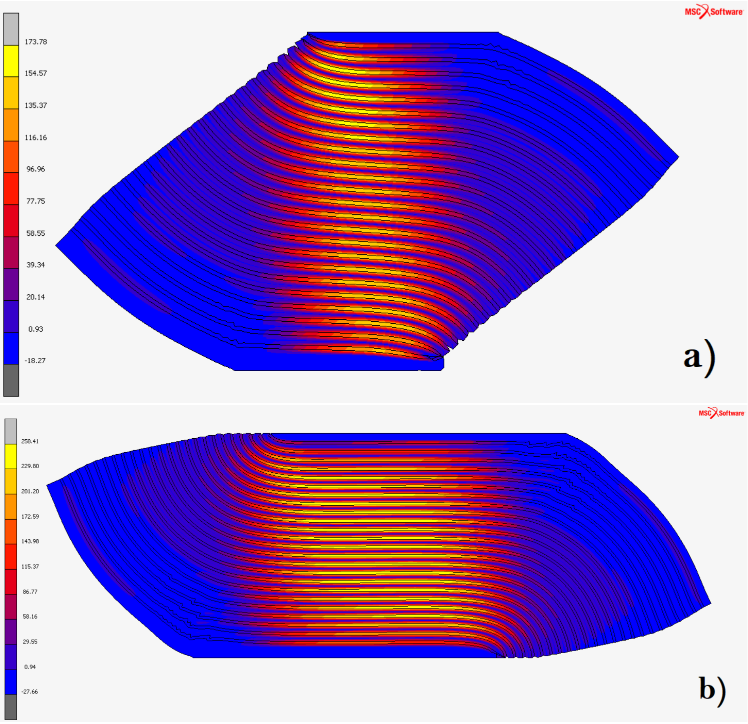

Figure 3.7: Maximum principal value of stress: (a) $2a = 250$ mm, (b) $2a = 400$ mm.

$S_2 \leq 2.5$) while it tends to decrease suggesting an horizontal line-up for larger values (i.e. $S_2 > 2.5$).

Figure 3.9 shows the peak shear strain and stress, against the primary shape factor S_1, for bearings with $2a = 300,\ 350,\ 400$ mm. From **Figures 3.9 (a)**, **3.9 (b)** and **3.9 (c)** it can be seen how the deformation capacity of the bearings is independent of the primary shape factor for values of pressure in the range 3.5 ÷ 4.0 MPa. Both the peak shear strain and stress are not affected by the primary shape factor if $S_1 > 30$.

However, if $S_1 < 30$ the effect of the primary shape factor on the peak shear response of the bearing changes with the vertical pressure: if $\sigma_v < 3.5$ MPa, the deformation capacity increases for $S_1 <$

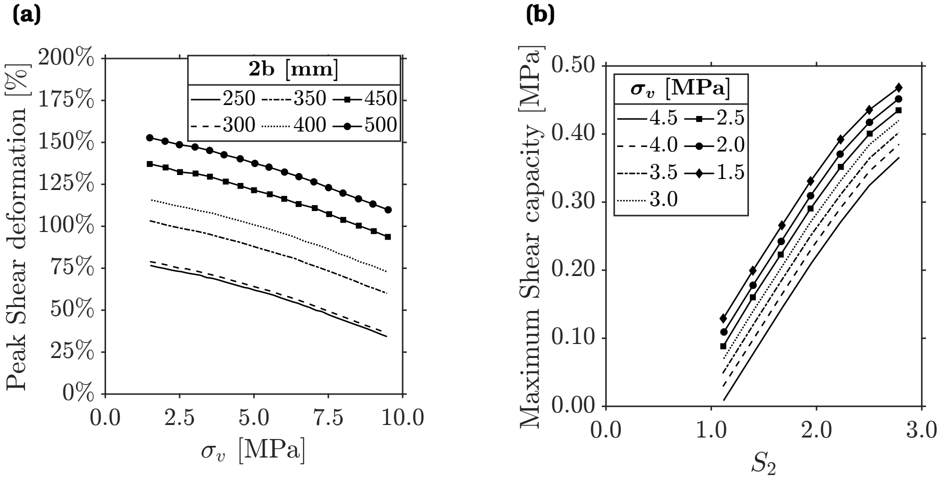

Figure 3.8: Lateral response peaks: (a) shear deformation vs axial pressure, (b) shear capacity vs secondary shape factor.

10 decreases for higher values; if $\sigma_v \geq 3.5$ MPa, the peak decreases when the primary shape factor is less than 10 and increases for higher values.

In both stress and strain trends, a concavity change of the curves can be observed for bearings with $2a = 350$ and $2a = 400$ then bearings with $2a = 300$. Bearings with larger secondary shape factor show an higher peak (in strain and stress) for smaller S_1 values and then a slight decrease followed by an S_1 independent response when $S_1 > 30$.

The influence of the shear modulus of the rubber on the shear strain and stress capacity of the bearings with base sides $2b = 300, 350, 400$ mm are plotted in **Figure 3.10**. As expected, the peak shear strain increases with the shear modulus G_e. For values of axial pressure above 6.0 MPa, the increase in shear strain is almost linear, while for smaller values of axial loads, even increasing if, the response is concave down. For values of axial pressure larger than 6.0 MPa, increasing the shear modulus of the rubber substantially increases the shear load capacity of the bearings. **Figures 3.10 (d)**, **3.10 (e)** and **3.10 (f)** show that the peak shear stress capacity of a

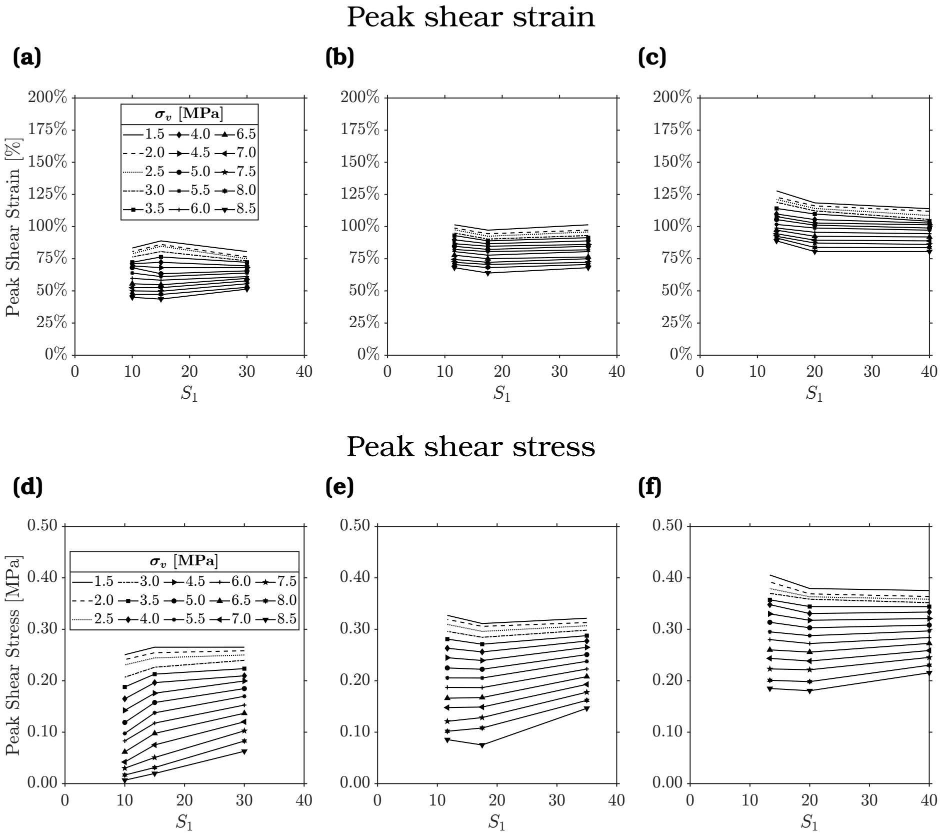

Figure 3.9: Peak shear stress - strain vs primary shape factor: (a), (d) $2a$ = 300 mm, (b), (e) $2a$ = 350 mm and (c), (f) $2a$ = 400.

Peak shear strain

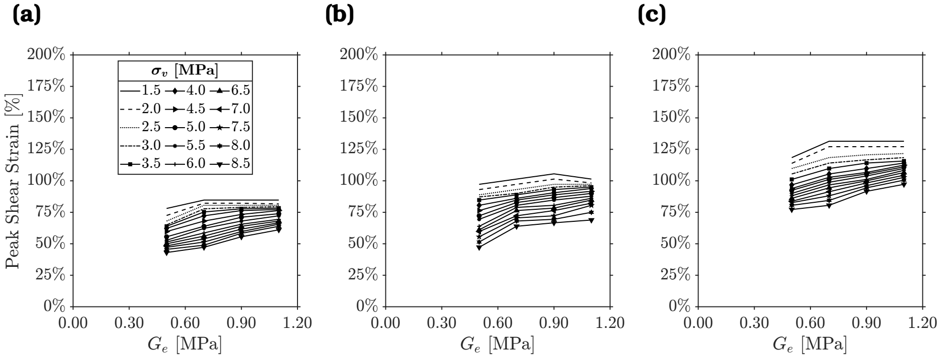

Peak shear stress

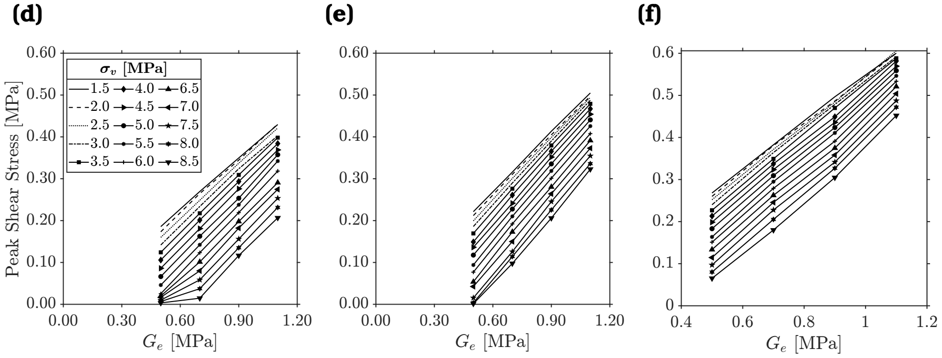

Figure 3.10: Peak shear stress - strain vs shear modulus of the rubber: (a), (d) $2a = 300$ mm, (b), (e) $2a = 350$ mm and (c), (f) $2a = 400$.

FREI always increases with increasing the shear modulus of the rubber, almost independently of the secondary shape factor.

Finally, the influence of the bulk modulus of the rubber on the horizontal response of a FREI is shown in **Figure 3.11**. The plots indicate that the peak lateral response of a FREI is not affected by the bulk modulus of the rubber: it only slightly change the peak shear strain, while having no influence on the peak shear stress capacity of these devices.

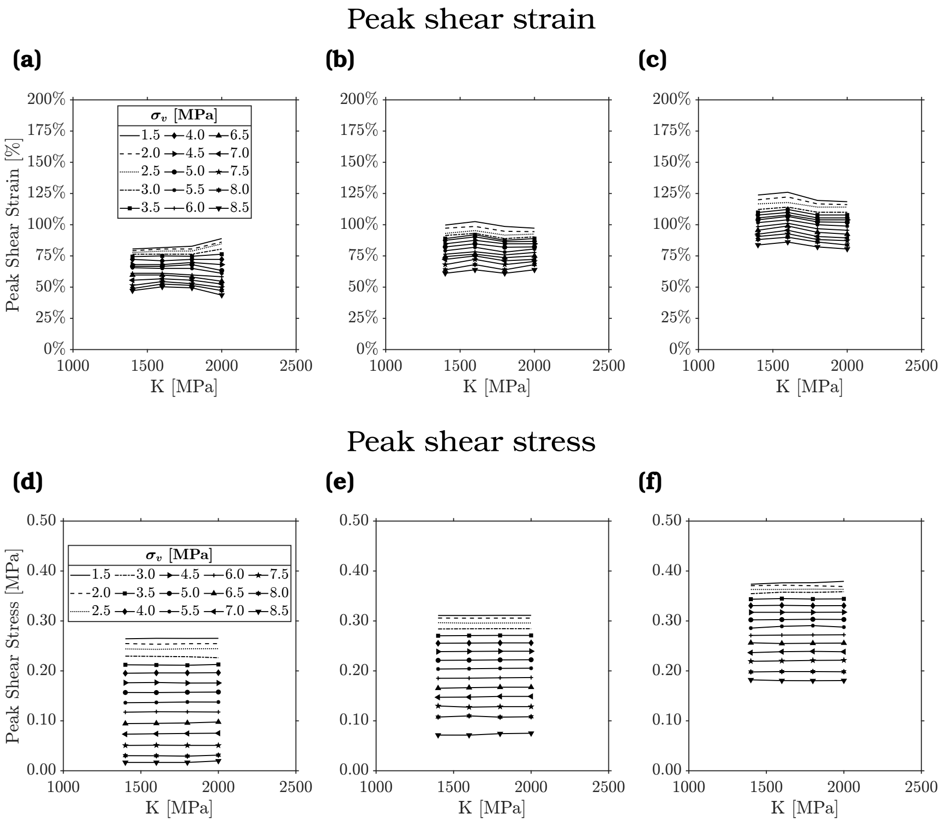

Figure 3.11: Peak shear stress - strain vs bulk modulus of the rubber: (a), (d) $2a = 300$ mm, (b), (e) $2a = 350$ mm and (c), (f) $2a = 400$.

3.3 Vertical displacements under combined axial and shear loads: analytical vs numerical solutions

The buckling behavior of elastomeric bearings with rigid reinforcement have been studied under combined tension and shear loads, obtaining an analytical solution for the vertical displacement at the top of such bearings under the same load conditions [130]. The same solution has been used for bearings with rigid reinforcement under compressive and shear loads [131].

The vertical stiffness of elastomeric bearings depends on the horizontal deformation, decreasing accordingly with the lateral load. The total vertical displacement δ_v^t can be divided into two adding terms: the vertical displacement due to pure compression δ_v^c (i.e. under solely vertical load) and the vertical displacement due to lateral deformation δ_v^s (i.e. under axial and shear load):

$$\delta_v^t = \delta_v^c + \delta_v^s \tag{3.10}$$

In [131] the two displacements are calculated as follows:

$$\delta_v^c = \frac{F_v}{K_v} = \frac{F_v \cdot t_r}{E_c A_c} \tag{3.11a}$$

$$\delta_v^s = \frac{\pi G_e A_c}{4F_{v,cr_0}} \left(\frac{\pi f_v - \sin \pi f_v}{1 - \cos \pi f_v} \right) \frac{\delta_H^2}{t_r} \tag{3.11b}$$

with the parameters:

- $K_v = \frac{4GS_1^2(2a)}{t_r}$.
- $F_{v,cr_0} = \frac{\pi}{H}\sqrt{EI_s \cdot G_e A_s}$.
- $f_v = F_v/F_{cr_0}$.
- $E_c I_s = 4G_e S_1^2 \left(\frac{2a^2}{15}\right)\frac{H}{t_r}$.
- $G_e A_s = G2aH/t_r$

Table 3.2: Variable parameters in the second set of FEMs for analytical/numerical comparison.

$2a$ [mm]	G_e [MPa]	t_e [mm]	H [mm]	t_f [mm]	E_f [MPa]	ν_f [-]	σ_v [MPa]
250	0.5	5	180	0.645	100000	0.1	2
300	0.7	10					4
350	0.9	15					
400	1.1						
450							
500							

obtained for a bearing with rigid reinforcement. In this thesis, **Equation 3.10** is applied to bearings with flexible reinforcement, modifying the parameters in the two terms of **Equations 3.11a** and **3.11b**. The effective compressive modulus and the buckling load are taken from **Equations 2.3a** and **2.20** respectively.

Further FEAs were conducted on the set of FEMs showed in **Table 3.2**. The vertical displacements obtained from these models were compared with those obtained from **Equation 3.10** accounting the flexibility of the reinforcement as said above. In each FEM, an horizontal displacement at least equal to half of its base has been imposed, to find out the axial deformation of the device at the peak horizontal force.

Figures 3.12 and **3.13** show the analytical vs experimental results for $\sigma_v = 2$ MPa and $\sigma_v = 4$ MPa, respectively, for different values of the shear modulus of the rubber and thickness of the elastomeric layers. Each total vertical displacement is computed at the horizontal displacement corresponding to the peak of the horizontal force, i.e. prior instability.

Clearly, the vertical displacement of a FREI under horizontal load increases with increasing axial loads (i.e., pressure). As expected, increasing the thickness of the individual rubber layer, leads to an increase in vertical displacement. The analytical and the numerical results are in good agreement when the applied pressure is equal to 2 MPa, especially for $t_e = 5,\ 10$ mm. Increasing the pressure to 4 MPa, the comparison is well calibrated when the thickness of the rubber is greater than 10 mm, while it is more approximate when the thickness decreases down to 5 mm. This is because **Equation 2.3a** underestimates the compressive modulus of bearings with larger elastomeric thicknesses. With this equation, the vertical stiffness drops as t_e increase, while from the FEMs the stiffness does not decrease as quickly.

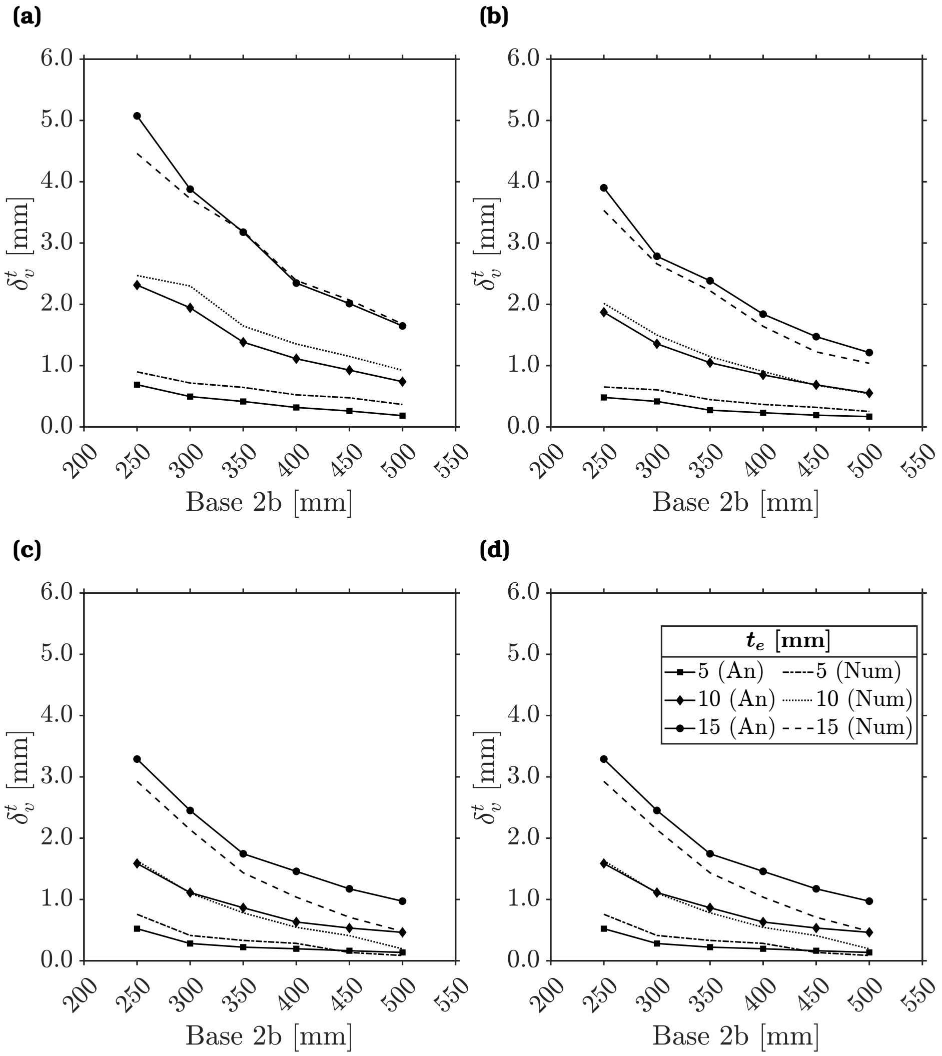

Figure 3.12: Total vertical displacement under $\sigma_v = 2$ MPa at peak horizontal displacement: (a) $G = 0.5$ MPa, (b) $G = 0.7$ MPa, (c) $G = 0.9$ MPa and (d) $G = 1.1$ MPa.

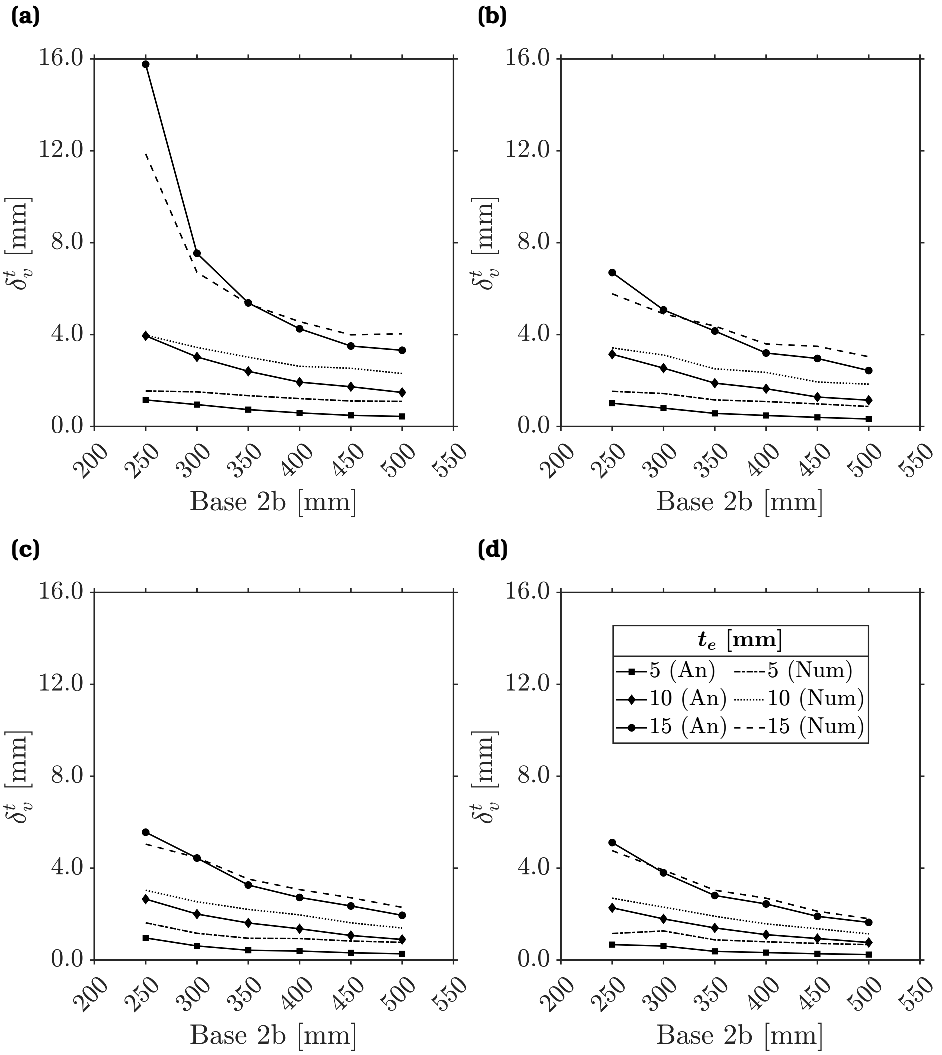

Figure 3.13: Total vertical displacement under $\sigma_v = 4$ MPa at peak horizontal displacement: (a) $G = 0.5$ MPa, (b) $G = 0.7$ MPa, (c) $G = 0.9$ MPa and (d) $G = 1.1$ MPa.

CHAPTER 4

VARIATION OF THE VERTICAL RESPONSE OF SQUARE-SHAPED FIBER REINFORCED ELASTOMERIC ISOLATORS

Summary

This chapter introduces an analytical solution to derive the vertical response parameters of the bearings as functions of the horizontal displacement. The variations of the vertical stiffness and the effective compressive modulus of square-shaped FREIs are studied. The analytical results are then validated through a comparison with the outcomes from a parametric finite element analysis on FREIs with different mechanical and geometric parameters
This chapter is based on the incoming paper [132] and conference paper [133].

4.1 Background and motivations

As seen in **Section 2.1**, the analytical solutions for the vertical response parameters of the FREIs, such as vertical stiffness and effective compressive modulus, have been proposed for bearings under pure compression and no horizontal displacement. FREIs in unbonded configuration subjected to axial and shear loads experience the rollover deformation as the marginal areas detach from the supports (see **Section 1.2.1.1**). As the rollover deformation reduces the loaded area, the vertical properties of the U-FREIs depend on the horizontal deformation. Their variation has been studied through finite element analyses [134] but no analytical solutions accounting this variation are available. This chapter introduces a closed-form solution for the vertical stiffness and the effective compressive modulus of U-FREIs under combined axial and shear loads, based on available analytical results on the vertical compression of these bearings. The proposed analytical solutions are applied to several square-shaped U-FREIs. A parametric finite element analysis is then conducted to validate the analytical results, proving how the proposed method could be used to account the variation of the vertical response of U-FREIs under simultaneous axial and shear loads.

4.2 Analytical solutions for U-FREIs under pure compressive load: overview

4.2.1 Vertical Stiffness and Effective Compressive Modulus

As already stated in **Section 2.1**, the vertical stiffness of ealstomeric bearings under a compressive load $F_v = \sigma_v \cdot A_c$, can be obtained with good accuracy using a linear elastic analysis. The generic i-th elastomeric layer is seen as a spring with stiffness equal to:

$$K_{v,i} = \frac{E_{c,i} A_{c,i}}{t_{e,i}} \tag{4.1}$$

where the effective compressive modulus $E_{c,i}$, i.e. the Young's modulus of the i-th elastomeric layers in between two reinforcement sheets, take into account the influence of the reinforcement.

The overall stiffness of the elastomeric bearing is then obtained considering all the spring in series:

$$\frac{1}{K_v} = \sum_i \frac{1}{K_{v,i}} = \sum_i \frac{t_{e,i}}{E_{c,i}A_{c,i}} \tag{4.2}$$

If the bearing is made by n equally spaced elastomeric layers, then $E_{c,i} = E_{c,n} = E_c$, $A_{c,i} = A_{c,n} = A_c$, $t_{e,i} = t_{e,n} = t_e$ and the vertical stiffness of the FREI is:

$$\frac{1}{K_v} = \frac{\sum_i t_{e,i}}{E_c A_c} = \frac{n \cdot t_e}{E_c A_c} \tag{4.3}$$

Recalling the definition of the total height of rubber ($t_r = \sum_i t_{e,i} = n \cdot t_e$), the vertical stiffness can be finally obtained using **Equation 2.1**. In this equation the only unknown is the effective compressive modulus. The Young's modulus of the i-th elastomeric layer in between two reinforcement sheets (i.e. of an equivalent elastic spring), is clearly defined as:

$$E_{c,i} = \frac{\sigma_{v,i}}{\varepsilon_{v,i}} = \frac{\sigma_{v,i} \cdot t_{e,i}}{\delta_{v,i}} \tag{4.4}$$

where $\delta_{v,i}$ is the compression of the i-th elastomeric layer (i.e. $t_e^d - t_e$, with t_e^d the thickness of the generic elastomeric layer after deformation). The effective compressive modulus of a bearing with n equally spaced elastomeric layers can be obtained as for the vertical stiffness considering all the spring (i.e. the rubber layers) in series:

$$E_c = \sum_i^n \frac{\sigma_{v,i}}{\varepsilon_{v,i}} = \frac{\sigma_v}{\sum_i^n \varepsilon_{v,i}} = \frac{\sigma_v \cdot n \cdot t_e}{\delta_v} = \frac{\sigma_v t_r}{\delta_v} \tag{4.5}$$

With the analytical methods, the effective compressive modulus can be calculated with one of the solutions proposed in **Section 2.1** and once E_c is known, the vertical stiffness of the elastomeric bearing can be consequently obtained.

4.2.2 Axial deformation of a FREI under vertical and lateral loads

In **Section 3.3**, the closed-form solution for the overall vertical deformation of strip-shaped elastomeric bearings has been adapted to an elastomeric bearing with flexible reinforcement using the available analytical equation proposed for the buckling load of strip-shaped FREIs.

A similar approach is herein proposed for a square-shaped FREI. For the sake of semplicity, the equation for the total vertical displacement is reported below:

$$\delta_v^t = \delta_v^c + \delta_v^s = \frac{F_v}{K_v} + \frac{\pi G_e A_c}{4F_{v,cr_0}}\left[\frac{\pi f_v - \sin(\pi f_v)}{1-\cos(\pi f_v)}\right]\frac{\delta_H^2}{t_r} \tag{4.6}$$

The buckling load for square-shaped elastomeric bearings with flexible reinforcement can be obtained solving the non-linear **Equation 2.19** for F_{v,cr_0}. All the other geometric parameters of **Equation 4.6** can be easely adapted to a square-shaped FREIs, as $A_c = 4a^2$ and $t_r = n \cdot t_e$.

4.3 Vertical stiffness and effective compressive modulus under axial and shear loads: analytical solution

The vertical stiffness of U-FREIs under combined axial and shear loads can be obtained as:

$$K_v^{\delta_H} = \frac{F_v}{\delta_v^t} = \frac{F_v}{\delta_v^c + \delta_v^s} \tag{4.7}$$

where the notation on the total vertical displacement introduced in **Equation 4.6** has been used. Multiplying and dividing **Equation 4.7** by the (greater than 0) displacement δ_v^c, the vertical stiffness as a function of the horizontal displacement becomes:

$$K_v^{\delta_H} = \frac{F_v}{\delta_v^c}\left(\frac{\delta_v^c}{\delta_v^c + \delta_v^s}\right) = K_v \cdot \psi(\delta_H) \tag{4.8}$$

Equation 4.8 shows how the vertical stiffness of a U-FREIs under combined axial and shear loads can be obtained starting from the vertical stiffness under pure compression through the function $\psi(\delta_H)$. This function tunes the vertical response of the U-FREI under combined axial and shear loads and is herein referred as *modulating function*.

The modulating function depends on the horizontal displacement via the vertical displacement δ_v^s and solely assumes values lower than or equal to 1, as the denominator $\delta_v^c + \delta_v^s$ is anyway greater than or at least equal to the numerator δ_v^c. Two limits value of this function can be immediately obtained as:

$$\lim_{\delta_H \to 0} \psi(\delta_H) = 1 \tag{4.9a}$$

$$\lim_{\delta_H \to \infty} \psi(\delta_H) = 0 \tag{4.9b}$$

Thus, the vertical stiffness under combined axial and shear loads ranges from 0 to a maximum value equal to K_v. Using **Equation 2.1**, the vertical stiffness $K_v^{\delta_H}$ can be also written as:

$$K_v^{\delta_H} = \frac{E_c A_c}{t_r} \cdot \psi(\delta_H) \tag{4.10}$$

A similar approach can be used for the effective compressive modulus under combined axial and shear loads. Using the definition given in **Equation 4.5**, this modulus can be obtained considering the total vertical displacement at the top of the bearing:

$$E_c^{\delta_H} = \frac{K_v^{\delta_H} t_r}{A_c} \tag{4.11}$$

and with the definition of $K_v^{\delta_H}$ given in **Equation 4.10**, the effective compressive modulus under combined axial and shear loads takes the form:

$$E_c^{\delta_H} = \psi(\delta_H) \cdot E_c \tag{4.12}$$

Equation 4.12 shows how the effective compressive modulus under combined axial and shear loads can be obtained from the effective compressive modulus under pure compression via the function $\psi(\delta_H)$, as indeed obtained for the vertical stiffness.

The analytical formulation of the function $\psi(\delta_H)$ can be obtained using the definition given in **Equations 4.6** and **4.8**:

$$\psi(\delta_H) = \frac{\delta_v^c}{\delta_v^c + \delta_v^s} = \frac{1}{1 + \frac{\pi G_e E_c A_c^2}{4 F_v F_{v,cr_0}} \left[\frac{\pi f_v - \sin(\pi f_v)}{1 - \cos(\pi f_v)} \right] \frac{\delta_H^2}{t_r}} \tag{4.13}$$

Note how this expression verifies the two expected limits given by **Equation 4.9**. With **Equation 4.13**, either the vertical stiffness or the effective compressive modulus can be calculated at a generic threshold of the horizontal displacement δ_H.

Considering that $S_1 = a/2t_e$, $S_2 = 2a/t_r$ and $\sigma_v = F_v/A_c$, **Equation 4.13** could be arranged in the following form:

$$\psi(\delta_H) = \frac{1}{1 + \pi \frac{G_e E_c}{F_v F_{v,cr_0}} S_1 S_2^2 A_{l,e} \left[\frac{\pi f_v - \sin(\pi f_v)}{1 - \cos(\pi f_v)} \right] \delta_H^2} \tag{4.14}$$

where $A_{l,e} = 2a \cdot t_e$ is the lateral area of a single elastomeric layer. **Equation 4.14** shows how the geometric and mechanical variable parameters of the bearing affects the shape of the modulating function. Indeed:

$$\lim_{S_1, S_2 \to 0} \psi(\delta_H) = 0 \tag{4.15a}$$

$$\lim_{S_1, S_2 \to \infty} \psi(\delta_H) = 1 \tag{4.15b}$$

while:

$$\lim_{E_c, G_e \to 0} \psi(\delta_H) = 0 \tag{4.16a}$$

$$\lim_{E_c,G_e\to\infty} \psi(\delta_H) = 1 \tag{4.16b}$$

$$\lim_{F_v\to 0} \psi(\delta_H) = 1 \tag{4.16c}$$

$$\lim_{F_v\to\infty} \psi(\delta_H) = 0 \tag{4.16d}$$

As the modulating function quantifies the reduction of the vertical stiffness and the effective compressive modulus with the horizontal deformation, a larger reduction of $\psi(\delta_H)$ results in lower values of the vertical response parameters of the bearings.

The vertical stiffness needs to be sufficiently higher than the horizontal stiffness to avoid rocking motion and support the weight of the structure [135]. Computing the vertical stiffness under simultaneous vertical and horizontal loads with the modulating function, a ratio of vertical to horizontal stiffnesses both functions of the horizontal displacement could be obtained:

$$\frac{K_v^{\delta_H}}{K_H^{\delta_H}} = \psi(\delta_H) \cdot \frac{K_v}{K_H^{\delta_H}} \tag{4.17}$$

where $K_H^{\delta_H}$ means a horizontal secant stiffness value at a generic horizontal displacement threshold. **Equation 4.17** shows how the ratio of stiffnesses at a generic horizontal displacement δ_H can be obtained through the modulating function starting from the ratio between the vertical stiffness under pure compression and the secant horizontal stiffness at the same horizontal displacement level. Using the definition of vertical stiffness under solely vertical load given in **Equation 2.1**, **Equation 4.17** becomes:

$$\frac{K_v^{\delta_H}}{K_H^{\delta_H}} = \psi(\delta_H) \cdot \frac{E_c \cdot A_c}{t_r \cdot K_H^{\delta_H}} \tag{4.18}$$

and recalling the definition of the secondary shape factor:

$$\frac{K_v^{\delta_H}}{K_H^{\delta_H}} = \psi(\delta_H) \cdot \frac{E_c \cdot 2a \cdot S_2}{K_H^{\delta_H}} \tag{4.19}$$

This ratio could be calculated with the analytical method using

Equation 4.14 for the modulating function, one of **Equations 2.4**, **2.6** and **2.7**, for the effective compressive modulus and one of the different solutions proposed for the horizontal stiffness of U-FREIs showed in **Section 2.2**.

4.3.1 Trends of the modulating function

In this section, **Equation 4.14** is applied to square-shaped FREIs using the following approach. For the effective compressive modulus under pure compression, either **Equations 2.4**, **2.6** and **2.7** are used, while **Equation 2.19** are solved for the buckling load. With this novel method, **Equation 4.6** are adapted and used for square-shaped U-FREIs. The three solutions for E_c, allows to estimate the differences between the assumption of compressible and incompressible elastomeric layers.

Figures 4.1, **4.2** and **4.3** show the trends of the function $\psi(\delta_H)$ with the shear strain $\gamma_H = \delta_H/t_r$ using **Equations 2.4a**, **2.6** and **2.7** respectively. In each figure, a shear strain of 200% has been set as maximum lateral deformation threshold, as this value approximately corresponds to the full rollover of the U-FREIs [25]. The figures show the dependence of the modulating function on the main geometric and mechanical parameters of **Equation 4.14**: the primary shape factor, the secondary shape factor and the aspect ratio (**Figures 4.1 (a)**, **4.2 (a)** and **4.3 (a)**), the shear modulus (**Figures 4.1 (b)**, **4.2 (b)** and **4.3 (b)**) and the vertical pressure (**Figures 4.1 (c)**, **4.2 (c)** and **4.3 (c)**).

In all these figures, the function $\psi(\delta_H)$ decreases with increasing values of shear strain, as expected. The dependence of the modulating function on the horizontal displacement (shear strain) is in line with the predicted limits given by **Equation 4.9**. The analytical expression used for the effective compressive modulus does not affect the shape of the modulating function, while the variable geometric and mechanical parameters do. The limits given by **Equations 4.15** and **4.16** are respected as:

- the reduction of $\psi(\delta_H)$ is greater for bearings with lower aspect ratio, primary and secondary shape factor. It can be noted how secondary shape factor lower than 2.5 return strongly decreasing values, while greater values of S_2 ensure a smoother decrease. In **Figures 4.1 (a)**, **4.2 (a)** and **4.3 (a)**, at $\gamma_H = 200\%$, the modulating function decreases by 95% if $S_2 = 1$, by 75% if $S_2 = 2$, by 60% if and if $S_2 = 3$ increases to 10, $\psi(\delta_H)$ is reduced by only 12%.

- the shear modulus slightly increases the capacity of the U-FREIs and a lower reduction of the modulating function corresponds to increasing values of G_e. However, the influence of this parameters is very little compared to the geometric ones. For example, for a bearing with $S_1 = 10$ and $S_2 = 2.04$, the reduction of the modulating function at $\gamma_H = 200\%$ is 78% with $G_e = 0.3$ MPa, while is 75% with $G_e = 2.1$ MPa (**Figures 4.1 (b)**, **4.2 (b)** and **4.3 (b)**).

- finally, lower values of σ_v are obtained for the same bearings under increasing vertical pressure.

The most significant influence on the shape of the modulating function is due to the geometric properties of the bearings. The great influence of the primary shape factor on the vertical response and of the secondary shape factor on the horizontal response of U-FREIs have been already proved [136]. These parameters both play a key role on the influence of the horizontal deformation on the vertical response of the U-FREIs. However, the secondary shape factor has a higher order and a greater influence on the increasing/decreasing trend of the modulating function.

4.4 Finite Element Analyses

The analysis were performed as explained in **Section 3.1** using MSC.Marc as well. However, 3D FEAs were run in this case. The specifications are shown below.

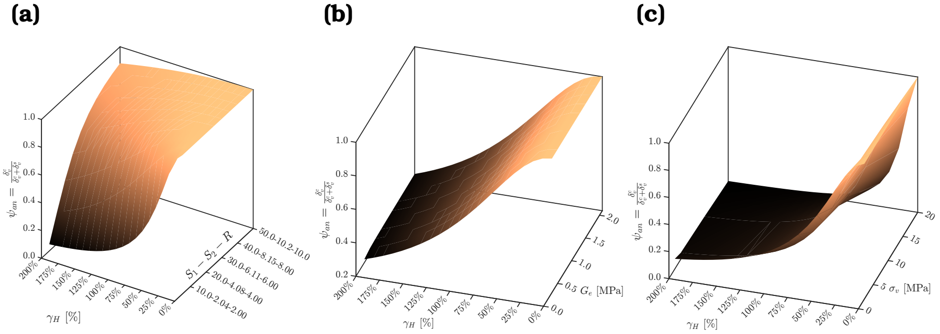

Figure 4.1: Trends of function $\psi(\delta_H)$ with the shear strain: analytical results using **Equation 2.4a** for E_c varying the: (a) geometry, (b) shear modulus and (c) vertical pressure.

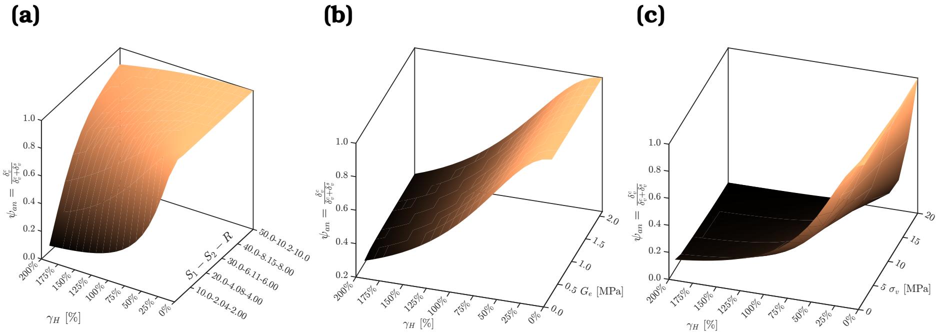

Figure 4.2: Trends of function $\psi(\delta_H)$ with the shear strain: analytical results using **Equation 2.6** for E_c varying the: (a) geometry, (b) shear modulus and (c) vertical pressure.

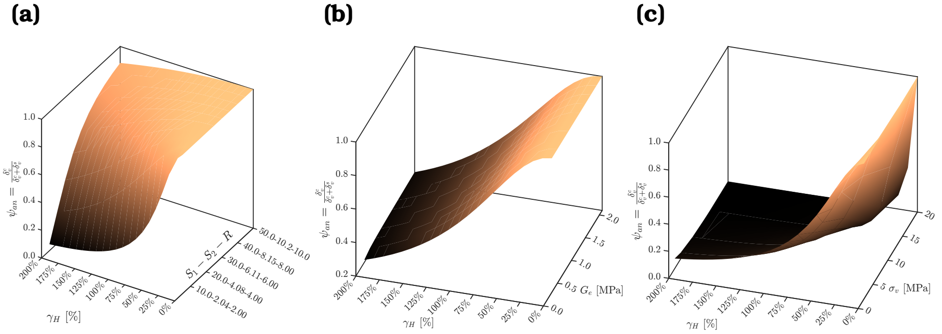

Figure 4.3: Trends of function $\psi(\delta_H)$ with the shear strain: analytical results using **Equation 2.7** for E_c varying the: (a) geometry, (b) shear modulus and (c) vertical pressure.

4.4.1 Set of Finite Element Models

A parametric study is presented in this section. Finite element analyses (FEAs) are carried out to a number of square-shaped U-FREIs with variable geometric and mechanical parameters. The modulating function are obtained from these analyses and compared with the analytical results of **Section 4.3.1**, in order to validate them.

Table 4.1 shows the set of square-shaped FREIs used for this parametric study, with the main geometric and mechanical parameters. A total number of 168 different FREIs are obtained considering a combination of two geometric (base dimensions $2a$ and thickness of the elastomeric layers t_e) and two mechanical parameters (shear modulus G_e of the elastomer and vertical applied pressure σ_v). The total height of the bearing H, the bulk modulus of the rubber K, the equivalent thickness of the fiber reinforcement t_f and its Young's modulus E_f are instead kept constant.

With the base sides and elastomeric layers thickness considered, 12 values of primary and secondary shape factors are obtained: S_1 ranges from 5.0 to 62.5, while S_2 ranges from 1.02 to 5.24. Finally, five values of the aspect ratio R from 1.00 to 5.00 are included.

Note how in the sets of **Table 4.1** different values of the shear modulus are considered if compared with **Table 3.1**. Combining the parameters of the two table, a wider sets of shear modulus

Table 4.1: Overview of the geometric and mechanical parameters used for the parametric finite element study.

$2a$ [mm]	H [mm]	R [-]	t_e [mm]	$S_1^{t_e=2}$ [-]	$S_1^{t_e=5}$ [-]	$S_2^{t_e=2}$ [-]	$S_2^{t_e=5}$ [-]	G_e [MPa]	σ_v [MPa]	K [MPa]	E_f [MPa]	t_f [mm]
100	100	1.00	2.00	12.5	5.00	1.05	1.02	0.40	4.00	2000	70000	0.100
150		1.50	5.00	18.8	7.50	1.57	1.53	0.80	6.00			
200		2.00		25.0	10.0	2.10	2.04	1.20	8.00			
250		2.50		31.3	12.5	2.62	2.55					
300		3.00		37.5	15.0	3.15	3.06					
350		3.50		43.8	17.5	3.67	3.57					
400		4.00		50.0	20.0	4.20	4.08					
450		4.50		56.3	22.5	4.72	4.59					
500		5.00		62.5	25.0	5.24	5.09					

ranges from 0.4 to 1.2 can be obtained, and the results refer to several rubber compounds.

4.4.2 FEAs specifications

In all the FEMs, at first the bearing is subjected to an increasing vertical load up to the peak value (**Table 5.1**). Then, while keeping the axial load constant, in a second stage, an horizontal displacement is imposed on the top of the bearing up to a shear strain of 200% under displacement control. This value of lateral deformation was found to approximately correspond to a complete roll-over of unbonded FREIs [25].

The elastomer has been modeled using a compressible Neo-Hookean hyperelastic material model while the fiber reinforcement with a linear elastic isotropic material model, and the equations shown in **Section 3.1.2.1** hold in the current section too.

In FEMs, three-dimensional arbitrarily distorted brick with Hermann formulation element (element 84 in Marc [128]) has been used for the elastomer. It is a eight-noded, isoparametric three-dimensional brick element. Nodes 1, 2, 3, and 4 are corners of one face, given in counterclockwise order when viewed from inside the element. Node 5 is on the same edge as node 1, node 6 as node 2, node 7 as node 3, and node 8 as node 4 **Figure 4.4 (a)**.

This element uses trilinear interpolation functions based on the following type of displacement assumption and mapping from the $x-y-z$ space into a cube in the ξ, η, ζ space:

$$x = a_0 + a_1\xi + a_2\eta + a_3\zeta + a_4\xi\eta + a_5\zeta\xi + a_6\xi\zeta + a_7\xi\eta\zeta \tag{4.20a}$$

$$\psi = b_0 + b_1\xi + b_2\eta + b_3\zeta + b_4\xi\eta + b_5\eta\zeta + b_6\xi\zeta + b_7\xi\eta\zeta \tag{4.20b}$$

Either the coordinate or function can be expressed in terms of the nodal quantities $x = \sum_{i=1}^{8} x_i\phi_i$ by the integration functions:

$$\phi_1 = \frac{1}{8}(1-\xi)(1-\eta)(1-\zeta) \quad \phi_5 = \frac{1}{8}(1-\xi)(1-\eta)(1+\zeta) \tag{4.21a}$$

$$\phi_2 = \frac{1}{8}(1+\xi)(1-\eta)(1-\zeta) \quad \phi_6 = \frac{1}{8}(1+\xi)(1-\eta)(1+\zeta) \tag{4.21b}$$

$$\phi_3 = \frac{1}{8}(1+\xi)(1+\eta)(1-\zeta) \quad \phi_7 = \frac{1}{8}(1+\xi)(1+\eta)(1+\zeta) \tag{4.21c}$$

$$\phi_4 = \frac{1}{8}(1-\xi)(1+\eta)(1-\zeta) \quad \phi_8 = \frac{1}{8}(1-\xi)(1+\eta)(1+\zeta) \tag{4.21d}$$

There are three degrees of freedom associated with each node and one extra node with a single degree of freedom (pressure) that uses a mixed formulation for incompressible analysis (**Figure 4.4 (b)**).

The reinforcement has been modeled using an hollow, isoparametric 4-node membrane in which a single strain members such as reinforcing rods or cords (that is, rebars) can be placed (element 147 in Marc [128]) (**Figure 4.5**). The element is then used in conjunction with the 4-node membrane to represent cord reinforced composite materials. It is assumed that several "layers" of rebars are presented. The rebar layers are assumed to be placed on the same spatial position as that of the element (although the rebar direction is arbitrary and the thickness of the layers can be different). The element is integrated using a numerical scheme based on Gauss quadrature.

Figure 4.6 (a) shows a schematic geometry of the bearing whereas **Figure 4.6 (b)** shows a view of a FEM used in this study.

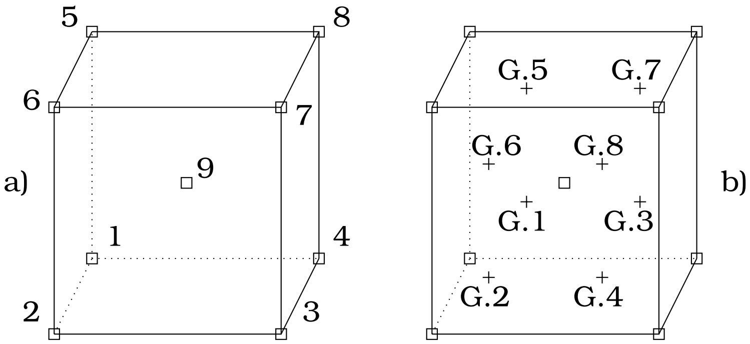

Figure 4.4: (a): Eight-node isoparametric element with extra node, (b): Gaussian integration points.

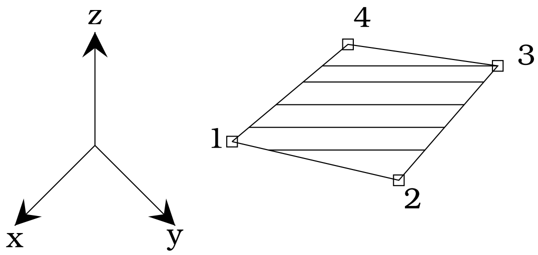

Figure 4.5: Layer of rebar membrane element.

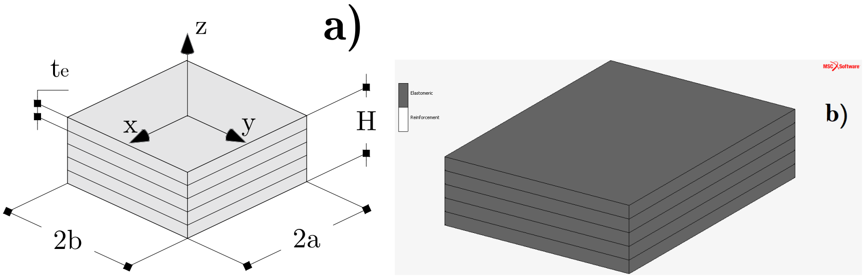

Figure 4.6: Square-shaped U-FREI: (a) schematic of the generic bearing, (b) view of the 3D FEM in MSC.Marc.

4.4.3 FEAs validation

A proper validation of the FEMs is herein proposed by comparing experimental and numerical results, as done in **Section 3.1.2.3**. Experimental tests were run by the authors on square-shaped bearings with different properties and secondary shape factors between 1.0 and 3.0, i.e. a relevant range for lateral stability. **Table 4.2** shows the main geometric and mechanical properties of the tested bearings: bearings US_1 and US_2 are made of layers of neoprene and fiberglass reinforcement and are manufactured following Caltrans specifications [129]; bearings $B_1 - B_3$, Bb_1, Bb_2 are made of recycled rubber and carbon fiber reinforcement. Bearings B_1, B_2 and B_3 have the same geometry but different compound; similarly, bearings Bb_1 and Bb_2 have the same geometry but different properties of the rubber layers. **Figure 4.7 (a)** shows a picture of the RR-FREIs B_1, B_2 and Bb_1 used for the experimental tests, while **Figures 4.7 (b)** and **4.7 (c)** the two samples B_1 and Bb_1 under test.

The shear tests were performed at the Department of Industrial Engineering of the University of Naples Federico II using the test frame shown in **Figure 4.8 (a)**. The specimen is placed between two steel plates. The vertical load is applied through the upper plate, up to a maximum of 190 kN. The bottom plate can freely slide sideways on roller bearings up to a maximum displacement of 200 mm and a maximum horizontal force of 50 kN. The sample bearing is subjected to simultaneous vertical and horizontal loading. The acquisition system consists of a load cell both in the vertical and horizontal direction, two LVDTs (Linear Variable Differential Transformers) to measure the horizontal displacement and two accelerometers at the base plate, used to measure the inertial force of the base plate which has to be subtracted from the recorded horizontal load.

The bearings were tested in unbonded configuration with the quasi-static horizontal displacement protocol shown in **Figure 4.8 (b)** and a strain rate of 1%/s up to a deformation $\gamma_H^{max} = 100\%$. During testing, a constant vertical load of 18.8 kN was applied on the bearings, with a of nominal axial pressure varying from 1.00 MPa for Bb_1 and Bb_2 to 7.52 MPa for US_1 (**Table 4.2**).

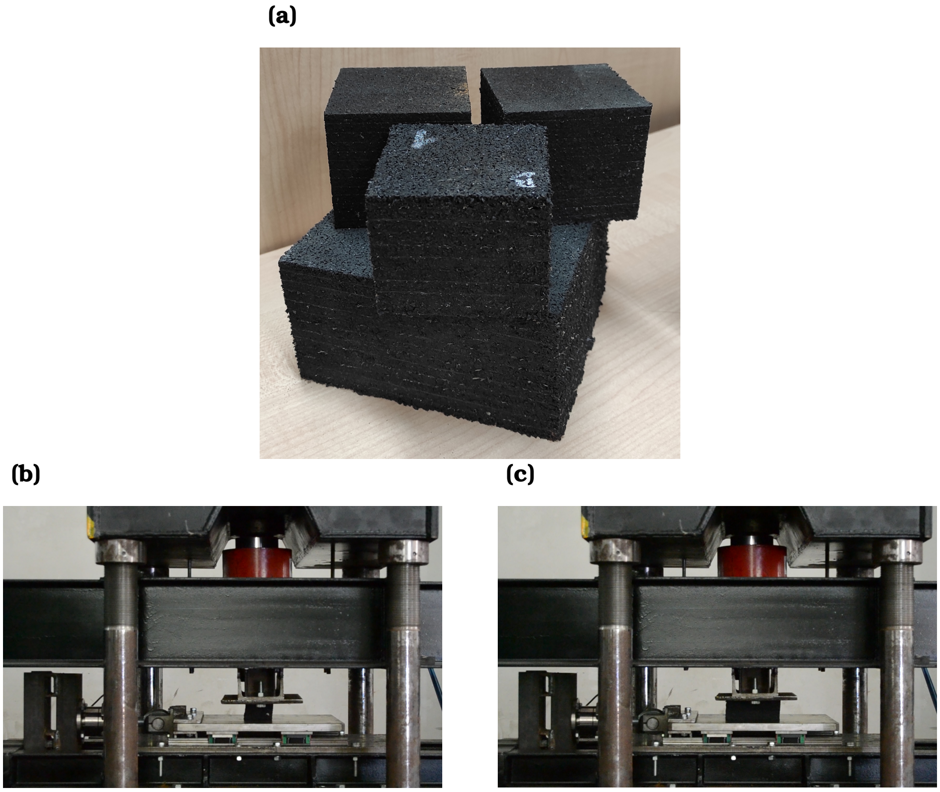

Figure 4.7: Experimental tests for FEAs validation: (a) RR-FREIs samples, (b) sample B_1 under test, (c) sample Bb_1 under test.

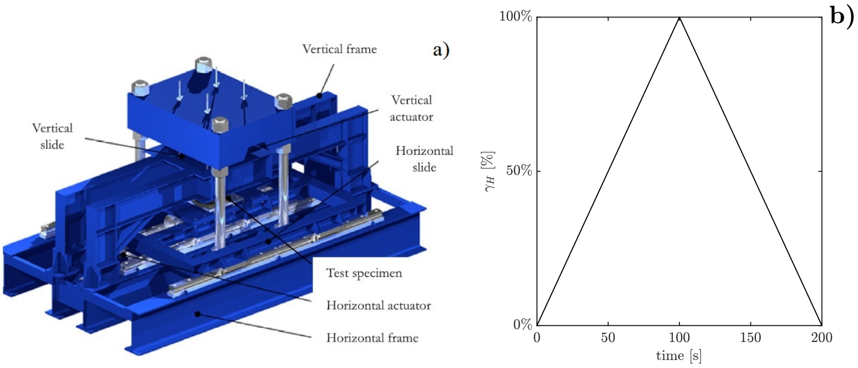

Figure 4.8: Experimental test specifications: (a) testing frame, (b) time-history of the imposed horizontal displacement.

Table 4.2: Samples FREIs compared with numerical models for FEAs validation.

Tested bearing [-]	$2a = 2b = B$ [mm]	H [mm]	t_e [mm]	S_2 [MPa]	Elastomer [-]	Fabric [-]	G_e [MPa]
US_1	50	50	6	1.00	Neoprene	Glass	1.2
US_2	130	50	6	2.60	Neoprene	Glass	1.2
B_1	70	60	5	1.17	Recycled	Carbon	2.4
B_2	70	60	5	1.17	Recycled	Carbon	2.0
B_3	70	60	5	1.17	Recycled	Carbon	1.6
Bb_1	140	60	5	2.33	Recycled	Carbon	0.8
Bb_2	140	60	5	2.33	Recycled	Carbon	0.74

Figure 4.9 shows a good matching between experimental and numerical results. In particular, the numerical models demonstrated a good level of accuracy for both unstable (US_1, B_1, B_2, B_3) and stable response (US_2, Bb_1, Bb_2). Furthermore, it can be noted that the FEM can predict, with satisfactory accuracy, the displacement at which the unstable curves show a peak, which is one of the aims of this study.

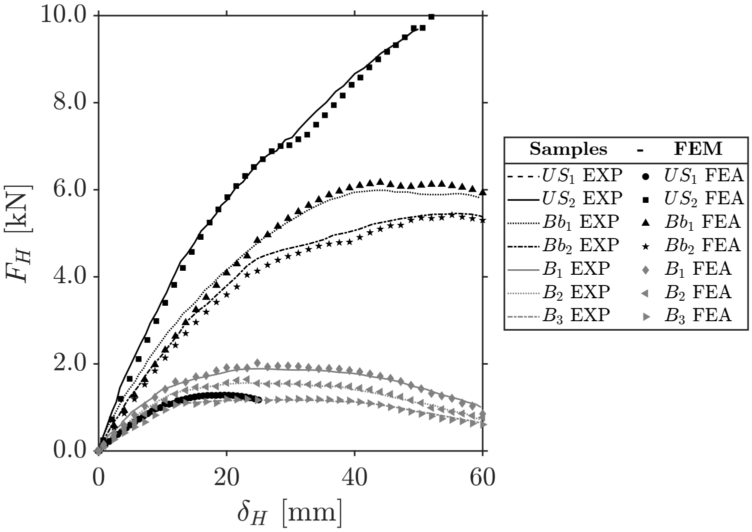

Figure 4.9: FEAs validation: experimental vs numerical tested bearings.

4.5 FEAs results

Figure 4.10 shows the trends of the modulating function with the shear strain from FEAs, obtained reversing the **Equation 4.8**:

$$\psi(\delta_H) = \frac{K_v^{\delta_H}}{K_v} \tag{4.22}$$

The numerical trends agree with the analytical ones and the modulating function always decreases with the shear strain. On the influence of the geometric and mechanical parameters, once again is proved how:

- $\psi(\delta_H)$ reduces less with increasing primary and secondary shape factors. These two parameters play the major role on the trends of the modulating function as already seen with **Figures 4.1**, **4.2** and **4.3**.
- increasing shear modulus ensures a lower reduction of the modulating function of bearings with the same geometry.

Figures 4.1, **4.2**, **4.3** and **4.10** show how the primary and the secondary shape factors affect the trends of the modulating function. As said, both parameters have a great influence on $\psi(\delta_H)$ and consequently on the vertical stiffness and the effective compressive modulus of U-FREIs under combined axial and shear loads. However in **Figure 4.10**, comparing bearings with the same shear modulus and secondary shape factor, but different primary shape factor (i.e. **Figure 4.10 (a)** with **Figure 4.10 (d)**, **Figure 4.10 (b)** with **Figure 4.10 (e)** and **Figure 4.10 (c)** with **Figure 4.10 (f)**), it appears that S_1 has a minor influence compared to S_2. This means that decreasing (or increasing) the base side of the U-FREIs affects the descendent (or ascendent) trend of $\psi(\delta_H)$ more than increasing (or decreasing) the thickness of the elastomeric layer.

Thus, the higher order of influence of the secondary shape factors compared to the primary shape factor already obtained with the analytical **Equation 4.14** is confirmed by FEAs. Even though S_1 is a key parameter for the vertical response of the bearings under pure compression, under combined axial and shear loads the vertical parameters response of the U-FREIs are mainly controlled by the secondary shape factor.

The roles of the primary and the secondary shape factor is further shown in **Table 4.3**, where the average reduction of the modulating function with the shear strain is highlighted. The percentage reductions of both elastomeric thickness layers are similar. It is clear how the modulating function decreases more when the secondary shape factor is less or equal to 2.5 – 2.6, with a minimum reduction percentage of 70%; larger values of S_2 ensure minor average reduction of $\psi(\delta_H)$.

4.6 Analytical - numerical comparison

For the sake of simplicity, **Figure 4.10** shows the average numerical trends on the 3 vertical pressure values of **Table 4.1**. A direct analytical – numerical comparison on the modulating function of bearings under $\sigma_v = 4,\ 6,\ 8$ MPa is shown in **Figures 4.11**, **4.12**

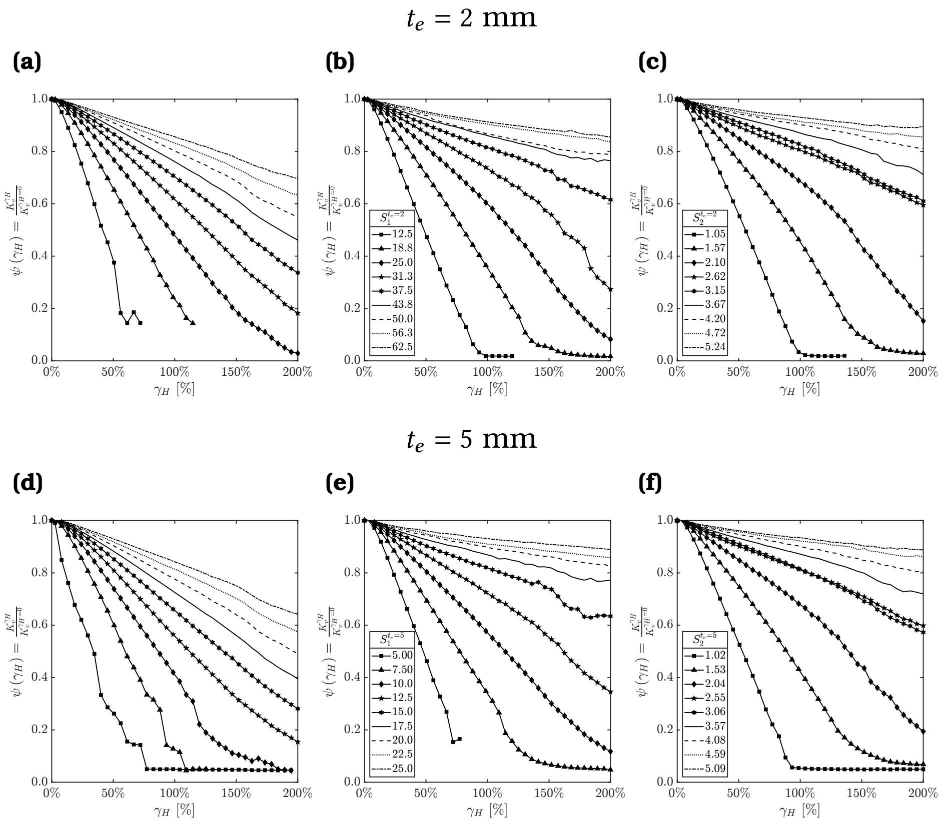

Figure 4.10: Numerical trends of the modulating function with the shear strain: (a), (d) G_e = 0.4 MPa, (b), (e) G_e = 0.8 MPa, (c), (f) G_e = 1.2 MPa.

Table 4.3: $\psi(\delta_H)$ reduction from zero lateral displacement to full rollover (average on the vertical pressure).

$S_2^{t_e=2}$	$S_2^{t_e=5}$	R	G_e = 0.4 MPa		G_e = 0.8 MPa		G_e = 1.2 MPa	
			t_e = 2 mm	t_e = 5 mm	t_e = 2 mm	t_e = 5 mm	t_e = 2 mm	t_e = 5 mm
1.02	1.05	1.00	88.1%	82.7%	93.1%	89.6%	94.0%	88.9%
1.53	1.57	1.50	87.1%	80.9%	93.6%	87.3%	89.2%	85.0%
2.04	2.10	2.00	82.7%	80.1%	89.3%	91.9%	86.6%	89.3%
2.55	2.62	2.50	81.1%	85.4%	75.2%	77.1%	70.2%	72.2%
3.06	3.15	3.00	56.7%	68.3%	58.3%	60.8%	51.2%	53.7%
3.57	3.67	3.50	53.5%	61.3%	42.2%	52.2%	35.8%	43.5%
4.08	4.20	4.00	44.4%	47.6%	35.6%	36.8%	25.3%	25.7%
4.59	4.72	4.50	37.7%	40.1%	26.3%	28.7%	15.4%	14.2%
5.09	5.24	5.00	32.3%	33.8%	23.1%	21.6%	11.1%	7.40%

and **4.13**. In **Figure 4.11** the analytical values of $\psi(\delta_H)$ are obtained using **Equation 2.6** for E_c, in **Figure 4.12 Equation 2.7** are used and **Figure 4.13** uses **Equation 2.4a**.

These figures show a general good agreement between numerical and analytical results. It can be noted that the matching is more accurate for bearings with lower values of the shear modulus (see **Figures 4.11 (a)**, **4.11 (b)** and **4.11 (c)**, **Figures 4.12 (a)**, **4.12 (b)** and **4.12 (c)** and **Figures 4.13 (a)**, **4.13 (b)** and **4.13 (c)**) or for lower secondary shape factors (see first curves from the bottom of **Figures 4.11**, **4.12** and **4.13**).

The numerical trends of the modulating function of bearings with larger values of G_e and S_2 are stiffer at large shear strain compared to the analytical ones. This is because the analytical formulation of $\psi(\delta_H)$ does not consider the full rollover. This phenomenon increases the vertical capacity of bearings at large horizontal displacement and has a greater influence in bearings with larger values of shear modulus and aspect ratio. Thus, some curves show a roughly constant branch (see **Figures 4.11 (f)**, **4.12 (f)** and **4.13 (f)**) starting from $\gamma_H = 150\%$ (i.e. approximately the shear strain threshold where half of the vertical sides of the bearings have become horizontal) or a gently decreasing trend (see **Figures 4.11 (e)**, **4.11 (g)**, **4.12 (e)**, **4.12 (g)**, **4.13 (e)** and **4.13 (g)**) for a combination of low vertical pressure and larger shear modulus. However, it can be noted how the analytical method returns safety predictions of the modulating function, i.e. smaller values of the vertical response parameters of the U-FREIs. Thus, **Equations 4.10** and **4.11** could be safely used in a design phase for a prediction of the vertical stiffness and the effective compressive modulus of U-FREIs under axial and shear loads.

For U-FREIs with smaller values of the secondary shape factor (i.e. $S_2 \leq 2.5$), the maximum shear strain of each trends are lower than 200% (see the first curves from the bottom of **Figures 4.11**, **4.12** and **4.13**). These bearings are unstable, i.e. their lateral responses show softening past the maximum stable shear strain (see **Section 2.3**).

In a design phase, for this type of bearings, the vertical response parameters under combined axial and shear loads may be calculated up to the maximum stable shear strain. In the next chapters it will be shown how to obtain these thresholds using the geometric and mechanical known properties of the bearing, through easy-to-use approximate formula or stability charts.

4.7 Effective compressive modulus and vertical stiffness

Using **Equations 4.10** and **4.12**, the vertical stiffness and the effective compressive modulus for bearings under axial and shear loads can be obtained with the analytical method. **Figures 4.14**, **4.15** and **4.16** show the trends of $E_c^{\delta_H}$ using **Equations 2.4a**, **2.6** and **2.7** respectively. These figures show the average trends of $E_c^{\delta_H}$ on the vertical pressure thresholds of **Table 4.1**, as the compressive load does not affects the shape of the modulating function (see **Section 4.6**). In **Figures 4.17**, **4.18** and **4.19** the vertical stiffness of the bearings under combined axial and shear loads obtained from **Equation 4.10** is shown, again considering an average value of the vertical pressure.

The reductions of the vertical response parameters with the shear strain clearly follow the same analytical trends of $\psi(\delta_H)$ seen in **Figures 4.1**, **4.2** and **4.3**, as both $E_c^{\delta_H}$ and $K_v^{\delta_H}$ are obtained multiplying constant values (E_c and $E_c A_c / t_r$) by the modulating function from **Equation 4.14**.

The hypothesis of incompressible rubber returns greater values of vertical response parameters (**Figures 4.16** and **4.19**) compared to the compressible rubber results (**Figures 4.15** and **4.16**, **Figures 4.18** and **4.19**). Under this assumption, with smaller values of the elastomeric layers thickness (i.e. greater S_1) the values of $E_c^{\delta_H}$ and $K_v^{\delta_H}$ calculated with **Equation 2.4a** are strongly increasing, being from 4.4 to 5.83 times greater than the same values obtained with **Equations 2.6** and **2.7**; increasing the elastomeric layers thickness (i.e. decreasing S_1), the vertical response parameters under the assumption of incompressible rubber are $3 \div 3.4$ times greater

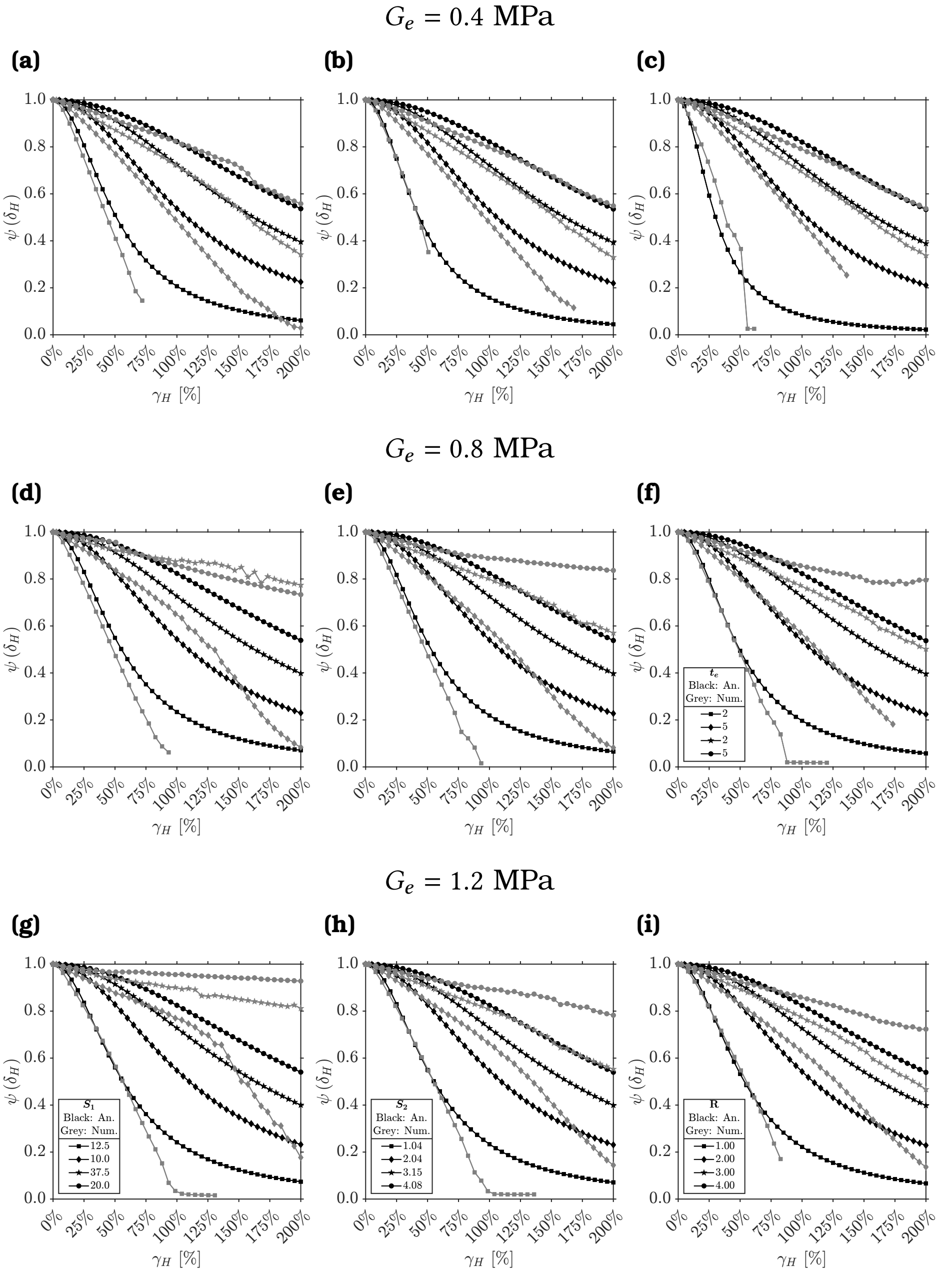

Figure 4.11: Analytical - numerical comparison on trends of the modulating function with the shear strain using **Equation 2.6** for E_c: (a), (d), (g) $\sigma_v = 4$ MPa, (b), (e), (h) $\sigma_v = 6$ MPa, (c), (f), (i) $\sigma_v = 8$ MPa.

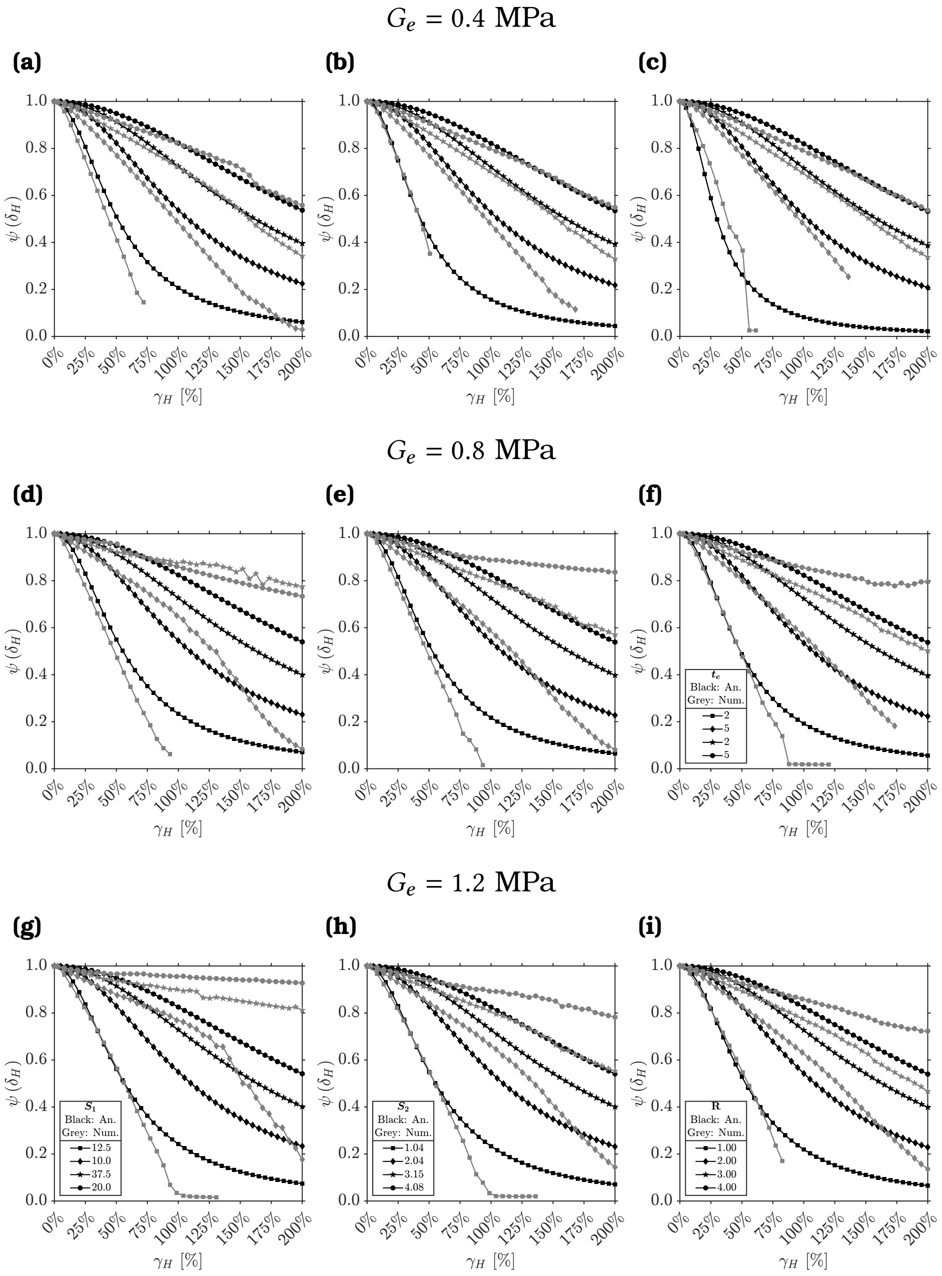

Figure 4.12: Analytical - numerical comparison on trends of the modulating function with the shear strain using **Equation 2.7** for E_c: (a), (d), (g) $\sigma_v = 4$ MPa, (b), (e), (h) $\sigma_v = 6$ MPa, (c), (f), (i) $\sigma_v = 8$ MPa.

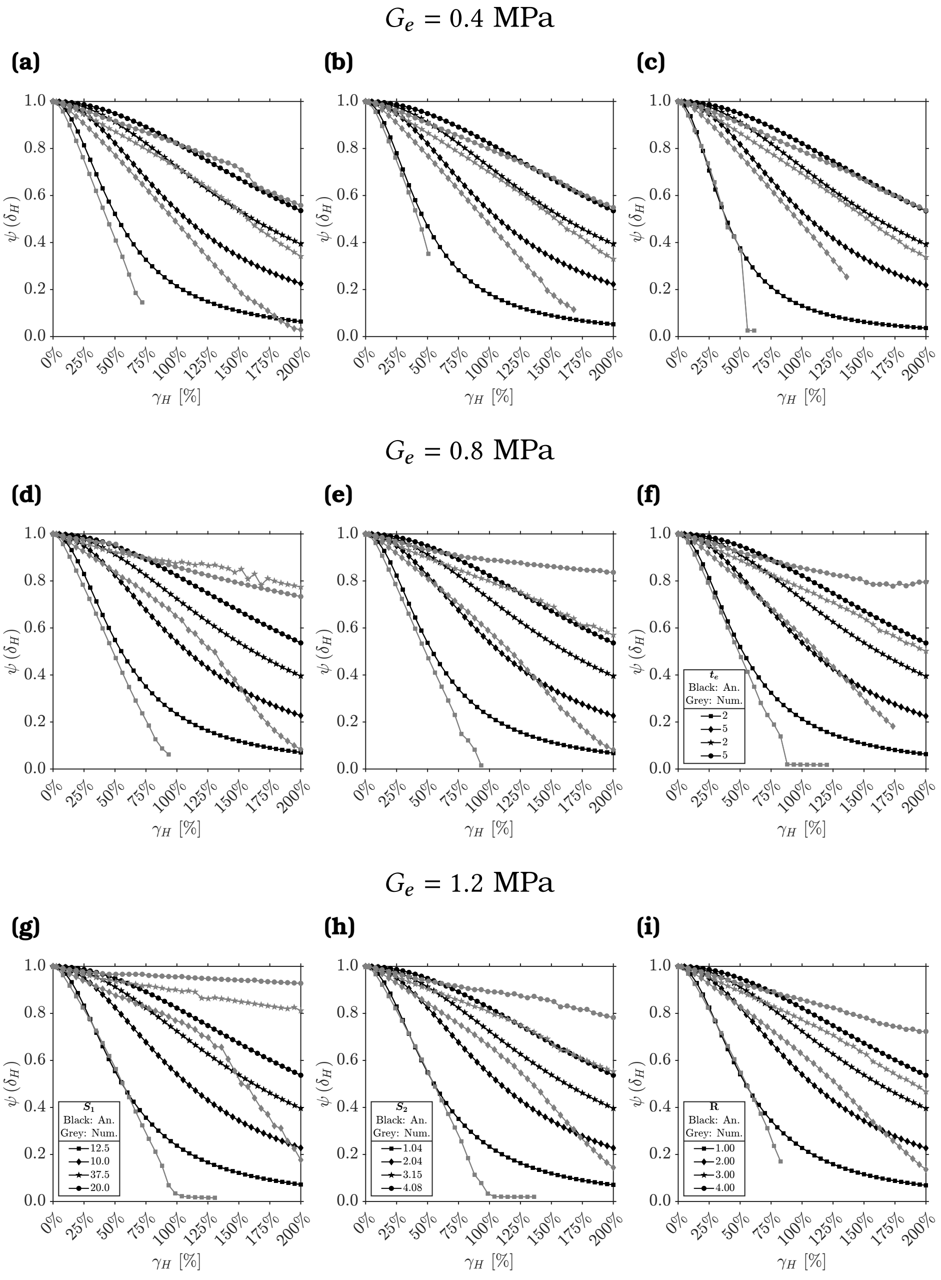

Figure 4.13: Analytical - numerical comparison on trends of the modulating function with the shear strain using **Equation 2.4a** for E_c: (a), (d), (g) σ_v = 4 MPa, (b), (e), (h) σ_v = 6 MPa, (c), (f), (i) σ_v = 8 MPa.

than $E_c^{\delta_H}$ and $K_v^{\delta_H}$ with compressible rubber. A thin incompressible elastomeric layer under a compressive load expierences a very little vertical deformation, showing a large vertical stiffness (see **Equation 4.1**).

These figures highlight again the key role of the secondary shape factor on the vertical response parameters of the U-FREIs under axial and shear loads, as:

- if $S_2 \leq 2.5$, both the vertical stiffness and the effective compressive modulus rapidly drop to zero. Around a shear strain of 50%, both these parameters are more than halved.

- As S_2 increases, the vertical response parameters are less affected by the lateral deformation of the bearing. Similar values of E_c and K_v (i.e. under pure compression) are obtained as S_2 increases and the curves of each bearing are closer comapred to the curves corresponding to lower values of the secondary shape factor.

The numerical trends of $E_c^{\delta_H}$ and $K_v^{\delta_H}$ with the shear strain are shown in **Figures 4.20** and **4.21**. Comparing analytical and numerical trends it can be seen how:

- **Equation 2.4a** returns values of the vertical response parameters strongly greater than the numerical ones. Assuming the rubber as incompressible, the vertical response of the bearings is overestimated, especially for small values of the thickness of the elastomeric layer (i.e. greater primary shape factors).

- **Equation 2.7** underestimates the vertical response of the bearings in any case. The results obtained with E_c given this equation, can be interpreted as lower bounds of the vertical response of the U-FREIs under axial and shear loads.

- **Equation 2.6** provides closest values to numerical results, altough understimated. The analytical predictions using this formula, can be seen as a safety evaluation of the vertical response parameters of the U-FREIs.

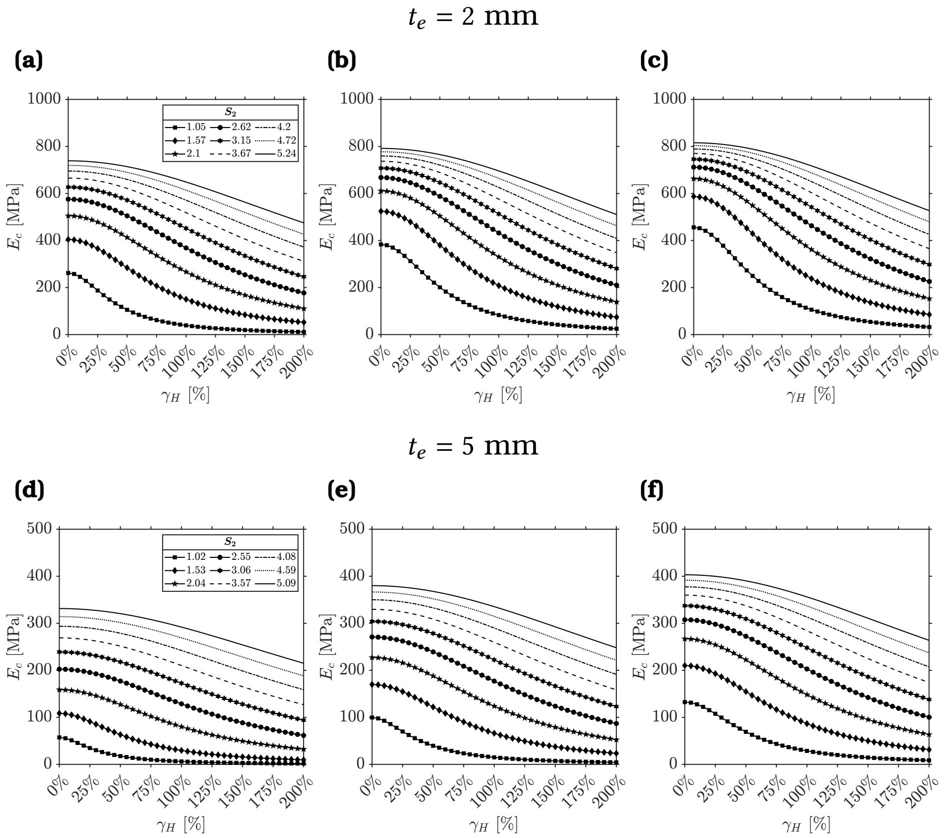

Figure 4.14: Analytical trends of $E_c^{\delta_H}$ using **Equation 2.6** for E_c.: (a), (d) $G_e = 0.4$ MPa, (b), (e) $G_e = 0.8$ MPa, (c), (f) $G_e = 1.2$ MPa.

Based on these results, the proposed analytical method can be used in a design phase to estimate the vertical response parameters (namely the vertical stiffness and the effective compressive modulus) of a U-FREI under combined axial and shear loads.

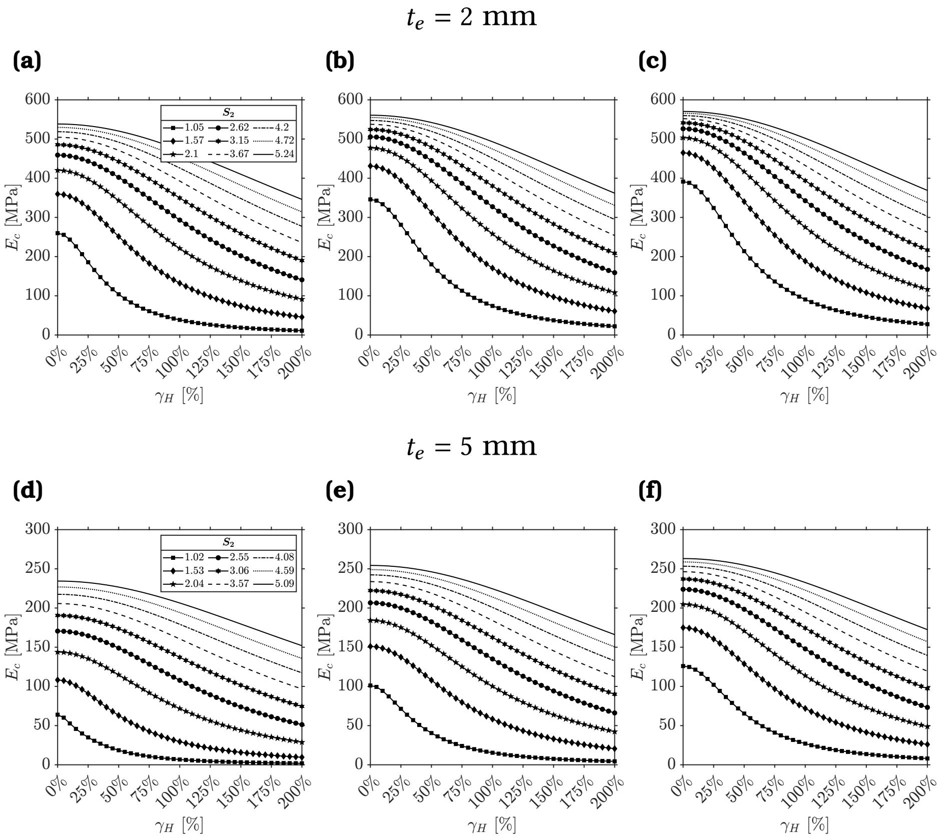

Figure 4.15: Analytical trends of $E_c^{\delta_H}$ using **Equation 2.7** for E_c.: (a), (d) $G_e = 0.4$ MPa, (b), (e) $G_e = 0.8$ MPa, (c), (f) $G_e = 1.2$ MPa.

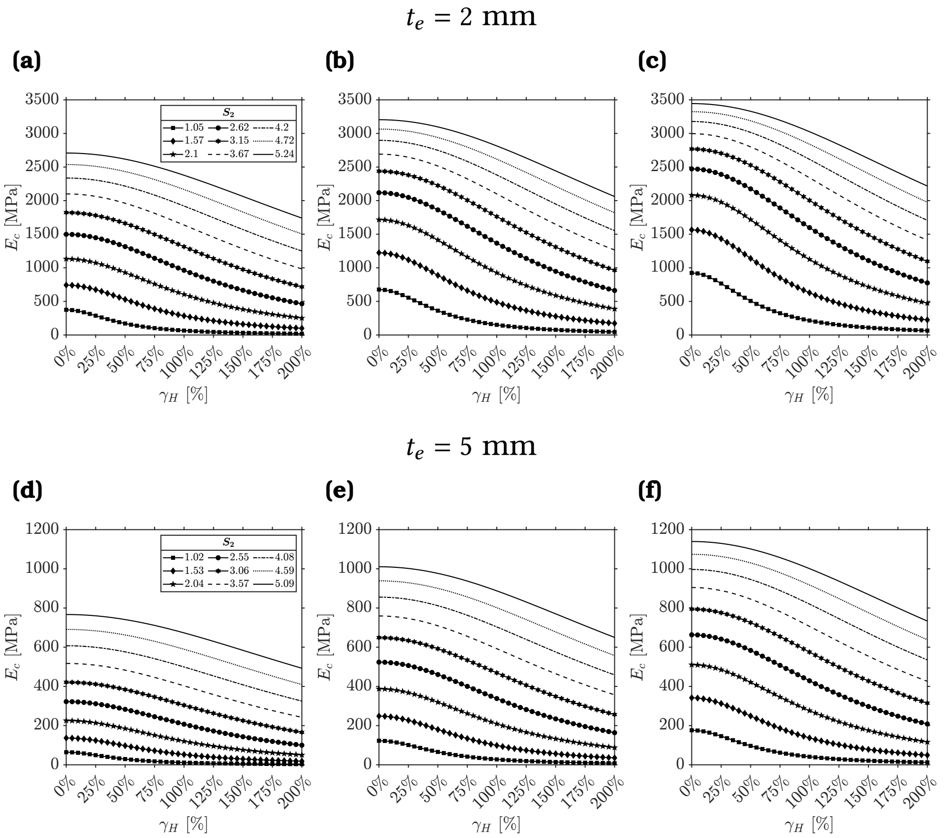

Figure 4.16: Analytical trends of $E_c^{\delta_H}$ using **Equation 2.4a** for E_c.: (a), (d) G_e = 0.4 MPa, (b), (e) G_e = 0.8 MPa, (c), (f) G_e = 1.2 MPa.

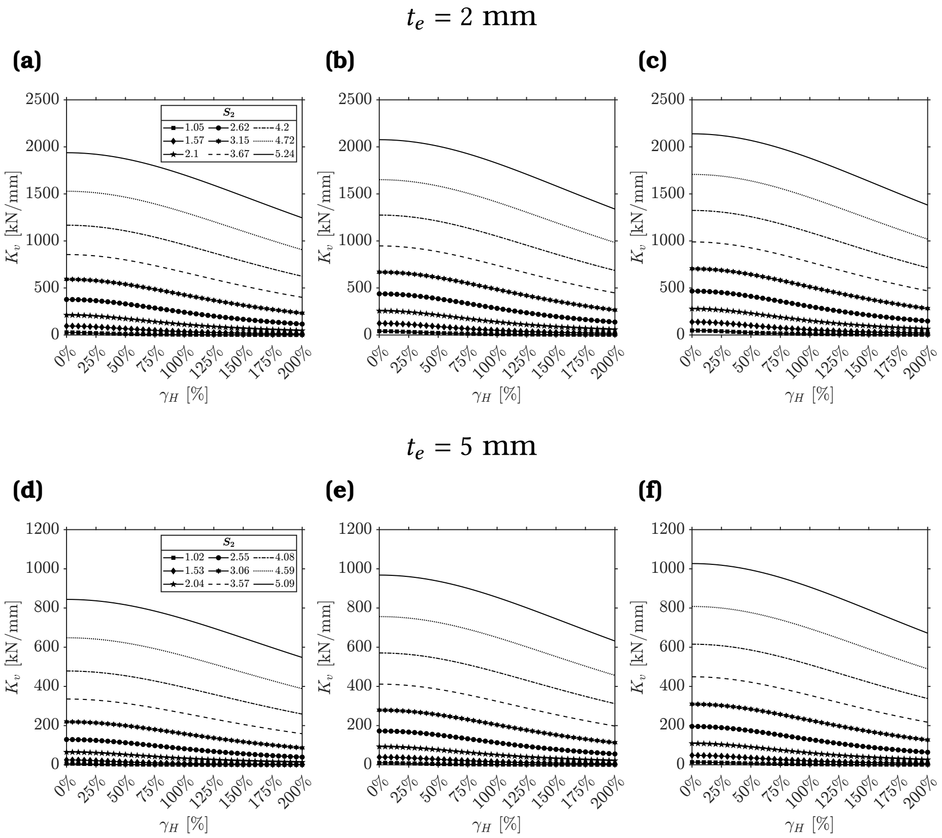

Figure 4.17: Analytical trends of $K_v^{\delta_H}$ using **Equation 2.6** for E_c.: (a), (d) $G_e = 0.4$ MPa, (b), (e) $G_e = 0.8$ MPa, (c), (f) $G_e = 1.2$ MPa.

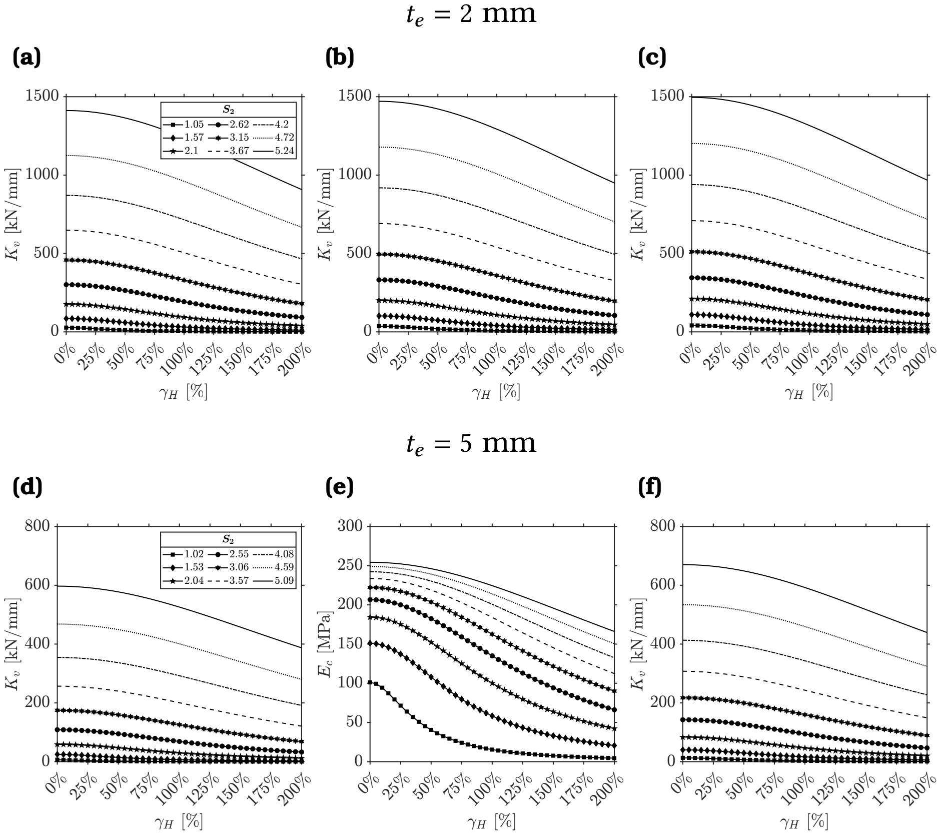

Figure 4.18: Analytical trends of Kv^{δ_H} using **Equation 2.7** for E_c.: (a), (d) $G_e = 0.4$ MPa, (b), (e) $G_e = 0.8$ MPa, (c), (f) $G_e = 1.2$ MPa.

$t_e = 2$ mm

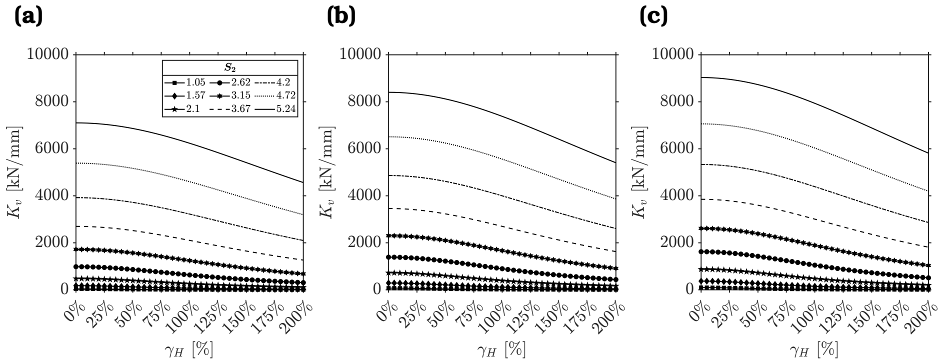

$t_e = 5$ mm

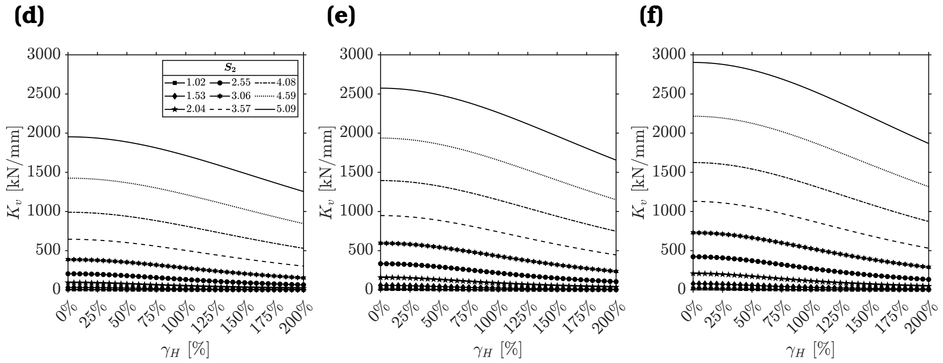

Figure 4.19: Analytical trends of $K_v^{\delta_H}$ using **Equation 2.4a** for E_c.: (a), (d) $G_e = 0.4$ MPa, (b), (e) $G_e = 0.8$ MPa, (c), (f) $G_e = 1.2$ MPa.

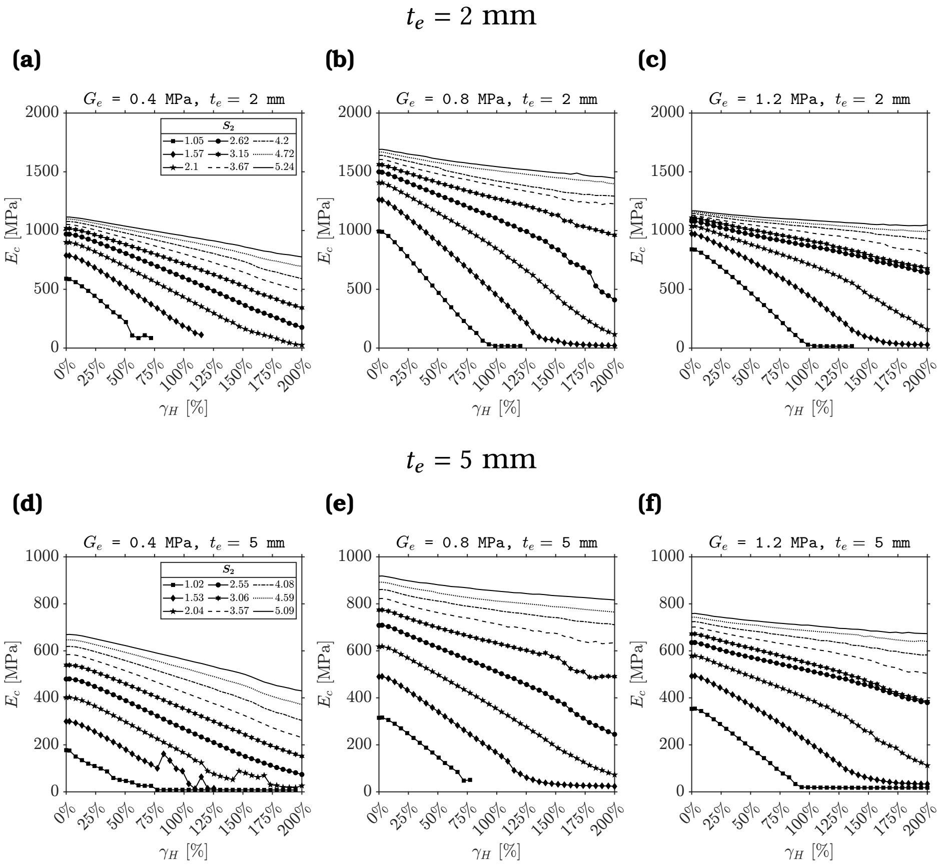

Figure 4.20: Numerical trends of $E_c^{\delta_H}$: (a), (d) $G_e = 0.4$ MPa, (b), (e) $G_e = 0.8$ MPa, (c), (f) $G_e = 1.2$ MPa.

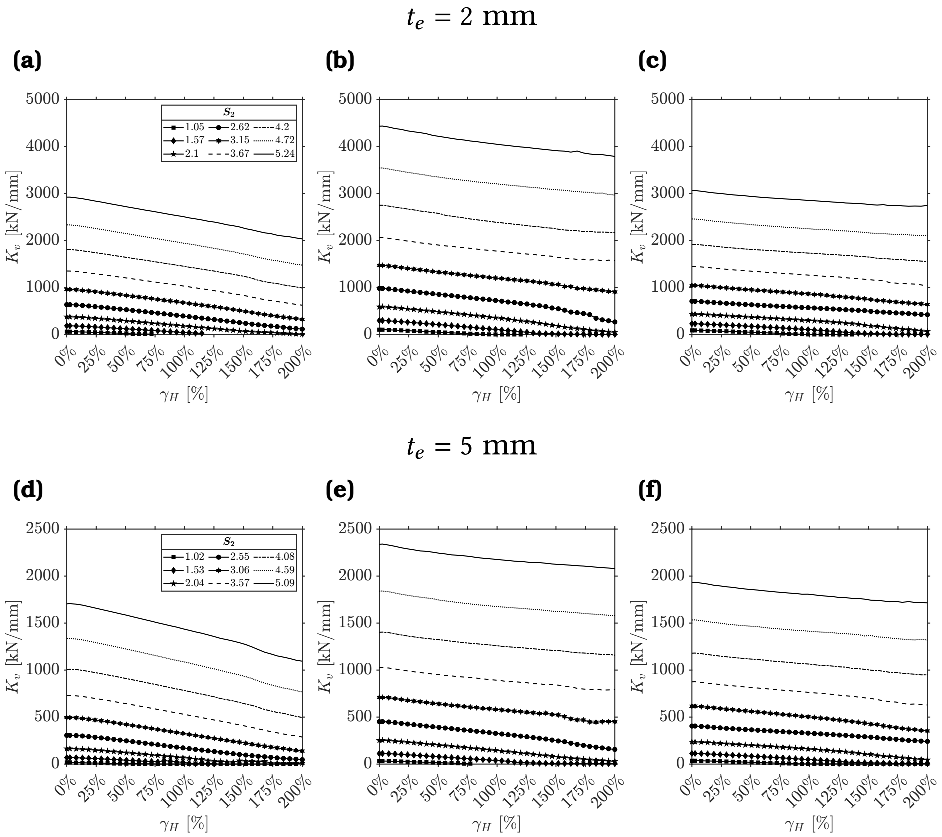

Figure 4.21: Numerical trends of $K_v^{\delta_H}$: (a), (d) G_e = 0.4 MPa, (b), (e) G_e = 0.8 MPa, (c), (f) G_e = 1.2 MPa.

CHAPTER 5

STABILITY OF SQUARE-SHAPED FIBER REINFORCED ELASTOMERIC ISOLATORS

Summary

In this chapter the results from parametric finite element analysis on square-shaped U-FREIs are presented. Buckling under vertical load and stable/unstable horizontal response of bearings in unbonded configuration were analyzed and compared with analytical equations. Particular emphasis has been placed on the key role of the secondary shape factor on the stability of U-FREIs. This is underlined by easy-to-use charts proposed.

This chapter is based on the journal paper [137].

5.1 Background and motivations

As forestall in **Section 2.3.2.1**, the lateral response of U-FREIs is mainly controlled by the secondary shape factor S_2. Depending on the value of S_2, the lateral response of a U-FREI can be *stable* or *unstable*. When stable (**Figure 5.1 (a)**, dash-dot line), the lateral force-displacement curve of the bearing shows an almost linear range of deformations [34] up to a displacement equal to approximately 50% of the total height of the elastomeric layers ("Range 1", **Figure 5.1 (a)**, top bearing **Figure 5.1 (b)**); a second range of stable softening with positive tangent stiffness ("Range 2", **Figure 5.1 (a)**, middle bearing in **Figure 5.1 (b)**); a third range goes from approximately when half of the originally vertical surfaces of the bearing become horizontal up to full rollover and the stiffness of the bearing sharply increases ("Range 3", **Figure 5.1 (a)**, bottom bearing of **Figure 5.1 (b)**) [37]. When U-FREIs are unstable (**Figure 5.1 (a)**, solid line), the linear and the softening range of the bearing remain unchanged, but instability could be reached in the middle part of the curve, where the tangent horizontal stiffness decreases and could become negative. The peak of lateral response of unstable bearings is referred to as *maximum displacement* $\delta_{H,max}$ ("Max" marker of **Figure 5.1 (a)**), while the point corresponding to the full roll over of the bearing is defined as the *ultimate displacement* $\delta_{H,ult}$ ("Ultimate" marker of **Figure 5.1 (a)**).

Only approximate formulations are available to describe the complex combined axial and shear response of U-FREIs (e.g., [23, 34, 36, 113]). Some of these studies suggest adopting a value of the secondary shape factor $S_2 \geq 2.5$ as a rule of thumb to achieve a stable lateral response ([20, 116]). Nevertheless, as shown by others, lower values of aspect ratio resulting in slender geometry are usually needed ($1 \leq S_2 \leq 2.5$) for application of U-FREIs to lightweight residential buildings due to limited mass ([62, 65, 66, 68]). This poses as major threat, and an horizontal displacement threshold must be known in order to prevent instability at the design stage.

5.2 Introduction

The analysis were performed as explained in **Section 4.4** modeling 3D FEMs using MSC.Marc. The same material's modeling and element's type shown in **Sections 3.1.2.1** and **4.4.2** are used for the set of FEMs herein reported.

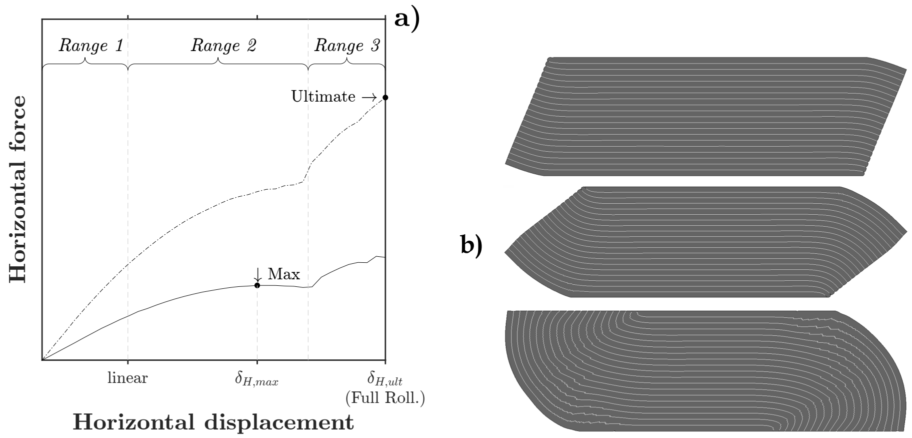

Figure 5.1: Stable vs unstable U-FREI: (a) horizontal force-displacement response curve, (b) deformed FREI under axial and shear loads.

5.2.1 Set of Finite Element Models

For this study, a total number of 216 analyses were carried out considering a combination of two geometrical (base dimensions $2a = 2b = B$ and thickness of the elastomeric layers t_e) and two mechanical parameters (shear modulus G_e of the rubber and vertical applied pressure σ_v). The values of the parameters for the analyses are listed in **Table 5.1**, where also the primary and secondary shape factor, as well as the aspect ratio considered, are shown.

Some parameters were kept constant in the analyses, such as the total height of the bearing H, the equivalent thickness of the fiber reinforcement t_f and its Young's modulus E_f.

In this study, an $E_f = 70$ GPa was assumed as common value for glass fiber fabrics. A preliminary sensitivity analysis demonstrated how E_f has a little influence on lateral response of FREIs. Indeed, the horizontal load-displacement curve is not affected by changes even doubling the value of this modulus, as shown in **Figure 5.2**.

Table 5.1: Set of variable and constant parameters in FEAs for the stability analyses of square-shaped FREIs.

$2a$ [mm]	H [mm]	R [-]	t_e [mm]	$S_1^{t_e=2}$ [-]	$S_1^{t_e=5}$ [-]	$S_2^{t_e=2}$ [-]	$S_2^{t_e=5}$ [-]	G_e [MPa]	σ_v [MPa]	K [MPa]	E_f [MPa]	t_f [mm]
100		1.00	2.00	12.5	5.00	1.05	1.02	0.40	2.00			
150		1.50	5.00	18.8	7.50	1.57	1.53	0.80	4.00			
200		2.00		25.0	10.0	2.10	2.04	1.20	6.00			
250		2.50		31.3	12.5	2.62	2.55		8.00			
300	100	3.00		37.5	15.0	3.15	3.06			2000	70000	0.100
350		3.50		43.8	17.5	3.67	3.57					
400		4.00		50.0	20.0	4.20	4.08					
450		4.50		56.3	22.5	4.72	4.59					
500		5.00		62.5	25.0	5.24	5.09					

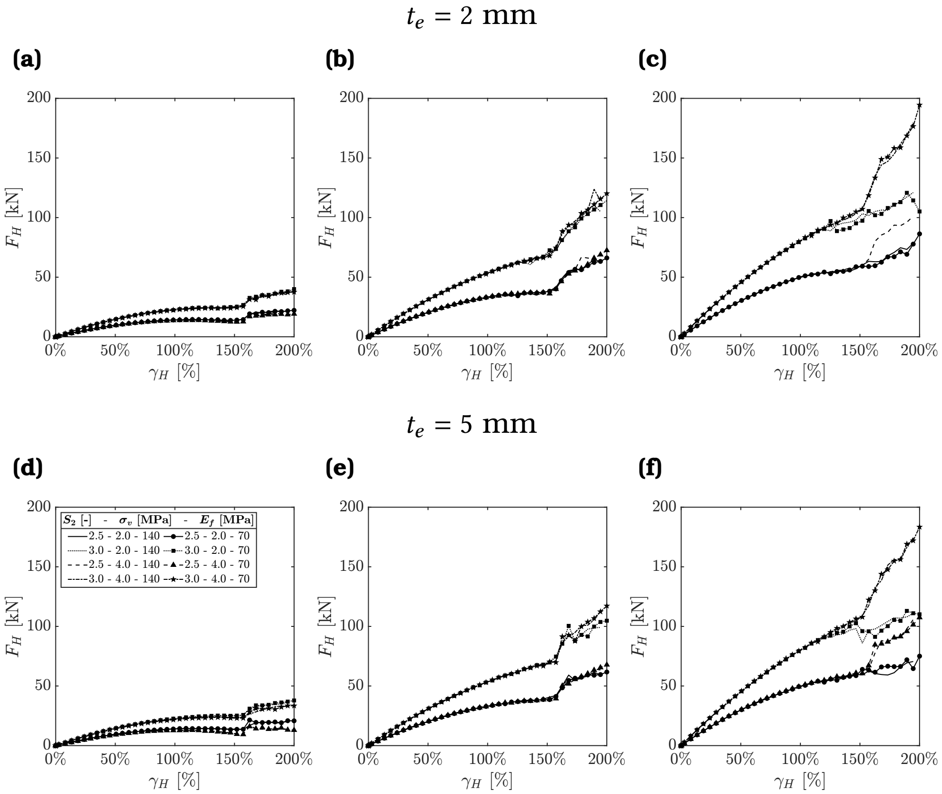

Figure 5.2: Comparison of the lateral response of different bearings with E_f = 70 GPa and E_f = 140 GPa: (a), (d) G_e = 0.4 MPa, (b), (e) G_e = 0.8 MPa, (c), (f) G_e = 1.2 MPa.

5.3 FEAs results

The results presented in this section will be divided into two parts: vertical and horizontal behavior. In the first case, the buckling of the square-shaped U-FREIs are studied, presenting an analytical - numerical comparison. In the second case, the influence of the main mechanical and geometric bearing's properties on the stability of the same set of square-shaped U-FREIs will be shown.

5.3.1 Vertical response: buckling

In this section, an analytical - numerical comparison on the buckling loads of the square-shaped U-FREIs is shown. **Equation 2.19** reported in **Section 2.3.1** has been solved to get the analytical buckling load F_{v,cr_0}^{an}; in FEAs, the buckling load F_{v,cr_0}^{num} is obtained as the vertical load where any horizontal displacement (however small) different from zero would result in non-positive horizontal stiffness.

Figure 5.3 shows the buckling pressure values $\sigma_{v,cr_0} = F_{v,cr_0}/A_c$ obtained by analytical equation (x axis) versus FEAs (y axis). The results are accurate for larger values of t_e (i.e. smaller values of S_1), as the values of the ratio $\sigma_{v,cr_0}^{num}/\sigma_{v,cr_0}^{an}$ are closer to 1 (dotted lines in each graph of **Figure 5.3**), especially for smaller values of S_2. The analytical solution tends to overestimate the buckling load as t_e decreases (i.e. S_1 increases). This is because in **Section 2.3.1** the rubber is assumed as incompressible and this hypothesis has been found to overestimate the vertical capacity of the bearing (see **Section 4.6**).

The numerical buckling load is only slightly affected by the primary shape factor, while the secondary shape factor plays a major role.

The deformed configuration obtained by using analytical formulation and FEAs for two different values of S_2 is shown in **Figure 5.4**. As the axial pressure on a FREI does not exceed $10 \div 15$ MPa, buckling under pure compression seems to be a reasonable failure mode only if $S_2 \leq 2.5$. It is worth noting that this result is based on the tested material (i.e., shear modulus of the rubber) and primary

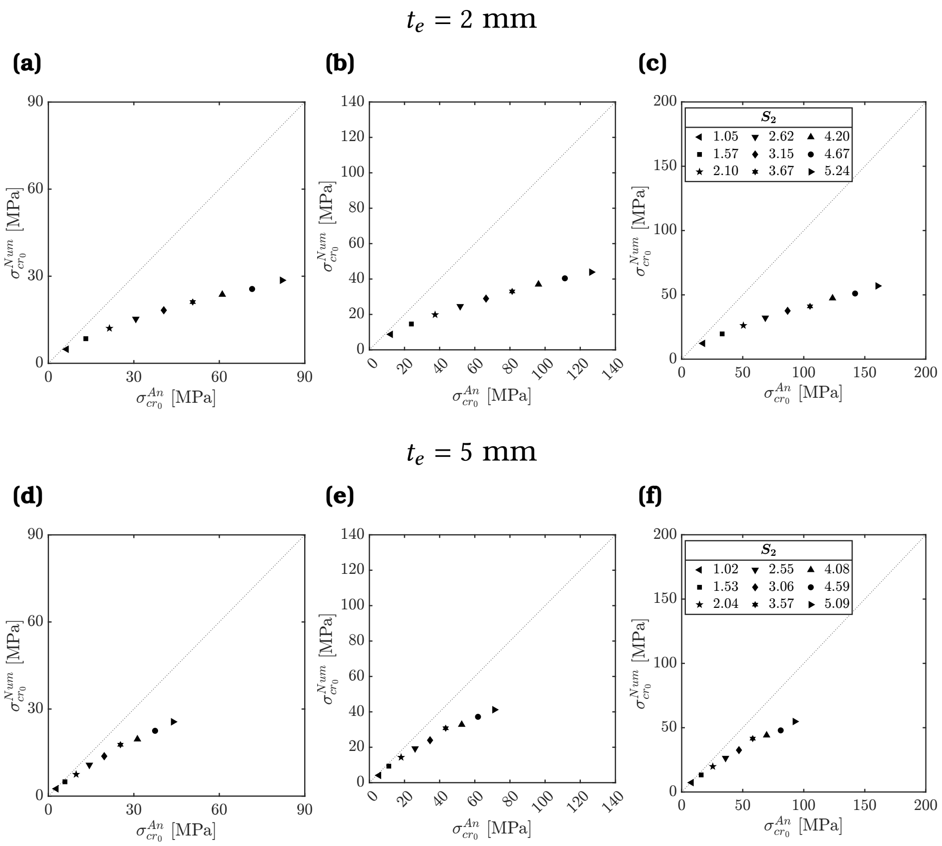

Figure 5.3: Analytical vs numerical buckling pressures: (a), (d) G_e = 0.4 MPa, (b), (e) G_e = 0.8 MPa, (c), (f) G_e = 1.2 MPa.

shape factor. Under combined axial and lateral load, for a given level of axial pressure, larger secondary shape factors are needed to achieve a stable response due to influence of rollover. At the same time, independently of S_2, if the bearing is subjected to a vertical pressure approaching σ_{v,cr_0}, a very limited lateral displacement capacity can be expected.

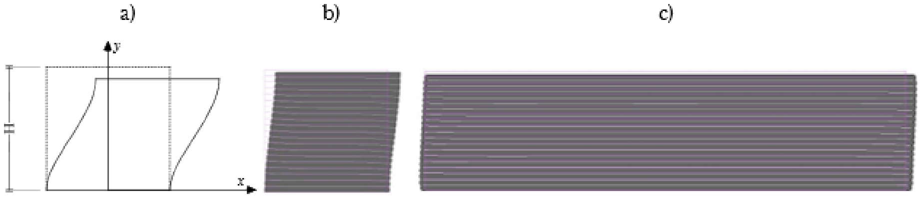

Figure 5.4: Deformed bearing configuration at buckling load: a) adapted from Tsai [33], b) $t_e = 2$ mm, $G_e = 0.4$ MPa, $S_2 = 1$, b) $t_e = 2$ mm, $G_e = 0.4$ MPa, $S_2 = 4$.

5.3.2 Horizontal response

The discussion of the horizontal behavior of the FEAs' bearings is divided in three classes:

Low S_2: U-FREIs with a low secondary shape factor ($S_2 \leq 2$, i.e. slender U-FREIs).

Medium S_2: U-FREIs with a medium secondary shape factor ($2 < S_2 < 3.5$).

Large S_2: U-FREIs with a large secondary shape factor ($S_2 \geq 3.5$, i.e. thick U-FREIs).

Figure 5.5 shows the horizontal force-displacement curves of the bearings within the ranges defined. Each spindle is limited by boundary curves corresponding to the extreme values of each class. A lower bound curve is obtained for a combination of maximum vertical pressure and minimum S_2; conversely, the upper bound curve corresponds to the combination of minimum vertical pressure and maximum S_2 in the range. Using this enveloping method, it was found that in the case of low and large secondary shape factors range, the response is characterized by unstable and stable rollover, respectively, while in the medium range of S_2 case the relative influence of different parameters may provide either response.

The following considerations can also be drawn:

- As already stated, the primary shape factor S_1 does not play a significant role on the lateral response of FREIs, as similar trends of achieved maximum values for limit curves can be observed in both **Figures 5.5 (a)**, **5.5 (b)** and **5.5 (c)** and **Figures 5.5 (d)**, **5.5 (e)** and **5.5 (f)**, except for a slight increase of lateral capacity with $t_e = 2$ mm.

- The bearings with $S_2 \geq 3.5$ show a stable response for any value of axial pressure. These bearings are stable (SU-FREIs), which means adequate to provide a positive tangent stiffness during roll-over.
- U-FREIs with $S_2 < 3.5$ require further investigation to define stability limits according to geometrical and mechanical parameters.

As an example of the U-FREIs pattern deformation, **Figure 5.6** shows the lateral deformation pattern of a bearing with $S_2 = 4$ by contour plots of equivalent elastic strain at different deformation levels up to complete roll-over. In this figure it can be seen how the wider stability range of U-FREIs with $S_2 \geq 3.5$ comes from the greater influence of the overlapping area compared to the rollover marginal parts. These portions provide shear strenght only for shear strain values higher than 150% (**Figure 5.6 (a)**).

5.3.2.1 Maximum stable shear strain

The stable/unstable response of U-FREIs is stated in this thesis defining the *maximum stable horizontal displacement* as:

$$\delta_{H,cr} = \min\left[\delta_{H,max}; \delta_{H,ult}\right] \tag{5.1}$$

corresponding to $\delta_{H,max}$ for unstable bearings and to $\delta_{H,ult}$ for stable bearings. Indeed unstable bearings shows a peak in the horizontal force-displacement curve and the response is stable up to the horizontal displacement threshold equal to $\delta_{H,max}$; conversely, SU-FREIs show positive horizontal tangent stiffness throughout the horizontal deformation and the ultimate displacement correspond to the full rollover. Accordingly, the *maximum stable shear strain* is defined as:

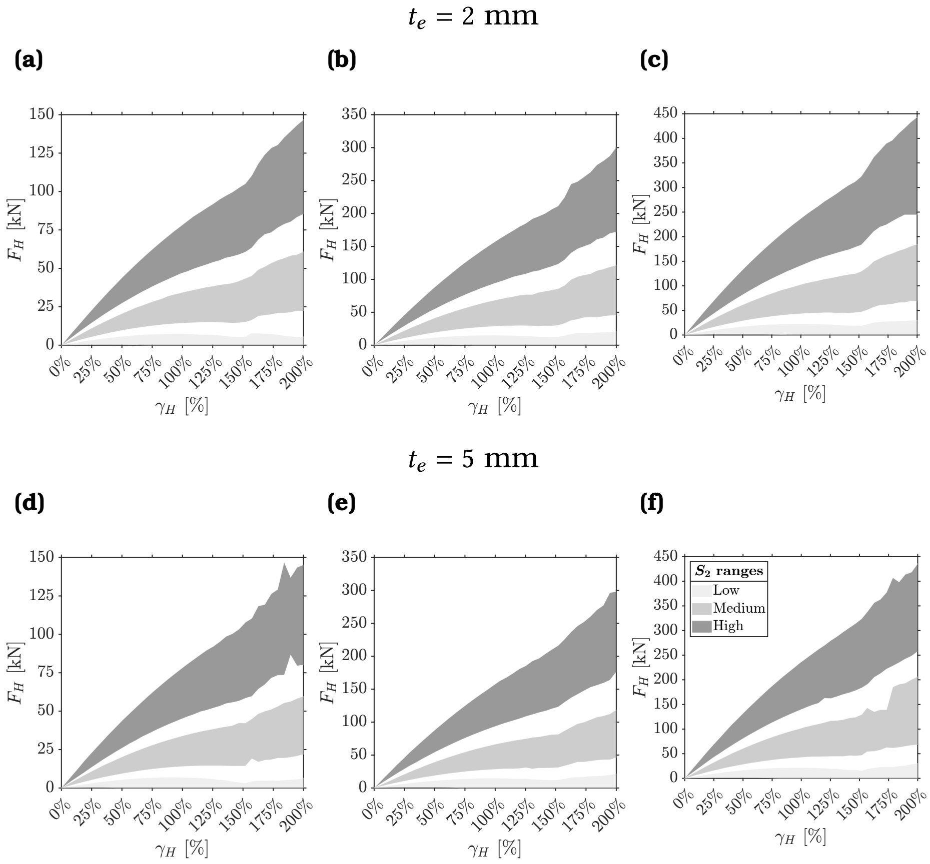

Figure 5.5: Horizontal force-displacement spindles: (a), (d) $G_e = 0.4$ MPa, (b), (e) $G_e = 0.8$ MPa, (c), (f) $G_e = 1.2$ MPa.

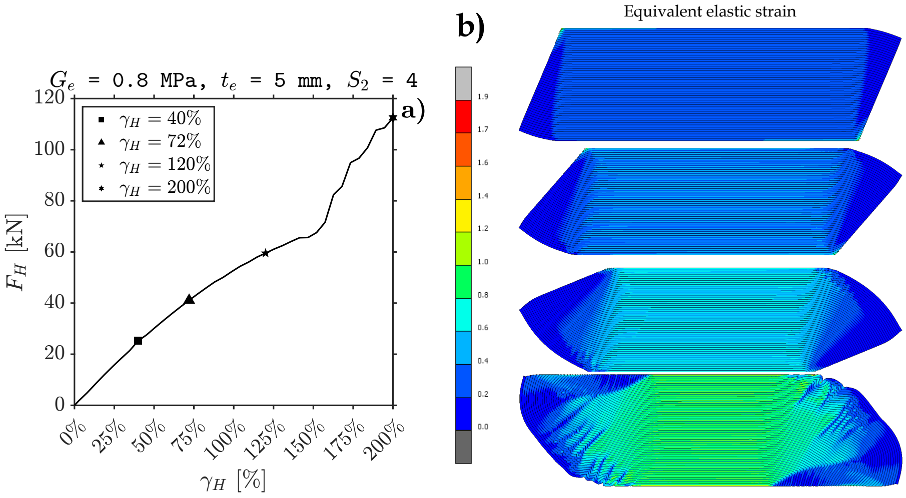

Figure 5.6: Horizontal pattern for an U-FREI with $S_2 = 4$: (a) horizontal force-displacement response curve, (b) equivalent elastic strain at (starting from the top): $\gamma_H = 40\%$, $\gamma_H = 72\%$, $\gamma_H = 120\%$, $\gamma_H = 200\%$

$$\gamma_{H,cr} = \min\left[\gamma_{H,max};\gamma_{H,ult}\right] = \min\left[\frac{\delta_{H,max}}{t_r};\frac{\delta_{H,ult}}{t_r}\right] \tag{5.2}$$

Figure 5.7 shows the trend of S_2 with $\gamma_{H,cr}$ for the different variable values of mechanical and geometric parameters in the FEAs. In each figure, four curves are shown each for a different value of vertical pressure.

These charts provide the secondary shape factor needed to tap into a maximum stable shear strain threshold and can be read as bearing stability ranges. Indeed, for each graphs:

- A vertical line starting from a given value of $\gamma_{H,cr}$ intersects the 4 curves of each charts in the needed values of S_2 to obtain a stable response up to at least $\gamma_{H,cr}$.

- An horizontal line drawn from a given value of S_2 provides the maximum stable shear strain related to the vertical applied pressure.

The stability range of $\gamma_{H,cr}$ in **Figure 5.7** varies between a minimum of 25% up to 200% and it is worth to point out the relative influence of different parameters:

- An increase in vertical pressure reduces the bearing capacity. This effect is more pronounced larger values of the thickness of the elastomeric layer. For $t_e = 5$ mm, an increase of vertical pressure from 2 MPa to 8 MPa produces an average decrease of 14.6% in maximum shear strain for different values of the shear modulus.

- The displacement capacity of the bearing increases with the shear modulus of the rubber. For fixed values of σ_v and t_e, the same $\gamma_{H,cr}$ can be reached with a lower S_2 in case of a larger modulus. For $t_e = 5$ mm, an average decrease of demand of 14.1% and 23.3% is obtained for $G = 0.8$ MPa and $G = 1.2$ MPa in comparison to $G = 0.4$ MPa, respectively. The same percentages reduce to 0.1% and 8.1% in case of $t_e = 2$ mm.

- Reducing the thickness of the elastomeric layer, i.e. increasing the primary shape factor, results in a moderate increase of the bearing stability: with a given shear modulus and applied vertical pressure, a lower S_2 is required to obtain a target shear strain. Reducing the thickness of the elastomeric layer from 5 to 2 mm, an average decrease in the secondary shape factor demand equal to 20% and 9% for $G = 0.4$ and $G = 1.2$ MPa is obtained, respectively.

From **Figure 5.7** it can be noted that all curves $S_2(\gamma_H)$ tend to provide a bilinear trend, where the first branch (i.e. $S_2 \leq 2 \div 3$) is steeper due to a major influence of the geometry up to a point representing a cusp. Generally, the coordinates of the cusp fall in the range of $100\% \leq \gamma_{H,cr} \leq 125\%$ (x axis) and $2 \leq S_2 \leq 3$ (y axis). Beyond the cusp, a limited increase of S_2 would provide a significantly higher stability limit. It can be noted that in the most unfavorable case due to a combination of $G = 0.4$ MPa and $\sigma_v = 8$ MPa, a minimum $S_2 = 3.5$ is required to achieve stable response up to $\gamma_{H,cr} = 200\%$; this value tends to reduce to 2.5 in case of higher modulus of the

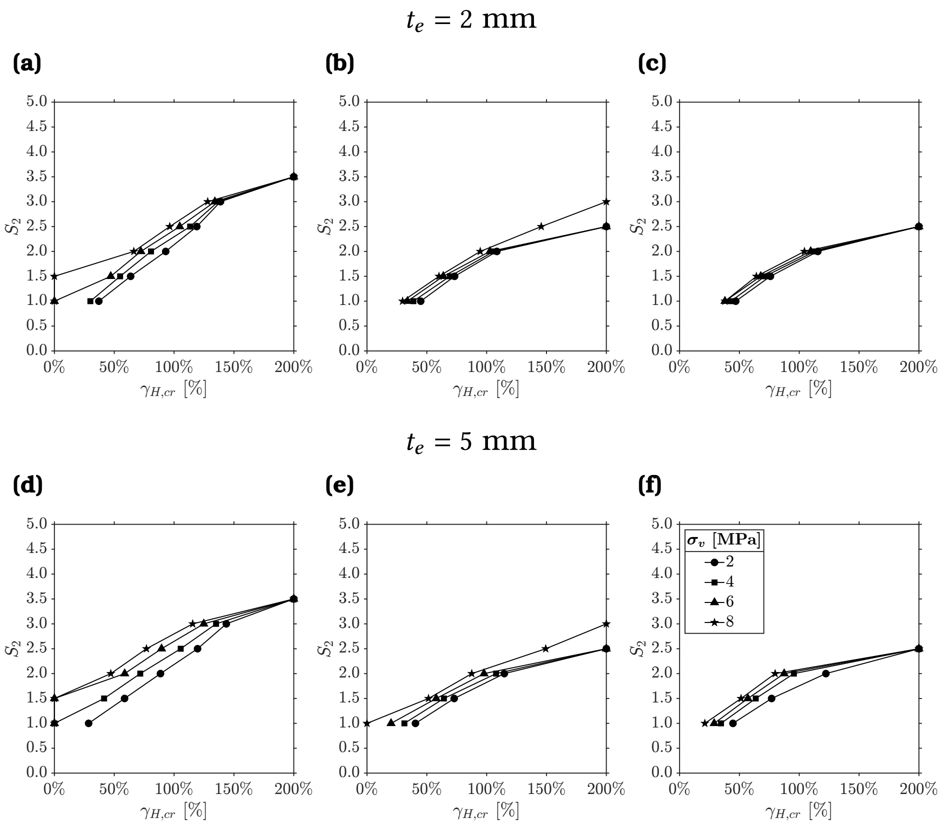

Figure 5.7: S_2 needed to achieve γ_{H_cr}: (a), (d) G_e = 0.4 MPa, (b), (e) G_e = 0.8 MPa, (c), (f) G_e = 1.2 MPa.

rubber and low-to-medium axial pressure, in agreement with the previous experimental findings ([20, 35, 113]). This comparison contributed to validate the numerical study and confirmed that the lateral response of unbounded FREIs is significantly affected by the secondary shape factor.

5.3.2.2 Expected maximum stable shear strain

In order to estimate the expected value of maximum shear strain for a given geometry and loading condition (i.e. σ_v, G, S_2, t_e), numer-

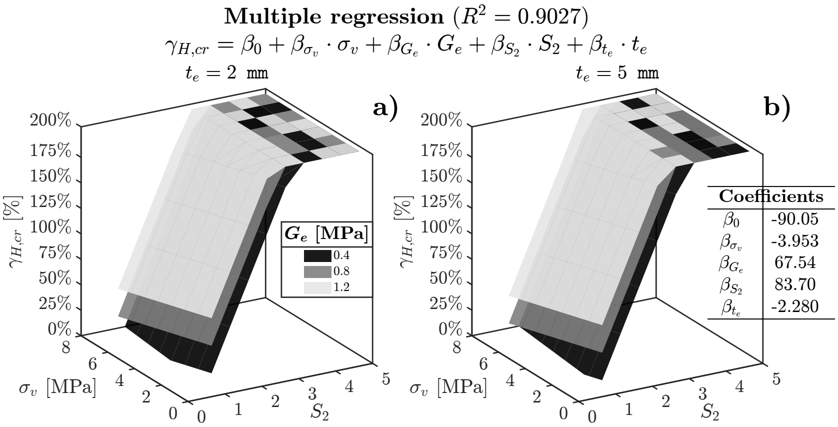

Figure 5.8: Linear multiple regression: values of $\gamma_{H,cr}$ with σ_v, G, S_2, t_e.

ical values in **Figure 5.7** have been fitted with a multiple linear regression:

$$\gamma_{H,cr}^{exp} = \beta_0 + \beta_{\sigma_v} \cdot \sigma_v + \beta_{G_e} \cdot G_e + \beta_{S_2} \cdot S_2 + \beta_{t_e} \cdot t_e \qquad (5.3)$$

The coefficients of the regression model have been calibrated on available discrete values and are given in **Figure 5.8**. The value of R^2 is approximately equal to 90%, demonstrating how **Equation 5.3** can be used with good accuracy for a preliminary estimate of $\gamma_{H,cr}$ defined for positive values.

In **Equation 5.3**, the maximum limit of $\gamma_{H,cr}^{exp}$ is set equal to 200%, since a bearing whose mechanical properties guarantee stability beyond this deformation level, can be considered stable up to complete rollover; the lower limit is instead set equal to 0%, because a bearing whose maximum stable deformation is negative would be unstable under pure vertical load (i.e. buckling load).

As can be noted, all coefficients are positive unless β_{σ_v} and β_{t_e}, i.e. the stability range decreases while increasing σ_v and t_e, respectively. The regression model also confirms again that the thickness of the elastomeric layer, i.e. the primary shape factor, is not significant on the stability of the bearings whereas the secondary shape factor has a key role.

5.3.2.3 Simplified approach to predict maximum stable shear strain

As said in **Section 5.3.2.1**, the data in **Figure 5.7** can be interpolated with good approximation with bilinear trends. The single branch can therefore be written in the form:

$$S_2^{(1)}\left(\gamma_{H,cr}\right) = c_{1,1} + c_{1,2} \cdot \gamma_{H,cr} \tag{5.4a}$$

$$S_2^{(2)}\left(\gamma_{H,cr}\right) = c_{2,1} + c_{2,2} \cdot \gamma_{H,cr} \tag{5.4b}$$

where the apices 1 and 2 stand for the single branch of the generic bilinear trend. The constants $c_{i,2}$ are the slopes of the branches, while $c_{i,1}$ represent the intersection of the branches with the vertical axis. Fitting the FEAs results leads to the curves shown in **Figure 5.9**.

However, an easy-to-use general method to assess the secondary shape factor corresponding to a maximum stable shear strain threshold is herein proposed, providing generic expressions for the constants $c_{i,j}$.

Consider the constant $c_{1,1}$. This it the value of $S_2\left(\gamma_{H,cr}\right)$ where the maximum stable shear strain is equal to zero, i.e. the bearing is unstable under pure compression load. For generic values of shear modulus G_e and pressure σ_v, the constant $c_{1,1}$ stand for the secondary shape factors of the bearings whose buckling pressures are exactly σ_v.

This constant can be analytically derived for each bearing inverting **Equation 2.19**, i.e. obtaining the base side $2a = 2b$ of the bearings whose buckling loads is equal to $F_{v,cr_0} = \sigma_v \cdot A_c = \sigma_v \cdot 4a^2 = \sigma_v \cdot 4b^2$; hence the secondary shape factor will be $S_2(0) = 2a/t_r = 2b/t_r$. The values for each t_e, G_e and σ_v are shown in **Table 5.2**.

The constant $c_{1,2}$ is given by the ratio:

$$c_{1,2} = \frac{S_2^{(1)}\left(\gamma_{H,cr}^{(1)}\right) - S_2(0)}{\gamma_{H,cr}^{(1)}(\sigma_v, G_e, t_e)} = \frac{S_2^{(1)}\left(\gamma_{H,cr}^{(1)}\right) - c_{1,1}}{\gamma_{H,cr}^{(1)}(\sigma_v, G_e, t_e)} \tag{5.5}$$

where $S_2^{(1)}\left(\gamma_{H,cr}^{(1)}\right)$ is the secondary shape factor related to a generic point $\gamma_{H,cr}^{(1)}(\sigma_v, G_e, t_e)$ belonging to the first branch; they are both function of the vertical pressure, the shear modulus and the thickness of the elastomeric layer.

Similarly, the constant $c_{2,2}$ is given by the ratio:

$$c_{2,2} = \frac{S_2^{(2)}(200\%) - S_2^{(2)}\left(\gamma_{H,cr}^{(2)}\right)}{200\% - \gamma_{H,cr}^{(2)}(\sigma_v, G_e, t_e)} \tag{5.6}$$

being $S_2^{(2)}(200\%)$ the minimum secondary shape factor to achieve full rollover and $\gamma_{H,cr}^{(2)}(\sigma_v, G_e, t_e)$ a point belonging to the second branch. Note that the only unknowns are the value $S_2^{(1)}\left(\gamma_{H,cr}^{(1)}\right)$, the deformation $\gamma_{H,cr}^{(1)}(\sigma_v, G_e, t_e)$ and $S_2^{(2)}(200\%)$.

For simplicity and for the sake of safety, it can be considered $S_2^{(1)}\left(\gamma_{H,cr}^{(1)}\right) = S_2^{(2)}\left(\gamma_{H,cr}^{(2)}\right) = S_2^{(2)}(200\%)$ and $\gamma_{H,cr}^{(1)}(\sigma_v, G_e, t_e) = \gamma_{H,cr}^{(2)}(\sigma_v, G_e, t_e) = 100\% \div 150\%$. Indeed, **Figure 5.9** shows how the second branch always starts in this range, where the initial vertical faces of the bearing gradually become horizontal and touching the supports.

The position made implies that the second branch has zero inclination, or that the secondary shape factor at full rollover is equal to that at $\gamma_{H,cr} = 100 \div 150\%$. With these impositions the unknowns are reduced to 1, i.e. the secondary shape factor at full rollover $S_2^{(2)}(200\%)$. This parameter can be assumed through the safety values obtained from the FEAs and shown in **Table 5.3**.

In this way it is possible to completely solve the problem and obtain the bilinear trends for each distribution of $S_2 - \gamma_{H,cr}$. **Figures 5.10** and **5.11** show the simplified bilinear trends for the FEAs bearings, using $\gamma_{H,cr}^{(1)}(\sigma_v, G_e, t_e) = \gamma_{H,cr}^{(2)}(\sigma_v, G_e, t_e) = 100\%$ and $\gamma_{H,cr}^{(1)}(\sigma_v, G_e, t_e) = \gamma_{H,cr}^{(2)}(\sigma_v, G_e, t_e) = 150\%$ respectively. As can be seen, in the first case, the actual capacity of the bearings is underestimated in a strongly safety evaluation of the stability ranges; in the second case, the method returns closest results to the FEAs values.

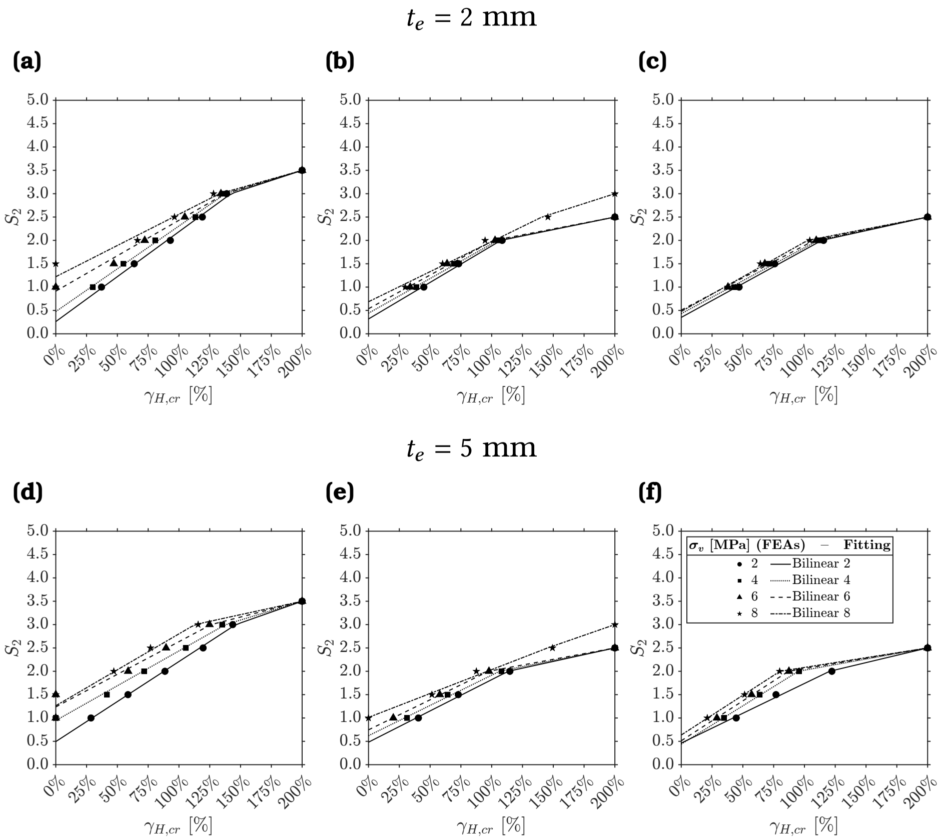

Figure 5.9: Bilinear trends of S_2 vs $\gamma_{H,cr}$ from FEAs data fitting: (a), (d) $G_e = 0.4$ MPa, (b), (e) $G_e = 0.8$ MPa, (c), (f) $G_e = 1.2$ MPa.

Table 5.2: Values of the constant $c_{1,1}$ for the bearings considered in the FEM

t_e [mm]	G_e [MPa]	σ_v [MPa]	$c_{i,1}$ [-]	$S_2(200\%)$ [-]
2	0.4	2	0.52	3.5
		4	0.772	3.5
		6	0.968	3.5
		8	1.14	3.5
	0.8	2	0.358	2.5
		4	0.529	2.5
		6	0.668	2.5
		8	0.786	3.0
	1.2	2	0.292	2.5
		4	0.422	2.5
		6	0.534	2.5
		8	0.632	2.5
5	0.4	2	0.82	3.5
		4	1.22	3.5
		6	1.53	3.5
		8	1.79	3.5
	0.8	2	0.57	2.5
		4	0.83	2.5
		6	1.05	2.5
		8	1.24	3.0
	1.2	2	0.46	2.5
		4	0.664	2.5
		6	0.84	2.5
		8	0.998	2.5

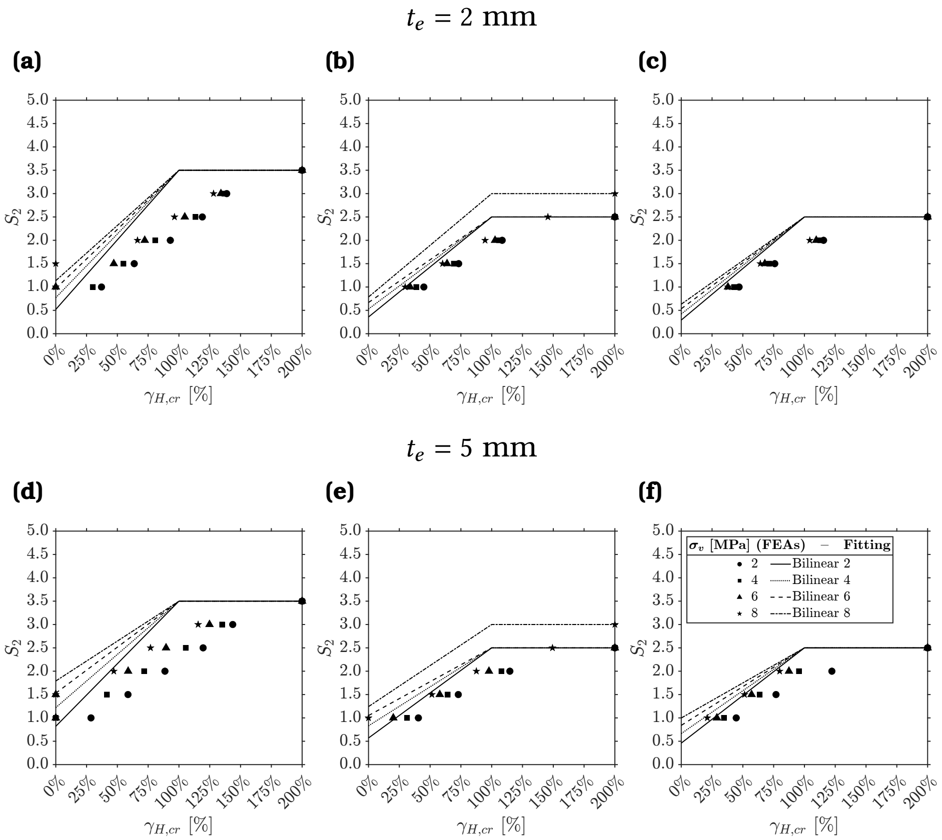

Figure 5.10: Bilinear trends of S_2 vs $\gamma_{H,cr}$ with simplified approach using $\gamma^{(1)}_{H,cr}(\sigma_v, G_e, t_e) = \gamma^{(2)}_{H,cr}(\sigma_v, G_e, t_e) = 100\%$: (a), (d) $G_e = 0.4$ MPa, (b), (e) $G_e = 0.8$ MPa, (c), (f) $G_e = 1.2$ MPa.

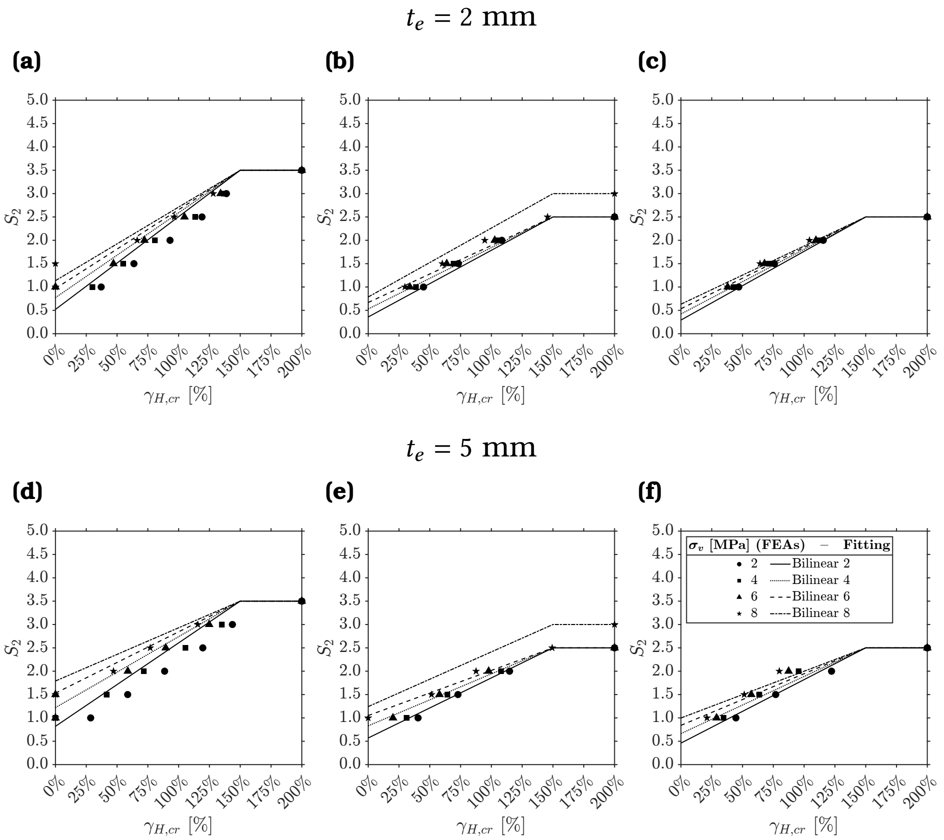

Figure 5.11: Bilinear trends of S_2 vs $\gamma_{H,cr}$ with simplified approach using $\gamma^{(1)}_{H,cr}(\sigma_v, G_e, t_e) = \gamma^{(2)}_{H,cr}(\sigma_v, G_e, t_e) = 150\%$: (a), (d) $G_e = 0.4$ MPa, (b), (e) $G_e = 0.8$ MPa, (c), (f) $G_e = 1.2$ MPa.

Table 5.3: Suggested values of $S_2^{(2)}(200\%)$ for different compound and vertical pressure

Compound	Vertical Pressure	$S_2^{(2)}(200\%)$
Soft (i.e. $G \leq 0.4$ MPa)	Low Range (i.e. $\sigma_v \leq 4$ MPa)	3.5
	Medium Range (i.e. $4 < \sigma_v < 8$ MPa)	3.5
	High (i.e. $\sigma_v \geq 8$ MPa)	3.5
Medium (i.e. $0.4 < G < 1.2$ MPa)	Low Range (i.e. $\sigma_v \leq 4$ MPa)	2.5
	Medium (i.e. $4 < \sigma_v < 8$ MPa)	2.5
	High (i.e. $\sigma_v \geq 8$ MPa)	3.0
Hard (i.e. $G \geq 1.2$ MPa)	Low Range (i.e. $\sigma_v \leq 4$ MPa)	2.5
	Medium (i.e. $4 < \sigma_v < 8$ MPa)	2.5
	High (i.e. $\sigma_v \geq 8$ MPa)	2.5

CHAPTER 6

STABILITY OF RECTANGULAR-SHAPED FIBER REINFORCED ELASTOMERIC ISOLATORS UNDER BIDIRACTIONAL SHEAR LOADS

Summary

In this chapter the results from parametric finite element analysis on rectangular-shaped U-FREIs are presented. The bearings were subjected to combined axial and bidirectional shear loads to evaluate the variation of the response with the several different mechanical and geometric parameters considered. Particular attention was given to the role of the secondary shape factor for bearings simultaneously loaded in two horizontal directions.
This chapter is based on the journal paper [138].

6.1 Background and motivations

In **Chapter 5** the secondary shape factor has been shown to play a key role on the stability of U-FREIs, according to literature results too. The transition range between stable and unstable response corresponds to a secondary shape factor in the range $2.5 \div 3.5$ depending on the shear modulus of the rubber and the vertical pressure.

However, these results were obtained for bearings loaded in shear along their base. Shaking table investigations on FREIs recently demonstrated that bidirectional motion can significantly affect the stability of the base isolation system [24]. On the other hand, it has been experimentally [20, 117, 120, 139] and numerically [140] demonstrated that square-shaped bearings improve their response when loaded along their diagonal, as the lateral stiffness at large displacements increases, while the stiffness at small displacements ($\gamma_H \leq 1$ [140]) remains almost unchanged. It can be argued that the larger stability limit for square isolators is obtained when these are loaded at an angle of 45° with their base [65], while for rectangular bearings this angle is a function of the ratio between the base sides and is not known *a priori*.

6.2 Introduction

The FEAs were performed as explained in **Section 5.2**. 3D full-scale FEMs were used in this case too, using the same procedure, elements' type and materials modeling specified in **Sections 3.1.2.1** and **4.4.2**.

6.2.1 Set of Finite Element Models

Table 6.1 shows all the main variables considered in the parametric FEMs, while a schematic of the geometry of the FREI (and the definition of the variables) is shown in **Figure 6.1**.

A combination of the variables listed in **Table 6.1** lead to a total of 480 FEMs. For the base of the FREIs, four different dimensions were considered along X ($2a$) and three along Y ($2b$) (refer to **Figure 6.1**). As a result, square, rectangular and strip-shaped (i.e. side ratio larger than 5) bearings were tested. Two different heights of the bearings, and two thicknesses of the elastomeric layer were considered leading to four values of total rubber height. Two vertical

Table 6.1: Mechanical and geometric parameters considered for the current set FEAs.

$2a$ [mm]	$2b$ [mm]	H [mm]	t_e [mm]	t_r [mm]	S_2 [-]	σ_v [MPa]	ϑ [°]
200	400	100	10	95.7	From	2	0
300	800	200	20	98.1	1.02	4	30
400	1200			191	To		45
500				196	12.5		60
							90

Table 6.2: Constant parameters defined for the current set of FEAs.

G_e [MPa]	K [MPa]	t_f [mm]	E_f [MPa]	ν_f [-]
1.00	2000	0.500	50000	0.100

pressure values were considered, corresponding to lightly loaded (i.e. $\sigma_v = 2$ MPa) and medium loaded bearings (i.e. $\sigma_v = 4$ MPa). Finally, five angles of horizontal loads ϑ were considered: 0° (the imposed load is parallel to X, i.e., parallel to the base with dimension of $2a$), 30°, 45°, 60° and 90° (the imposed load in parallel to Y, i.e. parallel to the side of the bearing with a dimension of $2b$). The angles are counterclockwise, measured from the X axis (**Figure 6.1**).

Other parameters of the models were set as constant. These are the shear modulus of the rubber, its bulk modulus, the equivalent thickness of the fiber layer, its Young's modulus and its Poisson's ratio (**Table 6.2**). The parameters of this table are chosen constant as the main scope of the current parametric finite element analysis is to investigate the influence of the different loading directions on U-FREIs of different geometry, i.e. the geometric point of view. However, further analyses could be conducted considering several shear moduli values, or different types of reinforcement.

The size of the mesh used for the analyses was calibrated after a sensitivity analysis, where the number of elements along the three directions was varied (bearing base and height, **Figure 6.2**). The

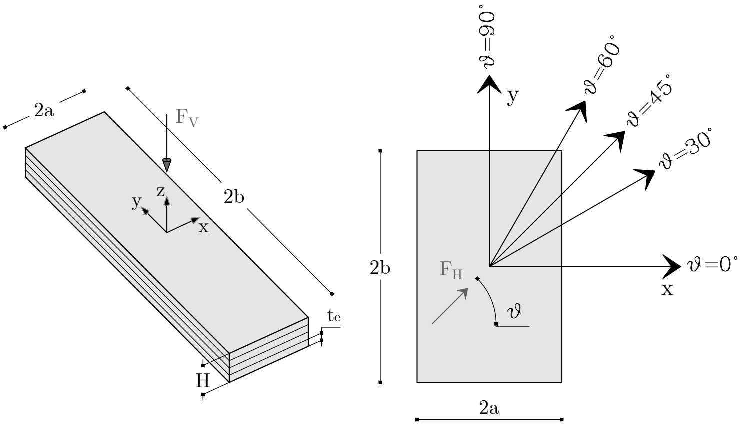

Figure 6.1: Rectangular U-FREI: geometric variable parameters and angles for the horizontal load.

aspect ratio of a single brick element was chosen equal to 1, i.e. the side of each element is 5 mm.

6.2.2 Labels' definition

In this thesis, the following parameters are introduced: the *horizontal displacement base side* $B(\vartheta)$, the *secondary shape factor in the horizontal displacement direction* S_2^ϑ, the *maximum stable horizontal displacement in the horizontal displacement direction* $\delta_{H,cr}^\vartheta$ and the *maximum stable shear strain in the horizontal displacement direction* $\gamma_{H,cr}^\vartheta$. Their definitions are given below (see also **Figure 6.3**):

$$B(\vartheta) = \begin{cases} \frac{2a}{\cos\vartheta} & \text{if } \vartheta \leq \arctan\left(\frac{2b}{2a}\right) \\ \frac{2b}{\sin\vartheta} & \text{if } \vartheta > \arctan\left(\frac{2b}{2a}\right) \end{cases} \tag{6.1a}$$

$$S_2^\vartheta = \frac{B(\vartheta)}{t_r} \begin{cases} \frac{2a}{t_r\cos\vartheta} & \text{if } \vartheta \leq \arctan\left(\frac{2b}{2a}\right) \\ \frac{2b}{t_r\sin\vartheta} & \text{if } \vartheta > \arctan\left(\frac{2b}{2a}\right) \end{cases} \tag{6.1b}$$

$$\delta_{H,cr}^\vartheta = \min\left[\delta_{H,max}^\vartheta, \delta_{H,ult}^\vartheta\right] \tag{6.1c}$$

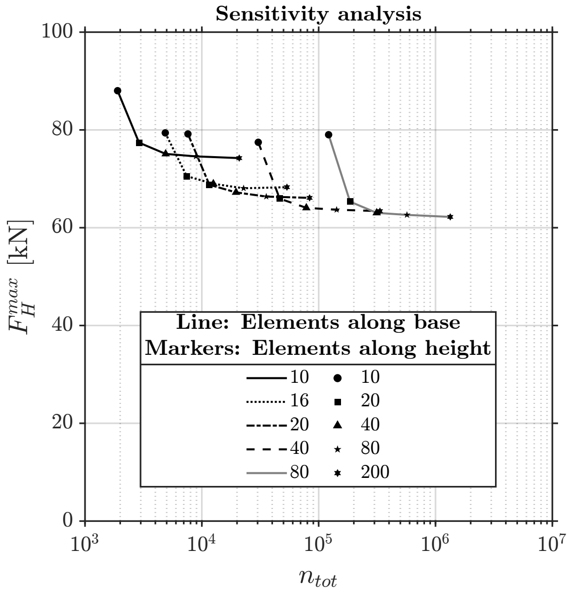

Figure 6.2: Sensitivity analysis: choice of mesh size.

$$\gamma_{H,cr}^{\vartheta} = \min\left[\gamma_{H,max}^{\vartheta}, \gamma_{H,ult}^{\vartheta}\right] = \min\left[\frac{\delta_{H,max}^{\vartheta}}{t_r}, \frac{\delta_{H,ult}^{\vartheta}}{t_r}\right] \tag{6.1d}$$

As intuition suggests, $B(\vartheta)$ is the size of the bearing along the direction of the applied horizontal load, and S_2^{ϑ} its ratio on the total height of the rubber; **Equations 6.1c** and **6.1d** follow directly from the definitions of maximum stable horizontal displacement and shear strain given in **Section 5.3.2.1**, conforming to the generic horizontal load direction ϑ. Clearly, when $\vartheta = 0°$ and $\vartheta = 90°$, **Equation 6.1** reduce to:

$$B(0°) = 2a \qquad B(90°) = 2b \tag{6.2a}$$

$$S_2^{0°} = \frac{2a}{t_r} \qquad S_2^{90°} = \frac{2b}{t_r} \tag{6.2b}$$

$$\delta_{H,cr}^{0°} = \min\left[\delta_{H,max}^{0°}, \delta_{H,ult}^{0°}\right] \quad \delta_{H,cr}^{90°} = \min\left[\delta_{H,max}^{90°}, \delta_{H,ult}^{90°}\right] \tag{6.2c}$$

$$\gamma_{H,cr}^{0^\circ} = \min\left[\frac{\delta_{H,max}^{0^\circ}}{t_r}, \frac{\delta_{H,ult}^{0^\circ}}{t_r}\right] \quad \gamma_{H,cr}^{90^\circ} = \min\left[\frac{\delta_{H,max}^{90^\circ}}{t_r}, \frac{\delta_{H,ult}^{90^\circ}}{t_r}\right] \tag{6.2d}$$

that are the classic definitions of base side, secondary shape factor and maximum stable horizontal displacement/shear strain.

6.3 FEAs Results

After the application of the vertical load, FREIs were then displaced horizontally up to full-rollover in the generic ϑ direction. As seen in **Chapter 5**, for unbonded bearings loaded along one of the base side, full-rollover corresponds approximately to a displacement level of $\delta_H = 2H$ (i.e. $\gamma_H \approx 200\%$). For U-FREIs loaded into two horizontal directions the ultimate value of deformation depends on the geometry of the device, and it is not known *a priori*.

6.3.1 Stability domain as function of $\gamma_{H,cr}^{\vartheta}$

For each bearing, either the maximum or ultimate shear strain was derived applying the horizontal displacement with the angles listed in **Table 6.1**.

Figure 6.4 shows the polar stability domains as a function of $\gamma_{H,cr}^{\vartheta}$, while **Figure 6.5** show the corresponding planar stability domains where the secondary shape factor S_2^{ϑ} in the horiontal displacement direction is given on secondary axes.

When the generic bearing is stable in any horizontal direction up to the full rollover, the domain connects all the $\gamma_{H,ult}^{\vartheta}$ along each horizontal loading direction, according to definition given in **Equation 6.1d**. If $\gamma_{H,ult}^{\vartheta}$ does not depend on the horizontal load direction (e.g. bearings with polar symmetry, i.e. circular), the domain is a circumference of radius $\gamma_{H,ult}^{\vartheta} = \gamma_{H,ult}$. FEAs demonstrated that a stable response along both X ($2a$) and Y ($2b$) results in stable response in any direction of loading.

In all the other cases, the stability limit tends to show a transition between a minimum value (corresponding to loading the bearings

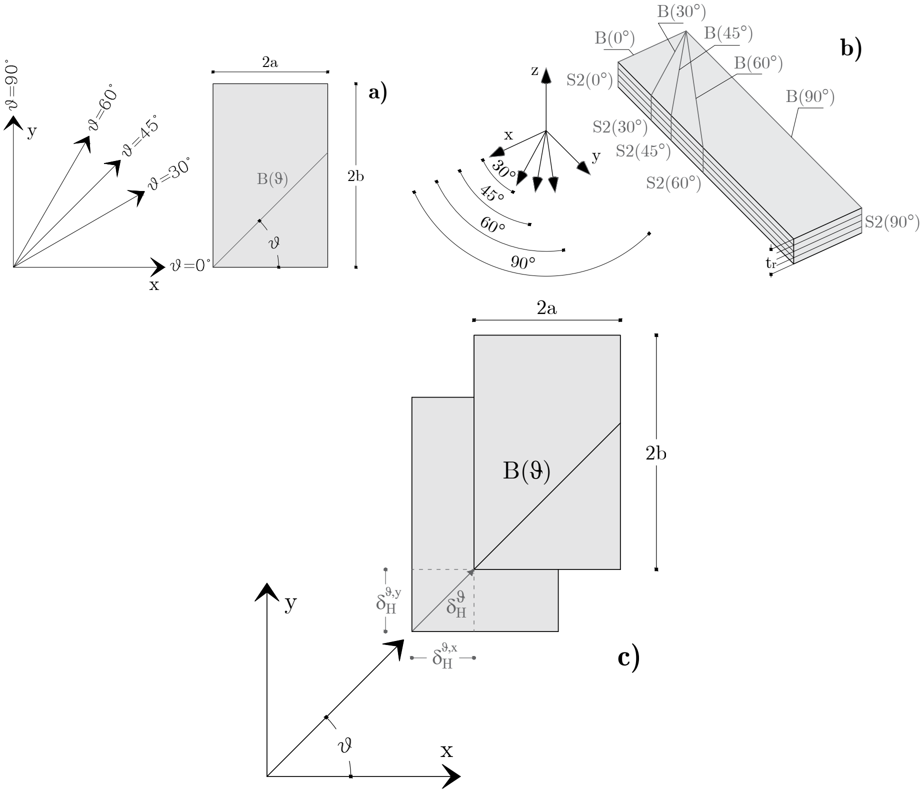

Figure 6.3: Parameters' label definition: (a) horizontal displacement base side, (b) secondary shape factor in the horizontal displacement direction and (c) maximum stable horizontal displacement in the horizontal displacement direction.

along their smaller side) and a maximum value (corresponding to loading the devices along their bigger side).

When loading along X (0°) or Y (90°), the influence of the out of plane dimension of the bearing on its displacement capacity is negligible. This confirms that 2D models are sufficient for the analysis of unbonded FREIs when these are loaded along their base.

In general, the stability range decreases with increasing vertical pressure, in line with results from **Chapters 3** and **5**. The maximum stable shear strain thresholds of unstable bearings decrease on average by 5.90% and 9.37% from $\sigma_v = 2$ MPa to $\sigma_v = 4$ MPa, for $t_e = 10$ mm and $t_e = 20$ mm respectively. Nevertheless, an increasing vertical load has a positive effect on the stability of larger bearings with large secondary shape factor (i.e. $S_2 \geq 3$, see **Figures 6.4 (g)** and **6.5 (j)**, circular markers) since the horizontal deformation results in a smaller reduction of the contact area compared to more slender bearings and the vertical stiffness of the bearing is less affected by the vertical pressure.

In **Figure 6.5**, two types of information are given: the *stability limit in the loading direction* and the *stability limit angle of a generig bearing*. Respectively:

- A generic straight line from the origin of the primary axes of these figures to the point of the domain provides the stability limit of the bearing in the loaded direction. The length of this segment is the maximum stable shear strain in the loading direction while its inclination corresponds to ϑ. Similarly, a straight line from the origin of the secondary axis to the S_2^{ϑ} curve gives the corresponding secondary shape factor in the direction ϑ.

- The stability limit angle can be obtained from the plots as rectangular bearings may have two very different secondary shape factors along X ($S_2^{0^\circ} = 2a/t_r$) and Y ($S_2^{90^\circ} = 2b/t_r$. The bearing could be stable in one of its main directions (e.g. 90°) and unstable along the other (e.g. 0°) and the transition between stable and unstable response could occur at an angle that is function of the ratio $2b/2a = b/a$.

In **Figure 6.6 (a)** an example of the response of a stable (square marker) and of an unstable (diamond marker) bearing is given. The dashed line defines the direction $\vartheta = 30°$: the stability limit for the unstable bearing ($2a$x$2b$xHxt_exσ_v = 200x400x200x10x4) is $\gamma_{H,cr}^{30°} = 0.51$ with a secondary shape factor $S_2^{30°} = 1.21$, while for the stable bearing ($2a$x$2b$xHxt_exσ_v = 400x400x100x10x4) is $\gamma_{H,cr}^{30°} = 2.00$ and $S_2^{30°} = 4.80$. When $\vartheta = 60°$, the unstable bearing provides $\gamma_{H,cr}^{60°} = 2.10$ and $S_2^{60°} = 2.10$ while the stable gives $\gamma_{H,cr}^{60°} = 2.00$ and $S_2^{60°} = 4.80$.

Figure 6.6 (b) shows the stability domain of a bearing which is stable along Y and unstable along Y ($2a$x$2b$xHxt_exσ_v = 200x400x100x10x4). In this case the transition between the stability limit angle is between $\vartheta = 60°$ ($S_2^{60°} = 4.08$) and $\vartheta = 45°$ ($S_2^{45°} = 4.08$).

The behavior of stable bearings is highlighted in **Figure 6.7**, where all the secondary shape factors of all the bearings that reach full rollover are plotted. Connecting the minimum values of S_2^{ϑ}, an envelope of unstable bearings is obtained. Any point outside this domain represents a stable bearing that can deform up to full rollover in any direction. The instability envelopes at $\sigma_v = 4$ MPa are larger than those at $\sigma_v = 2$ MPa. To obtain a stable response, a larger S_2^{ϑ} in the generic direction is needed as the vertical pressure increases. However, in the range of vertical pressure considered in this thesis, once again it is noted how the transition between stable and unstable behavior occurs in the range $2.5 \leq S_2^{\vartheta}$.

6.3.2 Horizontal stiffness

Figure 6.8 show the lateral secant stiffness of each bearing at $\gamma_{H,cr}^{\vartheta}$, with respect to the angle of the imposed lateral displacement. In these figures, the secondary shape factors S_2^{ϑ} of the bearings are plotted in gray. Combining the information from the two types of curves, the lateral stiffness with respect to the secondary shape factor of the bearing can be obtained.

The lateral secant stiffness at δ_H (or $\gamma_H = \delta_H/t_r$) is defined as the

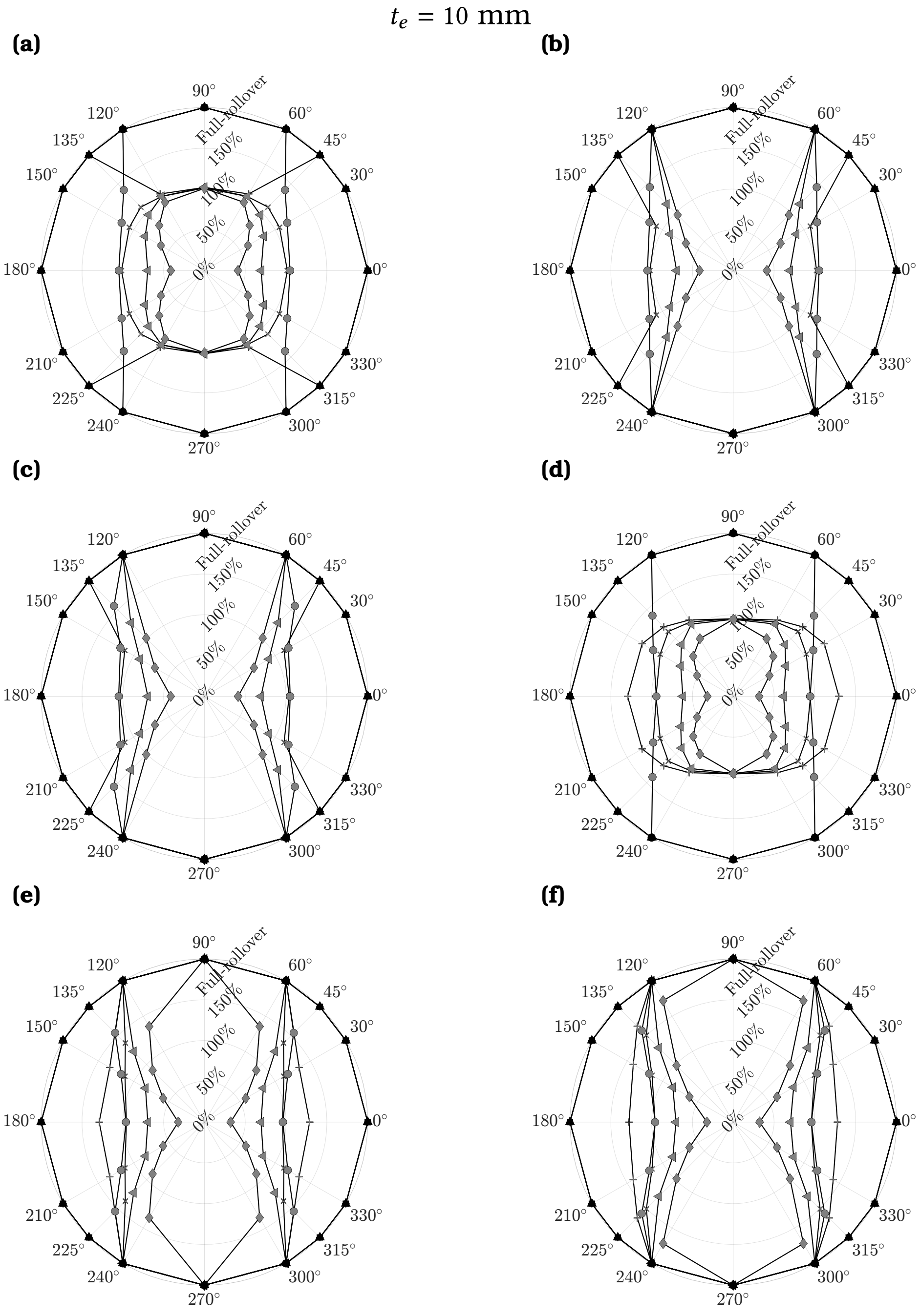

Continues on the next page →

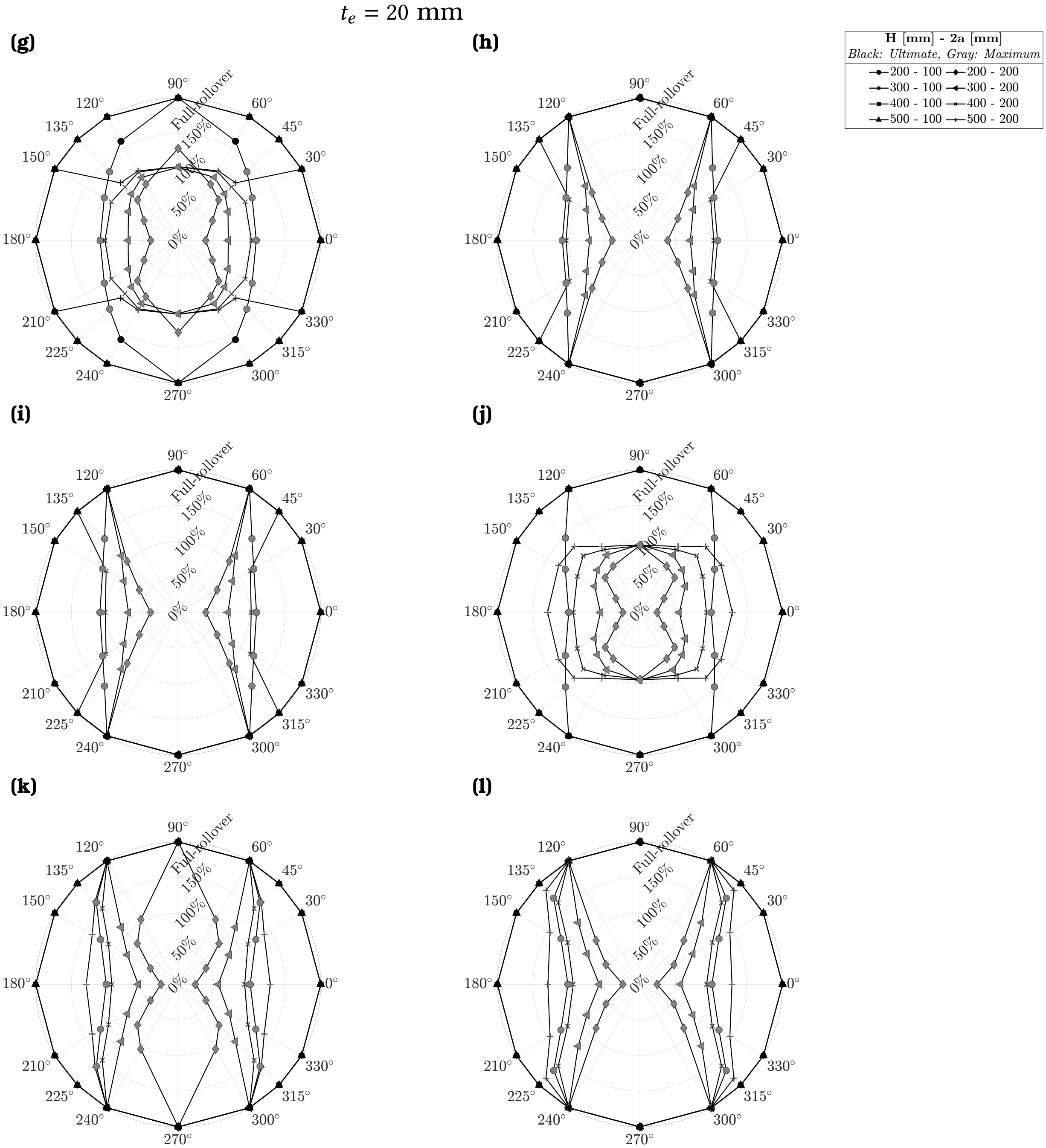

Figure 6.4: Polar stability domain $\gamma^{\vartheta}_{H,cr}$: (a), (d), (g), (j) $2b$ = 400 mm, (b), (e), (h), (k) $2b$ = 800 mm, (c), (f), (i), (l) $2b$ = 1200 mm; (a), (b), (c), (g), (h), (i) σ_v = 2 MPa, (d), (e), (f), (j), (k), (l) σ_v = 4 MPa.

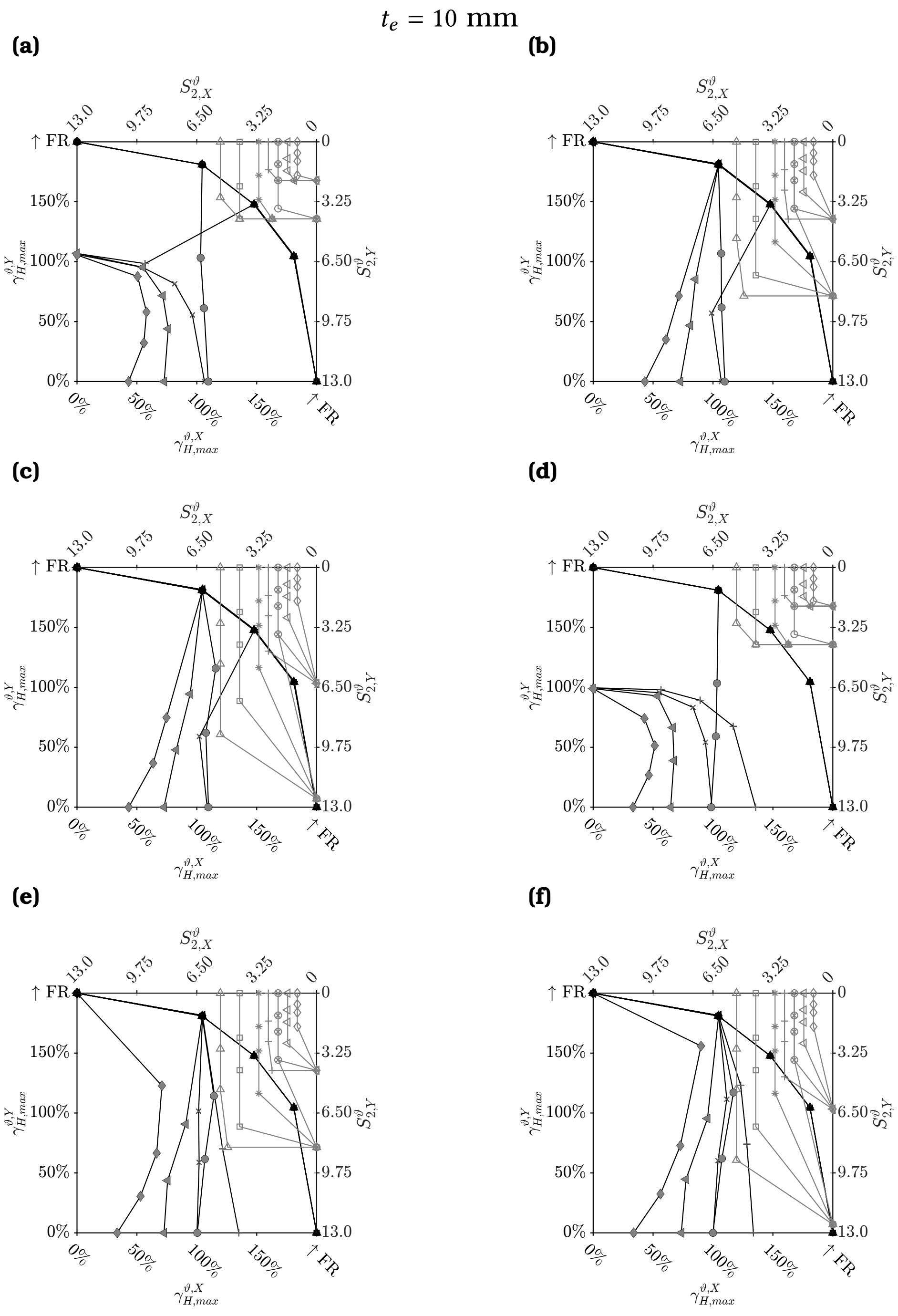

Continues on the next page →

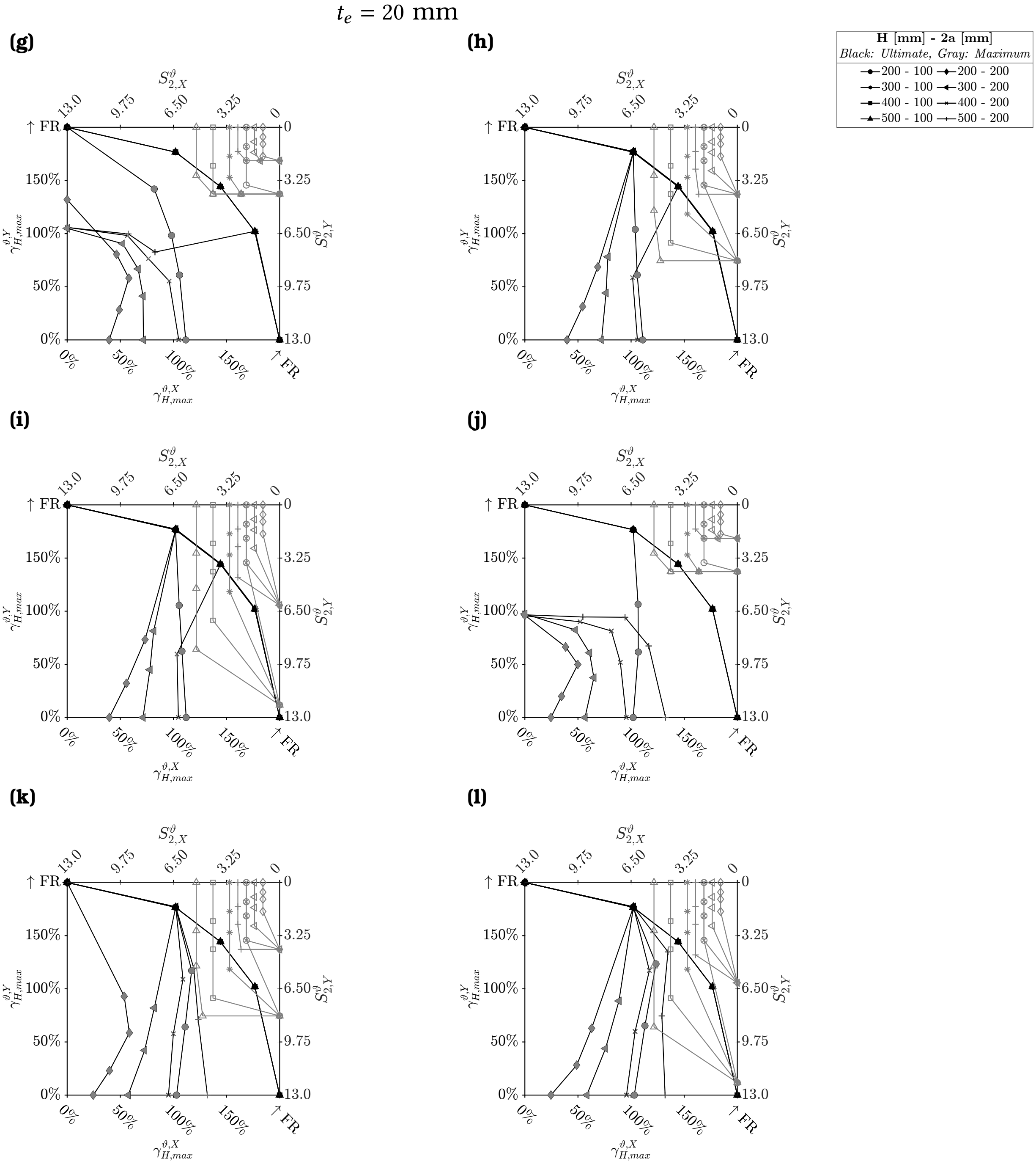

Figure 6.5: Planar stability domain $\gamma^{\vartheta}_{H,cr}$: (a), (d), (g), (j) $2b = 400$ mm, (b), (e), (h), (k) $2b = 800$ mm, (c), (f), (i), (l) $2b = 1200$ mm; (a), (b), (c), (g), (h), (i) $\sigma_v = 2$ MPa, (d), (e), (f), (j), (k), (l) $\sigma_v = 4$ MPa.

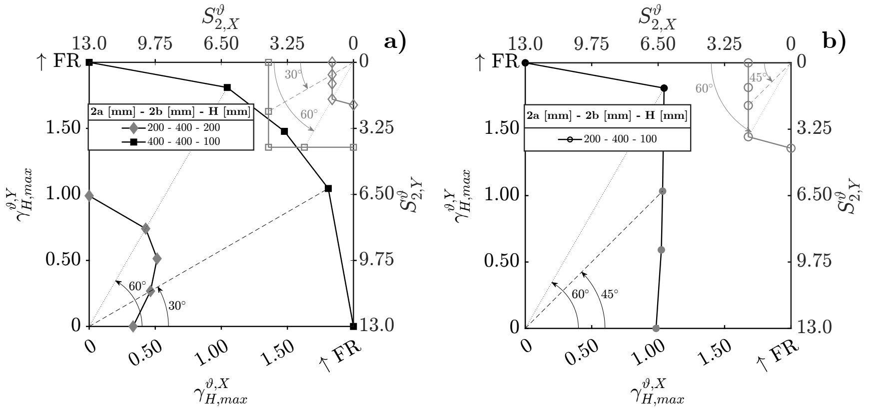

Figure 6.6: Use of stability domain: (a) stability ranges and (b) stability limit angle.

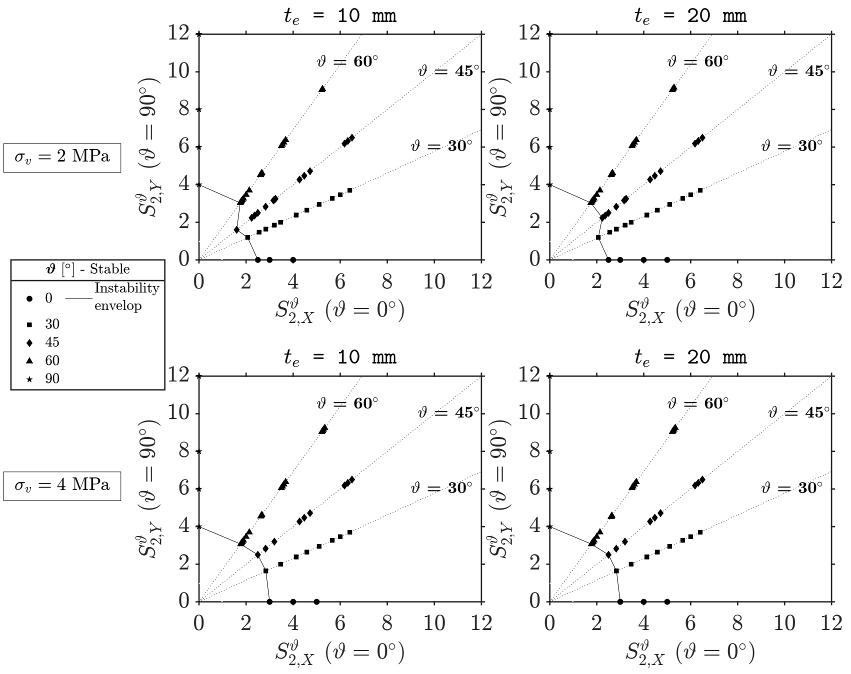

Figure 6.7: S_2^{ϑ} for all stable bearings: instability envelop

slope of the secant line to the lateral force – displacement curve at the same horizontal threshold:

$$K_H^{\delta_H} = \frac{F_H^{\delta_H}}{\delta_H} \tag{6.3}$$

In **Figure 6.8** the lateral secant stiffness has been obtained applied this equation to the output numerical horizontal force - displacement curves.

The lateral secant stiffness at the maximum stable shear strain tends to decrease as the applied vertical load increases. From $\sigma_v = 2$ MPa to $\sigma_v = 4$ MPa an average decrease of the secant stiffness equal to 1.23% and 7.15% for $t_e = 10$ mm and $t_e = 20$ mm respectively was found.

Stable bearings loaded along their base reach full rollover around a shear strain of 150 to 200%, and this is generally not the case when the bearings are loaded in a generic horizontal direction given by ϑ. Due to a partial rollover, stable bearings loaded along a generic direction show a lower horizontal secant stiffness than those loaded along their base.

6.3.3 Full Rollover

As introduced in **Section 6.1**, in previous research work it was found that the stability range of a bearing increases when these are loaded in a generic direction. To provide clear indications of this phenomenon, **Figure 6.9** show the ultimate shear strain ($\gamma_{H,ult}^{\vartheta}$) for all the stable bearings while **Figure 6.10** show the deformed shape at full rollover of a square- (**Figure 6.10 (a)**) and a rectangular- (**Figure 6.10 (a)**) shaped FREI.

The displacements where the rotation of the vertical faces begins at the onset of roll-over are shown with black markers, whereas the full rollover is depicted with gray markers. Starting from the smaller base side, when FREIs are loaded in a generic direction, their stable range increases with increasing secondary shape factor in the horizontal displacement direction. This is more pronounced for bearings with similar base dimensions (i.e. base/width ratio close

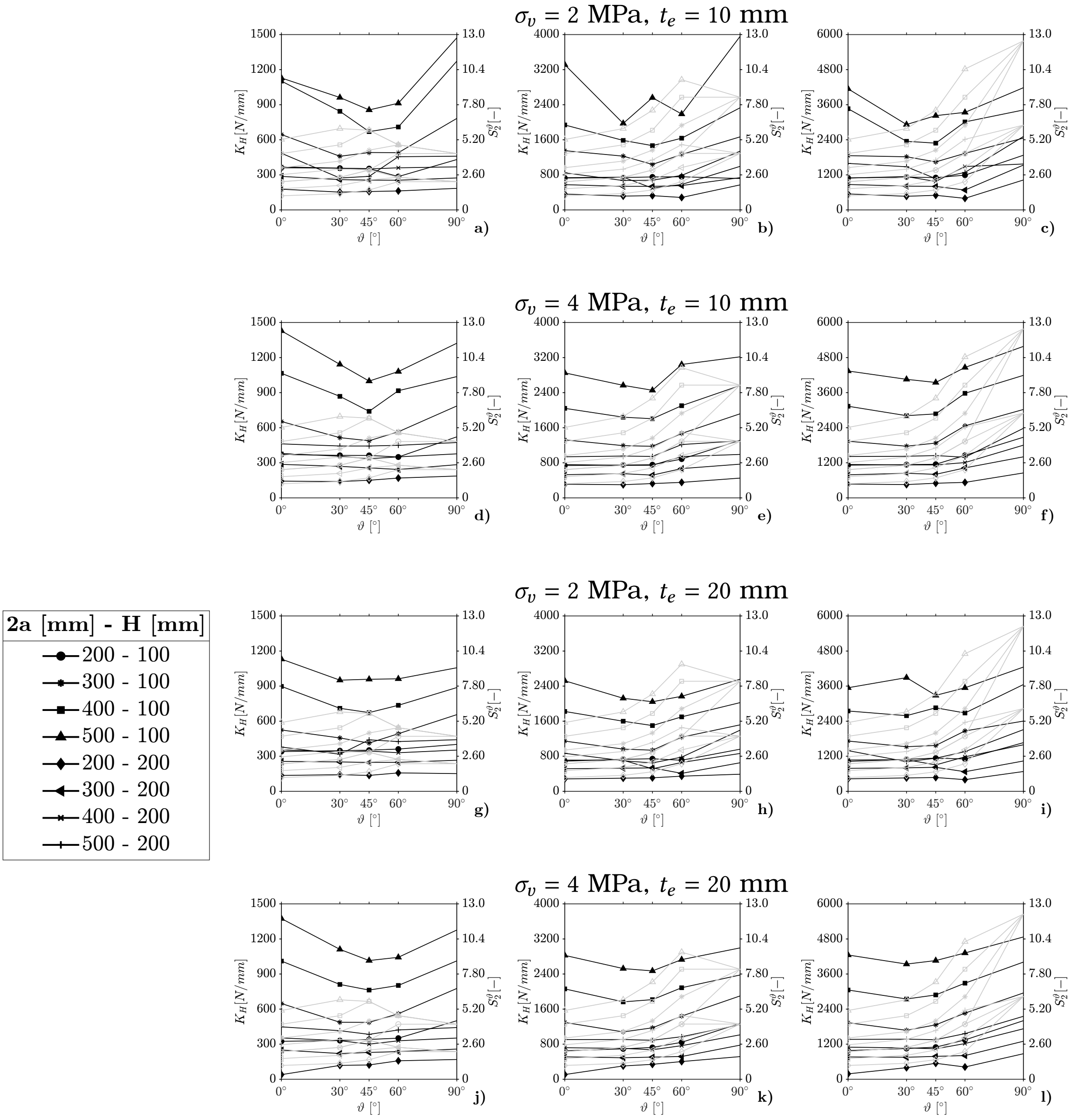

Figure 6.8: Lateral secant stiffness at maximum stable shear strain vs ϑ and S_2^ϑ: (a) $2b$ = 400 mm, (b) $2b$ = 800 mm, (c) $2b$ = 1200 mm, (d) $2b$ = 400 mm, (e) $2b$ = 800 mm, (f) $2b$ = 1200 mm, (g) $2b$ = 400 mm, (h) $2b$ = 800 mm, (i) $2b$ = 1200 mm, (j) $2b$ = 400 mm, (k) $2b$ = 800 mm, (l) $2b$ = 1200 mm.

to 1, **Figure 6.10 (a)**, refer also to **Figures 6.9 (a)**, **6.9 (d)**, **6.9 (g)** and **6.9 (j)** for additional details) then strip-shaped (**Figure 6.10 (b)**, **Figures 6.9 (c)**, **6.9 (f)**, **6.9 (i)** and **6.9 (l)**). For bearings with a base to width ratio close to 1 (e.g. square shape), the application of a shear strain in a generic direction does not reduce their deformation capacity.

6.4 Simplified formula for the stability range of bidirectional shear loaded U-FREIs

In **Section 2.3.2**, an easy-to-use design formula for the determination of the peak displacement (i.e. $\delta_{H,cr} = \delta_{H,max}$) in the lateral response of the FREIs was shown. According to this simplified approach, a local maximum in the force displacement response curve can be found for an horizontal displacement equal to half of the base of the bearing in the loaded direction (i.e. $\delta_{H,max} = a \vee b$). With this simplified approach the detached area is $A_d = 2b \cdot \delta_H^{2a}$ (**Figure 6.12 (a)**).

Based on this result, in this thesis a similar approach is proposed for the peak displacement of a force-displacement response curve of a FREI loaded in a generic horizontal direction. The maximum stable horizontal displacement of the bearing in the direction defined by ϑ can be approximately calculated as half of the corresponding dimension $B(\vartheta)$:

$$\delta_{H,max}^{\vartheta} = \frac{B(\vartheta)}{2} = \begin{cases} \frac{a}{\cos\vartheta} & \text{if } \vartheta \leq \arctan\left(\frac{2b}{2a}\right) \\ \frac{b}{\sin\vartheta} & \text{if } \vartheta > \arctan\left(\frac{2b}{2a}\right) \end{cases} \tag{6.4}$$

Figure 6.11 shows the comparison on maximum shear strain as obtained from FEAs and by **Equation 6.4**. In this figure the determination coefficient (R^2), the mean percent error ($\mathrm{PE}_{\%}$), the standard deviation (σ) and the variance (σ^2) are also shown and calculated as follow:

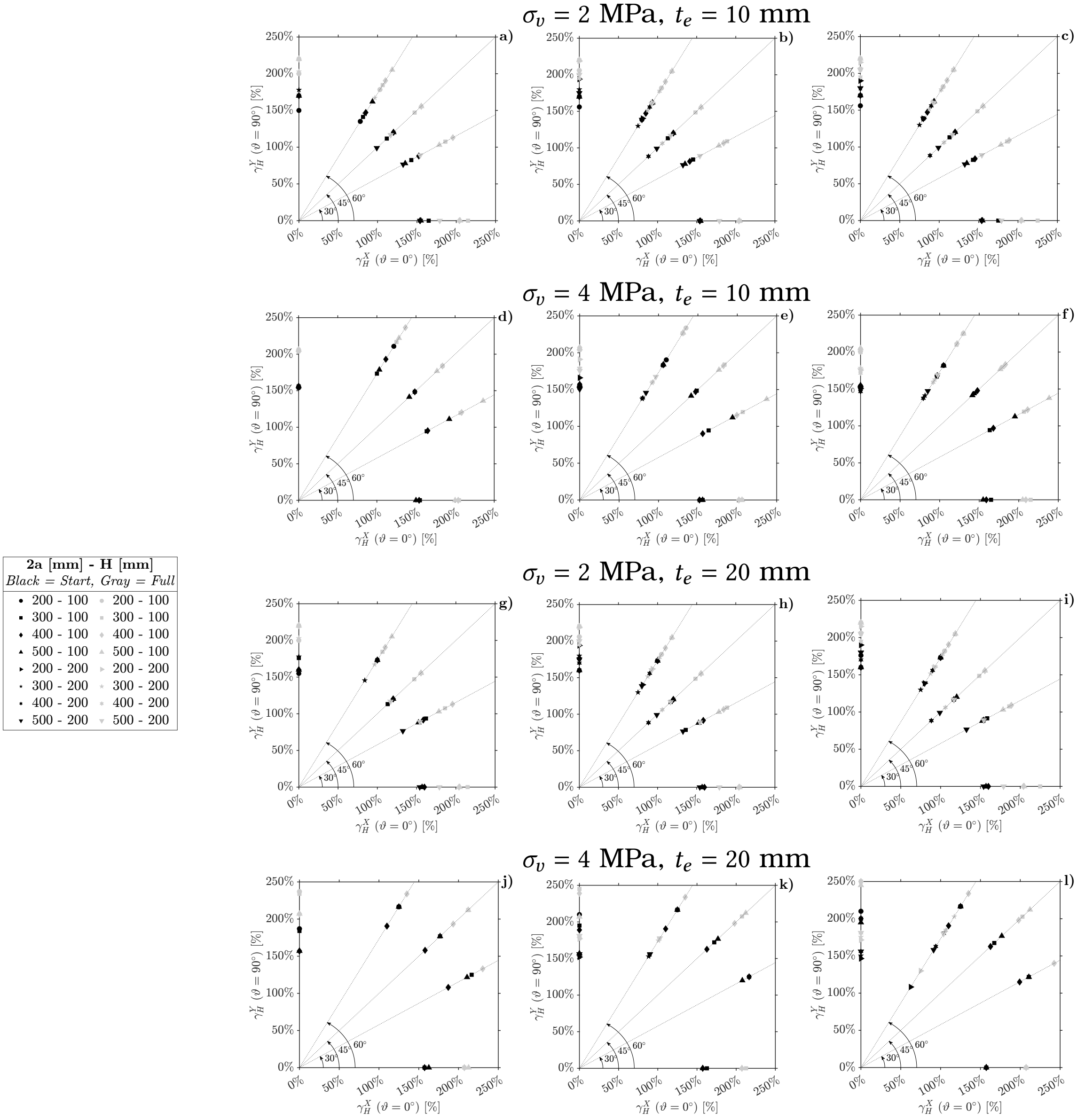

Figure 6.9: Ultimate behavior of stable bearings: (a) $2b$ = 400 mm, (b) $2b$ = 800 mm, (c) $2b$ = 1200 mm, (d) $2b$ = 400 mm, (e) $2b$ = 800 mm, (f) $2b$ = 1200 mm, (g) $2b$ = 400 mm, (h) $2b$ = 800 mm, (i) $2b$ = 1200 mm, (j) $2b$ = 400 mm, (k) $2b$ = 800 mm, (l) $2b$ = 1200 mm.

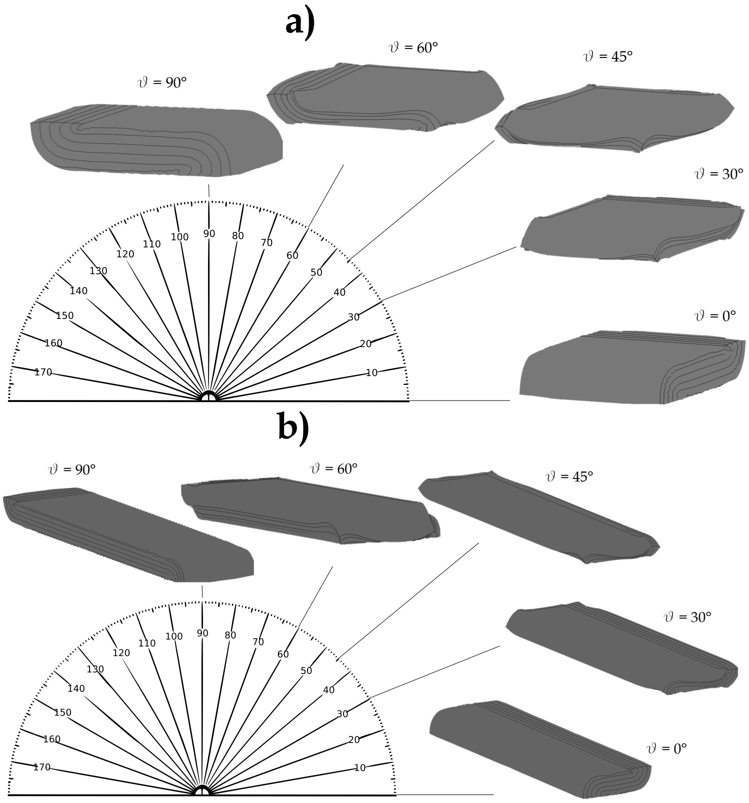

Figure 6.10: U-FREIs at full rollover for each horizontal loading direction: (a) square-shaped and (a) rectangular-shaped.

$$R^2 = 1 - \frac{\sum_{i=1}^{n}\left(\gamma_{H,max,i}^{num} - \gamma_{H,max,i}^{an}\right)^2}{\sum_{i=1^n}^{n}\left(\gamma_{H,max,i}^{num} - \frac{1}{n}\sum_{i=1}^{n}\gamma_{H,max,i}^{num}\right)^2} \tag{6.5a}$$

$$\mathrm{PE}_{\%} = \frac{1}{n}\sum_{i=1}^{n}\left[\frac{\left(\gamma_{H,max,i}^{num} - \gamma_{H,max,i}^{an}\right)}{\gamma_{H,max,i}^{an}} \cdot 100\right] \tag{6.5b}$$

$$\sigma = \sqrt{\frac{1}{n}\sum_{i=1}^{n}\left[\frac{\gamma_{H,max,i}^{num}}{\gamma_{H,max,i}^{an}} - \left(\frac{1}{n}\sum_{i=1}^{n}\frac{\gamma_{H,max,i}^{num}}{\gamma_{H,max,i}^{an}}\right)\right]^2} \tag{6.5c}$$

$$\sigma^2 = \frac{1}{n}\sum_{i=1}^{n}\left[\frac{\gamma_{H,max,i}^{num}}{\gamma_{H,max,i}^{an}} - \left(\frac{1}{n}\sum_{i=1}^{n}\frac{\gamma_{H,max,i}^{num}}{\gamma_{H,max,i}^{an}}\right)\right]^2 \tag{6.5d}$$

A good agreement is found between numerical and analytical values. The minimum coefficient of determination is equal to 0.77, the maximum standard deviation is 0.176, the maximum variance is around 3% and the percent error is less than 15%. **Figure 6.11** confirms that this formula can be applied for a preliminary assessment of the displacement capacity of unstable bearings in either direction of loading (i.e. for bearings with a secondary shape factor smaller than 2.5, 3).

With the proposed approach, the detached area becomes (**Figure 6.12 (b)**):

$$A_d\left(\delta_H^{\vartheta}\right) = \frac{\left(\delta_H^{\vartheta}\right)^2}{\sin\left(2\vartheta\right)} \qquad \text{if } \delta_H^{\vartheta} < 2a\cos\vartheta \tag{6.6a}$$

$$A_d\left(\delta_H^{\vartheta}\right) = 2a\left(\frac{\delta_H^{\vartheta}}{\sin\vartheta} - a\cot\vartheta\right) \qquad \text{if } 2a\cos\vartheta \le \delta_H^{\vartheta} \le 2b\sin\vartheta \tag{6.6b}$$

$$\begin{aligned} A_d\left(\delta_H^{\vartheta}\right) = -\frac{\csc\vartheta\sec\vartheta}{2}\Big[&2a^2 + 2b^2 + \left(\delta_H^{\vartheta}\right)^2 - 4a\delta_H^{\vartheta}\cos\vartheta + \\ &2\left(a^2+b^2\right)\cos\left(2\vartheta\right) - 4b\delta_H^{\vartheta}\sin\vartheta\Big] \qquad \text{if } \delta_H^{\vartheta} > 2b\sin\vartheta \end{aligned} \tag{6.6c}$$

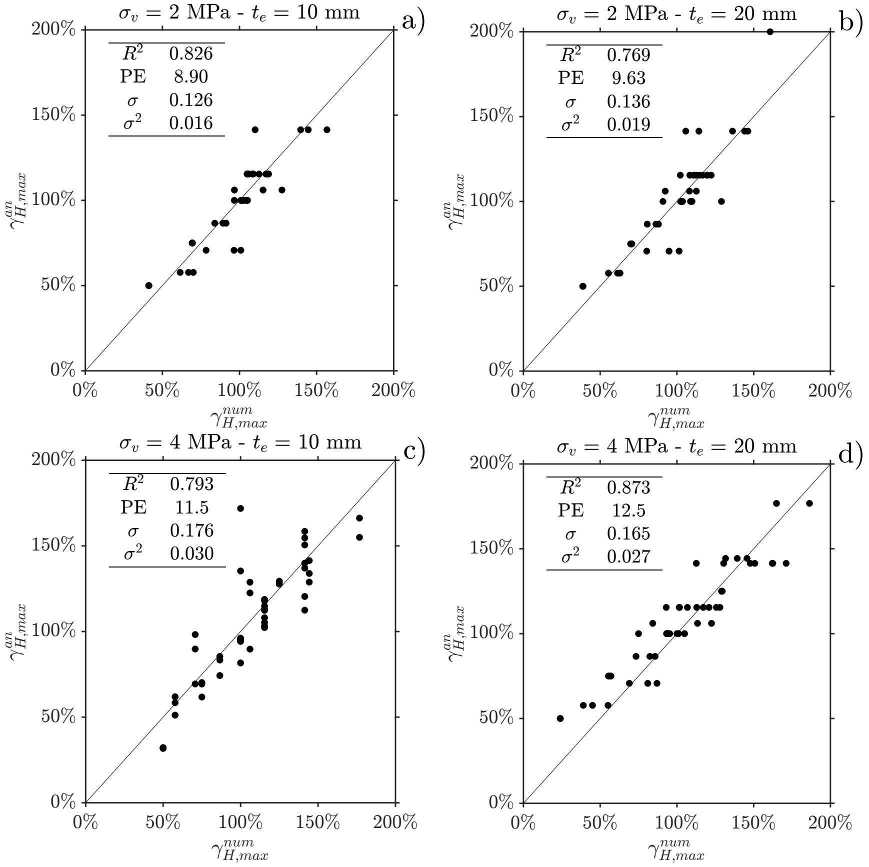

Figure 6.11: Maximum stable shear strain: analytical ($\gamma^{an}_{H,max}$) - numerical comparison ($\gamma^{an}_{H,max}$): (a) σ_v = 2 MPa and t_e = 10 mm, (b) σ_v = 2 MPa and t_e = 10 mm, (c) σ_v = 2 MPa and t_e = 10 mm, (d) σ_v = 4 MPa and t_e = 10 mm.

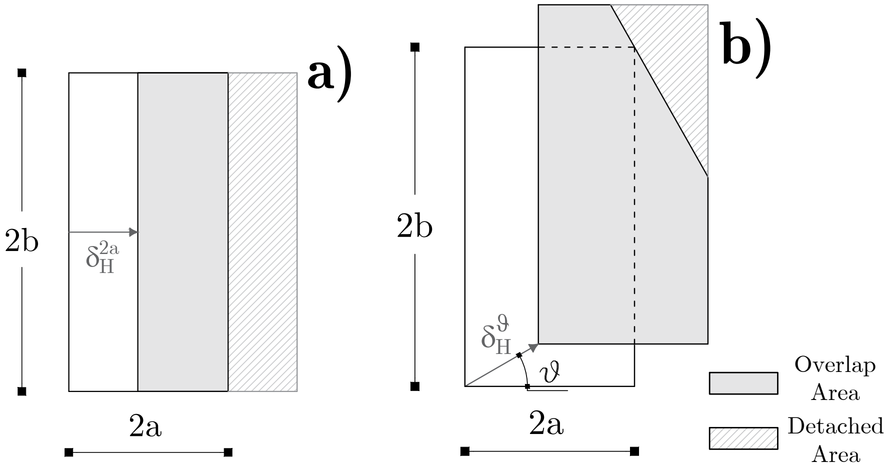

Figure 6.12: Overlapping and detached areas: (a) horizontal displacement along the base side $2a$ and (b) horizontal displacement along a base side in the direction ϑ.

Part III

Modified FREIs

CHAPTER 7

TUNING THE HORIZONTAL RESPONSE OF UNBONDED FIBER REINFORCED ELASTOMERIC ISOLATORS

Summary

A simple strategy to tune the horizontal stability of U-FREIs is shown in this chapter. Results of experimental tests on scaled modified U-FREIs show the improvement introduced on the horizontal response of the bearings. The same bearings tested experimentally were then modeled with finite elements software and the results of these analyses confirm the benefits of the modification.
Part of the informations of this chapter are based on the journal papers [141, 142] and conference paper [143].

7.1 Background and motivations

It is well known that the frequency of an elastomeric isolator depends on the applied vertical load ([12, 112]). While research studies have confirmed that U-FREIs are a viable base isolation strategy for residential buildings, including N-EB, in seismic-prone areas of developing countries [66, 68], due to a limited mass of such buildings, FREIs for these applications need to be slender, with a secondary shape factor slightly higher than 1.00. These types of FREIs would be unstable [65].

An ideal rubber-based device should be flexible and stable even under large lateral deformations. In addition, it should show hardening under large displacements. Hardening is needed to contain the deformation of the isolation layer within design limits and to prevent damage to the bearings.

For this reason, research work has been dedicated to identify strategies to improve the response of FREIs by modifying their geometry. As result, a variety of geometries have been tested, most of which have been obtained by creating vertical holes in FREIs, and the modified bearings were named MU-FREIs (Modified Unbonded Fiber Reinforced Elastomeric Isolators) [144–147]. Vertical holes led to an increase of the vertical pressure on the bearings, and a reduction of the horizontal stiffness. An elastomeric bearing modified with vertical holes, therefore, would be subjected to higher pressure providing a lower frequency to the isolation system. This, combined with the reduction of the horizontal stiffness, increases the efficiency of the isolation system.

However the introduction of vertical holes does not change the shape of the lateral response of the bearing. Therefore, an unstable bearing would remain unstable even when modified. Slender MU-FREIs would still have a narrow stability range.

In this thesis a novel geometry modification to the FREIs is proposed with the aim of obtaining:

i A controlled reduction of the horizontal stiffness.

ii A wider range of stable response in the range of nominal shear strain of interest.

iii Hardening under large lateral deformations prior to rollover

via experimental and numerical approach.

7.2 FEAs blind prediction

A blind prediction of the response of modified FREIs with horizontal holes was first performed using finite element analysis. An unbonded strip-shaped FREI with different layouts of holes in the longitudinal direction was modeled with planar 2D FEMs using MSC.Marc, following the same procedure shown in **Section 3.1.2**. Holes were introduced deleting elements of the elastomer and fiber-reinforcement mesh.

Four bearing configurations were modeled: one unmodified bearing (as a control FEMs) and three FREIs with an increasing number of square-shaped holes from 1 to 3. Each hole has a side equal to 30 mm and is placed at half height of the bearing (**Figure 7.1**).

Each FREI has a width of $2a = 400$ mm and a height of $H = 180$ mm, giving a width-to-height aspect ratio of 2.22. It comprises 36 rubber layers, each one having a thickness $t_e = 5$ mm. The primary shape factor of each pad is $S_1 = a/t = 40$, while the secondary shape factor is $S_2 = 2a/t_r = 2.24$. The shear and bulk moduli of the elastomer were set to $G_e = 0.69$ MPa and $K = 2000$ MPa respectively. Each fiber reinforcement layer has an equivalent thickness of $t_f = 0.05$ mm. The elastic modulus and the Poisson's ratio for the fiber reinforcement material were set to $E_f = 70000$ MPa and $\nu_f = 0.2$ respectively.

Each FREI were prior subjected to five different levels of vertical pressure: 1.5, 2, 2.5, 3, 3.5 and 4 MPa; then, an horizontal displacement up to at least 200 mm (i.e. $\gamma_H = 112\%$) has been applied.

As a verification of the model with no holes the vertical stiffness of the bearing obtained with FEA is compared against the solution from **Equation 2.5**, following a similar procedure of ref. [134]. With these results, a preliminar sensitivity analysis was conducted (**Figure 7.2**) with respect to the number of elements along the base and the height of the bearing. The relative percentage error between analytical and numerical results on vertical stiffness (i.e. $1 - K_v^{an}/K_v^{num}$) showed that 200 and 143 elements along the base and height of the bearing respectively, were enough to capture the global response of the FREIs with good accuracy.

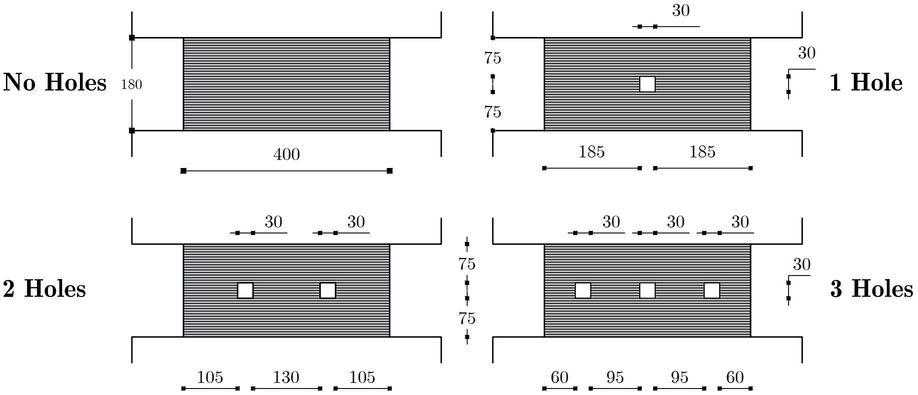

Figure 7.1: Schematic of the FREIs for the blind prediction (dimensions are in mm).

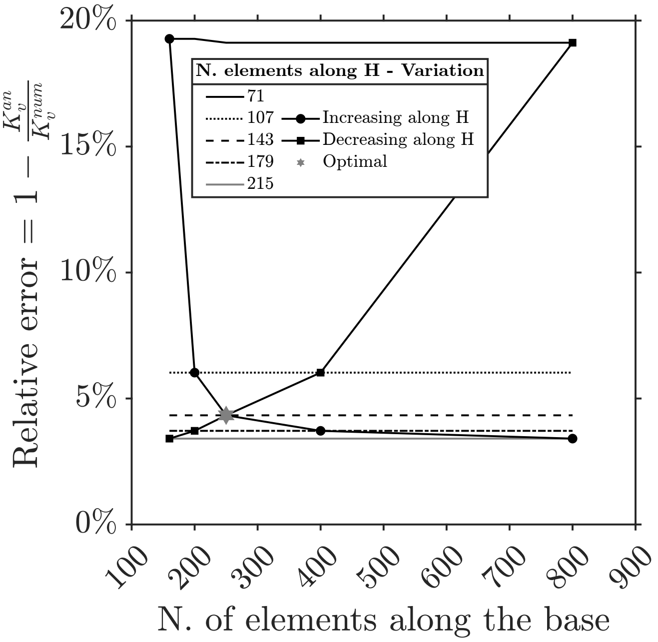

Figure 7.2: Sensitivity analysis of the FEAs blind prediction.

7.2.1 Blind prediction results

Figure 7.3 shows the horizontal curves response of the 4 configurations of bearings and for the different values of vertical pressure in the range $1.5 \div 4$ MPa. From this curves it can be deduced that:

- The presence of the holes decreases the initial lateral stiffness for each and all the values of vertical pressure.
- All bearings show a softening behavior. However, the bearing with 2 holes softens up to a shear strain $\gamma_H = 73\%$ and then it shows hardening.

The FREI with 2 holes thus exhibits desirable horizontal response under any of the vertical pressure value in the considered range. A focus on this bearing's horizontal response up to full rollover for the values of the vertical pressure in the range $1.5 \div 4$ MPa is given in **Figure 7.4**. There are no peaks in the horizontal force-displacement response curves of these modified bearings (**Figure 7.4 (a)**); the behavior is stable in the considered shear strain range, i.e. the tangent horizontal stiffness, although decreasing, is greater than zero throughout the deformation range (**Figure 7.4 (b)**).

The vertical and secant horizontal stiffnesses of the 4 configurations of FREIs are shown in **Figure 7.5**. From this figure it can be seen how the vertical stiffness of the bearing decreases with the number of holes (**Figure 7.5 (a)**), as does the horizontal secant stiffness at $\gamma_H = 100\%$ (**Figure 7.5 (b)**), as expected; however, their ratio, although decreasing, shows a minimum value of around 500 (**Figure 7.5 (c)**). The ratio of vertical and horizontal stiffness must be high enough to avoid rocking motions of the structure [112] and the modifications appear to achieve this goal.

In an effort to understand what causes the hardening, **Figure 7.6** plots the deformed configurations of the 4 bearings at the lowest compression stress of 1.5 MPa and increasing amplitudes. This figure shows that the hardening could be caused by a large shear deformation of the holes that causes them to essentially close with increasing horizontal displacement. However, according to the considered configurations of holes, the hardening response could depend on the percentage of removed rubber area and on the distance between two adjacent holes. In the first case with one central holes, the percentage of removed area is rather low ($\approx 1\%$) and the lateral response curve seems to be not affected by the geometric modification; in the second case, reducing the space between two adjacent holes (from 130 mm to 95 mm) the shape of the lateral response curve does not change, even though the peak shear force are clearly reduced.

7.3 Experimental tests on modified U-FREIs

The results obtained with the FEAs blind prediction shown in **Section 7.2.1** demonstrated how modification of the FREIs' geometry can potentially bring out improvements in their horizontal response. A wider stability range could be obtained in U-FREIs with horizontal holes.

Starting from these considerations, a number of modified FREIs samples were experimentally tested with the aim of investigating the actual changes to the response of a bearing when modified. The same bearings tested are then modeled with finite element software for further investigation of their response.

7.3.1 Description of the tested samples

The bearings tested in this study were manufactured by Kirkhill Manufacturing Company, Downey, CA following Caltrans specifications, as already described in **Section 3.1.2.3**. A total of 8 bearings were tested. **Table 7.1** gives an overview of the main geometric characteristics of the bearings. In this table, $V = A_c \cdot H$ is the volume of the bearing; Ø is the diameter of the single hole; V_{holes} is the total volume of the holes (i.e. total removed volume); V_{holes}/V is the total percentage removed volume. **Figure 7.7** shows a layout of the tested bearings. Two types of modifications are studied:

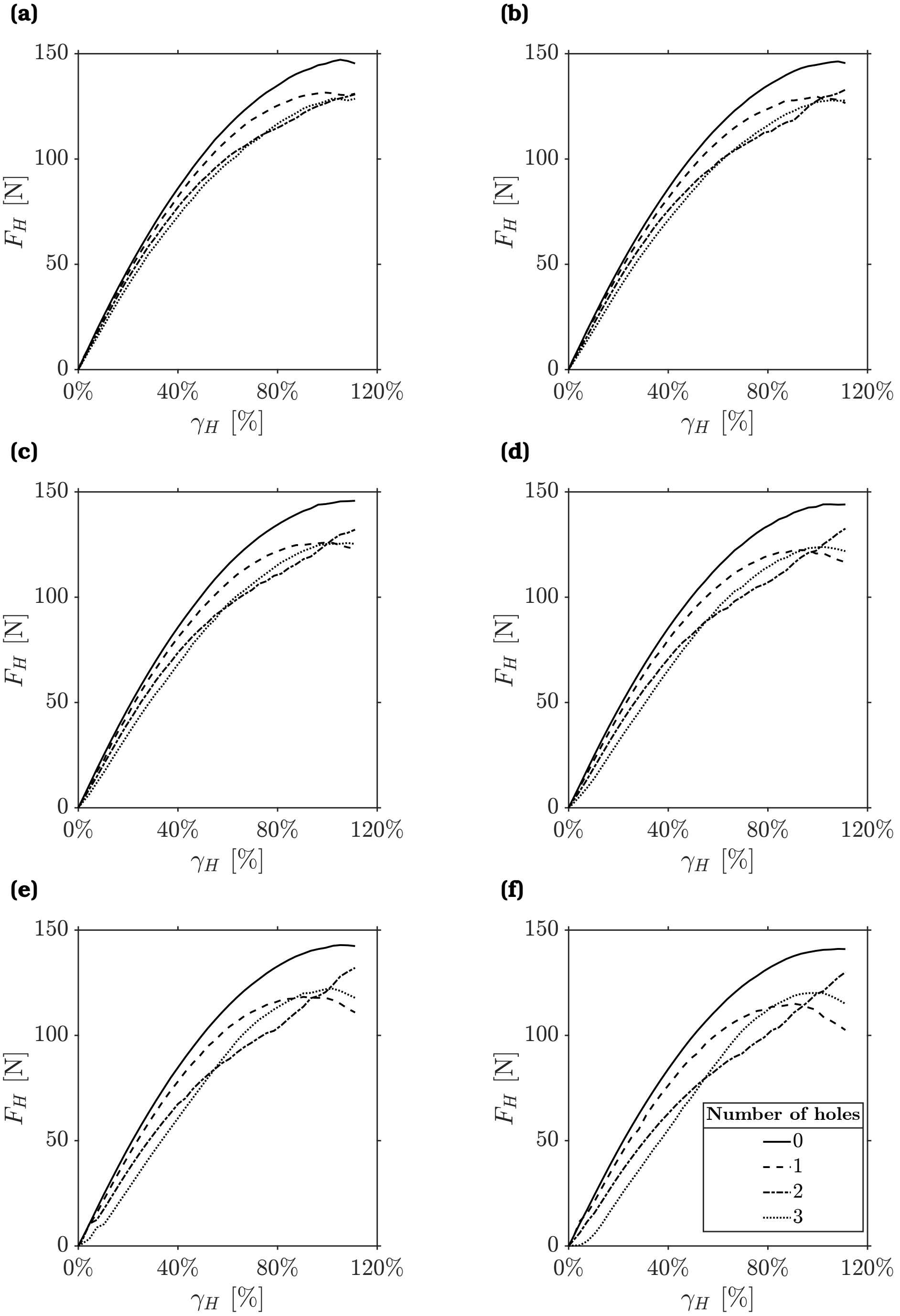

Figure 7.3: Curve response of the 4 modified configurations: (a) $\sigma_v = 1.5$ MPa, (b) $\sigma_v = 2$ MPa, (c) $\sigma_v = 2.5$ MPa, (d) $\sigma_v = 3$ MPa, (e) $\sigma_v = 3.5$ MPa, (f) $\sigma_v = 4$ MPa

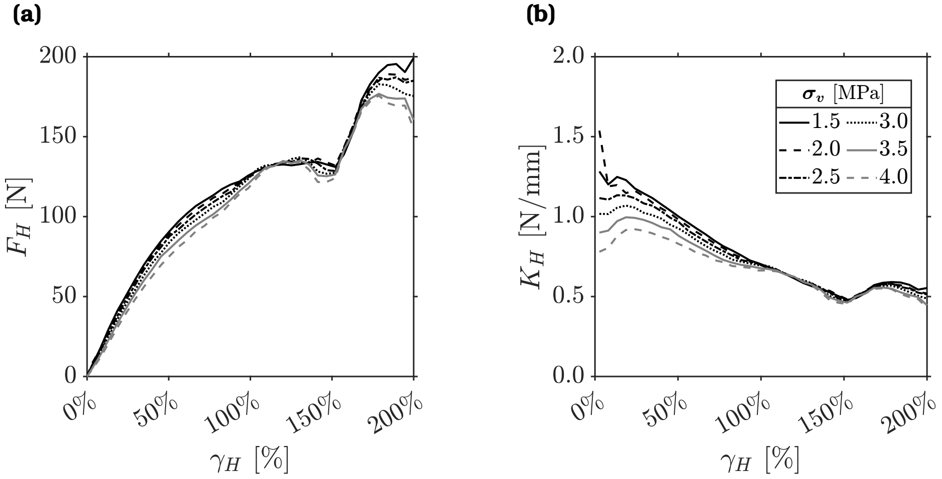

Figure 7.4: Horizontal response of modified FREI with two holes: (a) force-displacement curves, (b) tangent horizontal stiffness.

- The first four rows of **Table 7.1** refer to bearings with the same geometry ($2a = 130$ mm, $2b = 60$ mm and $H = 52$ mm) and a total number of holes ranging from 0 (unmodified control bearing) to 20 (**Figure 7.7 (a)**).
- The last four rows of **Table 7.1** refer to bearings with 12 holes and variable base side $2a$, ranging from 130 mm to 70 mm (**Figure 7.7 (b)**).

With the first type of modification, the effect of a variable number of holes on a given geometry can be determined. The second type of tests highlights the effect of a fixed set of holes on bearings of different geometries.

The holes were made along the side $2b$ of each bearing (**Figure 7.7**). The spacing of the holes along both the vertical and the horizontal direction is constant and equal to 13 mm and 12 mm, respectively (**Figure 7.7**). As clear from **Table 7.1**, the percentage of removed volume V_{holes} ranges from 1.67% to 9.32% of the total volume of the bearing.

The holes are of circular shape with 6 mm diameter and they are

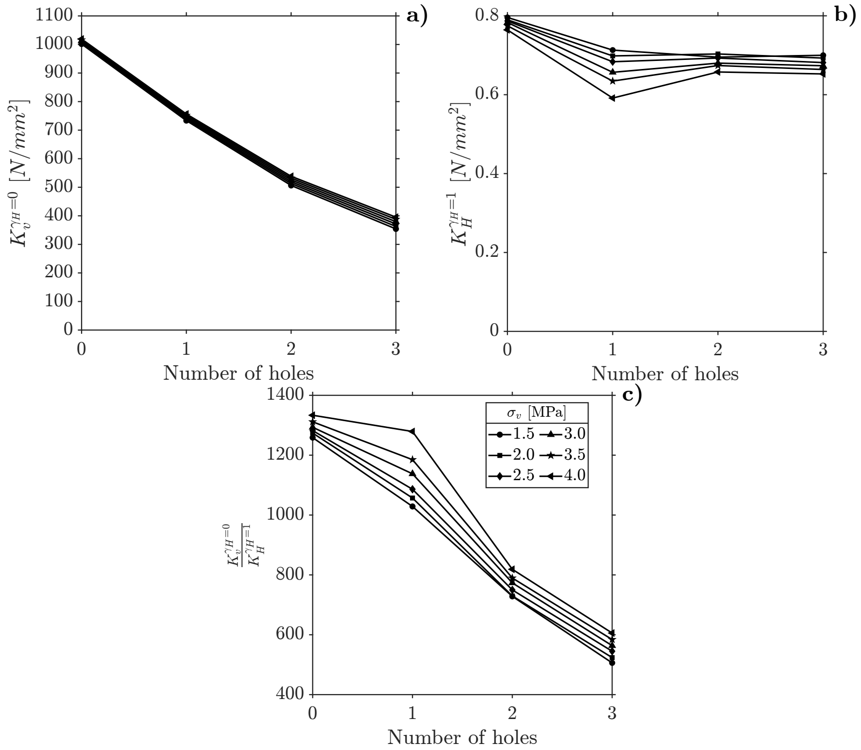

Figure 7.5: Stiffness of the 4 configurations: (a) Vertical stiffness under pure compression, (b) Horizontal stiffness at γ_H = 100%, (c) Ratio of vertical and horizontal stiffness.

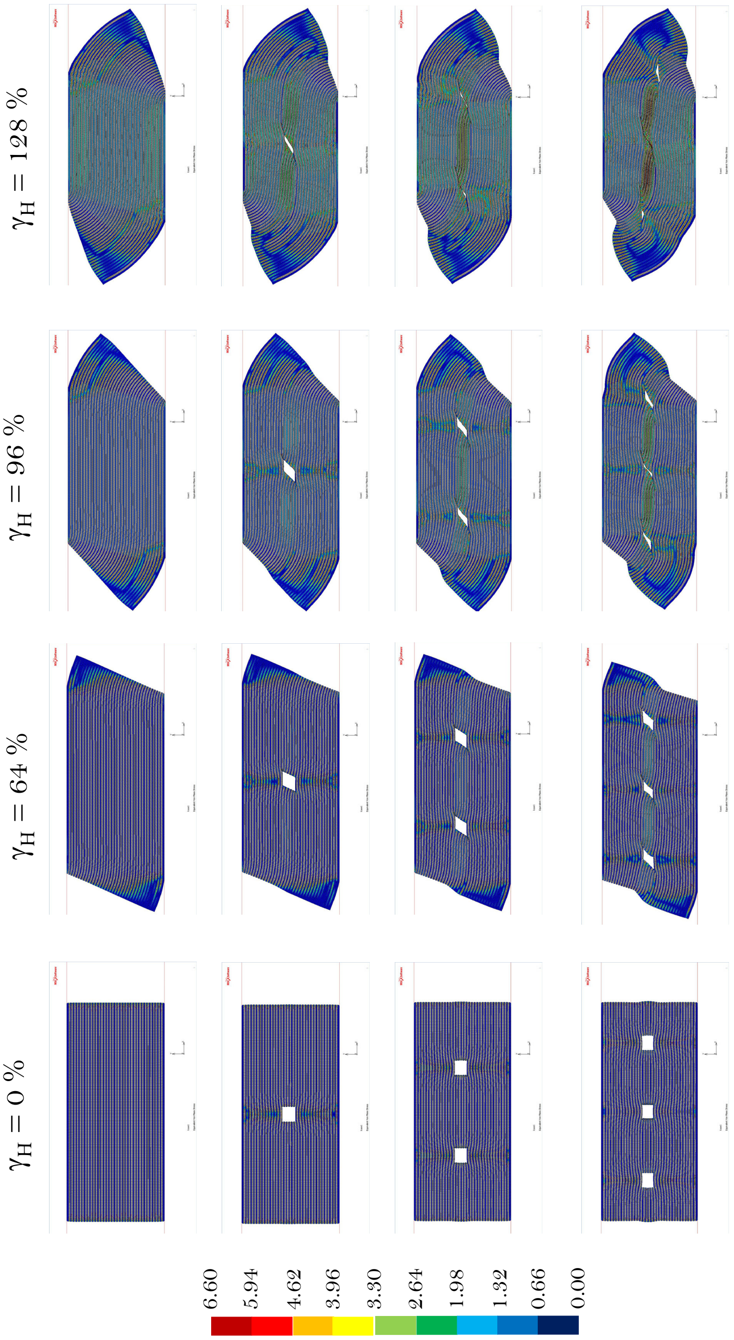

Figure 7.6: Deformation patters of the 4 configurations of FREIs: equivalent Von Mises stresses.

Table 7.1: Description of the tested samples.

N. test [-]	Modifies [-]	$2a$ [mm]	$2b$ [mm]	A [mm^2]	H [mm]	V [mm^3]	n. holes [-]	Ø holes [mm]	V_{holes} [mm^3]	V_{holes}/V [%]	Name [-]	F_v [kN]	σ_v [MPa]
1	Unmodified	130	60	7800	52	405600	0	6	0	0.00%	130x60 U	18.8	2.41
2	4 holes Ø6	130	60	7800	52	405600	4	6	67856	1.67%	130x60 4H		2.41
3	12 holes Ø6	130	60	7800	52	405600	12	6	20357	5.02%	130x60 12H		2.41
4	20 holes Ø6	130	60	7800	52	405600	2	6	33929	8.37%	130x60 20H		2.41
5	12 holes Ø6	130	60	7800	52	405600	12	6	20357	5.02%	130x60 12H		2.41
6	12 holes Ø6	110	60	6600	52	343200	12	6	20357	5.93%	110x60 12H		2.85
7	12 holes Ø6	90	60	5400	52	280800	12	6	20357	7.25%	90x60 12H		3.48
8	12 holes Ø6	70	60	4200	52	218400	12	6	20357	9.32%	70x60 12H		4.48

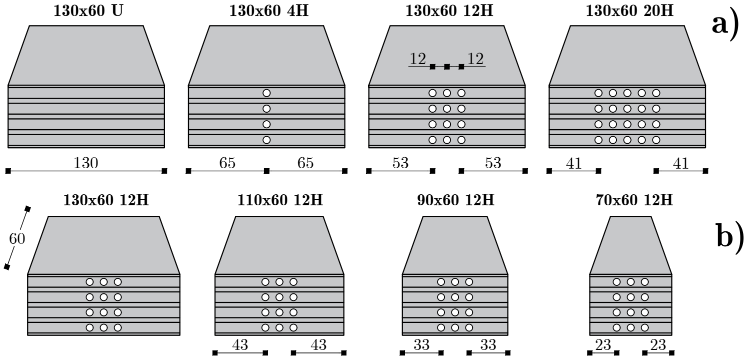

Figure 7.7: Schematic of the tested bearings: (a) FREIs with variable number of holes, (b) FREIs with variable base side $2a$.

made using a drill press while clamping the sample between two steel plates for alignment (**Figure 7.8 (a)**). A closer look to the holes pattern of a modified samples is shown in **Figure 7.8 (b)** for the bearing *130x60 12H*.

7.3.2 Description of the experimental tests

The shear tests were performed at the Department of Industrial Engineering of the University of Naples Federico II using the test frame already shown in **Figure 4.8 (a)**.

Each bearings were tested in unbonded configuration, using the same quasi-static lateral displacement protocol seen in **Section 4.4.3**, **Figure 4.8 (b)**. A strain rate of 1%/s up to a deformation $\gamma_H^{max} = 100\%$ was thus imposed to each FREI.

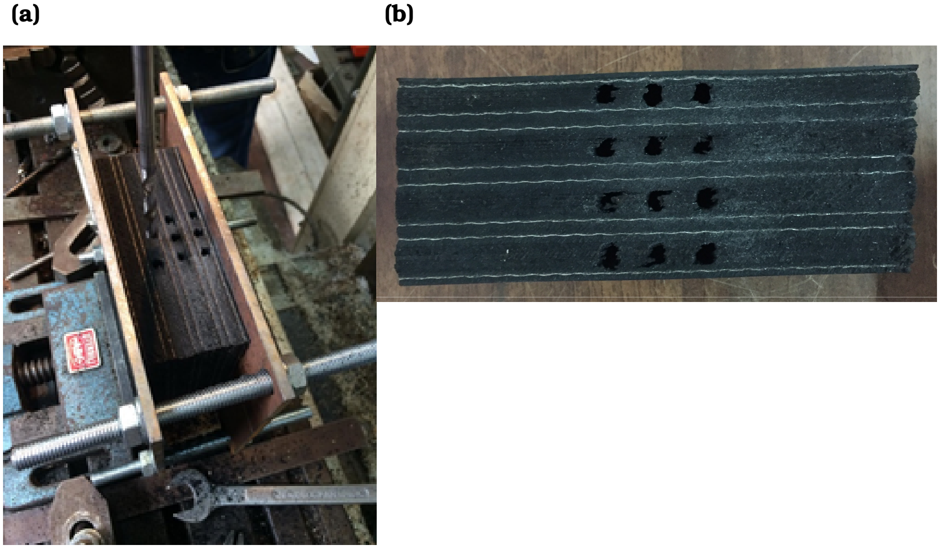

Figure 7.8: FREI's modification: (a) drill press for the holes pattern, (b) *130x60 12H* sample.

A constant vertical load of 18.8 kN was applied on the bearings, resulting in a nominal axial pressure (i.e., the ratio of the applied vertical force to the gross area $2a$ x $2b$) varying from 2.41 MPa for *130x60 U* to 4.48 MPa for *70x60 12H* (see **Table 7.1**).

An horizontal displacement was imposed on the bearings in the direction orthogonal to the holes, i.e. along the side $2a$ (**Figure 7.9**). This means that the secondary shape factor of the bearings is defined as $S_2 = 2a/t_r$.

7.3.3 Experimental test results: 1st type of modification

For the first set of experimental tests (i.e. test #1 to #4 of **Table 7.1**), bearings with the same geometry and a variable number of holes from 0 (control bearing *130x60 U*) to 20 (*130x60 20H*) were tested. The secondary shape factor for such bearings is $S_2 = 2.6$.

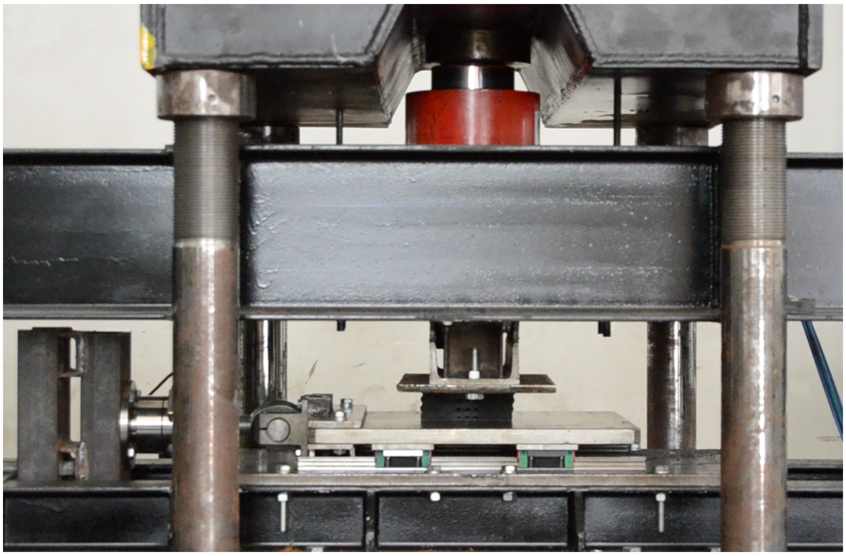

Figure 7.9: Holed U-FREI under test.

Figure 7.10 shows the deformed shape of the bearings during testing, with each column depicting different steps:

- Column 1 - full vertical load and zero lateral displacement;
- Column 2 - full vertical load and a shear deformation of 50%;
- Column 3 - full vertical load and shear deformation of 100%.

The four rows of **Figure 7.10** (a-d) show the first four bearings described in **Table 7.1** (i.e. row a: no modification, row d: 20 holes). As intuition suggests, larger vertical deformation corresponds to a larger number of holes. Nevertheless, the deformation is still negligible because of the very low volume of the rubber removed by drilling. All of the samples show the onset of a stable roll-over deformation well before $\gamma_H = 50\%$.

Figure 7.11 shows the horizontal force-displacement curves obtained from this first set of the experimental tests. The most noticeable effect of the holes is the reduction of the peak horizontal load in the force displacement response. Consequently, the secant lateral stiffness at peak horizontal load is reduced, as shown in **Table 7.2**.

As clear from **Figure 7.11**, sample *130x60 U* (solid line) shows an almost linear initial response with large horizontal stiffness. As the displacement increases past the initial deformation, the bearing shows softening and a peak of the response for a lateral deformation of 45 mm ($\gamma_{H,cr} \approx 86\%$). A similar result is obtained for the sample with one column of holes (*130x60 4H*, dashed line). The curve differs very little from the one of the unmodified *130x60 U*, which is not surprising considering the low percentage of removed volume (1.67%, see **Table 7.1**). For *130x60 4H*, the lateral secant stiffness differs less than 7% from that of the unmodified sample (**Table 7.2**). This bearing, compared to the bearing with no holes, shows a modest increase of the stability range.

Increasing the number of holes, the lateral response of the sample changes significantly. For the bearings *130x60 12H* (dotted line) and *130x60 20H* (dashed-dotted line) there is no local maximum of the lateral force response, and these bearings show a stable response up to $\gamma_H = 100\%$. Compared to the unmodified sample, for the bearings with 12 and 20 holes, the lateral stiffness is largely reduced. In general, the reduction of stiffness is approximately proportional to the volume of removed rubber from the sample (**Table 7.2**).

Figure 7.12 shows the trend of tangent lateral stiffness of the tested bearings. As expected, the stiffness always decreases with an increasing lateral displacement. The graph clearly shows how the stiffness of the *130x60 U* (**Figure 7.12 (a)**) and that of *130x60 4H* (**Figure 7.12 (b)**) become equal to zero around a shear deformation of 90% and the overall response is unstable.

The stability range matches what was previously found for medium/soft compound square and rectangular bearings (see **Chapters 5** and **6**). Samples *130x60 12H* (**Figure 7.12 (c)**) and *130x60 20H* (**Figure 7.12 (d)**) however, show a positive tangent lateral stiffness throughout the entire range of imposed deformation.

What these results show is that an unstable bearing can be

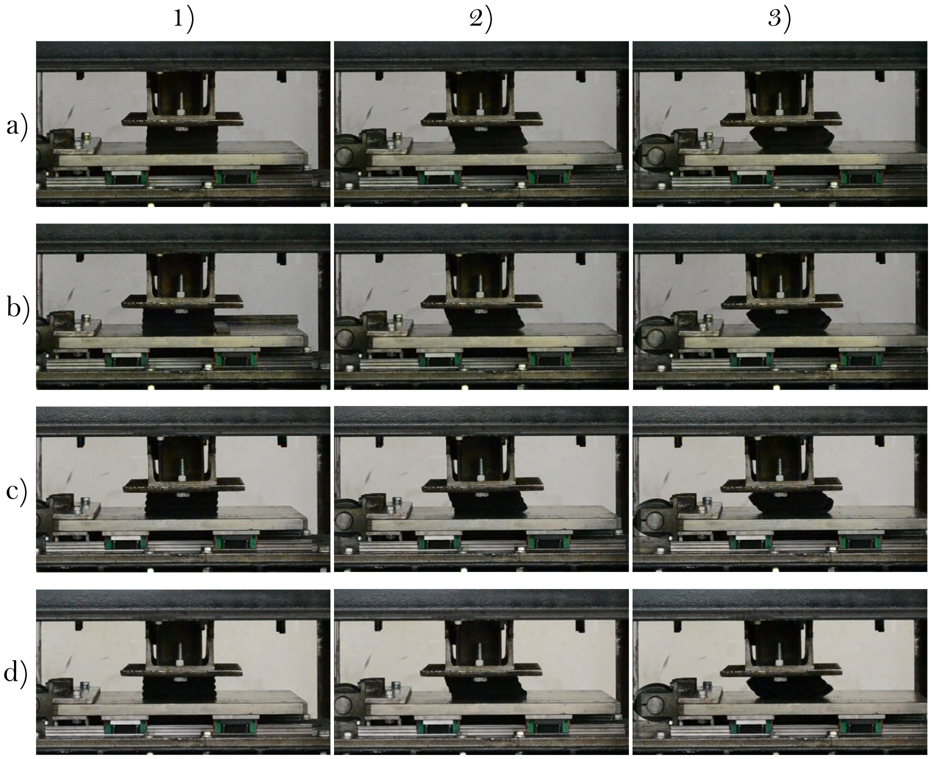

Figure 7.10: Tested samples at 1) $\gamma_H = 0\%$ with full compression, 2) $\gamma_H = 50\%$ and 3) $\gamma_H = 100\%$; a) *130x60 U*, b) *130x60 4H*, c) *130x60 12H*, d) 130x60 20H.

Table 7.2: Horizontal secant stiffness at different imposed deformations, for bearings with variable number of holes

δ_H	*130x60 U*	*130x60 4H*		*130x60 12H*		*130x60 20H*	
	K_H	K_H	$1-\%K_H^{130x60\ U}$	K_H	$1-\%K_H^{130x60\ U}$	K_H	$1-\%K_H^{130x60\ U}$
[mm]	[N/mm]	[N/mm]	[%]	[N/mm]	[%]	[N/mm]	[%]
5.0	192	181	5.5%	156	18.5%	119	38.1%
10	157	149	4.8%	123	21.5%	85.6	45.3%
15	134	126	6.1%	103	23.5%	75.1	44.2%
20	121	113	6.3%	87.8	27.3%	67.1	44.4%
25	110	103	6.8%	79.9	27.7%	58.0	47.5%
30	101	94.7	6.5%	72.0	28.9%	53.4	47.3%
35	93.7	87.3	6.9%	66.3	29.2%	50.7	45.9%
40	87.3	82.3	5.7%	62.8	28.1%	48.4	44.6%
45	80.2	77.4	3.5%	60.0	25.2%	46.6	41.9%
50	71.7	69.4	3.1%	58.5	18.3%	44.1	38.5%

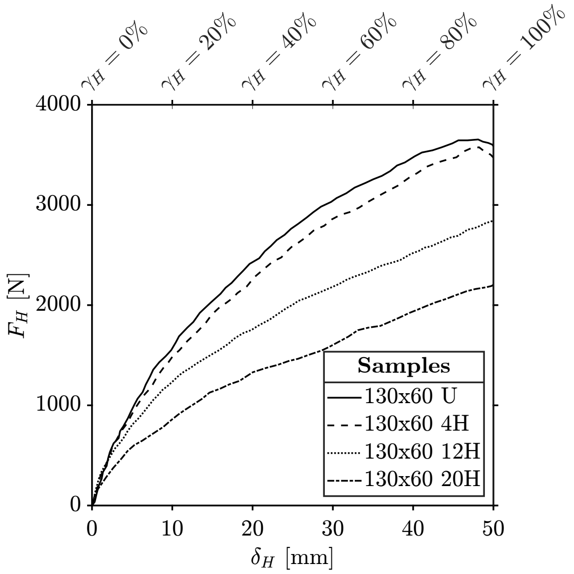

Figure 7.11: Horizontal force displacement response curve of samples with variable number of holes.

modified, by drilling horizontal holes, to achieve a stable response in the range of shear strain of interest. From these tests it was found that if the volume of removed rubber is less than 5% of the volume of the bearing, the modification of the response is negligible (**Figure 7.12 (b)**).

Figure 7.12 also shows how, for small imposed displacements, the tangent stiffness of the bearings is not modified by the holes (see **Figures 7.12 (c)** and **7.12 (d)**), with the effects of the modification becoming apparent for shear strain larger than 10%.

7.3.4 Experimental test results: 2nd type of modification

The second set of experimental tests (i.e. test #5 to #8 in **Table 7.1**) was performed on bearings with a total of 12 holes (3 columns of 4 holes) and a variable geometry. Different base dimensions, $2a$, in the direction of the horizontal displacement were tested (from 70 to 130 mm) to study the influence of the same modification on rectangular bearings with different base/depth ratios.

Modifying the base of the bearings, the secondary shape factor decreases from 2.6 (*130x60 12H*) to 2.2 (*110x60 12H*), 1.8 (*90x60 12H*) and 1.4 (*70x60 12H*). The percentage of removed volume is always greater than 5%, reaching a maximum of 9.32% (**Table 7.1**).

Figure 7.13 shows the bearings under test in the three load conditions described in **Section 7.3.3**: 1. pure compression, 2. $\gamma_H = 50\%$ and 3. $\gamma_H = 100\%$. This figure shows how these bearings exhibit a large lateral bulging (column 1, pure compression) as the base of the device decreases. The same figure shows how the rollover of the bearing changes as the base of the bearing and the loaded area decrease. For $\gamma_H = 50\%$, *130x60 12H* bearing shows a rollover deformation; while bearings *90x60 12H* and *70x60 12H* do not detach from the horizontal supports.

Figure 7.14 shows the lateral force-displacement curves of the bearings from which it is clear how a reduction of the base of the bearing causes a noticeable reduction of the peak lateral force (see **Table 7.3**). Based on findings from **Section 5.3.2.1**, an unstable

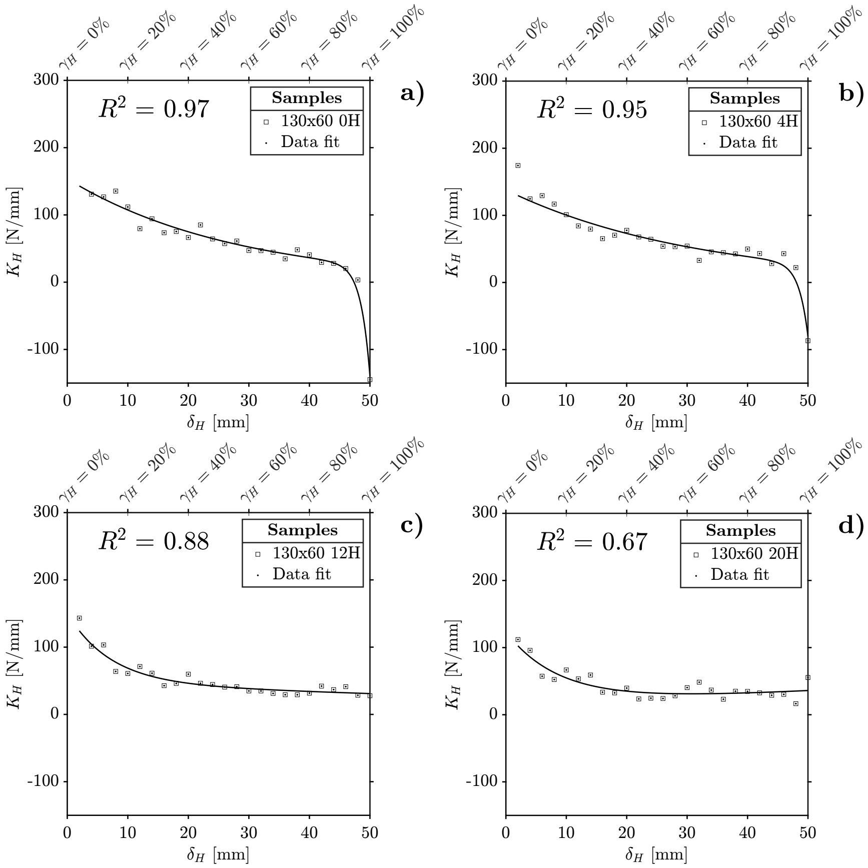

Figure 7.12: Tangent horizontal stiffness vs imposed displacement for bearings with variable number of holes: (a) *130x60 U*, (b) *130x60 4H*, (c) *130x60 12H*, (d) *130x60 20H*.

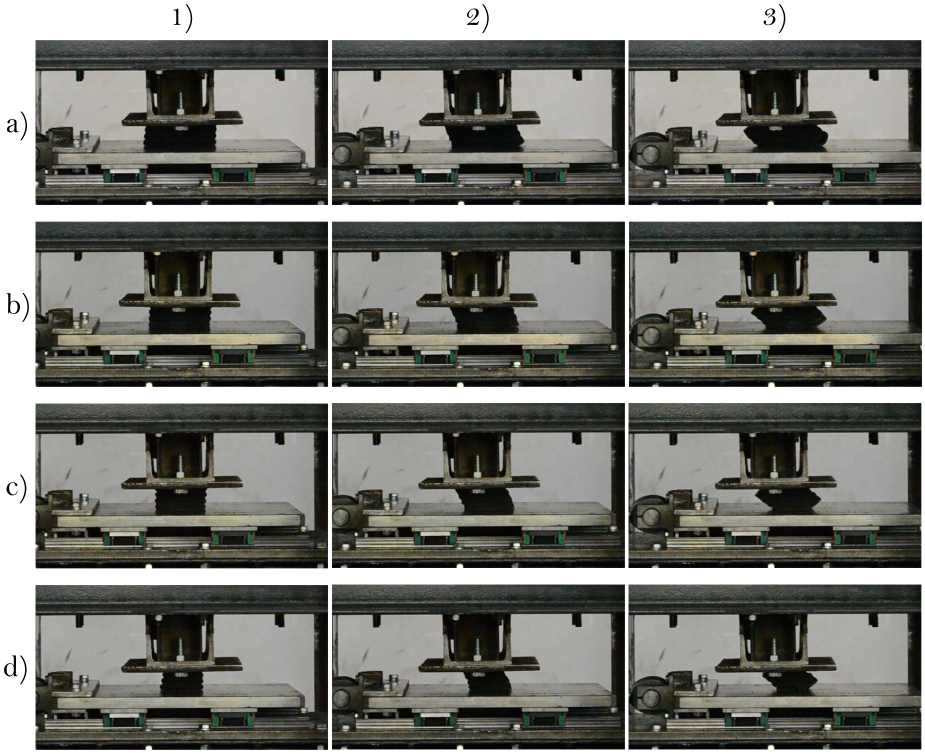

Figure 7.13: Tested samples at 1) $\gamma_H = 0\%$ with full compression, 2) $\gamma_H = 50\%$ and 3) $\gamma_H = 100\%$; a) *130x60 12*, b) *110x60 12H*, c) *90x60 12H*, d) 70x60 12H.

Table 7.3: Horizontal secant stiffness at different imposed deformations, for bearings with variable base side $2a$

δ_H	*130x60 12*	*110x60 12H*		*90x60 12H*		*70x60 12H*	
	K_H	K_H	$1 - \%K_H^{130x60\ 12H}$	K_H	$1 - \%K_H^{130x60\ 12H}$	K_H	$1 - \%K_H^{130x60\ 12H}$
5.0	156	119	24.0%	88.4	43.5%	51.0	67.4%
10	123	82.0	33.3%	57.2	53.5%	30.2	75.5%
15	103	64.9	36.8%	43.2	58.0%	21.1	79.5%
20	87.8	55.2	37.1%	36.6	58.3%	19.0	78.3%
25	79.9	49.4	38.2%	34.0	57.4%	18.4	77.0%
30	72.0	43.9	39.0%	33.0	54.2%	16.9	76.5%
35	66.3	40.5	38.9%	32.7	50.7%	16.0	75.9%
40	62.8	38.6	38.6%	33.2	47.2%	15.2	75.8%
45	60.0	38.5	35.8%	33.0	45.0%	14.2	76.4%
50	58.5	39.4	32.7%	31.8	45.8%	13.4	77.1%

response is expected for bearings with no holes, especially for those with a secondary shape factor lower than 2.0. Because of the horizontal holes, as depicted in **Figure 7.14**, none of the bearings shows a peak in the lateral response curve, remaining stable for the entire range of imposed deformations.

Figure 7.15 shows the trends of lateral tangent stiffness of the bearings against imposed displacement. It is worth mentioning that the tangent stiffness of the *70x60 12H* bearing (**Figure 7.15 (d)**) is quite low at large lateral displacements due to a secondary shape factor $S_2^{70x60} = 1.4$.

This states that the improvement in the lateral response of the bearing with horizontal holes is a function of both the percentage of removed volume and the secondary shape factor of the device. From **Figures 7.12** and **7.15** it is clear that the most significant improvement in the response of the bearing is obtained for a removed volume of around 5%, while negligible modifications to the lateral response of the device are obtained if the removed volume is less than 2% or more than 9% of the volume of the device.

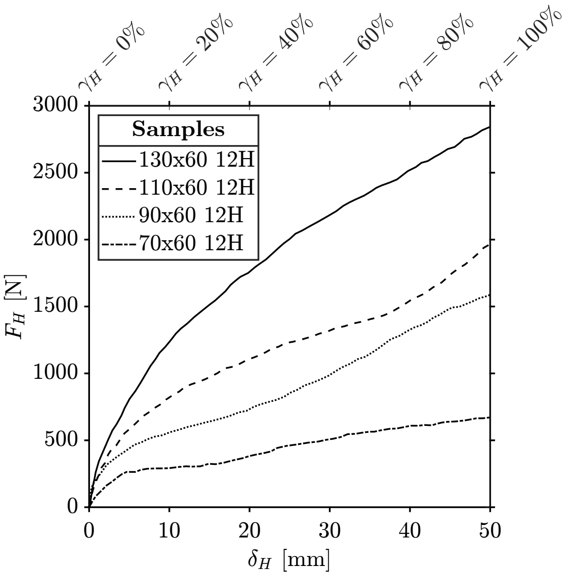

Figure 7.14: Horizontal force displacement response curve of samples with variable base side $2a$.

7.4 Experimental tests - Finite Element Analysis comparison

This section shows the results of finite element analysis on the FREIs' samples seen in **Sections 7.3.3** and **7.3.4**. The experimental-numerical comparison is intended to confirm the effectiveness of the proposed changes and to deepen the details of the response of the modified FREIs.

7.4.1 FEAs specifications

3D FEAs were performed using MSC.Marc, using the same procedure described in **Section 3.1** for material's modeling and load condition. Details of all the parameters used for the materials modeling in FEAs are defined in **Table 7.4**, where C_1 has been set as per specification considering how this constant is equal to

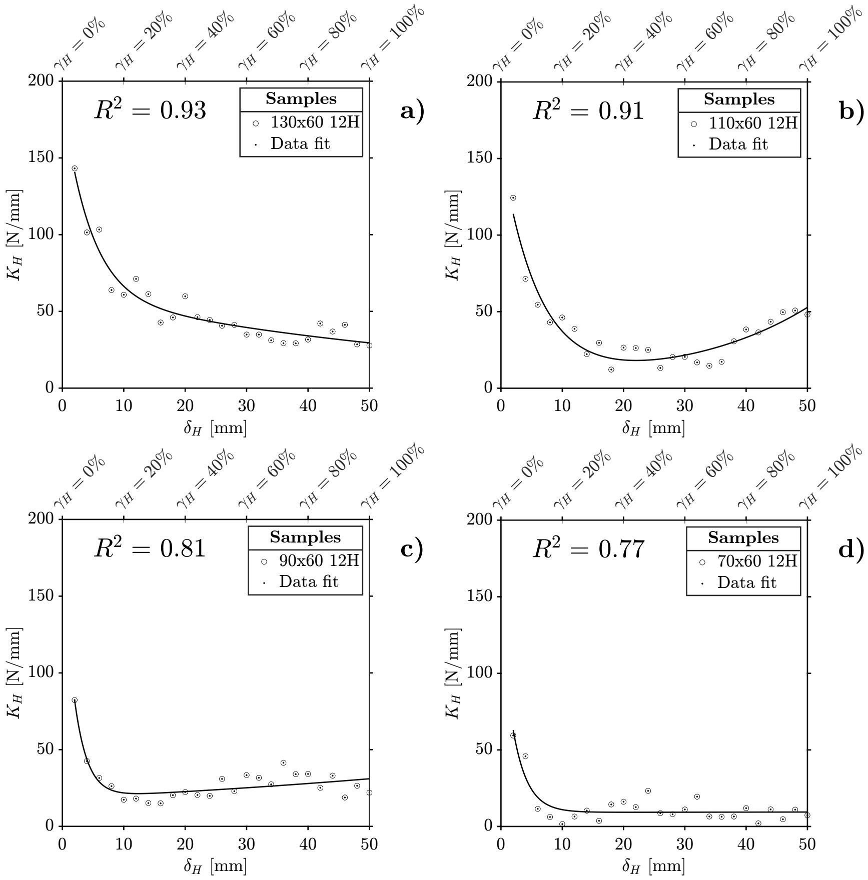

Figure 7.15: Tangent horizontal stiffness vs imposed displacement for bearings with variable base side $2a$: (a) *130x60 12H*, (b) *110x60 12H*, (c) *90x60 12H*, (d) *70x60 12H*.

Table 7.4: Parameters of the FEMs on modified FREIs.

C_1 [MPa]	K [MPa]	E_f [MPa]	ν_f [-]	t_f [mm]
0.750	2000	70000	0.1	1

half of the initial shear modulus of the rubber (i.e. shear modulus at a maximum threshold of shear strain equal to 25%, see **Section 3.1.2.1**).

The elasomeric layers were modeled using a three-dimentional, isoparametric, 4+1-node, low-order, tetrahedron element (element 157 in Marc [128]). Each element presents an additional pressure degree of freedom at each of the four corner nodes (**Figure 7.16 (a)**).

This element is written for incompressible or nearly incompressible three-dimensional applications. The shape function for the center node is a bubble function. Therefore, the displacements and the coordinates for the element are linearly distributed along the element boundaries. The stiffness of this element is formed using four Gaussian integration points. The degrees of freedom of the center node are condensed out on the element level before the assembly of the global matrix.

Figure 7.16 (b) shows a view of a 3D FEM used for FEAs of holed FREIs.

7.4.2 FEAs results: 1st type of modification

Figure 7.17 (a) shows the horizontal force-displacement curves obtained from FEAs. In general, a good agreement was found between numerical and experimental results (see **Figure 7.17 (b)**). From **Tables 7.2** and **7.5** it is evident that experimental tests and FEAs give the same values of horizontal stiffness for all of the tested bearings. Compared to the unmodified bearing, for bearings with 4, 12 and 20 holes, FEAs show an average reduction in secant horizontal stiffness of 6.2%, 26% and 47% respectively. From experimental results, with respect to the unmodified bearing (*130x60 U*), the reductions of stiffness were found to be 5.5%, 25%

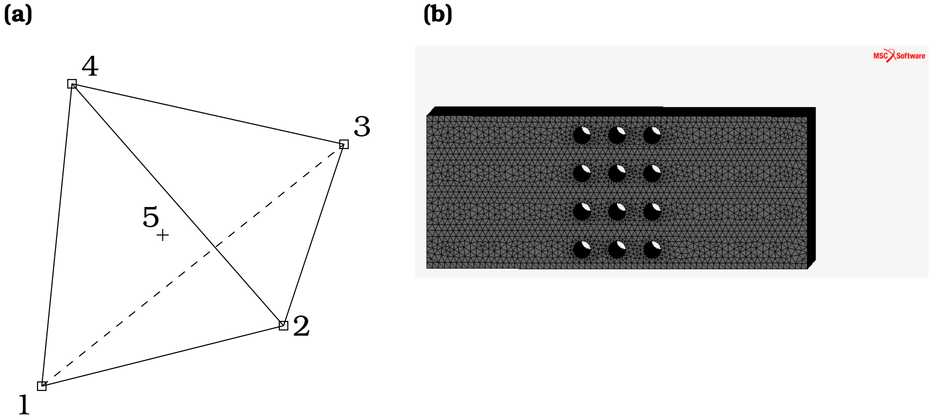

Figure 7.16: FEAs modeling of holed FREIs: (a) 4+1-node tetrahedron element, (b) FEMs of *130x60 12H* FREI.

and 44% for bearings *130x60 4H*, *130x60 12H* and *130x60 20H* respectively (refer to **Table 7.2**).

If compared to the control bearing *130x60 U*, bearings *130x60 12H* and *130x60 20H* show a clear improvement of the stable range (see **Figure 7.17 (a)**). **Figure 7.18** confirms that the lateral tangent stiffness of bearings with 12 (**Figure 7.18 (c)**) and 20 holes (**Figure 7.18 (d)**) remain positive, while bearings *130x60 U* (**Figure 7.18 (a)**) and *130x60 4H* (**Figure 7.18 (b)**) show a softening response starting from $\gamma_H = 90\%$.

7.4.3 FEAs results: 2nd type of modification

Figure 7.19 (a) shows the force-displacement curves obtained from the numerical analysis for bearings with 12 holes and base side $2a$ varying from 130 to 70 mm. In **Figure 7.19 (b)** the same curves are plotted against the corresponding experimental ones for a direct comparison. A very good agreement was found between numerical and experimental values (see **Table 7.6**).

When compared to sample *130x60 12H*, bearings *110x60 12H*, *90x60 12H* and *70x60 12H* show an average reduction of the secant stiffness of 42%, 57% and 79% respectively. For the same bearings,

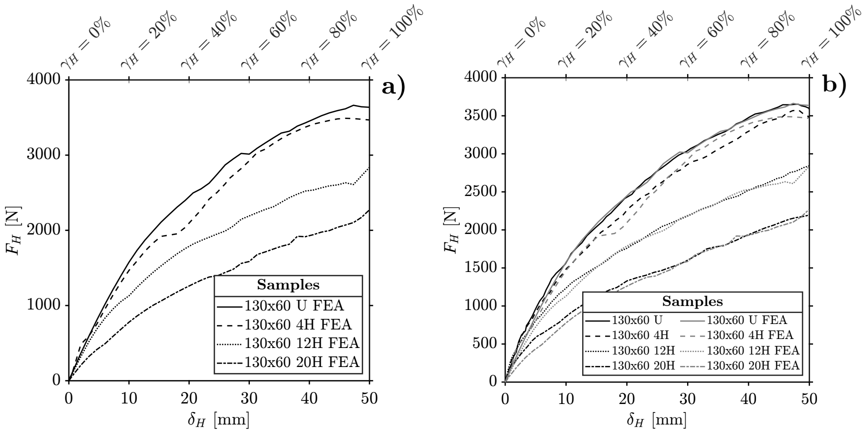

Figure 7.17: Horizontal force displacement response curve of samples with variable number of holes: (a) FEAs, (b) Experimental vs FEAs.

Table 7.5: Lateral secant stiffness at different imposed displacements for FREIs with variable number of holes (FEA).

δ_H	*130x60 12H*	110x60 12H		90x60 12H		70x60 12H	
	K_H	K_H	$1-\%K_H^{130x60\ U}$	K_H	$1-\%K_H^{130x60\ U}$	K_H	$1-\%K_H^{130x60\ U}$
5.0	171	160	6.5%	143	16.5%	85.4	50.1%
10	157	146	7.2%	116	26.4%	77.5	50.7%
15	140	128	8.5%	101	27.6%	70.4	49.7%
20	122	105	14.4%	89.4	27.0%	63.0	48.5%
25	111	101	8.8%	77.8	29.8%	56.0	49.5%
30	102	97.7	4.3%	73.1	28.4%	54.0	47.1%
35	94.1	91.9	2.3%	67.6	28.2%	51.0	45.8%
40	86.3	84.8	1.7%	63.2	26.7%	48.2	44.1%
45	79.5	76.9	3.3%	57.8	27.3%	45.3	43.0%
50	72.7	69.4	4.6%	56.8	21.9%	45.5	37.5%

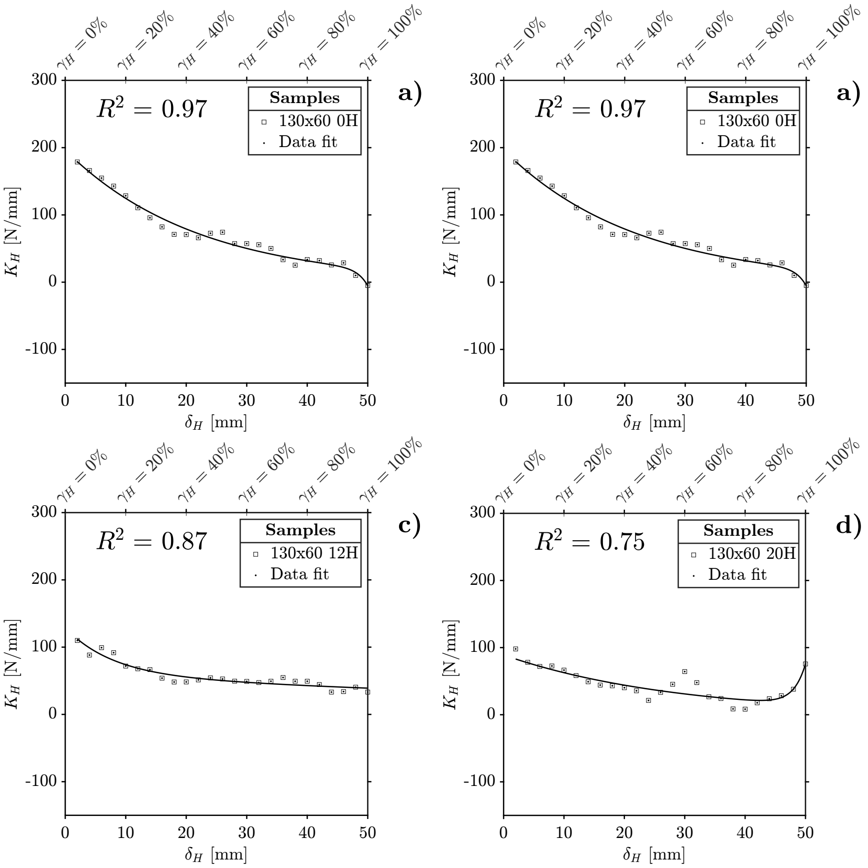

Figure 7.18: Tangent horizontal stiffness vs imposed displacement for bearings with variable number of holes (FEAs): (a) *130x60 U*, (b) *130x60 4H*, (c) *130x60 12H*, (d) *130x60 20H*.

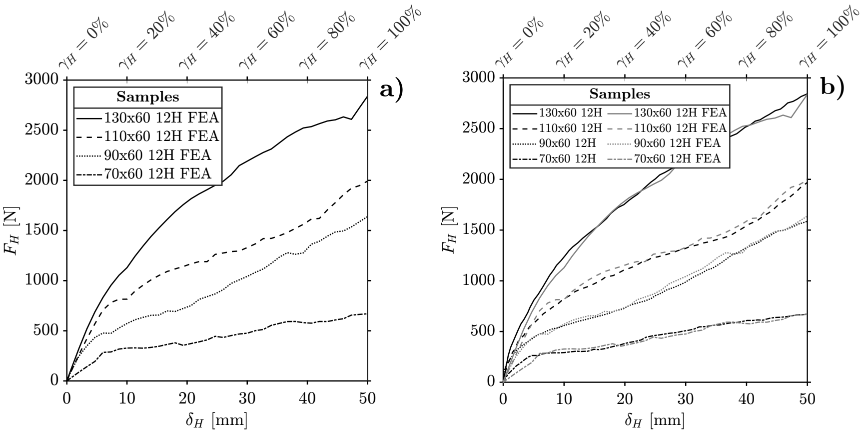

Figure 7.19: Horizontal force displacement response curve of samples with variable base side $2a$: (a) FEAs, (b) Experimental vs FEAs.

experimental tests showed a reduction of 35%, 51% and 76% (refer to **Table 7.3**).

Figure 7.20 shows the trends of tangent lateral stiffness of bearings with different base dimensions. Numerical analyses confirm the effectiveness of the proposed modification. The best hardening at large displacements is obtained for the *110x60 12H* bearing (**Figure 7.20 (b)**), corresponding to a removed volume of 6%. For the *70x60 12H* bearing (**Figure 7.20 (d)**) the stiffness tends to become constant at large displacements. This is in agreement with the experimental findings (**Figure 7.15 (d)**).

7.4.4 FEAs results: stress distribution in the bearings

In order to provide an insight into local stress-strain behavior of perforated bearings, **Figures 7.21** and **7.22** show the Von Mises stress contours at three levels of lateral deformations (as done for the experimental tests). For each specimen:

- Column 1 corresponds to the full application of the axial load without any imposed lateral deformation;

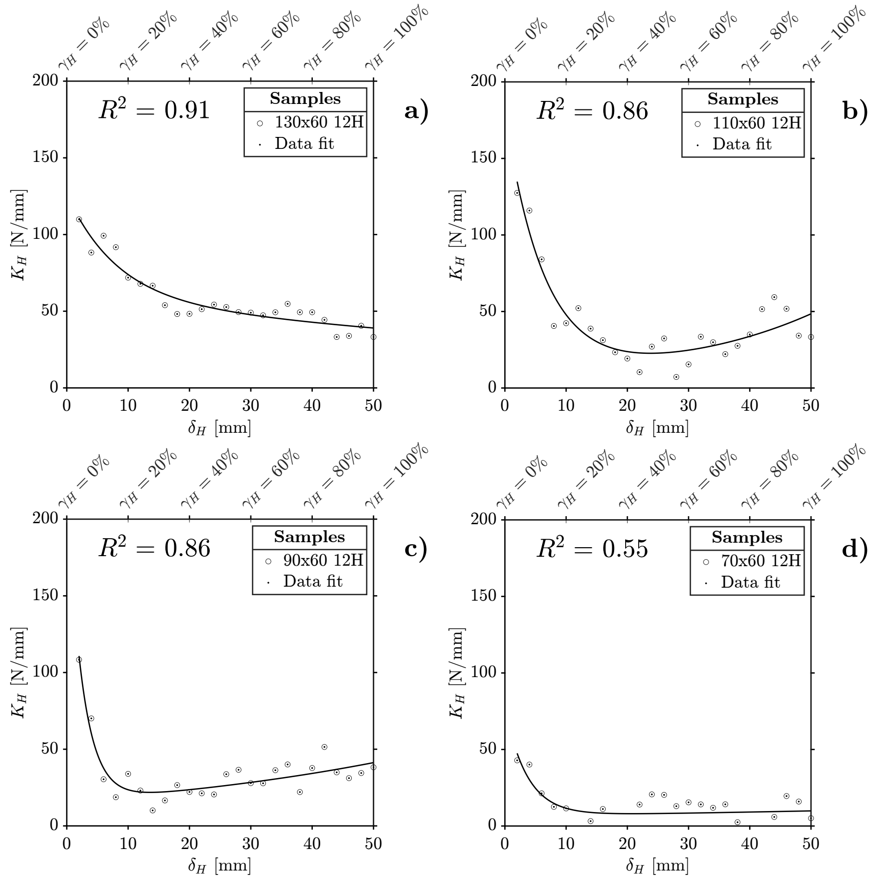

Figure 7.20: Tangent horizontal stiffness vs imposed displacement for bearings with variable base side $2a$ (FEAs): (a) *130x60 12H*, (b) *110x60 12H*, (c) *90x60 12H*, (d) *70x60 12H*.

Table 7.6: Horizontal secant stiffness at different imposed deformations, for bearings with variable base side $2a$ (FEA).

δ_H	*130x60 12*	110x60 12H		90x60 12H		70x60 12H	
	K_H	K_H	$1 - \%K_H^{130x60\ 12H}$	K_H	$1 - \%K_H^{130x60\ 12H}$	K_H	$1 - \%K_H^{130x60\ 12H}$
5	143	120	16.0%	86.2	39.6%	41.1	71.2%
10	130	86.5	33.4%	57.3	55.8%	32.9	74.7%
15	118	70.3	40.6%	44.8	62.2%	23.2	80.4%
20	103	57.8	43.7%	36.9	64.1%	18.2	82.3%
25	94.6	50.1	47.0%	35.1	62.9%	17.4	81.7%
30	89.0	44.4	50.1%	34.8	60.9%	16.2	81.8%
35	83.5	41.4	50.5%	34.7	58.5%	16.3	80.5%
40	79.8	39.7	50.3%	33.0	58.7%	14.5	81.9%
45	74.0	40.1	45.8%	32.9	55.5%	13.6	81.7%
50	70.2	39.8	43.2%	32.8	53.3%	13.4	80.9%

- Column 2 corresponds to a shear deformation of 50%.
- Column 3 corresponds to a shear deformation of 100%.

Each row in **Figure 7.21** shows bearings with variable number of holes (row a: *130x60 U*, row d: *130x60 20H*), while the rows in **Figure 7.22** show bearings with variable geometry (row a: *130x60 12H*, row d: *70x60 12H*).

As clear from **Figures 7.21** and **7.22** (column 1) the holes modify the stress distribution in the device under pure compression, with the bearing becoming mostly unloaded in its central area, while an increase of stress is measured in the lateral regions of the device. For a shear strain of $\gamma_H = 50\%$, the holes begin to collapse under the imposed loads (column 2). At this stage, the central holes of the different bearings are completely collapsed, while the external ones are largely deformed. This is because, under a lateral deformation, due to the rollover of the device, the vertical pressure in the center of the bearing increases.

Under large lateral displacements, all of the holes of the bearing tend to collapse due to the imposed deformation. The friction generated at the edges of the collapsed voids is responsible for the hardening response of the bearing under large lateral displacements (see **Figure 7.14** *110x60 12H* and **Figure 7.22** column 3 row b). In bearings with a low secondary shape factor (i.e. $S_2^{70x40} = 1.4$,

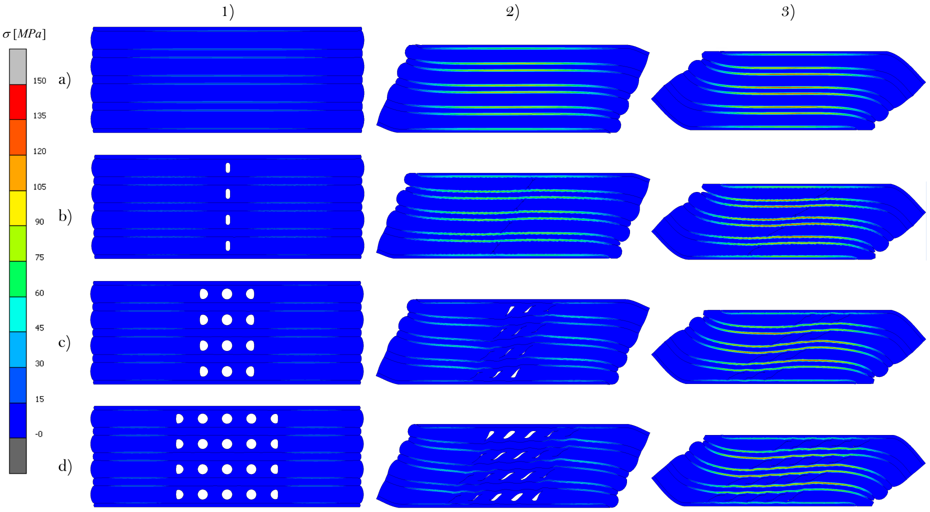

Figure 7.21: Equivalent Von Mises stresses: 1) $\gamma_H = 0\%$ with full compression, 2) $\gamma_H = 50\%$ and 3) $\gamma_H = 100\%$; a) *130x60 U*, b) *130x60 4H*, c) *130x60 12H*, d) *130x60 20H*.

Figure 7.22 column 3 row *d*, *70x60 12H*) the core of the device is significantly loaded is compression. In this case the holes close to the edge of the bearing fall within the area of the bearing that detaches from the top and bottom supports, which is stress free. For this reason, the deformation of these holes does not produce a hardening response.

The analysis of the stress distribution confirms that the position of the holes within a bearing is important and that the holes must be arranged in such a way that, when these are deformed, for the entire range of imposed displacement, the friction generated at the edges of the collapsed holes creates the desired hardening.

Based on FEAs results on *70x60 12H*, it appears that horizontal holes should be placed within the overlapping area of the bearing, i.e. the part of the device which is constantly loaded in compression during the roll-over deformation.

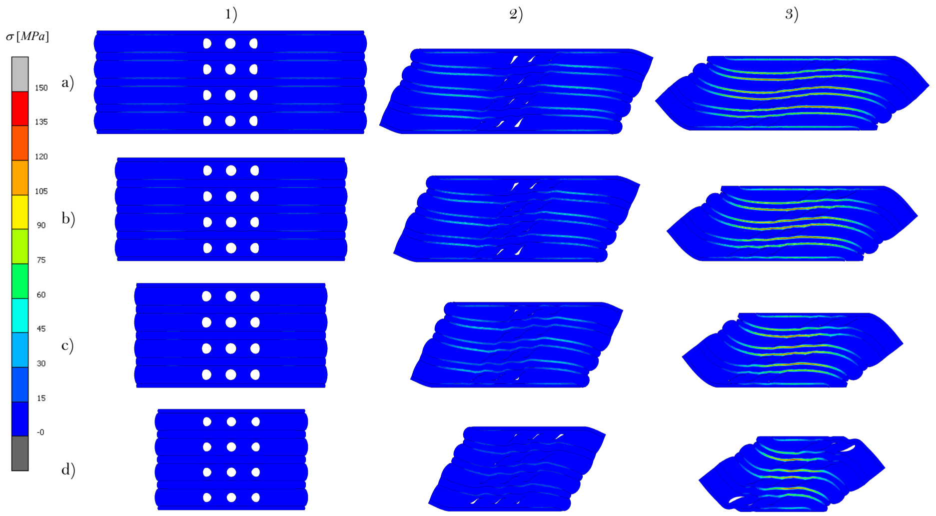

Figure 7.22: Equivalent Von Mises stresses: 1) $\gamma_H = 0\%$ with full compression, 2) $\gamma_H = 50\%$ and 3) $\gamma_H = 100\%$; a) *130x60 12H*, b) *110x60 12H*, c) *90x60 12H*, d) *70x60 12H*.

7.5 Parametric finite element analysis

7.5.1 Configurations

In **Section 7.4.4** it has been demonstrated how geometry of the holes within the elastomeric layers may significantly affect the lateral response of the modified U-FREI. The modification in the horizontal response (namely, a wider range of stable response and hardening) depends on several parameters including the size of the single hole, the clear distance between two adjacent holes, as well as mechanical parameters of the bearings (i.e. shear modulus of the rubber and vertical pressure).

In this section, a parametric finite element analysis (FEA) is conducted on the set of nominal base geometry showed in the previous section, i.e. *130x60*, *110x60*, *90x60* and *70x60* (mm x mm). For each of them, 18 different configurations of holes are considered by varying (**Figure 7.23**):

1. The total number of holes: from 2 to 12 total holes.
2. The size of each hole: two diameter values are used, $D_1 = 3$ mm and $D_2 = 7$ mm (i.e. small and large circular holes).
3. The disposition of the holes: smaller holes (i.e. $D_1 = 3$ mm) are placed within the thinner elastomeric layers, while larger holes (i.e. $D_2 = 7$ mm) are placed within the thickest rubber layers.
4. The distance between two adjacent holes: three clear distances between two adjacent holes are considered for each value of the diameter of the holes. For smaller holes $\varDelta_{11} = D_1$, $\varDelta_{11} = 2D_1$ and $\varDelta_{13} = 10D_1$ while for larger holes $\varDelta_{21} = D_2$, $\varDelta_{22} = 2D_2$ and $\varDelta_{32} = 5D_2$. For the modified U-FREI with nominal base geometry *70x60*, the distances $\varDelta_{13} = 10D_1$ and $\varDelta_{32} = 5D_2$ haven't been considered as they would exceed the base dimension of the bearing.

The first two variations, applied on bearings with variable geometry, result in several percentages of removed volume. As can be seen from **Table 7.7**, the percentage of removed rubber ranges from 0.21% to 12.7%.

With the second two configurations, the parametric finite element analysis aims to clarify the influence of the layout of the holes on the response of each modified U-FREI. To accounting also the mechanical properties involved, two values of the shear modulus, i.e. $G_e = 0.5$ MPa and $G_e = 1$ MPa, and two values of the vertical pressure, $\sigma_v = 2$ MPa and $\sigma_v = 4$ MPa, are considered for each configuration. **Table 7.8** summarizes the variable parameters of parametric finite element analysis. A combination of the parameters shown in this table, leads to a total of 264 FEMs.

7.5.2 Results

The stable/unstable response of each modified FREI is firstly monitored using the normalized response parameters maximum stable horizontal displacement and horizontal secant stiffness. The maximum stable horizontal displacement is defined in **Section 5.3.2.1**

Table 7.7: : Percentages of removed volumes for each FEMs.

$2a$ [mm]	$2b$ [mm]	t_r [mm]	V_r [mm^3]	n. holes [-]	D_{holes} [mm]	Dist. two holes [mm]	Name [-]	V_{holes} [mm^3]	V_{holes}/V_r [%]
130	60	52	405600	2	3	D, 2D, 10D	130x60 2H (D-2D-10D)	848	0.21%
				3	3	D, 2D, 10D	130x60 3H (D-2D-10D)	1272	0.31%
				4	7	D, 2D, 5D	130x60 4H (D-2D-5D)	9236	2.28%
				6	7	D, 2D, 5D	130x60 6H (D-2D-5D)	13854	3.42%
				9	3	D, 2D, 10D	130x60 9H (D-2D-10D)	3817	0.94%
				12	7	D, 2D, 5D	130x60 12H (D-2D-5D)	27709	6.83%
110	60	52	343200	2	3	D, 2D, 10D	110x60 2H (D-2D-10D)	848	0.25%
				3	3	D, 2D, 10D	110x60 3H (D-2D-10D)	1272	0.37%
				4	7	D, 2D, 5D	110x60 4H (D-2D-5D)	9236	2.69%
				6	7	D, 2D, 5D	110x60 6H (D-2D-5D)	13854	4.04%
				9	3	D, 2D, 10D	110x60 9H (D-2D-10D)	3817	1.11%
				12	7	D, 2D, 5D	110x60 12H (D-2D-5D)	27709	8.07%
90	60	52	280800	2	3	D, 2D, 10D	90x60 2H (D-2D-10D)	848	0.30%
				3	3	D, 2D, 10D	90x60 3H (D-2D-10D)	1272	0.45%
				4	7	D, 2D, 5D	90x60 4H (D-2D-5D)	9236	3.29%
				6	7	D, 2D, 5D	90x60 6H (D-2D-5D)	13854	4.93%
				9	3	D, 2D, 10D	90x60 9H (D-2D-10D)	3817	1.36%
				12	7	D, 2D, 5D	90x60 12H (D-2D-5D)	27709	9.87%
70	60	52	218400	2	3	D, 2D	70x60 2H (D-2D)	848	0.39%
				3	3	D, 2D	70x60 3H (D-2D)	1272	0.58%
				4	7	D, 2D	70x60 4H (D-2D)	9236	4.23%
				6	7	D, 2D	70x60 6H (D-2D)	13854	6.34%
				9	3	D, 2D	70x60 9H (D-2D)	3817	1.75%
				12	7	D, 2D	70x60 12H (D-2D)	27709	12.7%

Table 7.8: Set of FEMs: parametric finite element analysis of holed U-FREIs.

Bearing [-]	n. holes [-]	Diameter of the holes [mm]	Dist holes [mm]	G_e [MPa]	σ_v [MPa]
130x60, 110x60, 90x60	2	3	D_1	0.5	2
	3	7	$2D_1$	1.0	4
	4		$10D_1$		
	6		D_2		
	9		$2D_2$		
	12		$5D_2$		
70x60	2	3	D_1	0.5	2
	3	7	$2D_1$	1.0	4
	4		D_2		
	6		$2D_2$		
	9				
	12				

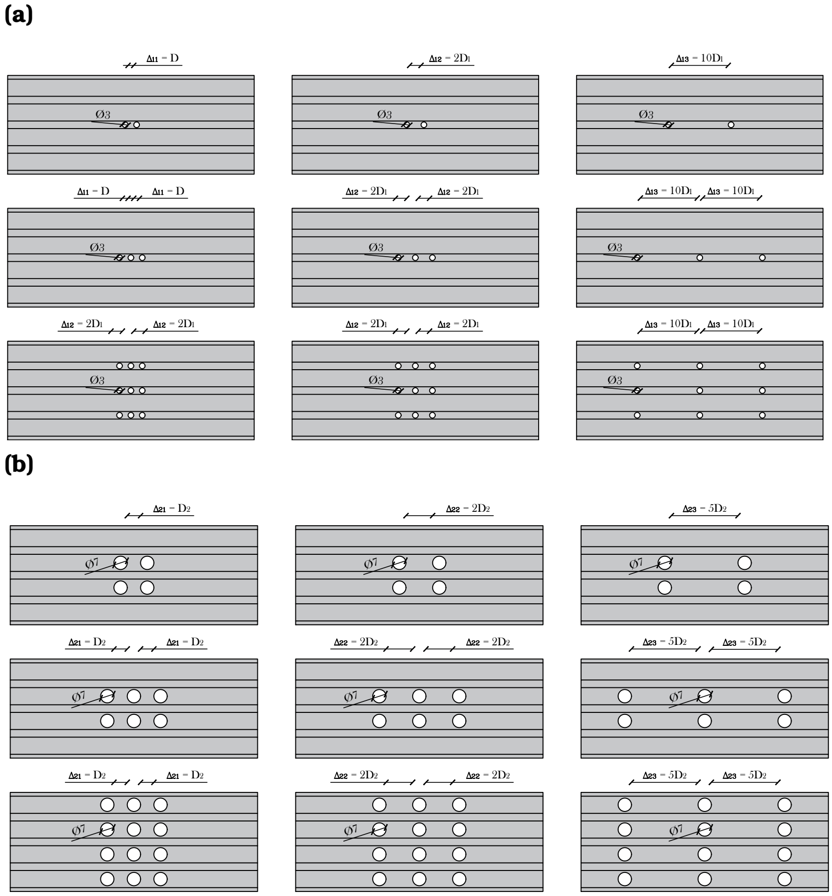

Figure 7.23: Schematic of the different configurations used in the parametric finite element analysis: (a) D_{holes} = 3 mm, (b) D_{holes} = 7 mm

as the minimum between the maximum and the ultimate displacement. These parameters have been obtained for each modified U-FREI ($\delta_{H,cr}^{mod}$ and K_H^{mod}) and compared with the corresponding maximum stable displacement and secant stiffness of the unmodified bearing of the set ($\delta_{H,cr}^{U}$ and K_H^U).

In **Figure 7.24** the ratios $\delta_{H,cr}^{mod}/\delta_{H,cr}^{U}$ (in percentage) are plotted with respect to each configuration of holes applied to bearing *70x60* (**7.24 (a)** to **7.24 (d)**), *90x60* (**7.24 (e)** to **7.24 (h)**), *110x60* (**7.24 (i)** to **7.24 (l)**) and *130x60* (**7.24 (m)** to **7.24 (p)**). In these column charts, black bins indicated a reduction of the stability range of the considered configuration against the unmodified bearing, while grey bins quantify the increasing percentage of the maximum stable horizontal displacement achieved with the same modification.

From these graphs the following information can be deduced:

i reduction of 100% of the stability range are related to modified bearings which experience buckling (i.e. instability under pure compression). The combination of shear modulus and removed volume of rubber (i.e. decreasing of the vertical capacity of the single bearing) makes the bearing buckles under the applied vertical load. This phenomenon mostly occurs for lower values of the shear modulus (**Figures 7.24 (a)**, **7.24 (f)**, **7.24 (i)**, **7.24 (j)** and **7.24 (n)**) or larger vertical pressure (**Figures 7.24 (d)**, **7.24 (h)** and **7.24 (l)**) and is related to the size of the holes (only for $D = 7$ mm) and to the clear distance between two adjacent holes (it occurs mostly for $\Delta = D$ and $\Delta = 2D$, see for example **Figures 7.24 (a)**, **7.24 (d)**, **7.24 (e)** and **7.24 (f)**).

ii some configurations of holes appear to not to change the stability range of the bearings, and the maximum stable horizontal displacement remains the same after the modification (see **Figures 7.24 (b)** and **7.24 (g)**).

iii a proper combination of size and positioning of the holes, with suitable shear modulus and vertical pressure, can improve the U-FREI response. An extension of the stability range by at least 50% is obtained due to the holes in several cases (see **Figures 7.24 (h)**, **7.24 (k)**, **7.24 (m)**, **7.24 (o)** and **7.24 (p)**).

Buckling under vertical load is mainly controlled by the clear distance between two adjacent holes. Closer large holes cause a stress increase in the marginal portion of the bearing (**Figures 7.26 (a)** and **7.26 (b)**) that tends to collapse when sheared; if the distance between two adjacent holes increases, the central area is loaded as the marginal portions (**Figure 7.26 (c)**) and the bearing is more stable. For soft bearings under larger values of vertical pressure, the minimum clear distance between two adjacent holes to prevent buckling appears to be $\delta = 5D$.

In **Figure 7.27** examples of improving modification are shown in terms of Von Mises stress distribution. Bearings initially unstable (i.e. 110x60 with $G_e = 1$ MPa under both $\sigma_v = 2$ and $\sigma_v = 4$ MPa) become stable up to full rollover with the corresponding configuration of holes. The lateral force – displacement response curves of those bearings show how a reduction in the horizontal stiffness clearly follows the modification for lateral displacement less than $50 \div 75$ mm (i.e. $\gamma_H \approx 150\% \div 150\%$); beyond this threshold, the originally vertical faces increasingly becoming horizontal up to full rollover and the horizontal stiffness gradually increases.

The results from **Figure 7.24** match what shown in the **Section 7.4**: an extension of the stability range of the bearings is more likely with larger values of the shear modulus and lightly loaded bearings (cf. **Figures 7.18 (d)** and **7.24 (m)**, **Figures 7.20 (b)** and **7.24 (m)**).

The focus on the horizontal stiffness is shown in **Figure 7.25** where the ratios between horizontal secant stiffnesses of modified and unmodified bearings are shown. For modified U-FREIs stable up to full rollover, these ratios are evaluated at $\gamma_H = 100\%$ of shear strain, while for unstable modified bearings at maximum stable shear strain. These plots show how the modifications reduce the horizontal stiffness of the bearings, as expected. The reduction appears to be proportional to the removed volume, i.e. an approximate decreasing trend can be found from left to right of each graph.

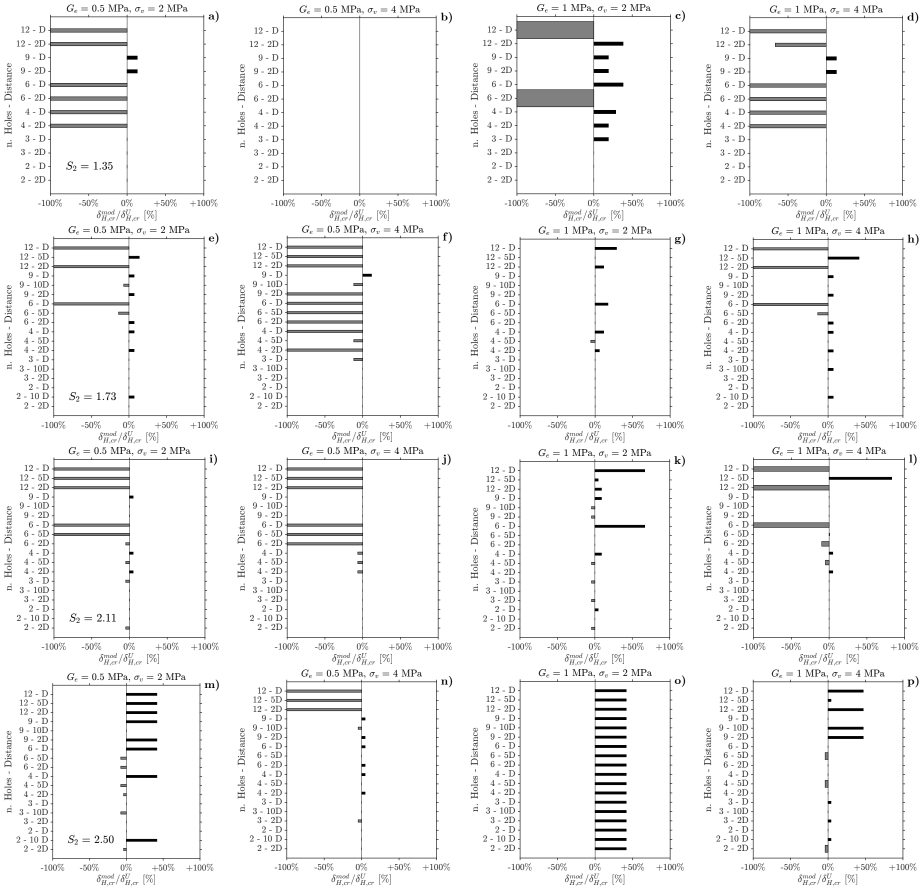

Figure 7.24: Ratio of maximum stable horizontal displacements of modified and unmodified bearings: 7.24 (a) to 7.24 (d) 70x60, 7.24 (e) to 7.24 (h) 90x60, 7.24 (i) to 7.24 (l) 110x60 and 7.24 (m) to 7.24 (p) 130x60.

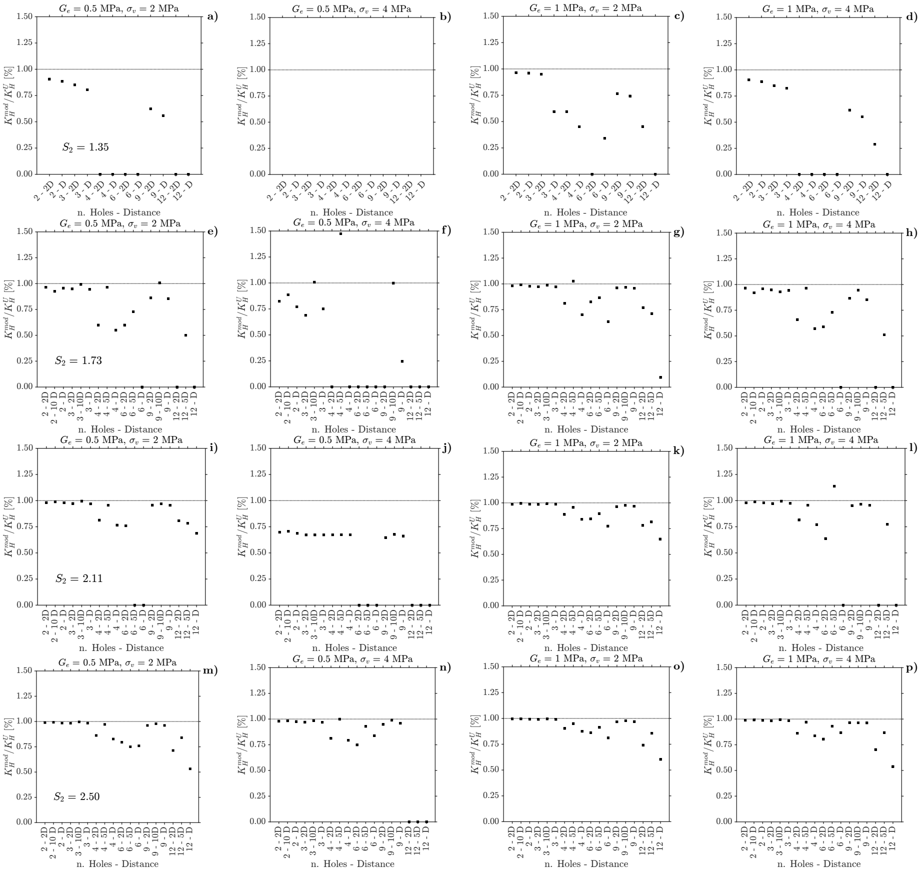

Figure 7.25: Ratio of horizontal stiffness of modified and unmodified bearings: 7.25 (a) to 7.25 (d) 70x60, 7.25 (e) to 7.25 (h) 90x60, 7.25 (i) to 7.25 (l) 110x60 and 7.25 (m) to 7.25 (p) 130x60.

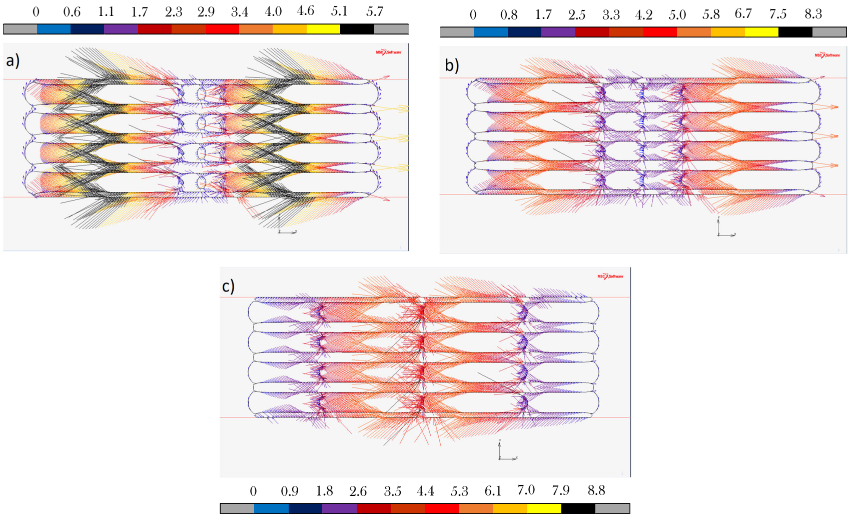

Figure 7.26: Vector plot of maximum principal value of stress for bearing 130x60 under full compression. Clear distance between two adjacent holes equal to: (a) D, (b) 2D and (c) 5D.

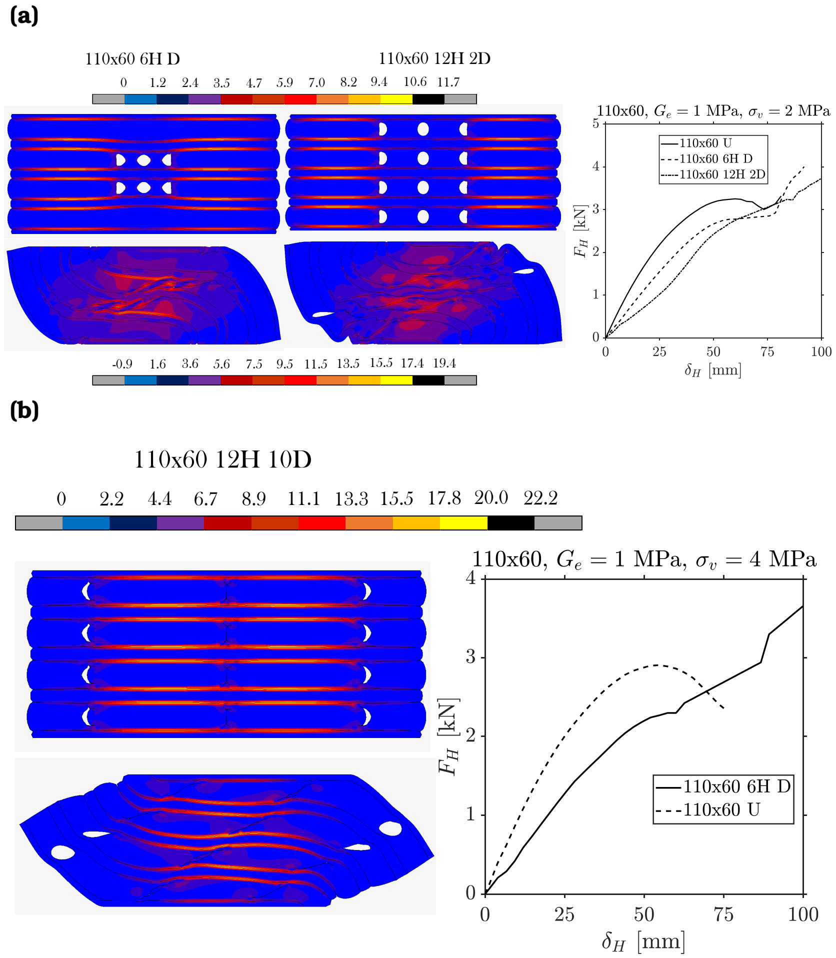

Figure 7.27: Comparison between modified and unmodified bearings: modification that ensure full rollover to prior unstable bearing: (a) *110x60 6H D, 110x60 12H 2D*, (b) *110x60 12H 5D*.

CHAPTER 8

CONCLUSIONS & OUTLOOK

8.1 Final comments

The main topic of this thesis was the stability of Unbonded Fiber Reinforced Elastomeric Isolators (U-FREIs) under combined vertical and horizontal loads. The investigation was conducted through three approaches:

1. *Analytical*: updated analytical solutions for the response parameters of U-FREIs under combined axial and shear loads are proposed.
2. *Numerical*: a large number of both 2D and 3D finite element analyses on FREIs of different shapes have been carried out.
3. *Experimental*: experimental tests on samples of U-FREIs in different configurations have been conducted.

Through the analytical approach it was firstly seen how to fit the analytical solutions obtained for elastomeric bearings with rigid reinforcements to bearings with flexible reinforcement. An analytical equation was proposed for the total vertical displacement δ_v^t at the top of an U-FREI subjected to combined axial and shear loads, starting from existing solutions. Divide the vertical displacement into two rates due to the vertical load (δ_v^c) and horizontal displacement (δ_v^s), respectively, brought results in line with the expected displacement values.

Analytical equations for the vertical stiffness K_v and the effective compressive modulus E_c of an U-FREI under simultaneous vertical and horizontal loads have been introduced. The solutions reported in this thesis allow to deduce the decreasing trend of these parameters with the horizontal displacement. With the proposed approach, both K_v and E_c can be obtained starting from the values under pure compression, through the function of the horizontal displacement $\psi(\delta_H)$.

Futhermore, simple analytical equation initially proposed for SREIs, has been extended to derive the maximum stable horizontal displacement of an U-FREIs under axial and bidirectional shear load. As a first estimate, this displacement can be seen as half of the side in the direction of the imposed horizontal displacement (i.e. combination of the two shear displacement).

With the numerical approach the stability of a large number of different-shaped FREIs with several combinations of geometric and mechanical parameters have been studied. A total number of 5024 finite element analyses have included strip-shaped, rectangular-shaped and square-shaped U-FREIs.

Finite element analyses of elastomeric devices are quite challenging for the well known issues with inelastic stress strain response of rubber-base devices. Thus, all the finite element analyses sets were prior adequately calibrated using results from experimental tests on FREIs' samples. A number of FREIs with different materials and geometries were tested, and the numerical-experimental comparisons have shown good accuracy of the FEMs.

Through the FEAs the influence of the secondary shape factor S_2 on the stability of an U-FREIs was specially studied. FEAs show how this parameter rules the stability of U-FREIs as its variation greatly affects the lateral response of the bearing. A stable response of an U-FREIs can be expected for minimum values of S_2 in the range 2.5 to 3.5, depending also on the shear modulus of the rubber G_e and the applied vertical pressure σ_v These results were achieved both for unidirectional and bidirectional shear loaded bearings.

Based on the results from FEAs, easy-to-use stability charts were proposed. These charts allow to derive the secondary shape factor required for a stable response up to a fixed threshold of shear strain. The stability charts have been proposed for both square-shaped, rectangular-shaped and strip-shaped U-FREIs, loaded in a generic horizontal direction.

Finally, a simple strategy to tune the horizontal response of U-FREI has been introduced. Modifying the geometry of bearings through horizontal holes along one of the base sides, the horizontal force-displcaement response curve can be modified. It has been seen how this modified geometry can lead unstable bearings to a stable response up to full rollover, avoiding unstable ranges in the lateral response. Experimental tests and finite element analyses on U-FREIs samples with different holes configurations have shown encouraging results.

8.2 Furher developments

This thesis presented preliminary results on the vertical and horizontal response of U-FREIs under combined axial and shear loads. Several results are obtained with simplified hypotheses, with the aim of provide easy-to-use outcomes, with a minimum number of involved parameters. Thus, constant values of the shear modulus have been considered in the FEAs, reproducing the secant shear modulus approach of a design phase. The results may be extended accounting the complex, rate-dependent response of different rubber compounds.

Also, experimental tests computing the variation of the vertical stiffness of U-FREIs under combined axial and shear loads may be conducted to validate the analytical – numerical outcomes of this work.

The proposed modification to improve the lateral response of U-

FREIs under combined axial and shear loads needs to be extended considering bearings loaded in different horizontal direction or different orientations of the holes, i.e. holes parallel to the direction of the horizontal displacement.

Finally, the hysteretic response of the U-FREIs may be addressed. Further investigations are needed to study the response of modified U-FREIs under hysteretic horizontal loads, or bidirectional quasi-static and hysteretic shear loads. An experimental campaign on U-FREIs with different elastomeric compounds and variable geometry could also help to shed some lights on the coupled axial-shear response of these devices.

BIBLIOGRAPHY

1. Galano, S. & Calabrese, A. **State of Art on Seismic Protection of Non-Engineered Building (N-EB) in Developing Countries** (see page 3).
2. Cruz-Cunh, Maria, M., Isabel, M. M. & Gonçalves, P. **Handbook of Research on ICTs for Human-Centered Healthcare and Social Care Services** (Hershey, 2013) (see page 3).
3. Bank, T. W. *World Development Indicators* https://datatopics.worldbank.org/world-development-indicators/the-world-by-income-and-region.html (see page 3).
4. *Seismic protection in developing countries: Where are the gaps in our approach?* Pacific Conference on Earthquake Engineering (Wellington, New Zeland, 2003) (see page 4).
5. Wikipedia. *Lists of 21st-century earthquakes* 2021. https://en.wikipedia.org/wiki/Lists_of_21st-century_earthquakes (see page 4).
6. Arya, A. **Guidelines for earthquake resistant non-engineered construction** (International Association for Earthquake Engineering, Tokyo, Japan, 1986) (see pages 4, 5).
7. *Earthquake Resistant Design of Non-Engineered Buildings In Indonesia* EQTAP Workshop IV (Kamakura, 2001) (see pages 4, 5).
8. Wikipedia. *Vernacular architecture* 2021. https://en.wikipedia.org/wiki/Vernacular_architecture (see page 5).

9. Karkee, M., Cuadra, C. & Sunuwar, L. **The challenges of protecting heritage architecture in developing countries from earthquake disasters**. *Structural Studies, Repairs and Maintenance of Heritage Architecture* **83,** 407–419 (see pages 5, 6).

10. Chopra, A. **Dynamics of structures: Theory and applications to earthquake engineering** (N.J. Prentice Hall, Englewood Cliffs, 1995) (see page 6).

11. Kelly, J. M. **Analysis of Fiber-Reinforced Elastomeric Isolators**. *Journal of Seismology and Earthquake Engineering* **2,** 19–34 (see pages 7, 8, 10, 22).

12. Naeim, F. & Kelly, J. M. **Design of seismic isolated structures: from theory to practice**. In (1999) (see pages 7, 22, 141).

13. Moon, B. Y., Kang, G.-J., Kang, B. & Kelly, J. M. **Design and manufacturing of fiber reinforced elastomeric isolator for seismic isolation**. *Journal of Materials Processing Technology* **130,** 145–150 (see pages 7, 10).

14. Ashkezari, G. D., Aghakouchak, A. A. & Kokabi, M. **Design, manufacturing and evaluation of the performance of steel like fiber reinforced elastomeric seismic isolators**. English. *Journal of Materials Processing Tech.* **197,** 140–150 (see pages 7, 10).

15. Tavio & Wijiaya, U. **Experimental Study of Indonesian Low-Cost Glass Fiber Reinforced Elastomeric Isolators (GFREI)**. English. *International Journal on Advanced Science Engineering Information* **10,** 311–317 (see page 7).

16. Moon, B., Kang, G., Kang, B., Kim, G. & Kelly, J. **Mechanical Properties of Seismic Isolation System with Fiber-Reinforced Bearing of Strip Type**. English. *International Applied Mechanics,* 1231–1239 (see pages 7, 10).

17. MOON, B.-Y., KANG, G.-J., KANG, B.-S. & KIM, H.-S. **Mechanical Property Analysis and Design of Shock Absorber System Using Fiber Bearing by Experimental Method**. *JSME International Journal Series C Mechanical Systems, Machine Elements and Manufacturing* **46,** 289–296 (see pages 7, 10).

18. Toopchi-Nezhad, H., Tait, M. J. & Drysdale, R. G. **Bonded versus unbonded strip fiber reinforced elastomeric isolators: Finite element analysis**. English. *Composite Structures* **93,** 850–859 (see pages 7, 37).

19. Kelly, J. & Calabrese, A. **Mechanics of Fiber Reinforced Bearings**. English. Tech. rep. (Headquarters at the University of California, Berkeley, 2012). https://peer.berkeley.edu/sites/default/files/webpeer-2012-101-james_m._kelly_and_andrea_calabrese.pdf (see pages 8, 10, 26).

20. Toopchi-Nezhad, H., Tait, M. J. & Drysdale, R. G. **Testing and modeling of square carbon fiber-reinforced elastomeric seismic isolators**. English. *Structural Control and Health Monitoring* **15,** 876–900 (see pages 8, 37, 98, 108, 118).

21. Kelly, J. M. **Seismic Isolation Systems for Developing Countries**. *Earthquake Spectra* **18,** 385–406 (see page 8).

22. Sierra, I. E. M., Losanno, D., Strano, S., Marulanda, J. & Thomson, P. **Development and experimental behavior of HDR seismic isolators for low-rise residential buildings**. *Engineering Structures* (see page 8).

23. Losanno, D., Madera Sierra, I. E., Spizzuoco, M., Marulanda, J. & Thomson, P. **Experimental assessment and analytical modeling of novel fiber-reinforced isolators in unbounded configuration**. *Composite Structures* **212,** 66–82. ISSN: 0263-8223. https://www.sciencedirect.com/science/article/pii/S0263822318338777 (see pages 8, 98).

24. Losanno, D., Madera Sierra, I. E., Spizzuoco, M., Marulanda, J. & Thomson, P. **Experimental performance of unbonded polyester and carbon fiber reinforced elastomeric isolators under bidirectional seismic excitation**. *Engineering Structures* **209,** 110003. ISSN: 0141-0296. https://www.sciencedirect.com/science/article/pii/S0141029619308089 (see pages 8, 118).

25. *Advances in Low-Cost Seismic Isolation with Rubber* U.S. National Conference on Earthquake Engineering (Anchorage, Alaska, 2014) (see pages 10, 70, 74).

26. Kelly, J. & Takhirov, S. **Analytical and Experimental Study of Fiber-Reinforced Elastomeric Isolators**. English. Tech. rep. (Headquarters at the University of California, Berkeley, 2001). https://peer.berkeley.edu/sites/default/files/0111_j._kelly_s._takhirov_.pdf (see page 10).

27. Tsai, H. & Kelly, J. **Stiffness Analysis of Fiber-Reinforced Elastomeric Isolators**. English. Tech. rep. (Headquarters at the University of California, Berkeley, 2001). https://peer.berkeley.edu/sites/default/files/0105_h._tsai_j._kelly.pdf (see pages 10, 22).

28. Tsai, H.-C. & Lee, C.-C. **Compressive stiffness of elastic layers bonded between rigid plates**. *International Journal of Solids and Structures* **35,** 3053–3069. ISSN: 0020-7683. https://www.sciencedirect.com/science/article/pii/S0020768397003557 (see pages 10, 22).
29. Tsai, H.-C. **Compression stiffness of infinite-strip bearings of laminated elastic material interleaving with flexible reinforcements**. *International Journal of Solids and Structures* **41,** 6647–6660. ISSN: 0020-7683. https://www.sciencedirect.com/science/article/pii/S0020768304003208 (see pages 10, 22).
30. Tsai, H.-C. **Compression stiffness of circular bearings of laminated elastic material interleaving with flexible reinforcements**. *International Journal of Solids and Structures* **43,** 3484–3497. ISSN: 0020-7683. https://www.sciencedirect.com/science/article/pii/S0020768305002751 (see pages 10, 22).
31. Pinarbasi, S. & Mengi, Y. **Elastic layers bonded to flexible reinforcements**. *International Journal of Solids and Structures* **45,** 794–820. ISSN: 0020-7683. https://www.sciencedirect.com/science/article/pii/S0020768307003617 (see page 10).
32. Tsai, H.-C. & Kelly, J. M. **Buckling load of seismic isolators affected by flexibility of reinforcement**. *International Journal of Solids and Structures* **42,** 255–269 (see pages 10, 34).
33. Tsai, H.-C. & Kelly, J. M. **Buckling of short beams with warping effect included**. *International Journal of Solids and Structures* **42,** 239–253. ISSN: 0020-7683. https://www.sciencedirect.com/science/article/pii/S0020768304004408 (see pages 10, 28, 33, 103).
34. Russo, G., Pauletta, M. & Cortesia, A. **A study on experimental shear behavior of fiber-reinforced elastomeric isolators with various fiber layouts, elastomers and aging conditions**. *Engineering Structures* **52,** 422–433 (see pages 10, 30, 98).
35. Pauletta, M., Cortesia, A. & Russo, G. **Roll-out instability of small size fiber-reinforced elastomeric isolators in unbonded applications**. *Engineering Structures* **102,** 358–368. ISSN: 0141-0296. https://www.sciencedirect.com/science/article/pii/S0141029615005180 (see pages 10, 108).

36. Engelen, N. C. V., Tait, M. J. & Konstantinidis, D. **Model of the Shear Behavior of Unbonded Fiber-Reinforced Elastomeric Isolators**. *Journal of Structural Engineering* **141,** 04014169. eprint: https://ascelibrary.org/doi/pdf/10.1061/%28ASCE%29ST.1943-541X.0001120. https://ascelibrary.org/doi/abs/10.1061/%28ASCE%29ST.1943-541X.0001120 (see pages 10, 98).

37. Al-Anany, Y. M., Engelen, N. C. V. & Tait, M. J. **Vertical and Lateral Behavior of Unbonded Fiber-Reinforced Elastomeric Isolators**. *Journal of Composites for Construction* **21,** 04017019 (see pages 10, 98).

38. Al-Anany, Y. M. & Tait, M. J. **A numerical study on the compressive and rotational behavior of fiber reinforced elastomeric isolators (FREI)**. English. *Composite Structures* **133,** 1249–1266 (see page 10).

39. Osgooei, P. M., Tait, M. J. & Konstantinidis, D. **Three-dimensional finite element analysis of circular fiber-reinforced elastomeric bearings under compression**. English. *Composite Structures* **108,** 191–204 (see page 10).

40. Mordini, A. & Strauss, A. **An innovative earthquake isolation system using fibre reinforced rubber bearings**. *Engineering Structures* **30,** 2739–2751. ISSN: 0141-0296. https://www.sciencedirect.com/science/article/pii/S014102960800093X (see page 10).

41. Angeli, P., Russo, G. & Paschini, A. **Carbon fiber-reinforced rectangular isolators with compressible elastomer: Analytical solution for compression and bending**. English. *International Journal of Solids and Structures* **50,** 3519–3527 (see pages 10, 27).

42. Engelen, N. C. V. & Kelly, J. M. **Correcting for the Influence of Bulk Compressibility on the Design Properties of Elastomeric Bearings**. *Journal of Engineering Mechanics-asce* **141,** 04014170 (see page 10).

43. Engelen, N. C. V., Tait, M. J. & Konstantinidis, D. **Development of Design Code Oriented Formulas for Elastomeric Bearings Including Bulk Compressibility and Reinforcement Extensibility**. *Journal of Engineering Mechanics* **142,** 04016024. eprint: https://ascelibrary.org/doi/pdf/10.1061/%28ASCE%29EM.1943-7889.0001015. https://ascelibrary.org/doi/abs/10.1061/%28ASCE%29EM.1943-7889.0001015 (see page 10).

44. Konstantinidis, D. & Moghadam, S. R. **Compression of unbonded rubber layers taking into account bulk compressibility and contact slip at the supports**. *International Journal of Solids and Structures* **87,** 206–221 (see page 10).

45. Naghshineh, A. K., Akyuz, U. & Caner, A. **Comparison of fundamental properties of new types of fiber-mesh-reinforced seismic isolators with conventional isolators: FIBER-REINFORCED ELASTOMERIC BEARINGS**. *Earthquake Engineering & Structural Dynamics* **43,** 301–316 (see page 10).

46. Kang, G. & Kang, B. **Dynamic analysis of fiber-reinforced elastomeric isolation structures**. *Journal of Mechanical Science and Technology* **23,** 1132–1141 (see page 10).

47. Strauss, A., Apostolidi, E., Zimmermann, T., Gerhaher, U. & Dritsos, S. **Experimental investigations of fiber and steel reinforced elastomeric bearings: Shear modulus and damping coefficient**. English. *Engineering Structures* **75,** 402–413 (see page 10).

48. Bakhshi, A., Jafari, M. H. & Valadoust Tabrizi, V. **Study on dynamic and mechanical characteristics of carbon fiber- and polyamide fiber-reinforced seismic isolators**. English. *Materials and Structures* **47,** 447–457 (see page 10).

49. Hedayati Dezfuli, F. & Alam, M. S. **Experiment-Based Sensitivity Analysis of Scaled Carbon-Fiber-Reinforced Elastomeric Isolators in Bonded Applications**. *Fibers* **4.** ISSN: 2079-6439. https://www.mdpi.com/2079-6439/4/1/4 (see page 10).

50. Castillo Ruano, P. & Strauss, A. **Finite Element Analysis for Nonlinear Unbonded Circular Fiber-Reinforced Elastomeric Bearings**. *Journal of Composites Science* **5.** ISSN: 2504-477X. https://www.mdpi.com/2504-477X/5/7/170 (see page 10).

51. Habieb, A., Milani, G., Tavio & Milani, F. **Seismic Performance of a Masonry Building Isolated With Low-Cost Rubber Isolators**. *Earthquake Resistant Engineering Structures* **172,** 71–82 (see page 10).

52. Habieb, A., Valente, M. & Milani, G. **Base seismic isolation of a historical masonry church using fiber reinforced elastomeric isolators**. *Soil Dynamics and Earthquake Engineering* **120,** 127–145 (see page 10).

53. Van Engelen, N. C., Konstantinidis, D. & Tait, M. J. **Structural and nonstructural performance of a seismically isolated building using stable unbonded fiber-reinforced elastomeric isolators**. *Earthquake Engineering & Structural Dynamics* **45,** 421–439. eprint: https://onlinelibrary.wiley.com/doi/pdf/10.1002/eqe.2665. https://onlinelibrary.wiley.com/doi/abs/10.1002/eqe.2665 (see page 10).

54. Chowdhury, M. A. & Hassan, W. **Comparative study of the Dynamic Analysis of Multi-storey Irregular building with or without Base Isolator**. In (2013) (see page 10).

55. Calabrese, A., Kelly, J., Onorii, C. & Serino, G. **Theoretical and experimental analysis of recycled rubber bearings with a flexible reinforcement for developing countries**. In. 7th World congress on joints, bearings and seismic systems for concrete structures (Las Vegas, Nevada, 2011) (see page 10).

56. Spizzuoco, M., Calabrese, A. & Serino, G. **Innovative low-cost recycled rubber–fiber reinforced isolator: Experimental tests and Finite Element Analyses**. English. *Engineering Structures* **76,** 99–111 (see page 10).

57. Onorii, C. & Serino, G. **Analytical modeling and experimental validation of a recycled rubber material**. In. 5th European Conference on Constitutive Models for Rubber, ECCMR (2007) (see pages 11, 12).

58. Guglielmotti, A., Lucignano, C. & Quadrini, F. **Production of rubber pads by tyre recycling**. English. *International Journal of Materials Engineering Innovation (IJMATEI)* **1** (see page 11).

59. Habieb, A., Milani, F., Milani, G. & Cerchiaro, R. **Rubber compounds made of reactivated EPDM for fiber reinforced elastomeric isolators: an experimental study**. English. *Iranian Polymer Journal* **29,** 1031–1043 (see page 11).

60. Montella, G., Calabrese, A. & Serino, G. **Mechanical characterization of a Tire Derived Material: Experiments, hyperelastic modeling and numerical validation**. *Construction and Building Materials* **66,** 336–341 (see pages 11, 12).

61. Onorii, C., Serino, G. & Calabrese, A. **Structural bearings made of recycled rubber: Theoretical aspects and experimental characterization**. In. 8th International Conference on Structural Dynamics, EURODYN 2011 (2011) (see page 12).

62. Calabrese, A., Serino, G., Strano, S. & Terzo, M. **Experimental investigation of a low-cost elastomeric anti-seismic device using recycled rubber**. *Meccanica* **50,** 2201–2218 (see pages 12, 98).

63. Losanno, D., Calabrese, A., Madera-Sierra, I. E., Spizzuoco, M., Marulanda, J., Thomson, P. & Serino, G. **Recycled versus Natural-Rubber Fiber-Reinforced Bearings for Base Isolation: Review of the Experimental Findings**. *Journal of Earthquake Engineering* **0,** 1–20. eprint: https://doi.org/10.1080/13632469.2020.1748764. https://doi.org/10.1080/13632469.2020.1748764 (see page 12).

64. Calabrese, A., Spizzuoco, M., Serino, G., Corte, G. D. & Maddaloni, G. **Shaking table investigation of a novel, low-cost, base isolation technology using recycled rubber**. *Structural Control & Health Monitoring* **22,** 107–122 (see page 12).

65. Losanno, D., Spizzuoco, M. & Calabrese, A. **Bidirectional shaking-table tests of unbonded recycled-rubber fiber-reinforced bearings (RR-FRBs)**. *Structural Control and Health Monitoring* **26.** e2386 STC-18-0124.R2, e2386. eprint: https://onlinelibrary.wiley.com/doi/pdf/10.1002/stc.2386. https://onlinelibrary.wiley.com/doi/abs/10.1002/stc.2386 (see pages 12, 98, 118, 142).

66. Calabrese, A., Losanno, D., Spizzuoco, M., Strano, S. & Terzo, M. **Recycled Rubber Fiber Reinforced Bearings (RR-FRBs) as base isolators for residential buildings in developing countries: The demonstration building of Pasir Badak, Indonesia**. *Engineering Structures* **192,** 126–144. ISSN: 0141-0296. https://www.sciencedirect.com/science/article/pii/S0141029618331572 (see pages 12, 98, 142).

67. Calabrese, A., Spizzuoco, M., Strano, S. & Terzo, M. **Hysteresis models for response history analyses of recycled rubber–fiber reinforced bearings (RR-FRBs) base isolated buildings**. *Engineering Structures* **178,** 635–644. ISSN: 0141-0296. https://www.sciencedirect.com/science/article/pii/S0141029618307582 (see page 12).

68. Losanno, D., Ravichandran, N., Parisi, F., Calabrese, A. & Serino, G. **Seismic performance of a Low-Cost base isolation system for unreinforced brick Masonry buildings in developing countries**. *Soil Dynamics and Earthquake Engineering* **141,** 106501. ISSN: 0267-7261. https://www.sciencedirect.com/science/article/pii/S0267726120311271 (see pages 12, 98, 142).

69. Turer, A. & Özden, B. **Seismic base isolation using low-cost Scrap Tire Pads (STP)**. *Materials and Structures* **41,** 891–908 (see pages 12, 13).

70. Madhekar, S. & Vairagade, H. **Innovative Base Isolators From Scrap Tyre Rubber Pads** () (see page 12).

71. Yamaguchi, N., Narafu, T., Turer, A., Iiba, M. & Imai, H. **Shaking Table Test of Simple and Affordable Seismic Isolation**. In. The 14th World Conference on Earthquake Engineering (Beijing, China, 2008) (see page 13).

72. Huma, Kanta, Mishra, Akira, Igarashi, Dang, Ji, Hiroshi & Matsushima. **Pseudo-Dynamic Testing for Seismic Performance Assessment of Buildings with Seismic Isolation System Using Scrap Tire Rubber Pad Isolators**. *Journal of civil engineering and architecture* **8,** 73–88 (see page 13).

73. Mishra, H. K. & Igarashi, A. **Experimental and Analytical Study of Scrap Tire Rubber Pad for Seismic Isolation**. *Journal of Civil and Environmental Engineering* **6,** 107–113 (see page 13).

74. Muñoz, A., Díaz, M. & Reyna, R. **Applicability study of a low cost seismic isolator prototype using recycled rubber**. *TECNIA* (see page 13).

75. Zisan, M. B. & Igarashi, A. **Lateral load performance and seismic demand of unbonded scrap tire rubber pad base isolators**. *Earthquake Engineering and Engineering Vibration* **20,** 803–821 (see page 13).

76. Lang, A. & Jeffrey, D. United States Brevetto US 6,862,848 B1, 08 03 2005 (see page 13).

77. Van de Lindt, J. & Atader, R. **Shake Table Test Results for a Half-Scale Reinforced Concrete Indonesian House with and Without Economical Base Isolation**. *Asian Journal of Civil Engineering (Building and Housing)* **9,** 1–13 (see pages 13, 14).

78. Hadad, H. A., Calabrese, A., Strano, S. & Serino, G. **A Base Isolation System for Developing Countries Using Discarded Tyres Filled with Elastomeric Recycled Materials**. *Journal of Earthquake Engineering* **21,** 246–266. eprint: https://doi.org/10.1080/13632469.2016.1172371. https://doi.org/10.1080/13632469.2016.1172371 (see pages 13, 14).

79. Morales, E., Filiatrault, A. & Aref, A. **Sustainable and Low Cost Room Seismic Isolation For Essential Care Units of Hospitals in Developing Countries**. In. 16th World Conference on Earthquake Engineering, 16WCEE 2017 (Santiago Chile, 2017) (see page 14).

80. Morales, E. E. R., Filiatrault, A. & Aref, A. J. **Seismic floor isolation using recycled tires for essential buildings in developing countries**. *Bulletin of Earthquake Engineering* **16,** 6299–6333 (see page 14).

81. Kelly, J. M. **Aseismic base isolation: review and bibliography**. *Soil Dynamics and Earthquake Engineering* **5,** 202–216 (see pages 15, 22).

82. Zayas, V. A., Low, S. S. & Mahin, S. A. **A Simple Pendulum Technique for Achieving Seismic Isolation**. *Earthquake Spectra* **6,** 317–333. eprint: https://doi.org/10.1193/1.1585573. https://doi.org/10.1193/1.1585573 (see page 15).

83. Arya, A. **Sliding concept for mitigation of earthquake disaster to masonry buildings**. In. Proceedings of Eight World Conference on Earthquake Engineering (1984) (see page 15).

84. Xiao, H., Butterworth, J. & Larkin, T. **Low-technology techniques for seismic isolation**. In. New Zealand Society for Earthquake Engineering (2004) (see page 15).

85. Nanda, R. P., Shrikhande, M. & Agarwal, P. **Low-Cost Base-Isolation System for Seismic Protection of Rural Buildings**. *Practice Periodical on Structural Design and Construction* **21,** 04015001 (see page 15).

86. Habieb, A. B., Milani, G., Tavio, T. & Milani, F. **Low cost friction seismic base-isolation of residential new masonry buildings in developing countries: A small masonry house case study**. *AIP Conference Proceedings* **1863,** 450009. eprint: https://aip.scitation.org/doi/pdf/10.1063/1.4992618. https://aip.scitation.org/doi/abs/10.1063/1.4992618 (see page 16).

87. Radhikesh, P. N., Pankaj, A. & Manish, S. **BASE ISOLATION SYSTEM SUITABLE FOR MASONRY BUILDINGS**. In (2012) (see page 16).

88. Nanda, R. **LOW COST SLIDING ISOLATORS FOR DEVELOPING COUNTRIES**. *Asian Journal of Civil Engineering* **17,** 417–425 (see page 16).

89. Pakpour, F., Agha Beigi, H. & Christopoulos, C. **Development of low-cost Seismic Isolation Platform (SIP) for mass implementation in developing countries**. In (Sept. 2019) (see page 16).

90. Ahmad, S., Ghani, F. & Adil, M. **Seismic friction base isolation performance using demolished waste in masonry housing**. *Construction and Building Materials* **23,** 146–152 (see page 16).

91. Kawamata, S., Funaki, N., Hori, N., Fujita, T. & Inoue, N. **BASE ISOLATION SYSTEM SUITABLE FOR MASONRY BUILDINGS**. In. 13th World Conference on Earthquake Engineering (Vancouver, B.C., Canada, 2004) (see page 16).

92. FUNAKI, N., FUJITA, T., HORI, N., INOUE, N. & KAWAMATA, S. **ROCKING PILLAR ISOLATION SYSTEM FOR MASONRY HOUSES**. *Journal of Structural and Construction Engineering (transactions of Aij)* **74,** 1567–1574 (see page 16).

93. Fujita, T., Funaki, N., Hori, N., Indue, N. & Kawamata, S. **Rocking pillar isolation system for masonry houses - Verifying vibration tests of a reduced scale test specimen**. **73,** 63–70 (see page 16).

94. Jampole, E., Deierlein, G., Miranda, E., Fell, B., Swensen, S. & Acevedo, C. **Full-Scale Dynamic Testing of a Sliding Seismically Isolated Unibody House**. *Earthquake Spectra* **32** (see page 16).

95. Banović, I., Radnić, J. & Grgić, N. **Shake Table Study on the Efficiency of Seismic Base Isolation Using Natural Stone Pebbles**. *Advances in Materials Science and Engineering* **2018,** 1–20 (see page 16).

96. Tsiavos, A., Sextos, A., Stavridis, A., Dietz, M., Dihoru, L. & Alexander, N. **Large-scale experimental investigation of a low-cost PVC 'sand-wich' (PVC-s) seismic isolation for developing countries**. *Earthquake Spectra* **36** (see page 16).

97. Tsiavos, A., Sextos, A., Stavridis, A., Dietz, M., Dihoru, L., Di Michele, F. & Alexander, N. A. **Low-cost hybrid design of masonry structures for developing countries: Shaking table tests**. *Soil Dynamics and Earthquake Engineering* **146,** 106675. ISSN: 0267-7261. https://www.sciencedirect.com/science/article/pii/S026772612100097X (see page 16).

98. Tsiavos, A., Sextos, A., Stavridis, A., Dietz, M., Dihoru, L. & Alexander, N. A. **Experimental investigation of a highly efficient, low-cost PVC-Rollers Sandwich (PVC-RS) seismic isolation**. *Structures* **33,** 1590–1602. ISSN: 2352-0124. https://www.sciencedirect.com/science/article/pii/S2352012421004434 (see page 16).

99. Bayraktar, A., Keypour, H. & Naderzadeh, A. **Application of Ancient Earthquake Resistant Method in Modern Construction Technology**. In (2012) (see page 16).

100. Tsang, H.-H. **Seismic isolation by rubber–soil mixtures for developing countries**. *Earthquake Engineering & Structural Dynamics* **37,** 283–303 (see page 18).

101. Edil, T. & Bosscher, P. **Engineering Properties of Tire Chips and Soil Mixtures**. *Geotechnical Testing Journal* **17,** 453–464 (see pages 18, 19).

102. Tsang, H.-H., Sheikh, M., Lo, S. & Lam, N. **Qushion: Earthquake Protection by Rubber-Soil Mixture** (see page 18).

103. Hazarika, H., Yasuhara, K., Hyodo, M., Karmokar, A. K. & Mitarai, Y. **MITIGATION OF EARTHQUAKE INDUCED GEOTECHNICAL DISASTERS USING A SMART AND NOVEL GEOMATERIAL**. In (2008) (see page 18).

104. Tsang, H., Lam, N., Yaghmaei-Sabegh, S., Sheikh, M. & Indraratna, B. **Geotechnical Seismic Isolation by Scrap Tire-Soil Mixtures**. In. International Conferences on Recent Advances in Geotechnical Earthquake Engineering and Soil Dynamics (Missouri University of Science and Technology, 2010) (see page 18).

105. Tsang, H.-H., Lo, S. H., Xu, X. & Sheikh, M. N. **Seismic isolation for low-to-medium-rise buildings using granulated rubber–soil mixtures: numerical study**. *Earthquake Engineering & Structural Dynamics* **41,** 2009–2024 (see page 18).

106. Brunet, S., De la Llera, J. & Kausel, E. **Seismic Isolation Using Recycled Tire-Rubber**. In. 16th World Conference on Earthquake (Santiago Chile, 2017) (see page 18).

107. Tsiavos, A., Alexander, N. A., Diambra, A., Ibraim, E., Vardanega, P. J., Gonzalez-Buelga, A. & Sextos, A. **A sand-rubber deformable granular layer as a low-cost seismic isolation strategy in developing countries: Experimental investigation**. *Soil Dynamics and Earthquake Engineering* **125,** 105731. ISSN: 0267-7261. https://

www.sciencedirect.com/science/article/pii/S0267726119303148 (see page 19).

108. Promputthangkoon, P. & Hyde, A. **Compressibility and liquefaction potential of rubber composite soils**. In. International workshop on scrap tire derived geomaterials - opportunities and challenges (2008), 161–170. ISBN: 9780415460705, 0415460700 (see page 19).

109. Masad, E., Taha, R., Ho, C. & Papagiannakis, A. **Engineering Properties of Tire/Soil Mixtures as a Lightweight Fill Material**. *Geotechnical Testing Journal* **19** (see page 19).

110. Kelly, J. M. **Earthquake-resistant design with rubber** (see page 22).

111. Kelly, J. M. & Engelen, N. C. V. **Single Series Solution for the Rectangular Fiber-Reinforced Elastomeric Isolator Compression Modulus**. English. Tech. rep. (Headquarters at the University of California, Berkeley, 2015). https://peer.berkeley.edu/sites/default/files/webpeer-2015-03_james_m._kelly_and_niel_c._van_engelen_.pdf (see page 26).

112. Kelly, J. M. & Konstantinidis, D. **Mechanics of Rubber Bearings for Seismic and Vibration Isolation**. ISBN: 9781119994015 (John Wiley & Sons, Ltd, 2011) (see pages 27, 32, 141, 145).

113. Toopchi-NezhadH. **Horizontal stiffness solutions for unbonded fiber reinforced elastomeric bearings**. *Structural Engineering and Mechanics* **49,** 395–410 (see pages 30, 98, 108).

114. Ehsani, B. & Toopchi-Nezhad, H. **Systematic design of unbonded fiber reinforced elastomeric isolators**. English. *Engineering Structures* **132,** 383–398 (see page 30).

115. Gerharer, U., Strauss, A. & Bergmeister, K. **Verbesserte Bemessungsrichtlinien für Bewehrte Elastomerlager**. *Bautechnik* **88,** 451–458. https://onlinelibrary.wiley.com/doi/abs/10.1002/bate.201101475 (see page 30).

116. De Raaf, M. G., Tait, M. J. & Toopchi-Nezhad, H. **Stability of fiber-reinforced elastomeric bearings in an unbonded application**. *Journal of Composite Materials* **45,** 1873–1884. eprint: https://doi.org/10.1177/0021998310388319. https://doi.org/10.1177/0021998310388319 (see pages 32, 37, 98).

117. Toopchi-Nezhad, H., Drysdale, R. G. & Tait, M. J. **Parametric Study on the Response of Stable Unbonded-Fiber Reinforced Elastomeric Isolators (SU-FREIs)**. *Journal of Composite Materials* **43,** 1569–1587. eprint: https://doi.org/10.1177/0021998308106322. https://doi.org/10.1177/0021998308106322 (see pages 32, 37, 118).

118. Konstantinidis, D., Kelly, J. & Makris, N. **Experimental Investigation on the Seismic Response of Bridge Bearings**. Tech. rep. EERC 2008-02 (June 2008) (see page 35).

119. Peng, T., Li, J. Z. & Fan, L. C. **Pilot study on the horizontal shear behaviour of FRP rubber isolators**. *Journal of Vibration and Shock* (see page 35).

120. Toopchi-Nezhad, H., Tait, M. J. & Drysdale, R. G. **Lateral Response Evaluation of Fiber-Reinforced Neoprene Seismic Isolators Utilized in an Unbonded Application**. *Journal of Structural Engineering* **134,** 1627–1637 (see pages 37, 118).

121. **Elastomeric seismic-protection isolators**. standards 22762-1 (ISO/TC 45/SC 4, 2018) (see page 37).

122. Calabrese, A., Spizzuoco, M., Galano, S., Tran, N., Strano, S. & Terzo, M. **A parametric study on the stability of fiber reinforced rubber bearings under combined axial and shear loads**. *Engineering Structures* **227,** 111441. ISSN: 0141-0296. https://www.sciencedirect.com/science/article/pii/S0141029620340426 (see page 41).

123. *Marc 2017.1: theory and user information* MSC Software Corporation (Newport Beach, California, 2017) (see page 42).

124. MacNeal, R. H. & Faulkner, L. **Finite Elements: their Design and Performance** (Marcel Dekker, Inc, New York, 1994) (see page 42).

125. *Marc 2017.1: program input* MSC Software Corporation (Newport Beach, California, 2017) (see page 42).

126. *MARC103 Experimental Elastomer Analysis* MSC Software Corporation (Newport Beach, California, 2017) (see page 44).

127. Jerrams, S. & Bowen, J. **Modelling the behaviour of rubber-like materials to obtain correlation with rigidity modulus tests**. *Journal of Composite Materials* **10,** 511–518. https://www.witpress.com/Secure/elibrary/papers/CMEM95/CMEM95056FU.pdf (see page 45).

128. *Marc 2017.1: element library* MSC Software Corporation (Newport Beach, California, 2017) (see pages 46, 47, 74, 75, 163).

129. **Bridge memo to designers.** Specifications (California Department of Transportation, Sacramento, CA., 1994) (see pages 49, 77).

130. Kelly, J. M. **Tension Buckling in Multilayer Elastomeric Bearings**. *Journal of Engineering Mechanics* **129,** 1363–1368. eprint: https://ascelibrary.org/doi/pdf/10.1061/%28ASCE%290733-9399%282003%29129%3A12%281363%29. https://ascelibrary.org/doi/abs/10.1061/%28ASCE%290733-9399%282003%29129%3A12%281363%29 (see page 57).

131. Kelly, J. & Marsico, M. **Stability and post-buckling behavior in nonbolted elastomeric isolators**. *Seismic Isolation and Protective Systems* **1,** 41–54 (see page 57).

132. Galano, S., Losanno, D. & Calabrese, A. **Analytical Solution for the Variation of the Vertical Response of Fiber Reinforced Elastomeric isolators (FREIs) Under Combined Axial and Shear Loads** (see page 63).

133. Galano, S. **On the Vertical Response of Fiber Reinforced Elastomeric Isolators (FREIs) Under Combined Vertical and Lateral Loading**. In. 8th ECCOMAS Thematic Conference on Computational Methods in Structural Dynamics and Earthquake Engineering (Athens, Greece, 2021), 2514–2532 (see page 63).

134. Osgooei, P. M., Konstantinidis, D. & Tait, M. J. **Variation of the vertical stiffness of strip-shaped fiber-reinforced elastomeric isolators under lateral loading**. *Composite Structures* **144,** 177–184 (see pages 64, 143).

135. Kelly, J. **Analysis of the run-in effect in fiber-reinforced isolators under vertical load**. *Journal of Mechanics of Materials and Structures* **3,** 1383–1401 (see page 69).

136. Toopchi-Nezhad, H., Tait, M. J. & Drysdale, R. G. **Influence of thickness of individual elastomer layers (first shape factor) on the response of unbonded fiber-reinforced elastomeric bearings**. *Journal of Composite Materials* **47,** 3433–3450. eprint: https://doi.org/10.1177/0021998312466686. https://doi.org/10.1177/0021998312466686 (see page 71).

137. Galano, S., Losanno, D. & Calabrese, A. **Stability analysis of unbonded fiber reinforced isolators of square shape**. *Engineering Structures* **245,** 112846. ISSN: 0141-0296. https://www.sciencedirect.com/science/article/pii/S0141029621009962 (see page 97).

138. Galano, S., Calabrese, A. & Losanno, D. **On the response of fiber reinforced elastomeric isolators (FREIs) under bidirectional shear loads**. *Structures* **34,** 2340–2354. ISSN: 2352-0124. https://www.sciencedirect.com/science/article/pii/S2352012421008195 (see page 117).

139. Ngo, T. V., Deb, S. K. & Dutta, A. **Effect of horizontal loading direction on performance of prototype square unbonded fibre reinforced elastomeric isolator**. *Structural Control and Health Monitoring* **25,** e2112. eprint: https://onlinelibrary.wiley.com/doi/pdf/10.1002/stc.2112. https://onlinelibrary.wiley.com/doi/abs/10.1002/stc.2112 (see page 118).

140. Osgooei, P. M., Tait, M. J. & Konstantinidis, D. **Finite element analysis of unbonded square fiber-reinforced elastomeric isolators (FREIs) under lateral loading in different directions**. *Composite Structures* **113,** 164–173. ISSN: 0263-8223. https://www.sciencedirect.com/science/article/pii/S0263822314000919 (see page 118).

141. Tran, C., Calabrese, A., Vassiliou, M. F. & Galano, S. **A simple strategy to tune the lateral response of unbonded Fiber Reinforced Elastomeric Isolators (FREIs)**. *Engineering Structures* **222,** 111128. ISSN: 0141-0296. https://www.sciencedirect.com/science/article/pii/S0141029620320137 (see page 141).

142. Galano, S., Calabrese, A., Losanno, D., Serino, G. & Strano, S. **Tuning the lateral response of unbonded fiber reinforced elastomeric isolators (U-FREIs) through horizontal holes: Experimental and numerical findings**. *Composite Structures* **289,** 115454. ISSN: 0263-8223. https://www.sciencedirect.com/science/article/pii/S0263822322002483 (see page 141).

143. Galano, S., Calabrese, A. & Losanno, D. **Tuning the lateral response of unbonded fiber reinforced elastomeric isolators (U-FREIs): experimental - numerical findings**. In. 8th ECCOMAS Thematic Conference on Computational Methods in Structural Dynamics and Earthquake Engineering (Athens, Greece, 2021), 2456–2467 (see page 141).

144. Van Engelen, N., Tait, M. & Konstantinidis, D. **Vertical Response Behaviour of Stable Unbonded Fiber Reinforced Elastomeric Isolators (SU-FREIs) with Holes in the Loaded Surface.** *Proceedings, Annual Conference - Canadian Society for Civil Engineering* **1** (see page 142).

145. Van Engelen, N., Tait, M. & Konstantinidis, D. **Horizontal Behaviour of Stable Unbonded Fiber Reinforced Elastomeric Isolators (SU-FREIs) with Holes**. In. 15th World Conferenc on Earthquake Engineering (Lisboa, Portugal, Sept. 2012) (see page 142).

146. Engelen, N. C. V., Osgooei, P. M., Tait, M. J. & Konstantinidis, D. **Experimental and finite element study on the compression properties of Modified Rectangular Fiber-Reinforced Elastomeric Isolators (MR-FREIs)**. *Engineering Structures* **74,** 52–64 (see page 142).

147. M. Osgooei, P., Van Engelen, N., Konstantinidis, D. & Tait, M. **Experimental and finite element study on the lateral response of modified rectangular fiber-reinforced elastomeric isolators (MR-FREIs)**. *Engineering Structures* **85,** 293–303 (see page 142).

DECLARATION OF AUTHORSHIP

I hereby declare that this thesis is my own unaided work. All direct or indirect sources used are acknowledged as references.

Naples, February 03, 2022

Simone Galano